



Hybrid semiconductor lasers for advanced coherent formats in datacenter interconnects

Théo Verolet

► To cite this version:

Théo Verolet. Hybrid semiconductor lasers for advanced coherent formats in datacenter interconnects. Optics / Photonic. Université Paris-Saclay, 2020. English. NNT : 2020UPAST006 . tel-03142749

HAL Id: tel-03142749

<https://theses.hal.science/tel-03142749>

Submitted on 16 Feb 2021

HAL is a multi-disciplinary open access archive for the deposit and dissemination of scientific research documents, whether they are published or not. The documents may come from teaching and research institutions in France or abroad, or from public or private research centers.

L'archive ouverte pluridisciplinaire **HAL**, est destinée au dépôt et à la diffusion de documents scientifiques de niveau recherche, publiés ou non, émanant des établissements d'enseignement et de recherche français ou étrangers, des laboratoires publics ou privés.

Hybrid Semiconductor Lasers for Advanced Coherent Formats in Datacenter Interconnects

Thèse de doctorat de l'université Paris-Saclay

École doctorale n° 575, electrical, optical, bio: physics and engineering
EOBE

Spécialité de doctorat: Electronique et Optoélectronique,
Nano- et Micro-technologies

Unité de recherche : Université Paris-Saclay, CNRS,
Centre de Nanosciences et de Nanotechnologies, 91120, Palaiseau, France.

Référent : Faculté des sciences d'Orsay

Thèse présentée et soutenue à Palaiseau, le 03 décembre 2020 par

Théo VEROLET

Composition du Jury

Béatrice DAGENS

Directrice de Recherche, CNRS/C2N

Présidente

Philippe GALLION

Professeur Emérite, IMT/ParisTech

Rapporteur & Examineur

Christophe PEUCHERET

Professeur, ENSSAT

Rapporteur & Examineur

Joël JACQUET

Directeur de la recherche, EIGSI / La Rochelle

Examineur

Abderrahim RAMDANE

Directeur de recherche, CNRS/C2N

Directeur de thèse

Alexandre SHEN

Ingénieur de recherche, Nokia Bell Labs / III-V Lab

Co-Encadrant &
Examineur

Frédéric BOEUF

Ingénieur de recherche, ST Microelectronics

Invité

Il faut simplement savoir les choses simples...

Remerciements

Ce manuscrit de thèse n'aurait pas pu voir le jour sans l'aide colossale apportée par tous ceux qui m'ont aidé dans ce travail. Ainsi, avant de dire merci aux différentes personnes m'ayant accompagné de différentes manières lors de mes trois années de thèse, je souhaite d'abord remercier les laboratoires du III-V Lab et C2N pour leur accueil chaleureux, et aussi Nokia Bell Labs France et le service CIFRE de l'ANRT sans qui la réalisation de ce manuscrit aurait été impossible.



C'est ainsi que je souhaite tout d'abord remercier, mon encadrant Alexandre Shen et mon directeur de thèse Abderrahim Ramdane de m'avoir accompagné lors de ces trois années de thèse. Les résultats discutés plus tard n'auraient pas pu voir le jour sans leur bienveillance, support quotidien et discussions techniques.

Je suis également très reconnaissant envers Messieurs les rapporteurs, et l'ensemble des membres du jury à la fois pour leurs remarques et questions pertinentes suite à la soutenance, et aussi pour leurs multiples compliments.

Je tiens à remercier fortement tous les chercheurs du III-V Lab m'ayant conseillé en caractérisation. Tout d'abord Jean-Guy Provost pour sa patience et son expérience dans la mise en place de banc de mesure. Filipe Jorge et Fabrice Blache pour leurs expertises en radiofréquence, et Karim Mekhazni pour ses excellents montages de puces sur embase.

Je tiens aussi à remercier Guy Aubin, pour son exactitude, sa précision, son expérience et sa praticité. Merci aussi à Kamel Merghem, car même si nous ne nous sommes croisés que brièvement, j'ai pu gracieusement utiliser ses bancs de mesure du C2N. Je remercie également ici Quentin Gaimard pour l'organisation particulière de la soutenance liée à la Covid-19.

Je suis aussi très reconnaissant envers l'équipe « Silicon Photonic » du III-V Lab, pour leur accueil durant ses trois dernières années. Merci à David Bitauld et Joan Ramirez.

Je suis aussi reconnaissant envers l'équipe de Sébastien Bigo à Nokia Bell Labs France de m'avoir accueilli plusieurs semaines pour réaliser de nombreuses expériences de transmission. Ainsi je remercie Sylvain Almonacil, Haik Mardoyan, Mijail Szczerban, Jose Estarán, Nihel Benzaoui et Eric Dutisseuil.

Also I would like to thank the Liam Barry's photonic research group in Dublin City University for their warm welcome during some scientific collaboration. Thanks a lot, to Liam Barry, Yi Lin, Amol Delmade, Colm Browning and Elias Giacomidis.

Je souhaite aussi remercier les équipes du CEA Leti avec qui nous avons collaborés. Encore merci à Ségolène Olivier, Karim Hassan, Benoit Charbonnier, Christophe Jany et Stéphane Malhouitre.

Ma gratitude va aussi envers tous les épitaxieurs et technologues III-V ayant réalisé nos circuits photoniques. Tout d'abord, merci à Jean Decobert, qui en plus d'avoir fabriqué d'incroyables structure à puits quantiques, m'a expliqué clairement le diagramme 'maille / bandgap'. Merci aussi à Delphine Néel pour notamment ses nombreuses explications concernant la fabrication. Ici, je tiens aussi à remercier Nicolas Vaissière et François Lelarge ayant épitaxiés la plupart des lasers présentés dans la thèse. Et également Arnaud Wilk et Alexandre Garreau pour les nombreuses discussions.

Ma gratitude va aussi envers Alfredo de Rossi, pour les nombreuses discussions techniques que nous avons eu au cours des dernières années. Je tiens aussi à remercier Sylvain Combré, Ines Ghorbel et Léa Constans.

Un grand merci aussi aux nombreux thésards du III-V Lab de m'avoir supporté lors des trois dernières années, Antonin Gallet, Hajar Elfaiki, Sylvain Boust, Pierre Fanneau, Thomas Poletti, Kebede Tesema, Claire Besancon, Romain Hersent et Sébastien Aroulanda.

Merci aux autres membres du III-V Lab que je n'ai pas encore remercié jusqu'à présent pour leurs discussions du coin café. Merci à François Duport, Frédéric Van Dijck, Cosimo Calo, Christophe Caillaud, Giancarlo Cerulo, Jean-Luc Reverchon, Alexandre Delga, Catherine Fortin, Harry. Garriah, Dalila Make, Colin Mismar, Delphine Lanteri et Alessandro Aimone. Merci également à Pascale Téfaïne pour sa gentillesse et l'aide régulière concernant les formalités administratives. Merci aussi à Hélène Debregeas pour les quelques discussions techniques lors de mes débuts de thèse.

Enfin, je suis très reconnaissant envers mes amis de Supélec qui m'ont suivi pendant la thèse. Notamment merci à Alexandre, Amaury, Arthur, Matthieu, Charles et Jean.

Finalement, je remercie toute ma famille et particulièrement mes parents.

Diodes Lasers Hybrides pour les Communications Cohérentes Avancées dans les Datacenters

(Résumé)

I. Abstract

L'augmentation exponentielle du transport d'information au sein des centres de données, ne peut être supportée que par de nouvelles technologies de transpondeurs optiques. Par rapport aux systèmes fondés sur les formats de modulation et détection directe, il est couramment reconnu que la technologie cohérente permet de transmettre à plus haut débit sur de plus longues distances, au dépend d'une plus grande complexité. Ainsi, la miniaturisation des systèmes cohérents est nécessaire pour réduire à la fois leurs coûts et consommations. Les travaux de thèse se concentrent sur l'étude de sources lasers compactes, dont les performances permettent l'utilisation de formats cohérents de complexité supérieure à 4 bit/symbole/polarisation.

Un premier chapitre introductif rappelle à la fois le fonctionnement et les spécifications des transpondeurs cohérents dans un datacenter. Dans ce chapitre, les caractéristiques souhaitées des diodes lasers intégrées dans ses transmetteurs sont quantifiées. Il est notamment montré que le bruit de phase du laser –souvent évalué par sa largeur de raie– est un paramètre crucial pouvant détériorer les performances des systèmes cohérents. Les trois chapitres suivants concernent l'étude de trois diodes lasers différentes de complexité croissante, toutes à faible bruit de phase et permettant de supporter des formats complexes. La première diode étudiée, est un laser à rétroaction distribuée (notée DFB pour «distributed feedback laser»), fabriquée dans la technologie III-V sur Silicium et émettant une raie optique ultra fine. Des simulations optiques permettant d'obtenir les paramètres optimaux du réseau de ce type cavités seront présentées. Ensuite nous étudierons un laser III-V sur Silicium, formé d'une cavité étendue rapidement accordable possédant des propriétés spectrales remarquables. Dans ce chapitre nous présenterons des résultats records de communication cohérentes par paquet optique. Le dernier chapitre se focalise sur l'étude de phénomènes de rétro-injection optique dans les lasers à verrouillage de mode émettant un peigne de fréquence. Il est notamment montré qu'un unique régime de rétroaction permet une réduction drastique des largeurs de chaque raie du peigne.

II. Chapitre introductif

Dans ce chapitre introductif, nous rappelons le principe des communications cohérentes. Le schéma le plus simple est composé d'un transmetteur mono canal, dans lequel un laser faible bruit émet un signal servant de porteuse optique. Un signal vectoriel est appliqué sur la porteuse grâce à un modulateur I/Q («in phase / quadrature»), permettant de changer à la fois les niveaux de la partie réel et imaginaire du signal laser. Ce signal est souvent amplifié par un amplificateur à semiconducteur (SOA «semiconductor optical amplifier») avant d'être transmis dans une fibre optique. A la détection, le signal transmis est mixé avec le signal d'un laser agissant comme oscillateur local, dans un schéma d'homodyne.

Après détection sur un set de photodiodes balancées, nous pouvons retrouver la phase et l'amplitude du signal transmis, ceux-ci sont équivalents à ses parties réelles et imaginaires après conversion polaire/cartésienne. Même si de nombreuses sources de bruits compliquent l'évaluation de l'amplitude du signal transmis, la majeure limitation des performances du lien optique est liée au bruit de phase du laser, pouvant être approximé par une trajectoire Brownienne. Ainsi de nombreux algorithmes ont été développés pour suivre la phase du laser, mais lorsque son évolution devient trop brusque, ces algorithmes ne sont plus efficaces. La figure 1 montre la pénalité de SNR («signal to noise ratio») entre l'optimum dérivé dans la théorie de l'information en ne supposant aucun bruit de phase, et les cas avec bruit de phase. Nous pouvons remarquer qu'une pénalité basse peut être obtenue seulement avec des lasers très stables (largeur de raies < 20 kHz), pour des formats complexes tel que le 64QAM. Ainsi, les lasers étudiés devront posséder des largeurs de raies réduites pour supporter les formats les plus complexes.

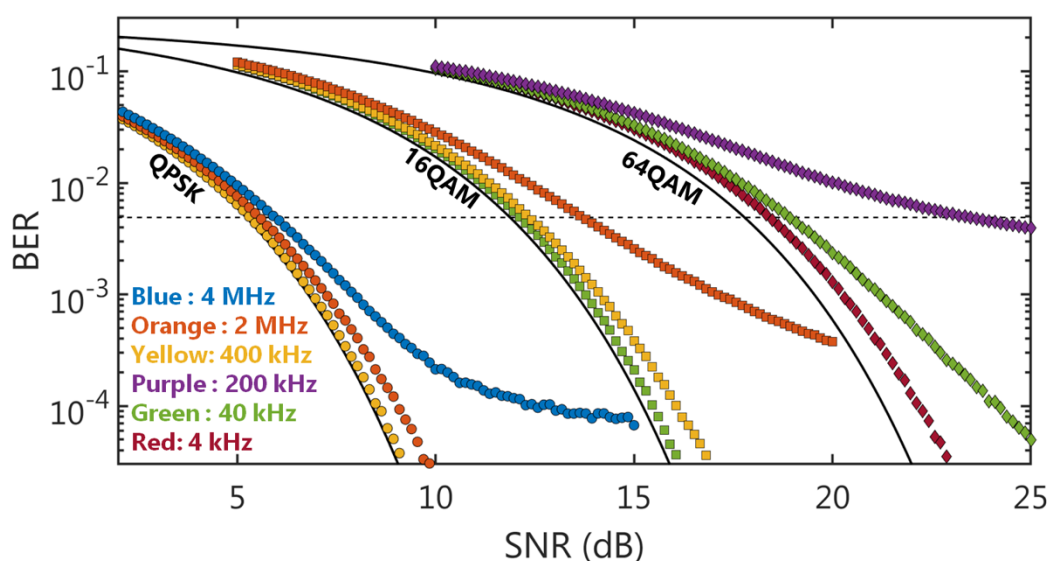


Fig.1 Taux d'erreur en fonction du format de modulation pour différentes largeurs de raie. Les courbes noires correspondent aux optimums théoriques.

III. Laser à rétroaction distribuée à grande cohérence

Dans ce premier chapitre nous étudions les propriétés spectrales de laser DFB à fort facteur de qualité (HQ pour « high quality») fabriqué dans la technologie III-V sur Silicium. Ce type de cavité a déjà été introduit par [1], mais l'optimisation de son réseau n'avait pas été étudié. Le principe de la cavité est fondée sur un réseau de type «cristal photonique» en une dimension, dont le centre est apodisé pour former un puits de potentiel photonique (Fig.2.a)). Ainsi les photons sont confinés au centre du DFB tandis que la profondeur et longueur du puits influent sur les propriétés modales de la cavité. De plus, les parties extérieures correspondant aux barrières (par analogie à l'électronique quantique), permet de choisir le facteur de qualité de la cavité.

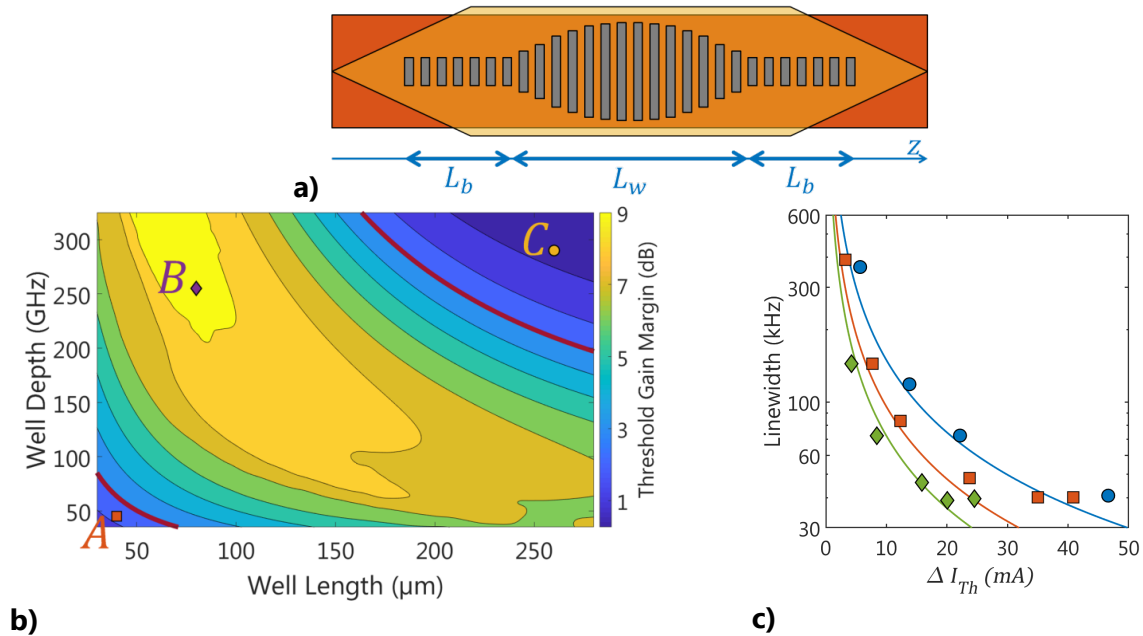


Fig.2. a) Schéma du laser DFB b) Différence de gain au seuil pour différents paramètres de réseau c) Largeur de raie simulée et mesurée pour différents designs

Le modèle de simulation développé au cours de la thèse est fondé sur le formalisme des matrices transferts. La matrice de transfert du DFB est ensuite développée au premier ordre autour de ses pôles pour extraire des équations de taux de population équivalentes. Ainsi, pour une taille de laser prédéfinie, en faisant varier la profondeur de son puits et de sa longueur nous pouvons simuler ses caractéristiques que sa différence de gain au seuil (Fig.2.b)), sa puissance émise, son temps de vie des photons... Ainsi nous pouvons obtenir le couple : profondeur/longueur du puits conduisant au fonctionnement optimal du laser.

Le modèle numérique a ensuite été confirmé par des résultats expérimentaux montrant la possibilité d'estimer les performances des DFBs HQ grâce à un simple modèle d'équation de

taux de population. Les mesures ont aussi démontrés que ce type de laser possédait une largeur de raie inférieur à 50 kHz (Fig.2.c)). Ainsi, nous avons démontré que ces lasers pouvaient servir de sources bas coût idéal pour les communications cohérentes.

IV. Accordabilité rapide de laser III-V sur Silicium

Dans le second chapitre de la thèse, les propriétés d'accordabilité rapide de laser à cavité étendue sont étudiées. Dans ce type de laser, la rétroaction optique permettant l'émission stimulée est fournie par un circuit en Silicium comportant deux anneaux en configuration Vernier comme montré dans la figure 3.a). Ainsi, la rétro-injection optique s'effectue sur un unique mode Fabry-Pérot. Finalement, en accordant le miroir sélectif en Silicium grâce aux effets électro-optiques [2], il est possible de reconfigurer la diode laser en quelques nanosecondes. Dans ce chapitre de thèse, nous avons mis en place une méthode de mesure permettant de mesurer les dérives fréquentiels du laser lors des sauts de mode. Grâce a cette méthode, nous avons pu caractériser la dynamique de reconfiguration de longueur d'onde du laser, et comme nous pouvons le voir dans la figure 3.b), le laser change de canal et se stabilise en un temps inférieur à 2 ns.

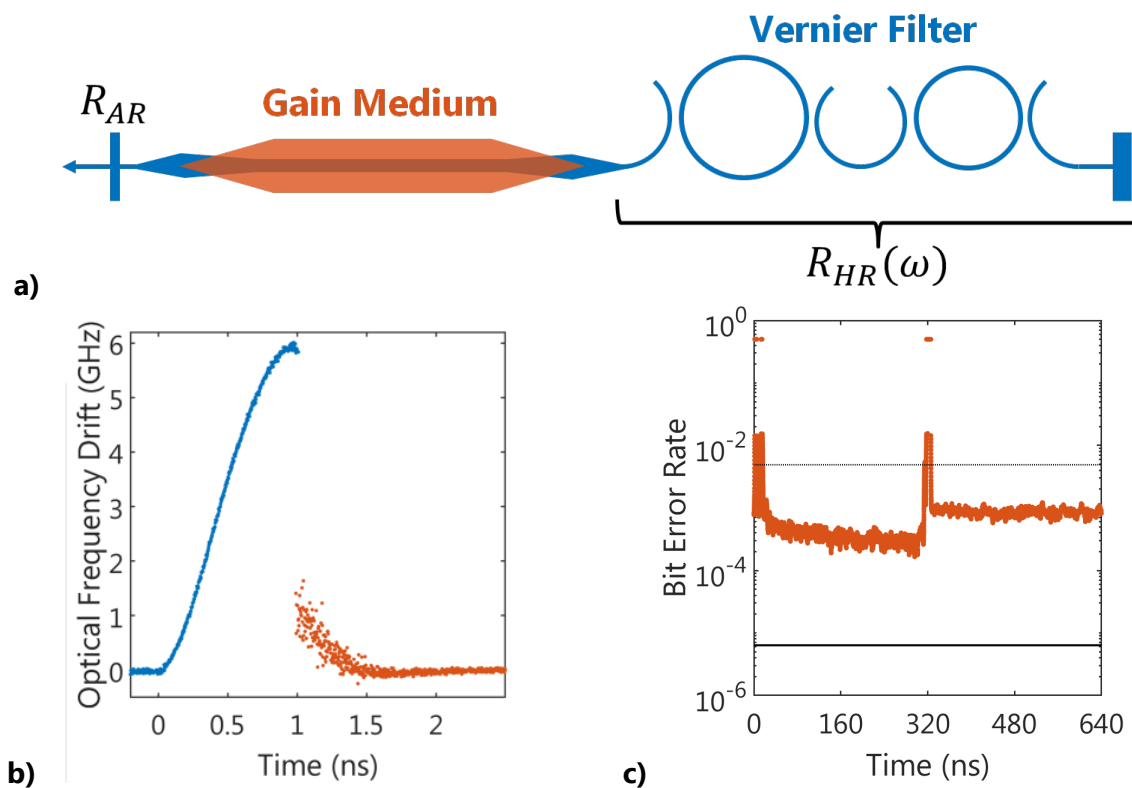


Fig.3. a) Schéma du laser à cavité étendue b) dérive fréquentielle lors d'un saut de mode de 400 GHz c) BER en utilisant un format DP-16QAM dans des communications par paquet.

Ensuite, nous avons étudié les propriétés de largeur de raie du laser à la fois de manière expérimentale et théorique en utilisant le formalisme de Kazarinov et Henry [3]. Nous avons notamment démontré que le bruit de phase du laser permet de transmettre des données dans un format 16QAM, utilisant aussi le multiplexage de polarisation avec un taux d'erreur sous la limite FEC (FEC pour «forward error correction»). Finalement, nous avons effectué - pour la première fois à notre connaissance- des transmissions cohérentes par paquet optique avec un temps de reconfiguration système de quelques nanoseconde. La figure 3.c) montre le taux d'erreur mesuré résolu temporellement lorsque des paquets de 320 nanosecondes et un format DP-16QAM étaient utilisés.

V. Réduction du bruit de phase dans les lasers à verrouillage de mode

Dans ce dernier chapitre de thèse, nous avons étudié les propriétés de bruit de phase de laser à verrouillage de mode (MLL pour «mode locked laser») sous rétro-injection optique [4]. Les propriétés de rétro-injection ont été étudiées avec un MLL utilisant une unique section de gain formée de bâtonnets quantiques. Le montage expérimental (Fig.4.a)) est composé d'une cavité externe en espace libre, permettant de rétro-injecter le signal laser sans dispersion ni rotation de polarisation. Ainsi, tout comme pour les lasers monomodes [5], nous avons souligné les différents régimes de rétro-injection du laser à verrouillage de mode, et nous avons démontré que sous certaines conditions de feedback les propriétés de bruit du laser peuvent être drastiquement améliorées.

Le laser à verrouillage de mode peut-être utilisé pour fournir un canal de communication basé sur le multiplexage en longueur d'onde (~ 50 GHz) (DWDM, pour «dense wavelength division mulitplexing»). Chaque raie optique de ce canal, peut ensuite servir de porteuse transmettant un signal cohérent. Ainsi, les propriétés spectrales de chaque mode longitudinal du laser jouent un rôle clé sur les performances du lien DWDM. Nous avons démontré que la rétro-injection optique permet de réduire considérablement le bruit de fréquence de chaque raie du peigne sortant du MLL, au prix d'harmoniques à la fréquence de la cavité externe.

Finalement, nous avons réalisé des expériences de transmission cohérentes en partenariat avec le groupe de recherche de Pr. L. Barry à DCU (Dublin City University), en utilisant le laser sous rétro-injection optique. Nous avons démontré que la rétro injection permet de réduire drastiquement la pénalité liée au bruit de phase, et en utilisant des signaux 16QAM, nous avons démontré des transmissions dont le débit serait supérieur à 4 Tbit/s.

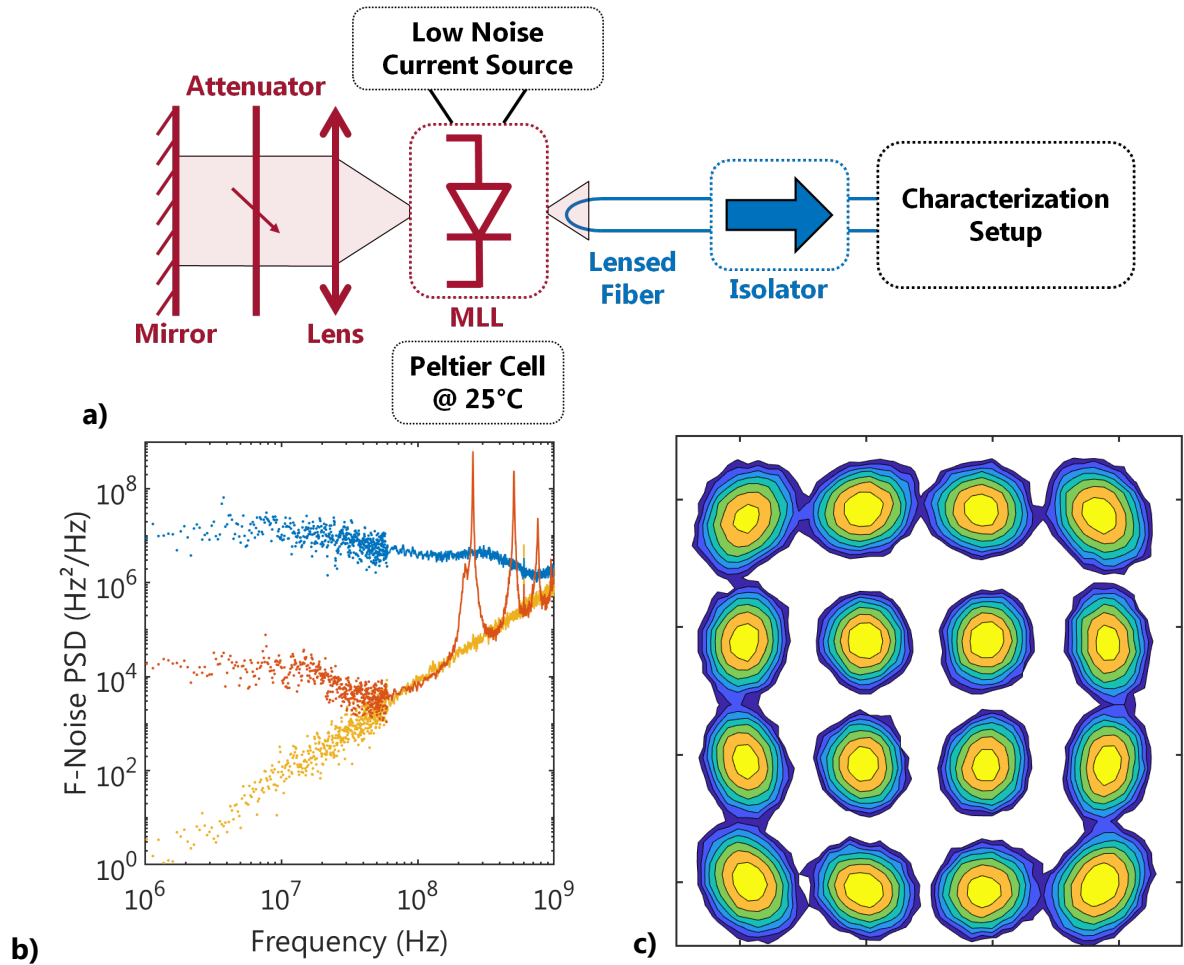


Fig.4. a) Montage expérimental pour mesurer les propriétés de rétro-injection b) Bruit de fréquence d'une raie c) BER résolu temporellement en utilisant un format DP-16QAM dans des communications par paquet.

VI. Conclusion

Pour conclure, nous avons étudié trois diodes lasers permettant d'améliorer les performances des liens de transmission cohérentes. Le premier laser étudié, consiste en un DFB dont la largeur de raie est très proche de l'état de l'art (<50 kHz). Ce dispositif, pourrait être communément répandu dans les systèmes cohérents à faible coût. Ensuite, le saut de canal rapide de laser à cavité étendu à été précisément analysé. Les propriétés d'accord de ce type de laser faible largeur de raie permettent d'utiliser les formats de modulation vectoriels avec les protocoles de communication par paquet optique. Finalement, les propriétés de bruit de phase de laser à verrouillage de mode ont été améliorées en utilisant le principe de

la réinjection optique, ce qui a permis de démontrer des transmissions cohérentes à plusieurs Tbit/s en utilisant une unique source de lumière.

VII. Références

- [1] C. T. Santis, S. T. Steger, Y. Vilenchik, A. Vasilyev, and A. Yariv, "High-coherence semiconductor lasers based on integral high-Q resonators in hybrid Si/III-V platforms," *Proc. Natl. Acad. Sci. U. S. A.*, vol. 111, no. 8, pp. 2879–2884, 2014.
- [2] R. Soref and B. R. Bennett, "Electro-optical effects in Silicon," *J. quantum Electron.*, vol. 74, no. 1, pp. 305–307, 1987.
- [3] R. F. Kazarinov and C. H. Henry, "The Relation of Line Narrowing and Chirp Reduction Resulting from the Coupling of a Semiconductor Laser to a Passive Resonator," *IEEE J. Quantum Electron.*, vol. 23, no. 9, pp. 1401–1409, 1987.
- [4] T. Verolet *et al.*, "Mode Locked Laser Phase Noise Reduction Under Optical Feedback for Coherent DWDM Communication," *J. Light. Technol.*, vol. 38, no. 20, pp. 5708–5715, 2020.
- [5] R. W. Tkach and A. R. Chraplyvy, "REGIMES OF FEEDBACK EFFECTS IN 1.5- μ m DISTRIBUTED FEEDBACK LASERS," *J. Light. Technol.*, vol. LT-4, no. 11, pp. 1655–1661, 1986.

Index

| | |
|---|-----|
| Chapter 1 : Introductive Chapter..... | 1 |
| I. Datacenter coherent links..... | 2 |
| II. Laser for coherent transmission systems..... | 7 |
| III. Conclusion..... | 27 |
| IV. References..... | 28 |
| Chapter 2 : Very High Coherence DFB Lasers..... | 33 |
| I. III-V on SoI Narrow Linewidth DFB Lasers..... | 35 |
| II. Transfer Matrix Simulation of HQ DFB Lasers..... | 44 |
| III. HQ DFBs characterizations..... | 56 |
| IV. Conclusion..... | 66 |
| V. References | 67 |
| Chapter 3 : Fast Tunability of Narrow-Linewidth III-V/Si Extended Cavity Laser..... | 71 |
| I. Introduction..... | 73 |
| II. Laser Fast Wavelength Tuning..... | 80 |
| III. Linewidth Properties..... | 92 |
| IV. Coherent optical slot switching..... | 100 |
| V. Conclusion..... | 107 |
| VI. References..... | 108 |
| Chapter 4 : Mode Locked Laser Phase Noise Reduction..... | 112 |
| I. Introduction..... | 114 |
| II. SS-QDash-MLL feedback regimes..... | 121 |
| III. Noise properties under coherent feedback..... | 132 |
| IV. Transmission experiments results..... | 140 |
| V. Conclusion..... | 147 |
| VI. References..... | 148 |
| Conclusion..... | 154 |
| Annex..... | 158 |
| I. Annex A : a possible justification of laser rate equations | 158 |
| II. Annex B : Wave propagation in periodic media..... | 162 |
| III. Annex C : Generalization of rate equations for complex cavity..... | 165 |

Chapter 1

Introductory Chapter

| | |
|--|----|
| Chapter 1 Introductory Chapter | 1 |
| I. Data center coherent links | 2 |
| I.1. Optical communication systems..... | 2 |
| I.2. Data center network | 4 |
| I.3. Optical coherent communication system | 7 |
| I.4. Conclusion..... | 15 |
| II. Lasers for coherent transmission systems..... | 17 |
| II.1. Laser phase noise : a theoretical approach | 17 |
| II.2. Technologies for narrow linewidth lasers | 22 |
| III. Conclusion | 27 |
| IV. References..... | 28 |

I. Data center coherent links

In this introductive part, we first give a brief historical presentation of fiber communications pointing out the high level frame of most optical communication systems. Then datacenter networks are briefly illustrated, showing how coherent technology is moving into datacenter facilities. In this section the principle of datacenter switches is also shortly explained. Finally, the physics of coherent communication is discussed and laser specifications required for high performance coherent systems are highlighted.

I.1. Optical communication systems

The science of optical communications emerged since the pioneering work of C. Kao *et. al.* [1] reporting on performance improvement of optical Silica fiber in the 1970's. However, major advances in optical transmission systems were made possible only after the demonstration of room temperature operation of laser diodes [2]. The simultaneous availability of low loss fibers and mass producible optical sources have paved the way to the development of optical links operating at few Gbit/s of data rate and allowing over 40 km of transmission reach in the early 1980's [3]. As four decades passed, major technological improvements have led to a drastic increase in both capacity and transmission reach of optical systems. Transmission experiments showing 172 Tbit/s over 2040 km were readily demonstrated in 2020 [4]. Even though this result corresponds to a 8600-fold increase of data rate compared to [3], the core principle of optical communication systems have remained similar during the evolution of the optical communication science.

Fig.1.1.a) illustrates the general frame of a fiber communication system. A laser diode is commonly used as a light source to generate a single frequency lightwave in the near infrared domain (from 1250 nm up to 1650 nm). This electromagnetic wave is used as an optical carrier in which data are encoded with a modulator. In a general case digital encoding is preferred over analog signals, as it benefits from both widely available digital electronic devices and the complete theoretical background of the information theory. The set of devices used to transmit data are often referred to as the transmitter (Tx). The optical signal then travels through optical fiber, and its propagation can be modeled with a generalized non-linear Schrödinger equation [5] taking into account light velocity dispersion, linear losses and third order non linearities. For a transmission reach over 50 km optical amplifiers, being key elements in fiber optic transmission, may be used to compensate the fiber attenuation. The receiver (Rx) consists of an optical detector converting the optical signal back into the electrical domain in which the data are finally recovered using digital electronics circuits.

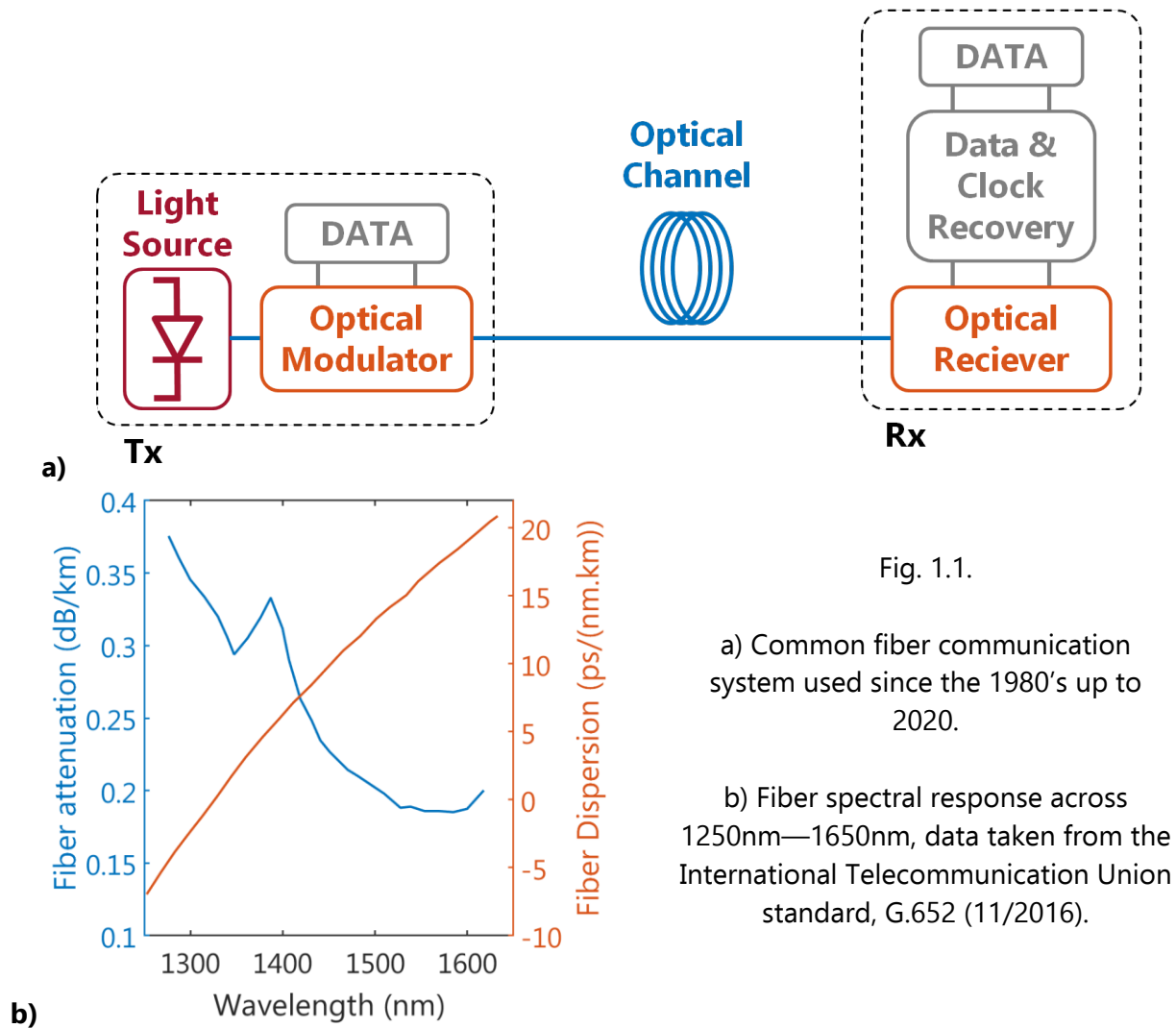


Fig. 1.1.

a) Common fiber communication system used since the 1980's up to 2020.

b) Fiber spectral response across 1250nm—1650nm, data taken from the International Telecommunication Union standard, G.652 (11/2016).

Optical fiber communications in single mode fiber (SMF) mainly occurs in two frequency bands named the O-band and C-band, with O standing for original and C for conventional. Fig.1.1.b) illustrates the standardized G.652.D SMF spectral response. Due to lower Rayleigh scattering, fiber absorption decreases for increases wavelength up to 1550 nm while for wavelength higher than 1550 nm fiber losses increase back due to the rise of the silica medium losses coefficient. Hence, the C-band which is widely used in the telecom domain corresponds to the frequency band 1535nm—1565nm achieving minimal fiber absorption, and also matching the amplification range of Erbium Doped Fiber Amplifiers (EDFA). However, due to the relatively high fiber dispersion in the C-band (around $17 \text{ ps}/(\text{nm.km})$ at 1550 nm), some communication systems also operate in the O-band, ranging from 1260nm to 1360 nm, in which the dispersion is close to zero. However, we will later see that coherent optical systems mostly operate in the C-band, as fiber dispersion can easily be compensated using state of the art coherent digital signal processing.

I.2. Data center network

In this section, the structure of a datacenter network is briefly illustrated, and the use of coherent technology in datacenter facilities is highlighted. We also describe the pluggable optical module used within datacenter racks in order to emphasize the importance of compact optical technologies.

I.2.a. Datacenter Network architecture and link standard

As seen in I.I, optical communication is an efficient way to transmit data both at a high rate and over long distances, so it became the preferred method used for datacenter communication. In datacenter networks, information transits from the servers up to the metropolitan network by being routed through a multitude of switching elements which may be organized in a tree pattern as shown in Fig 1.2. We note that Fig.1.2 only represents a simplified frame of a data center network.

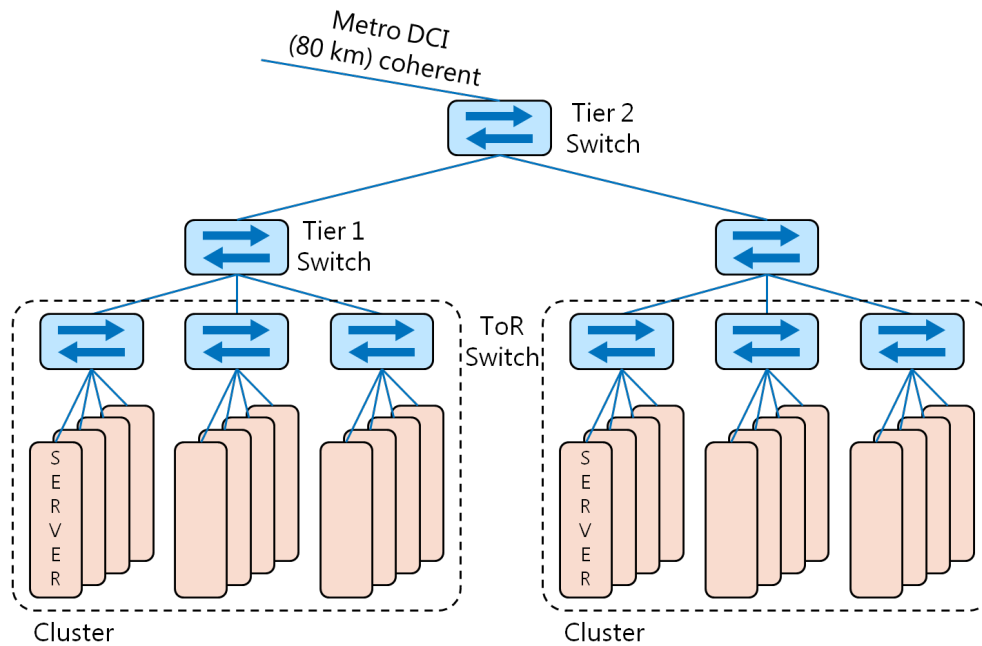


Fig. 1.2. Simplified schematic of a datacenter network

The first level of switches are placed on the top of the servers rack, hence their name “top of the rack (ToR) switches”. For these short distance links in the 3m—100m range, the roadmap for 2022 is to deploy 100G interfaces [6] with a N G interface meaning that the transmission link operates at N Gbit/s of net data rates. As today’s mega-datacenters comprise hundreds of thousands of servers [7] low cost technologies need to be deployed between ToR switches

and servers. For instance optical systems based on 850 nm vertical external cavity surface emitting lasers (VECSELs) (100GBase-SR4 interface) may be used. Note that, as link distance is relatively short, copper technology could also be used (100GBase-CR4 interface). The specifications of datacenter interconnect (DCI) interfaces referred in this section are summarized in Table 1.1.

Then information transits from the ToR switches up to “Tier 1” switches. As the transmission reach between ToR and Tier 1 switches is in the 100m—500m range, only optical technologies would be used, and as mentioned in [6] the roadmap for 2022 is to deploy 400G interfaces based on either 850 nm VECSELs (400GBase-SR8 interface) or silicon photonics circuits or directly modulated lasers (DMLs) (400GBase-DR4 interface).

After that, the information is routed from Tier 1 switches up to Tier 2 switches. For these links the transmission reach rise to the 500m—2km range and 400G interfaces should also be deployed in the next years [6]. As the transmission reach increases, 850 nm VECSEL technologies start to hit their limits and optical transceivers based on silicon photonics chips, DMLs, or electro modulated lasers (EMLs) could be used. Some of the different possible specified interfaces could be 400GBase-DR4, 400GBase-FR4 & 400GBase-FR8.

| Interface | Transmission Support | Communication Format per lane | Optical Transceivers technology |
|---------------------|--|--------------------------------|------------------------------------|
| 100GBase-CR4 | 4 // Twinmax Copper cable, <7m | 25.8 Gbit/s electrical signals | None |
| 100GBase-SR4 | 8 // MMF, <100m | 26.6 Gbaud NRZ, 850 nm | VECSELs array |
| 400GBase-SR8 | 16 // MMF, <100m | 26.6 Gbaud PAM4, 850 nm | VECSELs array |
| 400GBase-DR4 | 8 // SMF, <500m | 53.1 Gbaud PAM4 O-band | EML, DMLs and SiP. |
| 400GBase-FR8 | 2 // SMF, <2km | 8*26.6 Gbaud PAM4 CWDM O-band | Mostly EML (could be DMLs and SiP) |
| 400GBase-FR4 | 2 // SMF, <2km | 4*53.1 Gbaud PAM4 CWDM, O-band | Mostly EML (could be DMLs and SiP) |
| 400GBase-LR4 | 2 // SMF, <10km | 4*53.1 Gbaud PAM4 CWDM, O-band | Mostly EML and SiP (could be DMLs) |
| 400GBase-ZR | 2 // SMF, Mux / De-Mux, WDM link, <80 km | 64 Gbaud DP-16QAM, C-band | Coherent transceiver |

Table 1.1 400G datacenter interfaces [6] SMF : single mode fiber, MMF : multimode fiber, // for parallel, NRZ : non return to zero, PAM : pulse amplitude modulation, (De-)Mux : (de-)multiplexer. DP : dual polarization, QAM : quadrature amplitude modulations.

Finally the information is transmitted from the datacenter facility in the optical network. In this case the transmission reach drastically increases up to 80 km and 400G interface is being deployed. As intensity modulation / direct detection (IMDD) systems used for shorter links

are hitting a limit to reach 80 km with 400 Gbit/s of net data rate, coherent transceivers will be deployed. Moreover, signals coming from the Tier 2 switches are multiplexed before being transmitted in the network, which imply that these links rely on dense wavelength division multiplexing (DWDM) technology. As most DWDM systems, DCI performances are limited by the link spectral efficiency, pushing for higher order coherent format. We will later show that complex coherent systems require low noise lasers, so a major part of the thesis will report on the noise reduction of compact laser diodes which could then be used in 400GBase-ZR interfaces and beyond. In addition, to that these longer transmission links are becoming more and more common in mega-datacenters, and for applications such as cloud computing and disaggregated networks [8] highlighting the importance of low cost and high performances coherent transceivers.

I.2.b. Datacenter switches

As of 2020, the optical transceiver chipsets used in datacenters are packaged in different types of small form factor pluggable (SFP) modules. For instance, Fig.1.3.a) depicts a Quad SFP dual density (QSFP-DD) package which is one of the standardized SFP module. As we can see in Fig1.3.a), the relatively small size of the package, pushes for conceiving, fabricating and commercializing very compact optical components.

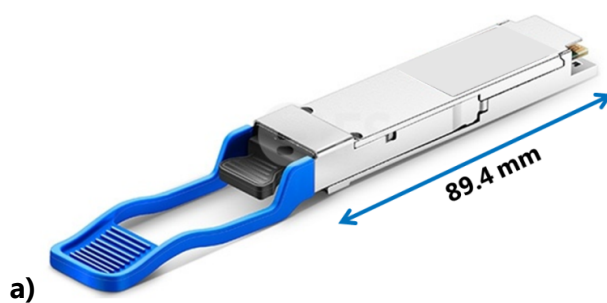


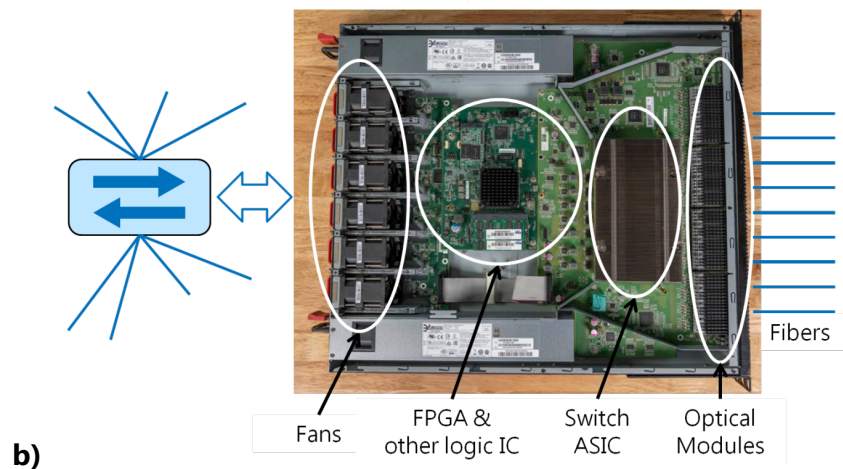
Fig. 1.3.

a) Quad SFP dual density (QSFP-DD) package taken from :

<https://www.cisco.com/>

b) Edgecore™ AS7712-32X switching fabric. Photo is from :

<https://www.servethehome.com/>



The SFP modules are then directly plugged in a switching rack as illustrated in Fig.1.3.b) which shows a datacenter switch commercialized by Edgecore™. Optical signals are down converted in the electrical domain by optical transceivers, and then electrical signals travel from the SFP modules to a switching application-specific-integrated-circuit (ASIC) through radiofrequency (RF) lines. The control electronics, power supply and fans used for cooling can be seen on the left of the switching rack. For order of magnitude, the power consumption of the Edgecore™ switch shown here is around 500W, and this figure does not take into account the optical modules power consumption. Moreover, the power consumption within a SFP module containing a 400G-ZR chipset should be under 15W, showing the importance of energy efficient lasers for coherent communication systems.

I.3. Optical coherent communication system

As the thesis targets design, modeling and characterization of lasers for high performance coherent links, a simple overview of coherent systems is given in the following subsections. First, the structure of a coherent link is detailed, and similarities with the generic optical link sketched in 1.1.a) can be noticed. Then the relation between the retrieved data with laser performances is derived, highlighting the influence of laser noise characteristics on the coherent system. It will then be seen that laser phase noise plays a key role in a coherent link, and digital methods traditionally used for phase noise mitigation will be discussed. Finally the trend taken by coherent systems will be examined.

I.3.a. Principle of coherent communication

To figure out laser specifications required in a coherent system, we briefly remind some of the fundamentals of fiber coherent communication. The reader could refer to e.g. [9] if complementary information is needed. As it can be seen in Fig.1.4.a) depicting a generic coherent link, the transmitter consists of a single mode laser diode which lightwave is modulated using coherent formats by an inphase/quadrature (IQ) modulator. The modulated signal may be amplified by a semiconductor optical amplifier (SOA) or an EDFA before transmission and an optical isolator is generally used to protect the laser diode from parasitic reflection. After propagated through single mode fiber, the transmitted signal is mixed with a second laser, referred to as a local oscillator (LO) in a homodyne scheme and usually, a two by four multimode interferometer is employed for mixing. Finally the mixed signals beat on two sets of balanced photodiodes (PDs), and transmitted data are retrieved in the electrical domain.

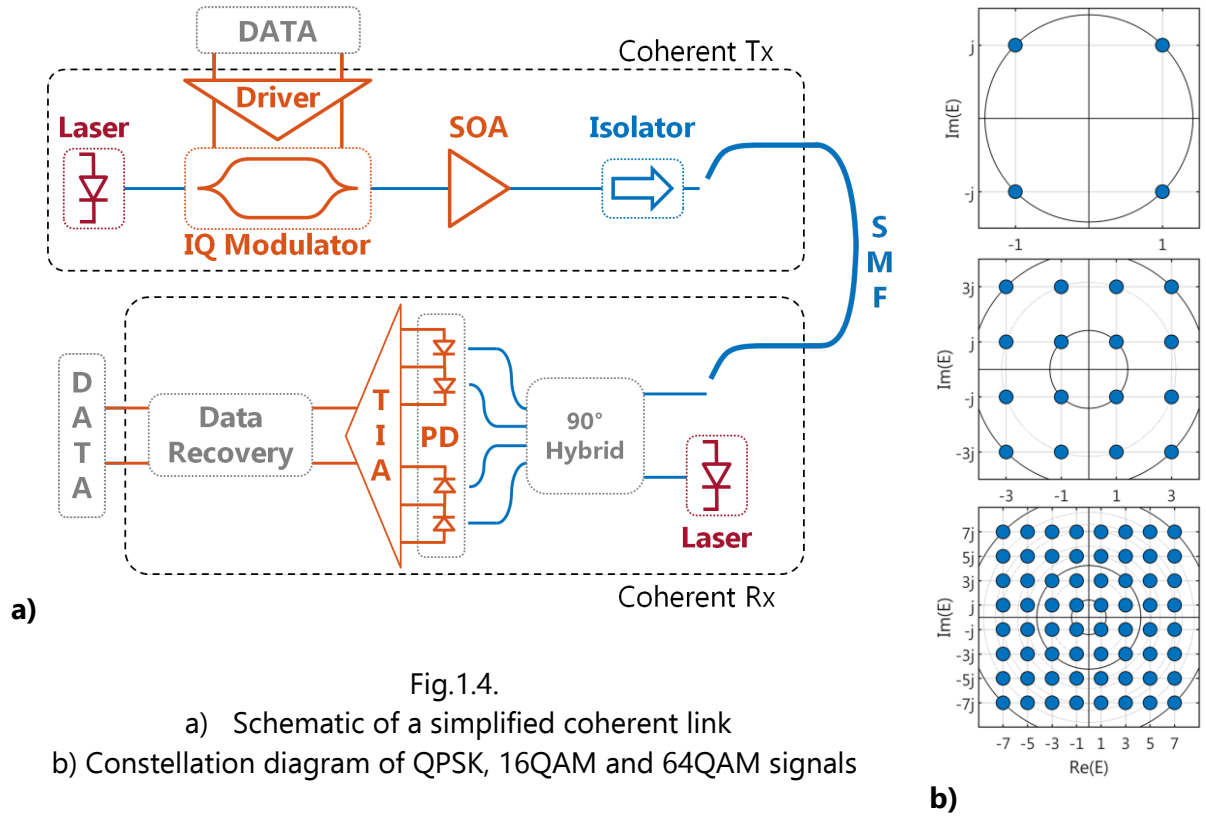


Fig.1.4.

a) Schematic of a simplified coherent link

b) Constellation diagram of QPSK, 16QAM and 64QAM signals

To quantify which laser characteristics are crucial in a generic coherent system, we will model all components depicted in Fig.1.4.a) –except the lasers– by ideal linear models, moreover neither chromatic dispersion (CD) nor non-linear effects are considered in the fibered link. In practical case both CD and fiber non-linearities (NL) impairments can be mitigated with digital signal processing (DSP) methods [10], [11]. While CD is always compensated with typical coherent DSP, the computational cost of non-linear back propagation algorithm makes it impractical to be used in low-cost systems [10]. For the sake of simplicity we will deal with single polarization format, and assume that the field polarization at the receiver remains unchanged. In real systems, time varying polarization rotations are alleviated using both a dual-polarization receiver and digital channel estimation methods such as constant modulus algorithm [10], [12].

The laser emitted wave is written $\sqrt{P_c}e^{j(\omega_c t + \varphi_c)}$ with P_c the laser power, ω_c the mode pulsation and φ_c the laser randomly fluctuating phase. In this model, laser relative intensity noise (RIN) is neglected. It can be justified by considering a poor white RIN floor at e.g. -145 dBc/Hz, and in this case the laser signal to noise ratio (SNR) in a 32 GHz bandwidth is around 40 dB. This SNR value will be shown to be more than sufficient for coherent communication up to 64 quadrature amplitude modulation (QAM) formats.

The modulating sequence is written $\{A_m e^{j\theta_m}\}$, and we assume that traditional Gray encoded quadrature phase shift keying (QPSK) and QAM format are used with their constellations illustrated in Fig.1.4.b). Note that $A_m \in [0,1]$, while Fig.1.4.b) plots the constellations on a usual scale for illustration purposes. Then, for simplicity we assume that the SOA operates in its linear regime of gain G , and also adds a white Gaussian noise. Under the strong hypothesis mentioned above, propagation inside SMF is modeled by only an attenuation coefficient L . Then, the transmitted signal $E_t = GL\sqrt{P_c} A_m e^{j(\omega_c t + \theta_m + \varphi_c)}$ is mixed with the LO lightwave $E_{LO} = \sqrt{P_{LO}} e^{j(\omega_{LO} t + \varphi_{LO})}$ written using the same nomenclature as for the carrier signal. Finally, the beating of the mixed signals $E_t \pm E_{LO}$ and $E_t \pm j E_{LO}$ results in photo-generated current equal to :

$$I_I(t) = KA_m \cos((\omega_c - \omega_{LO})t + \theta_m + \varphi_c + \varphi_{LO}) + i_{n,I} \quad (1.I.1)$$

$$I_Q(t) = KA_m \sin((\omega_c - \omega_{LO})t + \theta_m + \varphi_c + \varphi_{LO}) + i_{n,Q} \quad (1.I.2)$$

with $K = R\sqrt{P_{LO} P_c G L}$ and R corresponds to the photodiode responsivities. $i_{n,I\&Q}$ is a photo-generated current noise resulting from the LO and SOA additive white Gaussian noise (AWGN) beating, photodiodes shot noise and electronic thermal noise (see e.g. [13]–[15] deriving the different noise terms). Note that fiber non-linearity such as four wave mixing in a WDM link may also be included in i_N [5], [16], [17], setting the widely referred “Non-linear Shannon limit”. For datacenter interconnect the launch power per channel is often kept below 4 dBm, meaning that fiber non-linearities can be neglected.

The electrical continuous time currents are then sampled at one sample per symbol (sps) to be recovered in the digital domain, and the retrieved sequence $I_R[k]$ is given in (1.I.3)

$$I_R[k] = I_I[k] + jI_Q[k] = I_m[k]e^{(\theta_m[k] + \varphi[k])} + i_n[k] \quad (1.I.3)$$

$$\varphi[k] = \varphi_c[k] + \varphi_{LO}[k] \quad (1.I.4)$$

with $I_m = KA_m$ and $i_n = i_{n,I} + ji_{n,Q}$. As we can see in (1.I.3), two noise contributions i_n and φ may degrade the transmission performances. As these two terms are uncorrelated, we will separately discuss their impact on the received signal.

I.3.a.i. SNR limitation of a coherent link

As said previously, the noise term i_n corresponds to additive noise sources in the transmission link, and its variance is given in [14] :

$$\langle i_n^2 \rangle = \langle i_{Beat}^2 \rangle + \langle i_{Shot}^2 \rangle + \langle i_{Thermal}^2 \rangle \quad (1.I.5)$$

$$\langle i_{Beat}^2 \rangle = 2eR\eta (G - 1)n_{sp}P_{LO} B \quad (1.I.6)$$

$$\langle i_{Shot}^2 \rangle = e R P_{LO} B \quad (1.1.7)$$

$$\langle i_{Thermal}^2 \rangle = 2 kT B / Z_0 \quad (1.1.8)$$

with i_{Beat} , i_{Shot} , and $i_{Thermal}$ the noise terms respectively related to ASE-LO beating, photodiodes shot noise and electrical thermal noise. The quantities in (1.1.6) – (1.1.8) are detailed in Table 1.2, and using typical values from Table 1.2, we obtain :

$$\langle i_{Beat}^2 \rangle = 2 \times 10^{-8} A^2 \quad \langle i_{Shot}^2 \rangle = 1 \times 10^{-10} A^2 \quad \langle i_{Thermal}^2 \rangle = 6 \times 10^{-12} A^2$$

Hence, the ASE-LO beating is the limiting noise term, and the signal to noise ratio (SNR) can be approximated by :

$$SNR = \frac{\langle I_m^2 \rangle}{\langle i_n^2 \rangle} \cong \frac{\langle I_m^2 \rangle}{\langle i_{Beat}^2 \rangle} \cong \frac{P_C \lambda}{2 h c n_{sp} B} \langle A_m^2 \rangle \quad (1.1.9)$$

Finally, eq. (1.1.9) shows that laser power is of great importance to maintain a high value of SNR. As stated by the Shannon-Hartley theorem and reminded in [5], the capacity of a communication channel will inevitably be limited by the SNR, and Fig.1.5 shows the best achievable error rate of a coherent communication system as a function of its SNR. As it can be seen in Fig.1.5, to operate below a given error rate, the more advanced the format is, the higher the SNR needs to be. Hence, high performance coherent systems require high power laser diodes.

| | | |
|-----------------------|-----------|-------------|
| PD responsivity | R | 1.0 A/W |
| PD quantum efficiency | η | 80 % |
| SOA gain | G | 20 dB |
| SOA inversion factor | n_{sp} | 2 |
| LO emitted power | P_{LO} | 20 mW |
| Receiver temperature | T | 50 °C |
| Receiver impedance | Z_0 | 50 Ω |
| Signal Bandwidth | B | 32 GHz |
| Signal wavelength | λ | 1550 nm |

Table 1.2.

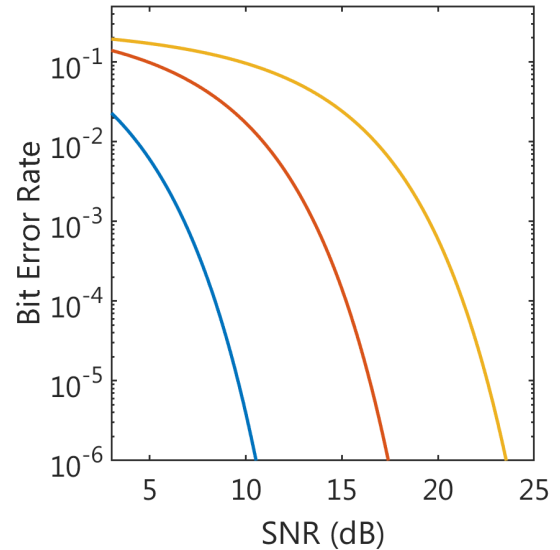


Fig 1.5. BER vs SNR for single polarization QPSK (blue), 16QAM (orange), 64QAM (yellow)

I.3.a.ii. Phase Noise mitigation in Coherent communication

(i) Effect of laser phase noise in a coherent system

After briefly studying the relation between laser power and SNR performance of a coherent link, we now discuss the effect of laser phase noise on a coherent system. Let's first assume $\langle i_n^2 \rangle = 0$ and in this case the phase of the retrieved signal, strictly given by (I.1.4), is strongly affected by the random laser phase drift. As we will see in section II, this random phase fluctuation can be accurately modeled by a Wiener process, which will "slowly rotate" the received constellation. Fig.1.6.a) shows numerically simulated phase evolution of a ~ 300 kHz linewidth laser, and here for simplification laser frequency noise is considered white as in [18]–[20] (and contrary to [21], [22] which takes into account laser dynamics). Note that only few works have focused on the effect of non-white laser phase noise on coherent systems [23], [24] and these works focus on excess "low frequency" noise rather than non-white noise due to the laser dynamics response. In the case of a white frequency noise, the variance of laser phase fluctuation during τ is given by eq. (1.I.10), and its derivation will be examined in part II.

$$\langle \Delta_\tau \varphi_c(t)^2 \rangle = \langle (\varphi_c(t + \tau) - \varphi_c(t))^2 \rangle = 2\pi \Delta \nu_c \tau \quad (1.I.10)$$

with $\Delta \nu_c$ the laser "linewidth". (1.I.10) shows that broad linewidth lasers have a strong fluctuation of their phase.

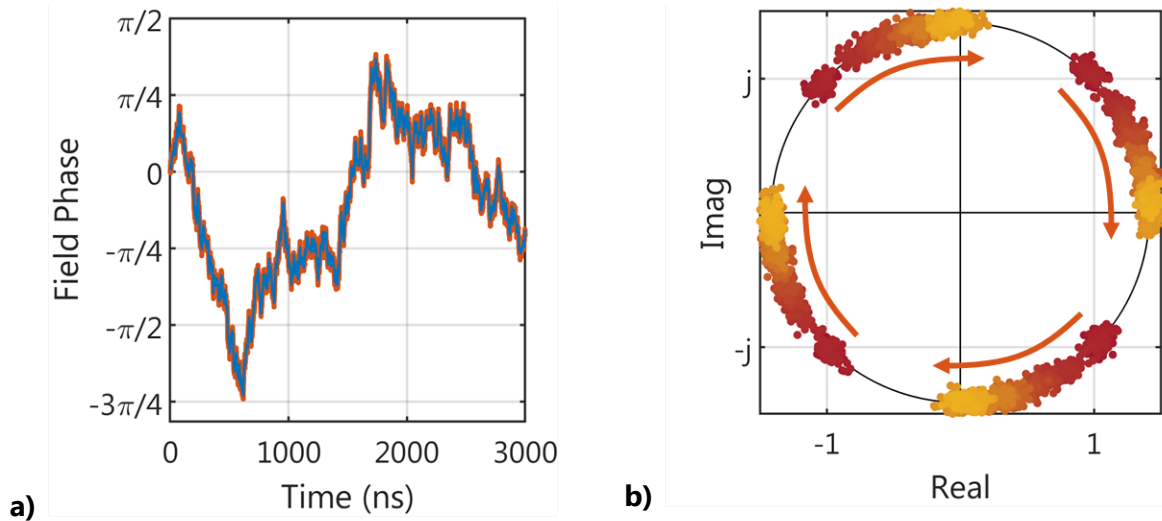


Fig.1.6. a) White random phase fluctuation of a 300 kHz linewidth laser over $3\mu s$.
b) Effect of 300 kHz linewidth laser phase drift on a QPSK constellation at 25 dB SNR, the red to yellow color waterfall corresponds to time evolving over 125 ns.

The effect of lasers phase drift on the received constellation is shown in Fig.1.6.b) which accumulates a QPSK random sequence at 64 Gbaud over 125 ns. In this plot, the LO is

considered noiseless, while the carrier is assumed to have a 300 kHz linewidth. Note that eq. (I.1.4) shows a symmetric role of LO and carrier phase noise. The rotation of the constellation inevitably causes phase errors and might also be the origin of cycle slips, corresponding to discontinuous $\pi/2$ rotations of the received constellation. Hence, phase recovery algorithms which track the lasers phase needs to be implemented in the coherent DSP.

(ii) Numerical methods used for phase recovery

Numerical methods tracking laser phase have been thoroughly studied in the last decades [25], and we will briefly discuss three of the approaches. Feed-forward methods have been widely used [26] as they can rely on highly parallelized ASIC architectures with a tens of times lower bandwidth than the symbol rates. However, they induce processing delay due to feedback loops [27]. Then, blind-phase search algorithms [28], [29] have a very high laser phase noise tolerance and can be universally applied to high order QAM formats. However these algorithms are a computational burden [11], [30], [31] and may not be preferred in low-cost and energy-efficient coherent systems. Finally, m-th power estimator based on the Viterbi & Viterbi (V&V) algorithm can be efficiently used to track the laser phase [32]. These methods which rely on symmetries of the QPSK constellation were also effectively applied on advanced modulation formats up to 64QAM [30].

(iii) Numerical Simulations

As m-th power estimator is commonly used to compensate random phase fluctuation, we numerically discuss the impact of lasers phase noise on coherent systems with a simple V&V carrier phase recovery (CPR). For the 16QAM and 64QAM case, only the outer most symbols of the constellation are used as a QPSK partition in the 4-th power estimator. The Monte-Carlo simulations are performed considering 64 Gbaud symbol rate written B , a noiseless LO, while the carrier linewidth is varying between 4 kHz and 4 MHz. We remind that the quantity of interest in the coherent link is the evolution of φ (see (I.1.4)) during "few" symbols (let's assume K symbols), which is given by the sum of carrier and LO phase fluctuations. Because these two processes are independent :

$$\langle \Delta_K \varphi[k]^2 \rangle = \langle (\varphi[k+K] - \varphi[k])^2 \rangle = 2\pi \frac{(\Delta\nu_c + \Delta\nu_{LO})}{B} K \quad (1.1.11)$$

The former equation shows both that -without CD compensation [33], [34]- considering only one noisy laser is sufficient to analyze a more general case and that high baud rate links are less sensitive to laser phase noise. Fig.1.7. shows the simulated BER vs SNR performances of single polarization QPSK and QAM formats with varying laser linewidth. A metric to study

optical link performances is to evaluate the link penalty at an acceptable error rate (ER). In this section we consider acceptable error rate (ER) at 4.9×10^{-3} , corresponding to a 7% forward error correction (FEC) limit [35]. The link penalty is then defined as the SNR impairment between the AWGN limit and the simulated ER in presence of phase noise to achieve ER below the FEC limit.

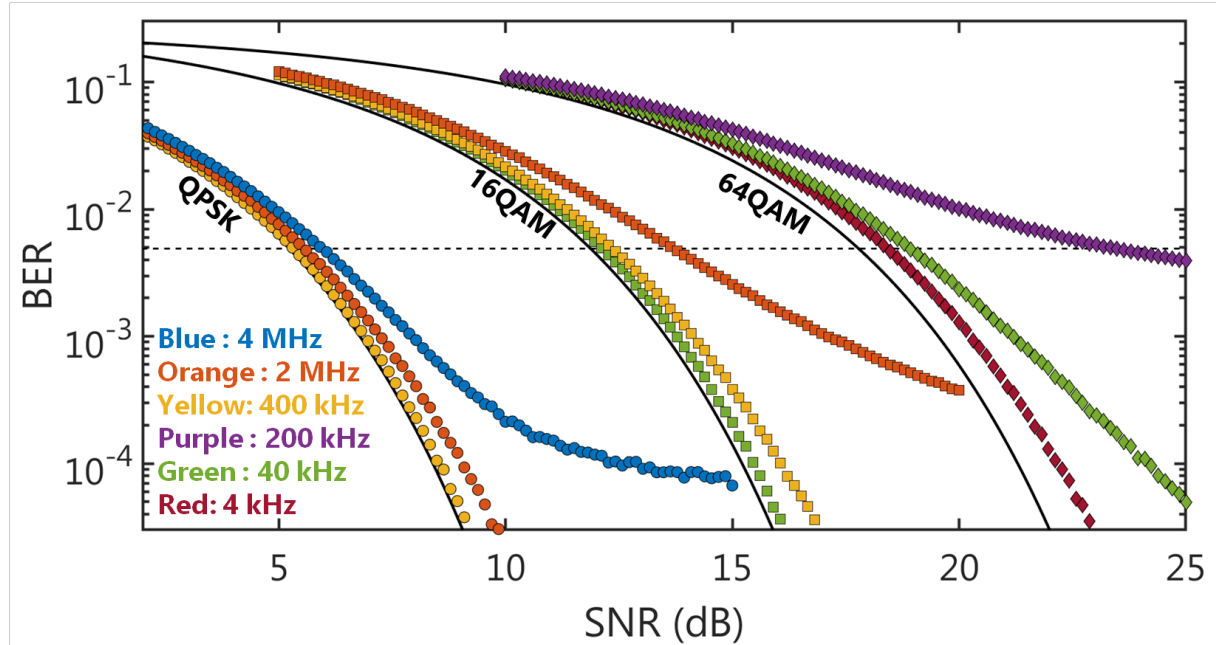


Fig. 1.7 BER vs SNR performances of single polarization coherent formats. Results are obtained using Monte-Carlo simulations. The black line corresponds to the theoretical optimum in the AWGN theory.

In the QPSK case, a laser linewidth of 4 MHz is responsible of a link penalty of only 0.8 dB. This means that this coherent format is relatively robust to laser phase noise, and traditional DFB laser could be used in QPSK systems with very low drawbacks. Then, in the 16QAM case, a laser linewidth of 2 MHz causes a link penalty over 1.5 dB, and much lower noise lasers (in the 200 kHz range) are required to reduce the link penalty close to 0. Finally, in the 64QAM case the linewidth requirement for a lightweight DSP coherent system drastically increases to the kHz range. Indeed even 200 kHz linewidth lasers are responsible of over 5dB of impairment using this lightweight DSP.

(iv) Conclusion

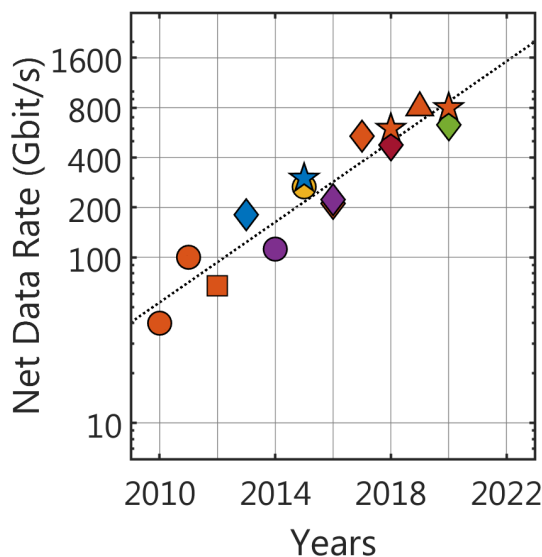
In this section we have assumed a white laser frequency noise model to show the effect of laser linewidth on coherent system performances. We have first remind a basic relation allowing to estimate the laser phase drift variance as a function of its linewidth, and this relation will be further discussed in part II. Then, we have shown how laser phase noise tends

to rotate the received constellation, causing phase errors and cycle slips. After discussing few of the commonly used numerical methods used to mitigate the phase errors, we performed numerical simulation using 4-th power method to quantify the effect of laser phase noise on the link penalty. It was shown that each increment of QAM order necessitates much narrower linewidth, and using this very basic carrier phase estimation method a linewidth in the kHz range was required for high performances 64 Gbaud systems relying on 64QAM signals.

I.3.b. State of the art coherent transceivers for datacom

To show the trend followed by coherent communication in datacenters, we recall some of the main dual polarization (DP) coherent transmission results reported in the past ten years with sub-systems suitable for DCI. The achieved net data rates per channel are displayed in Fig.1.8, where both the research group performing the experiments and the vectorial format used, are marked by different symbols.

As we can see on the graph, the demonstrated net data rate has followed an exponential growth in the last decade, and a two fold increase of data throughput was achieved every 2.5 years. A slight inflection of the exponential trend is noticeable after 2018, which might imply that aggressive innovation will be required to support the 1.6 Tbit/s datacenter interface as suggested in [6].



| | QPSK | 8QAM | 16QAM | 32QAM | 64QAM |
|------------|------|------|-------|-------|-------|
| Infinera | | | | | |
| Acacia | | | | | |
| Nokia | | | | | |
| Bell Labs | | | | | |
| Elenion | | | | | |
| NTT | | | | | |
| ETH Zurich | | | | | |

Fig. 1.8 Reported coherent transmission results for datacenter communication in the past ten years [36]–[50]

Using InP based transceivers, Infinera is among the main actors producing compact coherent devices. Their transceiver technology is based on InP optical devices [36], [37], [43]–[48] co-packaged with both SiGe transimpedance amplifier (TIA) [45]–[48] and drivers [46]–

[48]. Among the other actors proposing coherent sub-systems for datacoms, Infinera is the only one proposing transceivers operating on several parallel channels.

Contrary to Infinera, the optical technology of which relies on III-V materials, Acacia, (now acquired by Cisco), shows pioneering DP-QPSK and DP-16QAM transmission at 30 Gbaud with silicon photonics (SiP) transceivers [49], [50]. Comparing to the III-V technology, the silicon platform benefits from mature CMOS processing allowing to use 300 mm wafers with very high fabrication yield at the cost of a rather complex integration with optical gain. Similarly to Acacia, Elenion [38] (now acquired by Nokia), Nokia Bell Labs [39] and NTT [41] demonstrated coherent transmission using SiP transceivers. Contrary to the other actors relying on well established photonics platforms, ETH Zurich shows coherent transmission using plasmonic-organic hybrid (POH) modulators integrated on silicon on insulator wafers [42]. Compared to state of the art III-V or Silicon modulators, POH modulators offer much larger modulation efficiency (in terms of $V_{\pi}L_{\pi}$), allowing for a 1300-fold reduction of device area. This smaller size inherently reduces the device RC frequency cutting and does not require travelling-wave design resulting in much higher bandwidth than traditional Mach-Zehnder modulators at the cost of much higher insertion losses.

Fig.1.8 also shows that the increase in throughput was supported by higher QAM formats. Indeed most published results before 2015 were performed using DP-QPSK format and the bit rate did not exceed 400 Gbit/s. Since 2015, DP-16QAM format started to be widely used, and data rates suitable for the 400GBase-ZR standards were achieved. However, DP-16QAM, might not be suitable for the next datacenter generation operating at 800 Gbit/s, and as of 2020 only higher order QAM was shown to be suitable for the 800G interface. This trends points out that ultra low noise lasers will be key enablers in future coherent modules for DCI.

I.4. Conclusion

After briefly introducing optical communication systems, we have shown how optical links are implemented in datacenter networks. In this sub-section, we highlighted few requirements for next generation optical transceivers in datacenters. First, optical chipset needs to be integrated into small form factor pluggables which are around $90 \times 15 \text{ mm}^2$. Then, we pointed out that energy consumption of datacenter transceivers needs to be kept as low as possible as datacenter facilities are tremendously building up.

After discussing the importance of coherent technologies in future datacenter networks, we briefly examined critical laser characteristics for coherent technologies. Here, we have shown that both laser emitted power and phase noise play a key role on the performances of a coherent link. Indeed, a high laser emitted power is required to obtain a high value of SNR,

setting the optimum value of achievable error rate. Moreover, high QAM formats –which are required to increase system data rates for a given transceiver bandwidth- necessitate much higher SNR than traditional QPSK format to operate below a specified error limit. Then, we have succinctly studied the effect of laser phase noise on coherent transmission performances, and we have shown that even if coherent transmission can be performed with relatively high phase noise, efficient coherent systems relying on advanced coherent formats and a lightweight DSP require very low phase noise lasers.

Finally, a careful study of published coherent transmission results for datacenter interconnects has shown that coherent systems operate at higher and higher QAM formats. This trend confirms that narrow linewidth compact laser diodes will be key components for future coherent systems.

II. Lasers for coherent transmission systems

In the previous part, the laser requirements for a coherent link were briefly analyzed and we have in particular pointed out that both laser power and linewidth play a key role in a coherent system. As the thesis work focuses on three types of laser diodes enabling low cost coherent systems, laser parameters achieving both high power and low phase noise will be discussed in a first section. Here, some basis theory of laser phase noise will be outlined. Then, we will review different reported methods used to demonstrate narrow linewidth lasers and finally the heterogeneous III-V/Si integration process used in chapter I and II of the thesis will be described.

II.1. Laser phase noise : a theoretical approach

In this section we remind some concepts of laser phase noise theory. This will be useful to relate laser physical parameters, such as losses, phase/amplitude coupling factor, etc. to its emitted signal noise properties. For additional references the reader may refer to e.g. the Agrawal text book [51] and AT&T Bell Laboratories papers [18], [21], [52], [53].

II.1.a. Rate equation formalism

In the all three following chapters, the modeling of laser diodes uses rate equation formalism as introduced in [54]. By considering the most simplified laser diode model, i.e. a Fabry-Pérot cavity which is assumed to emit only a single longitudinal mode it is shown in Annex A that the photon density P , emitted field phase φ , and carrier density N follow the dynamical model :

$$\frac{dN}{dt} = \frac{I}{qV} - \frac{N}{\tau_N} - GP + F_N \quad (1. II. 1)$$

$$\frac{dP}{dt} = \left(G - 1/\tau_P\right) P + R_{sp} + F_P \quad (1. II. 2)$$

$$\frac{d\varphi}{dt} = \alpha_H \frac{(G - 1/\tau_P)}{2} + F_\varphi \quad (1. II. 3)$$

with I the injected current, q the electronic charge, V the laser active volume, τ_N the carrier lifetime, G the modal gain, τ_P the photon lifetime and α_H the phase/amplitude coupling factor, also widely referred to as linewidth broadening or Henry factor [18]. In (1.II.1 – 3), $F_{N,P,\varphi}$ correspond to the Langevin forces which diffusion coefficient can be found in e.g. [18], [51], [53] and R_{sp} is the spontaneous emission rate and arises from the non-zero-mean power value of spontaneous emission coupling into the lasing mode.

As semiconductor laser phase noise arises from small perturbations of the emitted field and laser carrier density due to spontaneous emission, it can be treated using a small signal model :

$$\frac{d}{dt} \begin{pmatrix} \delta N \\ \delta P \\ \varphi \end{pmatrix} = \bar{M} \begin{pmatrix} \delta N \\ \delta P \\ \varphi \end{pmatrix} + \begin{pmatrix} F_N \\ F_P \\ F_\varphi \end{pmatrix} \quad (1.II.4)$$

with $\{\delta N, \delta P\}$ small perturbations of a stable steady state solution $\{N_0, P_0\}$, and \bar{M} given in (1.II.5). Note that in (1.II.4), φ can be considered as a phase evolution from an arbitrary value, but does not correspond to a “small” phase fluctuation around a fixed point as it can be approximated by a Brownian motion. Then, in (1.II.5), $\Gamma_{N,P}$ are damping coefficients detailed in e.g. [21] and $G_{N,P}$ correspond to the values of the derivative of G relatively to N and P taken at $\{N_0, P_0\}$.

$$\bar{M} = \begin{pmatrix} -\Gamma_N & -(G_P P_0 + 1/\tau_P) & 0 \\ G_N P_0 & -\Gamma_P & 0 \\ \alpha_H G_N / 2 & \alpha_H G_P / 2 & 0 \end{pmatrix} \quad (1.II.5)$$

II.1.b. Laser phase noise in coherent systems

As we have seen in part I, the effect of laser phase noise on coherent communication performances may be quantified by the variance of the phase drift in the time interval τ corresponding to the duration of “few” symbols. This quantity $\langle \Delta_\tau \varphi(t)^2 \rangle$ can be analytically obtained from the small signal model following the procedures of e.g. [21], [22], [55]. We may notice that the phase/amplitude coupling through the factor $\alpha_H G_P / 2$ has been neglected in [21], [22], [55].

The value of $\langle \Delta_\tau \varphi(t)^2 \rangle$ for τ much longer than the laser dynamical response -which depends on the oscillation relaxation frequency f_R and could be assumed in the 0.1ns — 10ns timescale- is often reported in the literature [18], [19], and reminded in equation (1.II.6).

$$\langle \Delta_{\tau \gg \frac{1}{f_R}} \varphi(t)^2 \rangle \approx 2\pi \Delta \nu_{ST} (1 + \alpha_H^2) \tau \quad (1.II.6)$$

with $\Delta\nu_{ST}$ the Schawlow-Townes linewidth, the expression of which derived in e.g. [18] will be given later. Eq. (1.II.6), which does not take into account carrier dynamics, introduces the Schawlow-Townes & Henry (STH) linewidth $\Delta\nu_{STH} = \Delta\nu_{ST} (1 + \alpha_H^2)$ corresponding to the full width at half maximum (FWHM) of the laser field autocorrelation when no excess current source noise is considered. As current source noise power spectral density (PSD) is often contained in a <10 MHz band, it is easily tracked by traditional coherent DSP. Hence, in the thesis we will neglect 1/f frequency noise, and for complementary information the reader may refer to numerous study focusing on the effect of excess noise on laser lineshape such as [56], [57]. These works notably show that the 1/f frequency noise aggregate a Gaussian section at the center of the line profile, leading to a Voigt lineshape finally broadening the 3 dB bandwidth of the field autocorrelation.

The STH linewidth might be the most widely used metric to quantify laser phase noise. However, as it is related to the phase drift variance at timescales much longer than the duration of "few" symbols in high speed coherent links (<100 ps) it may not be the quantity of most interest to quantify the performances of a coherent link [20], [24], [58]. Nonetheless, this value can easily be characterized using self-heterodyne methods [59], [60] based on widely accessible frequency shifting devices which are slower than the laser dynamic response. In addition, as the STH linewidth is commonly used as a metric to quantify phase noise, it is convenient to use it for comparison with other research groups.

The frequency noise power spectral density (FN-PSD) $S_{\delta\nu}$ is another metric used to characterize laser phase fluctuations. As the laser instantaneous frequency $\delta\nu$ is given by $\delta\nu = (1/2\pi)(d\varphi/dt)$, we can relate it to the phase evolution $\Delta_\tau\varphi(t) = \varphi(t + \tau) - \varphi(t)$ using the following block diagram (Fig.2.1.) :

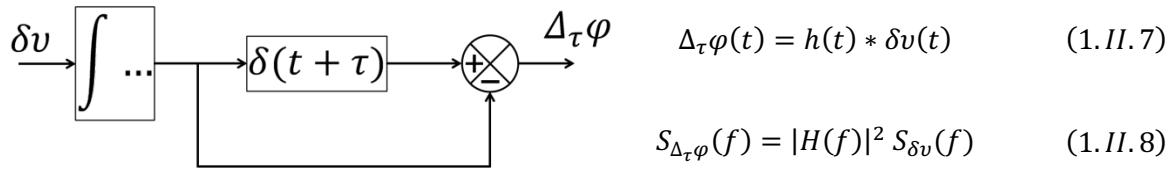


Fig. 2.1.) Relation between laser instantaneous frequency and phase drift

$$\langle \Delta_\tau \varphi^2 \rangle = 4 \int_0^\infty S_{\Delta_\tau \varphi}(f) df \quad (1.II.9)$$

Thus, we can derive the equation giving the phase evolution variance as a function of the FN-PSD using the Wiener-Lee theorem (1.II.8) and with $|H(f)| = |\sin(\pi f \tau)/f|$.

$$\langle \Delta_\tau \varphi^2 \rangle = 4 \int_0^\infty \left(\frac{\sin(\pi f \tau)}{f} \right)^2 S_{\delta\nu}(f) df \quad (1.II.10)$$

We note that the factor 4 in (1.II.10) arises because single-sideband PSD are considered. As $|H(f)|^2$ is drastically decreasing for $f > 1/\tau$, the variance of the laser phase evolution during τ is mostly affected by the value of $S_{\delta\nu}(f)$ in the $[0, 1/\tau]$ range. Thus, for digital coherent

systems, a complete assessment of phase errors would require theoretical or experimental analysis of the FN-PSD on the modulating signal bandwidth.

Evaluating experimentally the FN-PSD on a very wide band is challenging. Indeed it first requires an ultra-fast frequency-shifter. Then, the white phase noise induced by the experimental self-heterodyne setup, which arises from the thermal noise or optical amplifiers, induces a f^2 limit of the FN-PSD. This limits characterization of the FN-PSD of narrow linewidth at high frequency [61].

Also, as coherent modulating signal baudrate is generally higher than the laser relaxation oscillation frequency, laser dynamics should not be neglected to study the coherent system phase errors. In this case, it can be shown that [62] :

$$S_{\delta v}(f) = \frac{\Delta v_{ST}}{\pi} \left(1 + \alpha_H^2 \left| \frac{f_R^2}{(f_R^2 - f^2) + j \left(\frac{\Gamma f}{2\pi} \right)} \right|^2 \right) \quad (1.II.11)$$

Neglecting carrier dynamics in (1.II.11) is equivalent to study $S_{\delta v}$ over a frequency band, the upper limit of which is much lower than f_R , hence it revolves to consider a white frequency noise with a floor at $S_{\delta v}(f \ll f_R) = \Delta v_{ST}/\pi$. However, due to the finite response time of the laser, its frequency noise at higher frequency and around coherent signal baudrate is reduced by $(1 + \alpha_H^2)$ to $S_{\delta v}(f \gg f_R) = \Delta v_{ST}/\pi$. Hence, according to [58] for a laser with relaxation oscillation frequency much below the coherent system baudrate, the effect of α_H *might* not play a major role in the coherent system performances.

II.1.c. Laser noise simulation

To illustrate the effect of carrier dynamics on laser phase noise, Monte-Carlo simulations of the laser small signal model with Langevin forces generated using the method from [63], [64] were performed. We consider a single mode laser with an inversion population factor $n_{sp} = 2$, an ideal injection efficiency η_I , a relatively long photon lifetime $\tau_P = 70$ ps to simulate narrow linewidth laser and an injection current offset from threshold $\Delta I_{Th} = 200$ mA. With these parameters, the Schawlow-Townes (ST) linewidth given by the formula (1.II.12) in e.g. [18] is around 3.3 kHz while the STH linewidth is around 16 kHz.

$$\Delta v_{ST} = \frac{q n_{sp}}{8\pi \eta_I} \times \frac{1}{\tau_P^2} \times \frac{1}{\Delta I_{Th}} \quad (1.II.12)$$

The ST formula shows that a long photon lifetime is crucial to obtain narrow linewidth lasers. As $\tau_P = 1/(v_g \alpha_{tot})$ with v_g the group velocity of the laser waveguide and α_{tot} the

laser losses comprising extraction and propagation losses, narrow linewidth laser diodes require waveguide processing achieving very low losses.

By considering the following laser dynamical parameters, a phase/amplitude coupling factor $\alpha_H = 2$, relaxation oscillation frequency $f_R = 1 \text{ GHz}$ and a damping factor $\Gamma = 3.8 \text{ GHz}$, Monte-Carlo simulation results are plotted in Fig.2.2.a) & b). The simulated FN-PSD (Fig.2.2.a) may be relatively well fitted by the analytical formula of (1.II.11) and the discrepancy at high frequency might be due to numerical errors occurring in the stochastic Euler integration method. Note that, as shown in the annex, the rate equations model is only valid inside a spectral band much narrower than the cavity roundtrip frequency f_{rep} which could be in the 10 GHz range. Hence, in a practical case, we cannot precisely study laser phase noise on a wide frequency band using single mode rate equations model.

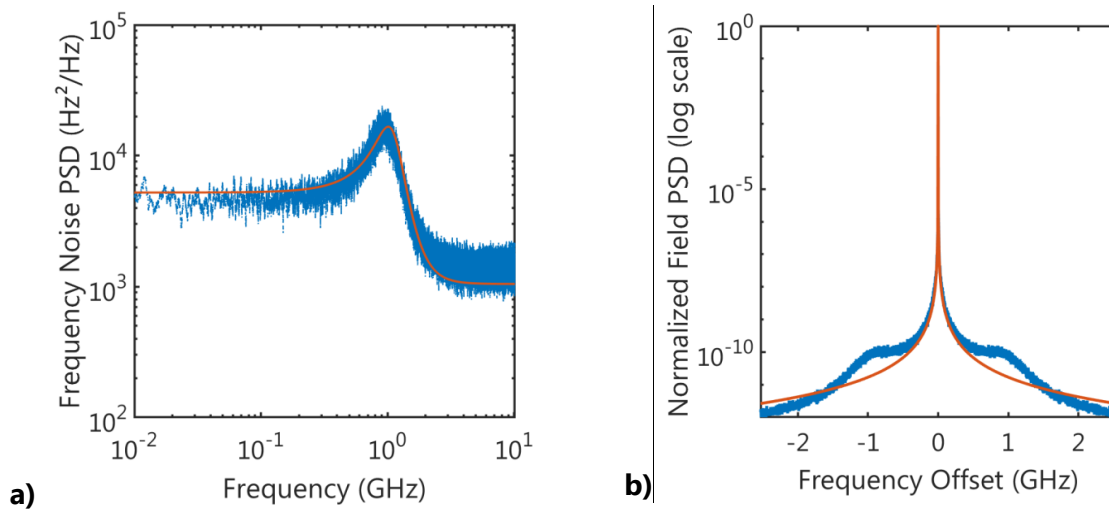


Fig. 2.2.) a) FN-DSP, blue (resp. orange) corresponds to numerical simulation (resp. analytic formula with carrier dynamics). b) Line structure, blue (resp. orange) corresponds to numerical simulation (resp. STH linewidth)

The field PSD, widely referred to as the laser lineshape [21], is plotted in Fig.2.2.b). While the reader may refer to [20] giving the relation between lineshape and FN-PSD, it can be approximated by a Lorentzian function when no carriers effect are considered (orange line). Relatively to the STH linewidth, taking into account carrier dynamics both increases the noise at frequencies close to the relaxation oscillation one and reduces it at timescale much faster than the laser dynamics. For additional information, the reader may refer to [21], [22], [55] studying laser phase noise by taking into account the carrier response and notably analytically deriving the lineshape formula while non neglecting the laser response time.

II.1.d. Passive/active integration for linewidth narrowing

As already discussed, in eq. (1.II.12) a very long photon lifetime is required to achieve a laser with narrow ST and STH linewidths. Due to the technological challenge to fabricate low loss PIN laser waveguides, other approaches which induce STH linewidth reduction need to be devised. For instance, as reported in [52], [65], [66], drastic laser linewidth reduction can be achieved with passive/active integration. Indeed, as we will thoroughly discuss in chapter 2 part III, the integration of a passive high quality (HQ) factor resonator coupled to a laser diode may provide a negative feedback loop often referred to as "detune loading" which can stabilize the laser. In this case the modified STH linewidth $\Delta\nu_{STH}$ may be written [52], [67]

$$\Delta\nu_{STH} = \Delta\nu_{ST} \frac{1 + \alpha_H^2}{F^2} \quad (1.II.12)$$

with F a factor which scales with the passive resonator quality factor. We will later show that F -factors over 10 can easily be achieved using passive waveguides with relatively modest propagation losses. Note that this formula is obtained by the linearization of the oscillating condition [66] and may be only valid on a relatively narrow band.

II.2. Technologies for narrow linewidth lasers

In this section, we discuss widely used different photonic technologies to fabricate low noise tunable laser sources. We will see that these technologies rely on the integration of low loss passive waveguides integrated with a gain medium. Then we briefly present the III-V on Silicon platform used in this thesis to fabricate the low noise lasers studied in chapter I and II.

II.2.a. State of the art

Some published results concerning narrow linewidth lasers are shown in Fig.2.3, plotting the optical power and Schawlow-Townes & Henry (STH) linewidth of different lasers emitting at telecom wavelength. In Fig.2.3 the different colors represent different laser technologies. Note that some published works characterize the laser output power using a wide photodetector while other consider the fiber coupled power, thus the x-axis only shows a tendency.

The monolithic InP technology is represented in blue, and as we can see in Fig.2.3 this historic platform may achieve relatively high optical power, -e.g. 70 mW is reported in [68]- at a cost of relatively broader linewidths. Indeed, the narrowest reported linewidth to our

knowledge is 3.6 kHz in [69], while the average results are ~ 100 kHz. The relatively broader linewidth compared to that of other technologies might be related to the uncommon monolithic integration between active and passive waveguides, as it should rely on e.g. butt joint [70] or selective area growth [71]. Hence, most of the works from this technology do not benefit from the F^2 reduction [52], [67] discussed above, and the linewidth narrowing is often obtained with complex DFB designs. Note that even if the passive integration is not ideal, some narrow linewidth lasers rely on it, such as sampled Bragg grating reflector (SG-DBR) lasers [68], [72] or ring extended lasers [73], [74]. In this case the achieved linewidth is often broader compared to that of III-V / group IV photonic platform, because III-V waveguides tend to be more lossy.

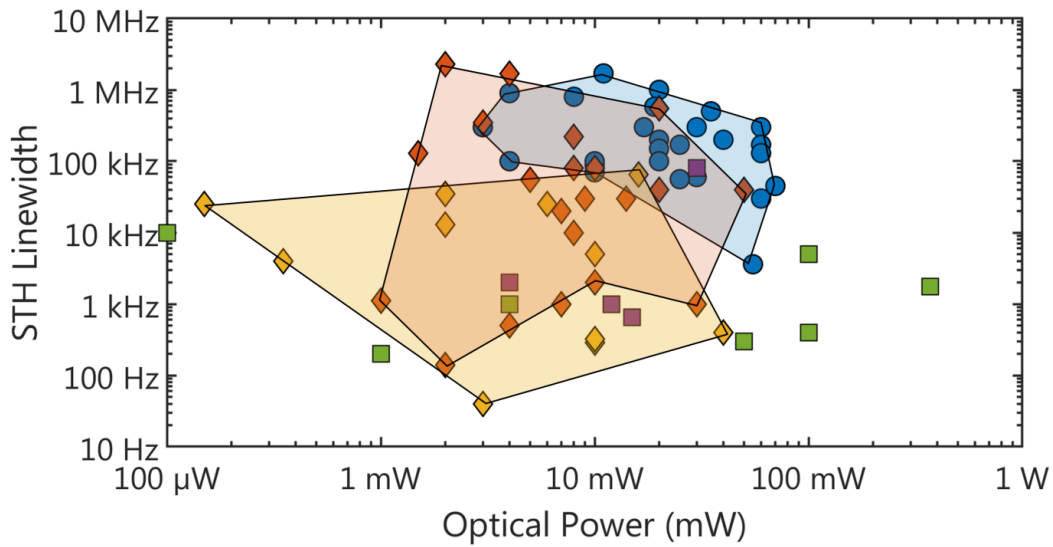


Fig. 2.3. Reported characteristics of narrow linewidth tunable laser from the literature Blue circles correspond to III-V monolithic lasers, Orange diamond correspond III-V/Si lasers, Yellow diamond correspond III-V/SiN lasers, Purple squares correspond to III-V/Silica planar waveguide extended lasers, green squares correspond to III-V laser diodes stabilized using non integrated components.

As we have briefly seen in section II.1, the use of a passive selective mirror is a great method to reduce lasers STH linewidth. Thus, the heterogeneous integration of III-V gain medium with low loss passive waveguides has been proven to be an efficient technology to fabricate narrow linewidth laser diodes. Power and linewidth characteristics of Silicon extended cavity lasers are reported with orange diamonds in Fig.2.3. To our knowledge the narrowest linewidth achieved by III-V/Si lasers is ~ 500 Hz [75], a value related to the ultra-low propagation losses of their Silicon waveguides (0.16 dB/cm). Indeed high quality factor reflecting filters are required to improve the F value from [52] related to linewidth narrowing. However, the emitted power of this laser diode is relatively low (below 5 mW), which might be due to the fact that high quality factor silicon resonators could significantly suffer from non linear losses such as two photon absorption (TPA) in the telecom bands. To fabricate silicon extended lasers with high power e.g. [76], the selective mirror should rely on lower

quality factor resonator increasing the onset for non-linearities but deteriorating the linewidth properties. Hence, a trade-off might be required between laser power and linewidth using a silicon platform due to the adverse effect of non-linearities at telecom wavelengths.

In order to drastically reduce the impact of non linear effects on the emitted power and linewidth, the laser cavity can be extended with Silicon nitride (SiN) waveguides, resulting in narrow linewidth laser with relatively higher emitted power than that of Silicon extended cavity lasers. For instance a SiN extended laser operating at around 40 mW with a linewidth below 400 Hz was very recently reported in [77]. Moreover, SiN/SiO₂ waveguides have a lower refractive index contrast than Silicon on insulator waveguides, so they also benefit from lower scattering losses achieving laser linewidth below 40 Hz [77]. We note that even though very attractive power and linewidth performances have been achieved using the SiN platform, this latter however shows several drawbacks compared to the Silicon one. For instance the thermo-optic coefficient of SiN is 10 times lower than the one of Silicon, requiring higher power consumption for laser tuning. Laser integration with other components such as modulators might also be challenging in the SiN platform.

Other narrow linewidth lasers based on bulkier and more complex technologies such as Silica planar lightwave circuits [78], fibered Bragg gratings [79] and MgF₂ waveguide gallery mode resonators [80] have also been demonstrated. These laser diodes might operate with ultra narrow linewidth but may not be compact enough for datacenter interconnects. Hence, their performances are summarized in Fig.2.3 but will not be detailed further.

II.2.b. The III-V on Silicon platform (from CEA Leti / III-V Lab)

As we have seen in II.1.a. the heterogeneous integration of Silicon with III-V material is a promising technology to fabricate compact narrow linewidth lasers. Hence, in this thesis we will study two types of single mode laser suitable for coherent communications made using the III-V on silicon platform of CEA Leti & III-V Lab. The reader can refer to [81] for a complete description of the III-V on Silicon process used, which is very similar to the one of the Ghent University Photonics Research Group [82] and the one of Bowers *et. al.* research group [83]. A subtle difference between the III-V lab approach and the one from UCSB revolves in the fact that Bowers et al. do not etch the III-V material to fabricate a single mode III-V waveguide. For clarity, the III-V on Silicon process used in the thesis is briefly reviewed in the following and illustrated in Fig.2.4.a).

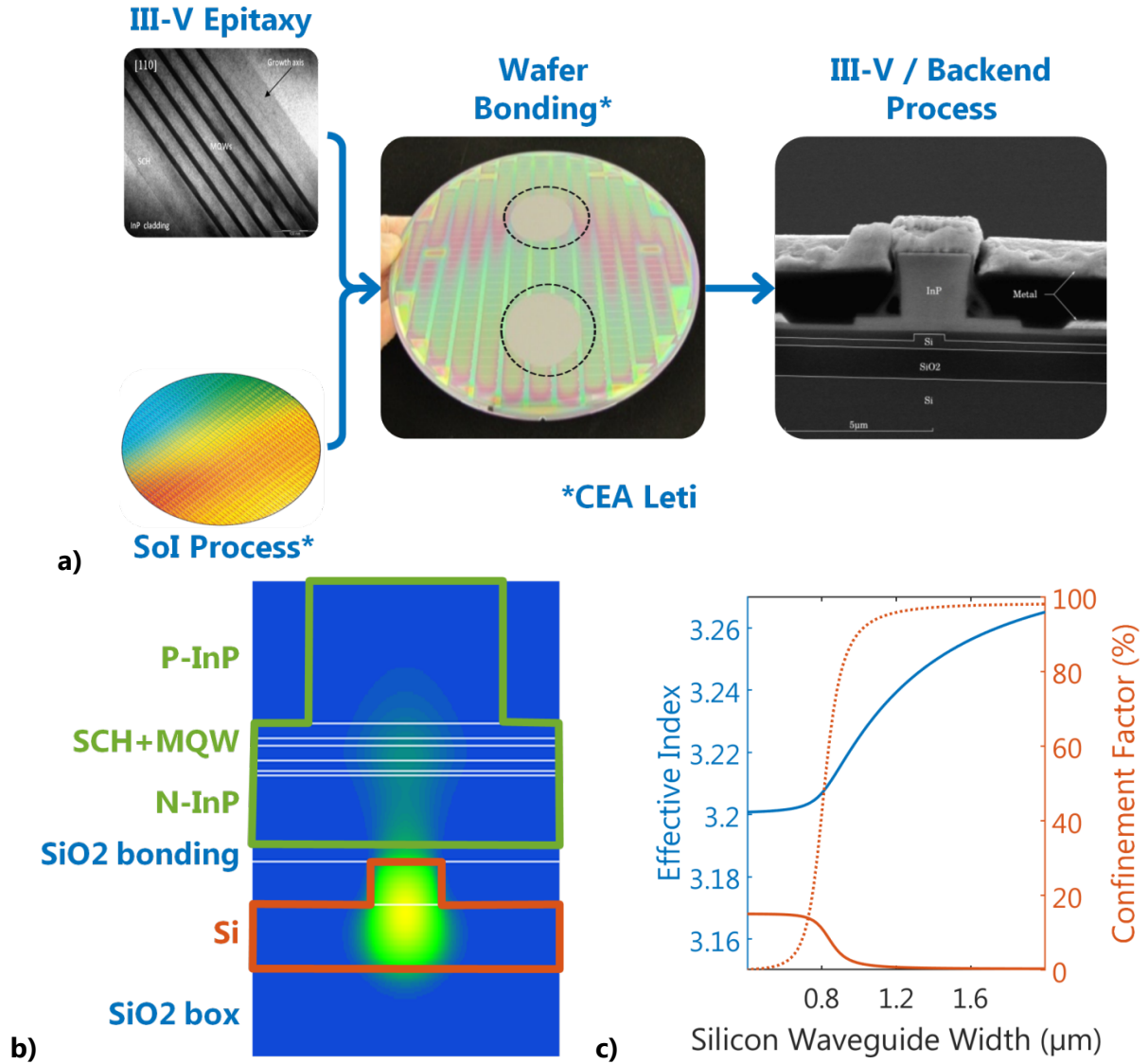


Fig.2. a) Summary of the CEA Leti / III-V Lab process. b) III-V on Silicon waveguide structure c) Fundamental mode effective index (blue), quantum well confinement (orange plain line) and silicon confinement (orange dotted line).

First, a III-V three inch layer stack is epitaxied at III-V Lab which is sketched, at the end of the process, in Fig.2.4.b). The devices presented in chapter I and II of the thesis utilize a metal organic vapour phase epitaxy (MOVPE) containing eight aluminium based quantum wells emitting in the C-band. In the meantime a 200 mm Silicon on Insulator (SoI) wafer is processed at CEA Leti. The processing consists in several etching steps to define different SoI waveguides geometry such as 500/300 nm and 300/150 nm thick rib waveguides, and 300 nm thick strip waveguides. The 500/300 nm rib waveguide is used for III-V and Silicon coupling while the smaller ones are used for Silicon passive functions. After etching, Silicon waveguides are encapsulated using a micrometer thick deposition of Silica. This oxide is later planarized with a chemical mechanical polishing step and the remaining thickness of Silica is ~80 nm. This layer can be called the "bonding layer" as III-V materials will be bonded on its

surface using Van der Waals interaction. Hence, the roughness and thickness of the bonding layer need to be precisely controlled to :

- Avoid the formation of bonding defect.
- Guarantee identical performances on a 3 inches area corresponding to the size of the bonded epitaxy. In fact, transverse lasing mode characteristics are strongly affected by the bonding oxide thickness.

After bonding, the III-V stack is processed using traditional III-V shallow ridge processing, to form a coupled waveguide structure as shown in Fig.2.4.b) The backend III-V process finally consists of metal deposition to provide carrier injection in the laser PIN diode, fabrication of NiCr based heater to control III-V/Silicon laser emitted wavelength and encapsulation.

One key feature of the III-V on Silicon coupled waveguide structures is that the fundamental transverse mode properties can be engineered by playing on the III-V waveguide width. This is illustrated in Fig.2.4.c) showing the effective index and confinement factor inside different layers of the fundamental mode. The fundamental mode which is often referred to as the symmetric or even mode e.g. [84], can finally transit from the Silicon to the III-V using an adiabatic mode transformer [85]–[87]. By following the design method presented in [88], the mode transformer can provide extremely low coupling losses (<10%) and negligible parasitic reflection between the III-V/Si coupled waveguide structure providing the gain and the Silicon extended cavity.

III. Conclusion

In this introductory chapter we have seen that coherent technology, which was previously used for long haul transmission link, is becoming a topic of interest in datacenter communication. However, to produce low-cost, compact and energy-efficient coherent transceivers, narrow linewidth laser diodes are key enablers. Hence, in this thesis we study three types of laser diodes suitable for coherent systems.

The first chapter will analyze compact distributed feedback (DFB) laser diodes with a very low phase noise. These devices are fabricated using the III-V on silicon platform, making them ideal for integration with Silicon based coherent transceivers. Thus, these DFB lasers would be suitable for ultra-low cost coherent application. In this chapter, after presenting their grating principle, we will show numerical simulations pointing out design parameters leading to optimal performances. Finally, characterization results will be analyzed, confirming the numerical model. These results also experimentally highlight which laser design achieves best performances.

In the second chapter a novel fast tunable laser (FTL) diode is presented and contrary to previously reported FTLs designs, this laser exhibits a much narrower linewidth. The combination of nanosecond timescale switching and narrow linewidth performances enables coherent burst communication protocol, which would be crucial for low-latency and capacity-hungry applications. After describing the laser architecture, we carefully examine the laser switching characteristics using novel experimental methods. After that, some of the theory explaining its relatively low value of linewidth is presented, and simulation results will be supported by linewidth measurements. Finally, we present record coherent slot switching experimental results performed using this laser.

In the final chapter, we study optical feedback in quantum dash (QDash) based mode-locked laser (MLL), and we notably show that one regime of feedback –referred to as *coherent* feedback- can drastically improve the phase noise performances of the MLL. The emitted frequency comb with low noise in each line enables energy efficient application operating in the few Tbit/s range. In this chapter, after studying the feedback regimes of the MLL, we thoroughly investigate the MLL phase noise reduction in the regime of coherent feedback. Finally, transmission experiments prove the possible use of optical feedback in MLLs to enhance dense wavelength division multiplexing (DWDM) coherent systems performances.

IV. References

- [1] K. C. Kao and G. A. Hockham, "Dielectric-fibre surface waveguides for optical frequencies," *Elektron*, vol. 14, no. 5, pp. 11–12, 1997.
- [2] I. Hayashi, M. B. Panish, P. W. Foy, and S. Sumski, "Junction lasers which operate continuously at room temperature," *Appl. Phys. Lett.*, vol. 17, no. 3, pp. 109–111, 1970.
- [3] J. I. Yamada, S. Machida, and T. Kimura, "2 Gbit/s optical transmission experiments at 1.3 μm with 44km single-mode fibre," *Electron. Lett.*, vol. 17, no. 13, pp. 479–480, 1981.
- [4] G. Rademacher, R. S. Lu, B. J. Puttnam, and R. Ryf, "172 Tb / s C + L Band Transmission over 2040 km Strongly Coupled 3-Core Fiber," no. 1, pp. 5–7, 2020.
- [5] R. J. Essiambre, G. J. Foschini, P. J. Winzer, G. Kramer, and B. Goebel, "Capacity Limits of Optical Fiber Networks," *J. Light. Technol.*, vol. 28, no. 4, pp. 662–701, 2010.
- [6] C. Urricariet, "Trends in 400G Optics for the Data Center." *Nanog 75*, 2019.
- [7] Q. Zhang, V. Liu, H. Zeng, and A. Krishnamurthy, "High-resolution measurement of data center microbursts," *Proc. ACM SIGCOMM Internet Meas. Conf. IMC*, vol. Part F1319, pp. 78–85, 2017.
- [8] N. Benzaoui *et al.*, "CBOSS: Bringing traffic engineering inside data center networks," *J. Opt. Commun. Netw.*, vol. 10, no. 7, pp. B117–B125, 2018.
- [9] K. Kikuchi, "Fundamentals of coherent optical fiber communications," *J. Light. Technol.*, vol. 34, no. 1, pp. 157–179, 2016.
- [10] S. J. Savory, "Digital coherent optical receivers: Algorithms and subsystems," *IEEE J. Sel. Top. Quantum Electron.*, vol. 16, no. 5, pp. 1164–1179, 2010.
- [11] M. S. Faruk and S. J. Savory, "Digital Signal Processing for Coherent Transceivers Employing Multilevel Formats," *J. Light. Technol.*, vol. 35, no. 5, pp. 1125–1141, 2017.
- [12] K. Kikuchi, "Performance analyses of polarization demultiplexing based on constant-modulus algorithm in digital coherent optical receivers," *Opt. Express*, vol. 19, no. 10, p. 9868, 2011.
- [13] J. R. Barry and E. A. Lee, "Performance of Coherent Optical Receivers," 1990.
- [14] K. Kikuchi and S. Tsukamoto, "Evaluation of sensitivity of the digital coherent receiver," *J. Light. Technol.*, vol. 26, no. 13, pp. 1817–1822, 2008.
- [15] B. Zhang, C. Malouin, and T. J. Schmidt, "Design of coherent receiver optical front end for unamplified applications," *Opt. Express*, vol. 20, no. 3, p. 3225, 2012.
- [16] P. P. Mitra and J. B. Stark, "Nonlinear limits to the information capacity of optical fibre communications," *Nature*, vol. 411, no. 6841, pp. 1027–1030, 2001.
- [17] J. M. Kahn and K. P. Ho, "Spectral efficiency limits and modulation/detection techniques for DWDM systems," *IEEE J. Sel. Top. Quantum Electron.*, vol. 10, no. 2, pp. 259–272, 2004.
- [18] C. H. Henry, "Theory of the Linewidth of Semiconductor Lasers," *Quantum*, no. 2, pp. 259–264, 1982.
- [19] K. Vahala, "Semiclassical Theory of Noise in Semiconductor Lasers-Part 1," *IEEE J. Quantum Electron.*, vol. QE-19, no. 6, pp. 1096–1101, 1983.
- [20] K. Kikuchi, "Characterization of semiconductor-laser phase noise and estimation of bit-error rate performance with low-speed offline digital coherent receivers," *Opt. Express*, vol. 20, no. 5, p. 5291, 2012.

- [21] C. H. Henry, "Theory of the Phase Noise and Power Spectrum of a Single Mode Injection Laser," *IEEE J. Quantum Electron.*, vol. 19, no. 9, pp. 1391–1397, 1983.
- [22] K. Vahala and A. Yariv, "Semiclassical Theory of Noise in Semiconductor Lasers-Part II," *IEEE J. Quantum Electron.*, vol. 19, no. 6, pp. 1102–1109, 1983.
- [23] T. N. Huynh, A. T. Nguyen, W. C. Ng, L. Nguyen, L. A. Rusch, and L. P. Barry, "BER performance of coherent optical communications systems employing monolithic tunable lasers with excess phase noise," *J. Light. Technol.*, vol. 32, no. 10, pp. 1973–1980, 2014.
- [24] M. Al-Qadi, M. O'Sullivan, C. Xie, and R. Hui, "Phase Noise Measurements and Performance of Lasers with Non-White FM Noise for Use in Digital Coherent Optical Systems," *J. Light. Technol.*, vol. 38, no. 6, pp. 1157–1167, 2020.
- [25] M. G. Taylor, "Detection Using Digital Signal Processing," *J. Light. Technol.*, vol. 27, no. 7, pp. 901–914, 2009.
- [26] E. Ip and J. M. Kahn, "Addendum to 'Feedforward Carrier Recovery for Coherent Optical Communications,'" *J. Light. Technol.*, vol. 27, no. 13, pp. 2552–2553, 2009.
- [27] V. Rozental, D. Kong, B. Corcoran, D. Mello, and A. J. Lowery, "Filtered Carrier Phase Estimator for High-Order QAM Optical Systems," *J. Light. Technol.*, vol. 36, no. 14, pp. 2980–2993, 2018.
- [28] T. Pfau, S. Hoffmann, and R. Noé, "Hardware-efficient coherent digital receiver concept with feedforward carrier recovery for M-QAM constellations," *J. Light. Technol.*, vol. 27, no. 8, pp. 989–999, 2009.
- [29] J. Li, L. Li, Z. Tao, T. Hoshida, and J. C. Rasmussen, "Laser-linewidth-tolerant feed-forward carrier phase estimator with reduced complexity for QAM," *J. Light. Technol.*, vol. 29, no. 16, pp. 2358–2364, 2011.
- [30] S. M. Bilal, G. Bosco, J. Cheng, A. P. T. Lau, and C. Lu, "Carrier Phase Estimation Through the Rotation Algorithm for 64-QAM Optical Systems," *J. Light. Technol.*, vol. 33, no. 9, pp. 1766–1773, 2015.
- [31] N. Argyris, S. Dris, C. Spatharakis, and H. Avramopoulos, "High performance carrier phase recovery for coherent optical QAM," *Opt. Fiber Commun. Conf. OFC 2015*, vol. 1, pp. 2–4, 2015.
- [32] A. M. Viterbi, "Nonlinear Estimation of PSK-Modulated Carrier Phase with Application to Burst Digital Transmission," *IEEE Trans. Inf. Theory*, vol. 29, no. 4, pp. 543–551, 1983.
- [33] T. Xu, G. Jacobsen, S. Popov, J. Li, A. T. Friberg, and Y. Zhang, "Analytical estimation of phase noise influence in coherent transmission system with digital dispersion equalization," *Opt. Express*, vol. 19, no. 8, p. 7756, 2011.
- [34] T. Xu *et al.*, "Analysis of chromatic dispersion compensation and carrier phase recovery in long-haul optical transmission system influenced by equalization enhanced phase noise," *Optik (Stuttg.)*, vol. 138, pp. 494–508, 2017.
- [35] J. M. Estarán *et al.*, "140/180/204-Gbaud OOK Transceiver for Inter- and Intra-Data Center Connectivity," *J. Light. Technol.*, vol. 37, no. 1, pp. 178–187, 2019.
- [36] J. Rahn *et al.*, "Low-power, polarization tracked 45.6 GB/s per wavelength PM-DQPSK receiver in a 10-channel integrated module," *Opt. InfoBase Conf. Pap.*, pp. 1–3, 2010.
- [37] R. Nagarajan *et al.*, "10 channel, 100Gbit/s per channel, dual polarization, coherent QPSK, monolithic InP receiver photonic integrated circuit," *Opt. InfoBase Conf. Pap.*, pp. 1–3, 2011.
- [38] A. Novack *et al.*, "A silicon photonic transceiver and hybrid tunable laser for 64 Gbaud

- coherent communication," *2018 Opt. Fiber Commun. Conf. Expo. OFC 2018 - Proc.*, no. c, pp. 1–3, 2018.
- [39] P. Dong *et al.*, "224-Gb/s PDM-16-QAM Modulator and Receiver based on Silicon Photonic Integrated Circuits," vol. 1, no. c, pp. 6–8, 2013.
 - [40] F. Buchali, G. Böcherer, W. Idler, L. Schmalen, P. Schulte, and F. Steiner, "Experimental demonstration of capacity increase and rate adaptation by probabilistically shaped 64-QAM 1 . Introduction 2 . Probabilistic Shaping 3 . Experimental Setup 4 . Transmission Experiments," *Eur. Conf. Opt. Commun.*, no. 2, pp. 1–22, 2015.
 - [41] S. Yamanaka *et al.*, "Silicon Photonics Coherent Optical Subassembly with EO and OE Bandwidths of over 50 GHz," *2020 Opt. Fiber Commun. Conf. Exhib. OFC 2020 - Proc.*, pp. 4–6, 2020.
 - [42] C. Haffner, W. Heni, Y. Fedoryshyn, B. Baeuerle, and A. Josten, "Ultra-Compact Plasmonic IQ-Modulator," pp. 10–12, 2015.
 - [43] D. Krause *et al.*, "854 Gb/s superchannel InP transmitter and receiver photonic integrated circuits utilizing Real-Time Detection of PM-8QAM," *Opt. InfoBase Conf. Pap.*, pp. 1–3, 2012.
 - [44] V. Lal *et al.*, "Full C-Band Tunable Coherent Transmitter and Receiver InP Photonic Integrated Circuits," *Eur. Conf. Opt. Commun.*, pp. 10–12, 2016.
 - [45] M. Lauermann *et al.*, "Multi-Channel, Widely-Tunable Coherent Transmitter and Receiver PICs Operating at 88Gbaud/16-QAM," *OFC*, 2017.
 - [46] R. Going *et al.*, "4 x 600 Gb / s Photonic IC Transmitter and Receiver Modules 4-Channel Tx / Rx PIC Assemblies 66 GBd , 64QAM after 200 km Transmission," *Eur. Conf. Opt. Commun. ECOC*, no. c, pp. 4–6, 2018.
 - [47] S. Wolf *et al.*, "2-channels \times 100 GBd 32QAM transmission over 500 km enabled by InP PICs and SiGe ASICs," *IET Conf. Publ.*, vol. 2019, no. CP765, pp. 2–4, 2019.
 - [48] V. Lal *et al.*, "1.6Tbps Coherent 2-Channel Transceiver using a Monolithic Tx/Rx InP PIC and Single SiGe ASIC," *2020 Opt. Fiber Commun. Conf. Exhib. OFC 2020 - Proc.*, vol. 2, pp. 6–8, 2020.
 - [49] C. Doerr *et al.*, "Single-chip silicon photonics 100-Gb/s coherent transceiver," *Opt. InfoBase Conf. Pap.*, pp. 7–9, 2014.
 - [50] C. Doerr *et al.*, "O , E , S , C , and L Band Silicon Photonics Coherent Modulator / Receiver," pp. 6–8, 2016.
 - [51] G. P. Agrawal and N. Dutta, *Semiconductor Lasers*, 2nd Editio. Kluwer Academic Publishers, 1993.
 - [52] R. F. Kazarinov and C. H. Henry, "The Relation of Line Narrowing and Chirp Reduction Resulting from the Coupling of a Semiconductor Laser to a Passive Resonator," *IEEE J. Quantum Electron.*, vol. 23, no. 9, pp. 1401–1409, 1987.
 - [53] C. H. Henry, "Phase Noise in Semiconductor Lasers," *J. Light. Technol.*, vol. 4, no. 3, 1986.
 - [54] H. Statz and G. A. DeMars, "Quantum Electronics." p. 530, 1960.
 - [55] P. Spano, S. Piazzolla, and M. Tamburini, "Phase Noise in Semiconductor Lasers: A Theoretical Approach," *IEEE J. Quantum Electron.*, vol. 19, no. 7, p. 1195, 1983.
 - [56] L. B. Mercer, "1/f Frequency Noise Effects on Self-Heterodyne Linewidth Measurements," *J. Light. Technol.*, vol. 9, no. 4, pp. 485–493, 1991.
 - [57] G. M. Stéphan, T. T. Tam, S. Blin, P. Besnard, and M. Têtu, "Laser line shape and spectral density of frequency noise," *Phys. Rev. A - At. Mol. Opt. Phys.*, vol. 71, no. 4, pp. 1–9,

- 2005.
- [58] D. Kim, M. Harfouche, H. Wang, N. Satyan, G. Rakuljic, and A. Yariv, "Suppression of linewidth enhancement factor in high-coherence heterogeneously integrated silicon/III-V lasers," *2017 Conf. Lasers Electro-Optics, CLEO 2017 - Proc.*, vol. 2017-Janua, no. c, pp. 1–2, 2017.
 - [59] T. Okoshi, K. Kikuchi, and A. Nakayama, "Novel method for high resolution measurement of laser output spectrum," *Electron. Lett.*, vol. 16, no. 16, pp. 630–631, 1980.
 - [60] L. E. Richter, H. I. Mandelberg, M. S. Kruger, and P. A. McGrath, "Linewidth Determination from Self-Heterodyne Measurements with Subcoherence Delay Times," *IEEE J. Quantum Electron.*, vol. 22, no. 11, pp. 2070–2074, 1986.
 - [61] T. Verolet *et al.*, "Mode Locked Laser Phase Noise Reduction Under Optical Feedback for Coherent DWDM Communication," *J. Light. Technol.*, vol. 38, no. 20, pp. 5708–5715, 2020.
 - [62] K. Kikuchi and T. Okoshi, "Measurement of FM Noise, AM Noise, and Field Spectra of 1.3 μm InGaAsP DFB Lasers and Determination of the Linewidth Enhancement Factor," *IEEE J. Quantum Electron.*, vol. 21, no. 11, pp. 1814–1818, 1985.
 - [63] M. Ahmed, M. Yamada, and M. Saito, "Numerical modeling of intensity and phase noise in semiconductor lasers," *IEEE J. Quantum Electron.*, vol. 37, no. 12, pp. 1600–1610, 2001.
 - [64] I. Fatadin, D. Ives, and M. Wicks, "Numerical simulation of intensity and phase noise from extracted parameters for CW DFB lasers," *IEEE J. Quantum Electron.*, vol. 42, no. 9, pp. 934–941, 2006.
 - [65] K. J. Vahala and A. Yariv, "Detuned loading in coupled cavity semiconductor lasers - Effect on quantum noise and dynamics," *Appl. Phys. Lett.*, vol. 45, no. 5, 1984.
 - [66] P. Gallion and G. Debarge, "Relationship between linewidth and chirp reductions in gain-detuned composite-cavity semiconductor lasers," *Electron. Lett.*, vol. 23, no. 25, pp. 1375–1376, 1987.
 - [67] G. H. Duan, P. Gallion, and G. Debarge, "Analysis of the Phase-Amplitude Coupling Factor and Spectral Linewidth of Distributed Feedback and Composite-Cavity Semiconductor Lasers," *IEEE J. Quantum Electron.*, vol. 26, no. 1, pp. 32–44, 1990.
 - [68] M. C. Larson, "Narrow linewidth tunable DBR lasers," *Conf. Dig. - IEEE Int. Semicond. Laser Conf.*, vol. 2, pp. 2–3, 2016.
 - [69] M. Okai, M. Suzuki, and T. Taniwatari, "Strained multiquantum-well corrugation-pitch-modulated distributed feedback laser with ultranarrow (3.6 kHz) spectral linewidth," *Electron. Lett.*, vol. 29, no. 19, pp. 1696–1697, 1993.
 - [70] X. F. Chen *et al.*, "Photonic integrated technology for multi-wavelength laser emission," *Chinese Sci. Bull.*, vol. 56, no. 28–29, pp. 3064–3071, 2011.
 - [71] T. M. Cockerill, D. V. Forbes, H. Han, and J. J. Coleman, "Monolithic Integration of a Strained-Layer InGaAs—GaAs—AlGaAs Quantum-Well Laser with a Passive Waveguide by Selective-Area MOCVD," *IEEE Photonics Technol. Lett.*, vol. 5, no. 4, pp. 448–450, 1993.
 - [72] M. Miyata, H. Tanaka, M. Shibata, Y. Oka, T. Kaneko, and H. Kawamura, "+18 dBm high-power tunable laser modules for digital coherent optical communication systems," *SEI Tech. Rev.*, no. 83, pp. 30–34, 2016.
 - [73] S. Matsuo and T. Segawa, "Microring-resonator-based widely tunable lasers," *IEEE J.*

- Sel. Top. Quantum Electron.*, vol. 15, no. 3, pp. 545–554, 2009.
- [74] S. Andreou, K. A. Williams, and E. A. J. M. Bente, "Electro-Optic Tuning of a Monolithically Integrated Widely Tuneable InP Laser with Free-Running and Stabilized Operation," *J. Light. Technol.*, vol. 38, no. 7, pp. 1887–1894, 2020.
 - [75] D. Huang *et al.*, "High-power sub-kHz linewidth lasers fully integrated on silicon," *Optica*, vol. 6, no. 6, p. 745, 2019.
 - [76] R. Tang, T. Kita, and H. Yamada, "Narrow spectral linewidth Si photonic wavelength tunable laser diode for digital coherent optical communication," *Conf. Dig. - IEEE Int. Semicond. Laser Conf.*, pp. 96–97, 2014.
 - [77] K. J. Boller *et al.*, "Hybrid integrated semiconductor lasers with silicon nitride feedback circuits," *Photonics*, vol. 7, no. 1, 2020.
 - [78] H. Debregeas *et al.*, "2kHz linewidth C-band tunable laser by hybrid integration of reflective SOA and sio2 plc external cavity," *Conf. Dig. - IEEE Int. Semicond. Laser Conf.*, pp. 50–51, 2014.
 - [79] P. W. Juodawlkis, W. Loh, F. J. O'Donnell, M. A. Brattain, and J. J. Plant, "Ultralow-noise packaged 1.55- μ m semiconductor external-cavity laser with 0.37-W output power," *Conf. Lasers Electro-Optics*, pp. 7–9, 2009.
 - [80] R. R. Galiev *et al.*, "Spectrum collapse, narrow linewidth, and Bogatov effect in diode lasers locked to high-Q optical microresonators," *Opt. Express*, vol. 26, no. 23, p. 30509, 2018.
 - [81] G. H. Duan *et al.*, "Hybrid III - V on silicon lasers for photonic integrated circuits on silicon," *IEEE J. Sel. Top. Quantum Electron.*, vol. 20, no. 4, 2014.
 - [82] G. Roelkens *et al.*, "III-V/silicon photonics for on-chip and intra-chip optical interconnects," *Laser Photonics Rev.*, vol. 4, no. 6, pp. 751–779, 2010.
 - [83] J. E. Bowers, A. W. Fang, H. Park, R. Jones, O. Cohen, and M. J. Paniccia, "Hybrid silicon evanescent photonic integrated circuit technology," *Opt. InfoBase Conf. Pap.*, vol. 19, no. 4, 2007.
 - [84] A. Yariv, "Coupled-Mode theory for guided-wave optics," *IEEE J. Quantum Electron.*, vol. 9, no. 9, pp. 919–933, 1973.
 - [85] X. Sun and A. Yariv, "Engineering supermode silicon/III-V hybrid waveguides for laser oscillation," *J. Opt. Soc. Am. B*, vol. 25, no. 6, p. 923, 2008.
 - [86] S. Keyvaninia *et al.*, "Demonstration of a heterogeneously integrated III-V/SOI single wavelength tunable laser," *Opt. Express*, vol. 21, no. 3, p. 3784, 2013.
 - [87] M. Lamponi *et al.*, "Low-threshold heterogeneously integrated InP/SOI lasers with a double adiabatic taper coupler," *IEEE Photonics Technol. Lett.*, vol. 24, no. 1, pp. 76–78, 2012.
 - [88] X. Sun, H.-C. Liu, and A. Yariv, "Adiabaticity criterion and the shortest adiabatic mode transformer in a coupled-waveguide system," *Opt. Lett.*, vol. 34, no. 3, p. 280, 2009.

Chapter 2

Very High Coherence DFB Lasers

| | |
|---|----|
| Chapter II Very High Coherence DFB Lasers | 33 |
| I. III-V on SoI Narrow Linewidth DFB Lasers..... | 35 |
| I.1. State of the art..... | 35 |
| I.2. III-V on Silicon structure with low propagation losses | 37 |
| I.3. DFB Grating Design with low extraction loss..... | 39 |
| I.4. Conclusion..... | 43 |
| II. Transfer Matrix Simulation of HQ DFB Lasers..... | 44 |
| II.1. Simulation Methodology..... | 44 |
| II.2. Simulation Results | 47 |
| III. HQ DFBs characterizations | 56 |
| III.1. Measured spectra | 56 |
| III.2. HQ DFB Light-Intensity characteristics..... | 59 |
| III.3. HQ DFB noise characteristics | 63 |
| IV. Conclusion | 66 |
| V. References | 67 |

Optical coherent data transmission is evolving from the low-volume market of long-haul submarine and terrestrial network to the mass markets of passive optical network links, 5G radio over fiber fronthaul, data-center interconnects and internet of things free space applications. In this context, low cost coherent transceivers are of great interests and inexpensive laser diode sources with coherent compliant linewidth are key enablers.

It is well known that DFB lasers are efficient light sources with numerous benefits over extended cavity lasers (ECLs). For instance, they can be produced at a much lower cost. Indeed, an ECL requires the alignment of an external selective mirror with a gain chip to achieve single mode operation which highly contributes to its final cost. Whereas DFB lasers do not require such an alignment since the longitudinal mode filtering element of DFBs is their monolithically integrated distributed grating. Also, DFBs operational cost may be tremendously reduced as compared to that of ECLs. On one hand, wavelength detuning between the lasing mode and external mirror resonance of ECLs makes their spectral properties very sensitive to the operating point, and they need to be precisely stabilized using electronics feedback controls. On the other hand, the spectral characteristic of a single mode DFB remains similar on a large operating range making long term parasite wavelength drift less important.

However, contrary to ECL traditional DFB structures such as $\lambda/4$ phase-shifted DFBs and HR/AR DFBs suffer from high phase noise, making them impractical for coherent communication. In this chapter we study a novel DFB laser having very low phase noise, making it ideal for low-cost coherent transmission applications. We will first introduce the DFB laser structure based on a high quality factor cavity, then using numerical simulations we will relate the design parameters with the laser performances and finally measurements results will confirm that the DFB phase noise properties are notably improved using this particular design.

I. III-V on SoI Narrow Linewidth DFB Lasers

As we have discussed in the introductory chapter, laser linewidth is highly affected by optical losses occurring in a cavity roundtrip. Hence, in this part we will study a novel DFB laser with very low cavity losses fabricated using the III-V on Silicon integration platform. The DFB structure is based on the work of Caltech [1], and will be referred to as high quality factor DFB (HQ DFB). After reviewing various approaches leading to improved DFB phase noise properties, we show that the waveguide of a III-V on Silicon DFB can be engineered to optimize propagation losses inside the laser cavity. Then, we qualitatively describe how the DFB grating can procure very low mirror losses. In this part we will see that the waveguide corrugation is based on an apodized 1D photonic crystal structure, and the light confinement inside the laser diode will be illustrated using photonic band diagrams. Finally, with the help of couple mode theory we will link the DFB design parameters to the corrugated waveguide refractive index profile.

I.1. State of the art

In the past 30 years, many approaches to reduce DFB phase noise have been devised. The obtained linewidths for different methods leading to low phase DFBs are summarized in Fig.1.1.

The first and most straightforward approach to achieve low phase noise DFBs has been to reduce cavity losses. For instance, in [2]–[6], long uniform gratings with high strength were used to reduce mirror losses. Their results are marked by green diamonds. In [2]–[6] the laser diode waveguide was also engineered to achieve low propagation losses. Among the different method used, the work of [3] relies on a separate confinement heterostructure (SCH) guiding layer, while the laser diode p-doping level is kept as low as possible in [4], [5] or an asymmetrical cladding is epitaxied in [6]. Moreover, it was experimentally demonstrated in [2] that the wavelength detuning between DFB lasing mode and laser gain peak was a key parameter affecting the linewidth. Indeed a blue shift between lasing wavelength and gain peak tends to improve laser noise performances [7].

A second approach to reduce DFB phase noise was to limit the effect of linewidth rebroadening happening at high injection currents. The measured linewidths obtained with this method are plotted using blue squares. Considering a simple FP cavity, we have seen in

eq. (1.II.12) that laser linewidth value should be inversely proportional to pump current. However due to several effects not taken into account in this simple model such as spatial-hole burning (SHB) [8], non linear gain compression [9], mode partition noise with laser side modes [10] and recombination current in SCH layers [11] DFB linewidth tends to rebroaden at high current injection. Hence, the work of [12]–[15] focused on limiting the linewidth rebroadening at high injection current by using lower κL grating to limit SHB [12], increased active volume to reduce carrier overflow [14] and changing the facet phase to reduce SHB [15].

The third approach was to use optical feedback to narrow down DFB linewidth [16]. Measured linewidth in [16] is reported with a purple circle in Fig.1.1. The author will not enter into details of optical feedback to narrow laser linewidth in this chapter, because a more extensive study can be found in chapter IV. However, optical feedback is very sensitive to operating conditions, as detuning between the DFB emitting wavelength and feedback cavity resonances need to be precisely controlled. Hence, this approach is not robust because to the operating point, which makes the overall system harder to operate and leads to higher operational cost.

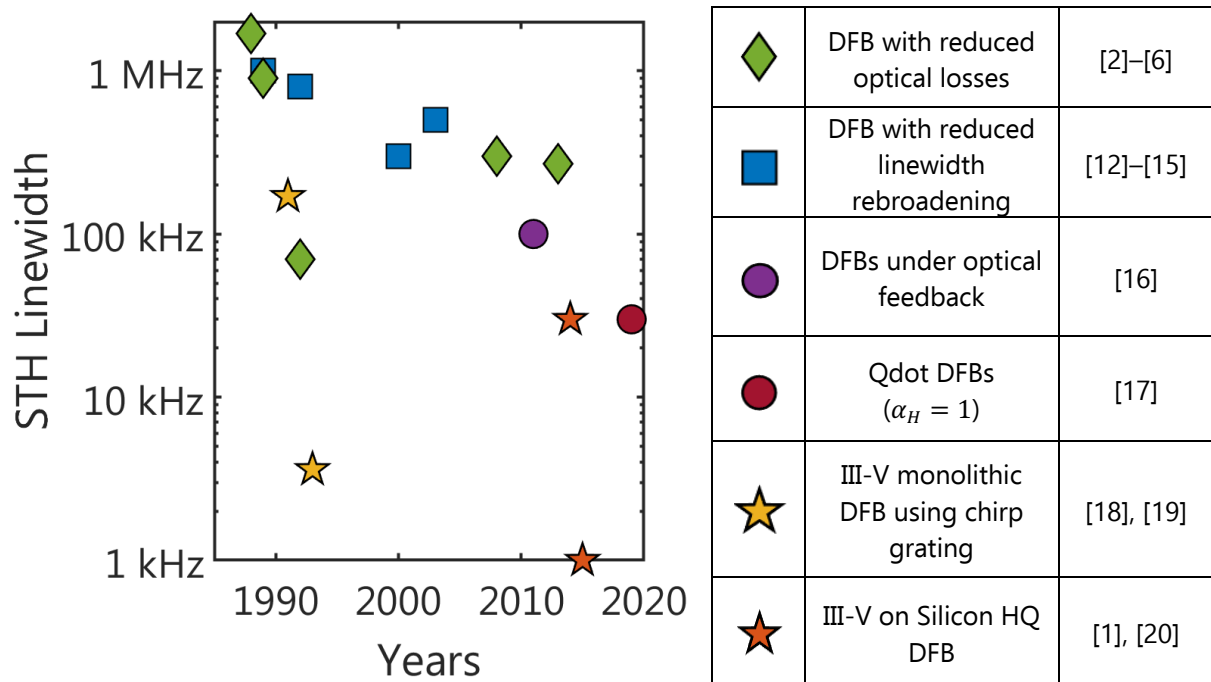


Fig.1.1 Measured linewidth of low noise DFB in the previous 30 years.

We have seen that semiconductor laser linewidth can be written as the original Schawlow-Townes linewidth broadened by a factor $(1 + \alpha_H^2)$ related to phase/amplitude coupling, with α_H the Henry factor. Numerous experimental results have reported a value of α_H around 2.5 using quantum well gains medium at 20°C. However, recent results published in [17] used

quantum dot medium to obtain an “atom-like” gain and reports a α_H value under 1 at 20°C. The measured Lorentzian linewidth is as low as 30 kHz and marked with a red circle in Fig.1.1.

In the last reported approach, and similarly to the study presented in this chapter, an apodized grating is used to reduce laser linewidth. The results reported with this approach are plotted using pentagrams in Fig.1.1. It is commonly thought that the work of Caltech [1], [20] introduced this type of HQ DFB, but the previous work of Hitachi [18], [19] have used a similar grating design to achieve very narrow linewidth DFB laser. However, in [18], [19], the relation between the DFB structure and the laser phase noise was not clearly stated. In addition to the chirp grating reducing mirror losses, the works of Caltech also benefit from the III-V on Silicon integration platform to engineer the transverse mode shape and reduce propagation losses. We note that relatively to other reported results, this approach has demonstrated DFB lasers with the narrowest linewidth.

I.2. Low Losses III-V on Silicon Structure

In this section we detail the reduction of DFB waveguide propagation losses using the III-V on Silicon platform. As we have seen in the introductory chapter, photonic integrated circuit (PIC) fabricated in this heterogeneous platform may rely only on a single III-V epitaxial stack, chosen to accommodate a wide variety of components. The unique design parameter which could reduce propagation losses is the silicon waveguide width placed under III-V materials.

It is well known that propagation losses in a semiconductor laser operating at telecom wavelength are governed by inter-valence band absorption (IVBA) inside P-doped semiconductors. Indeed, P-doped materials have the top of their valence band depleted and as illustrated in Fig.1.2.a) IVBA losses are due to radiative recombinations occurring between electrons from the spin-orbit (SO) band and holes from the heavy-hole (HH) conduction band. Measurements results from [21] showed that IVBA inside P-doped InP can be modeled by an absorption coefficient $\alpha_{InP(P)}$ corresponding to (at 1550nm) :

$$\alpha_{InP(P)} = 20 N_A \text{ cm}^{-1} \quad (2.I.1)$$

with N_A the doping concentration in 10^{18} cm^{-3} . While being much less lossy than P-doped InP, N-doped InP also contributes to modal losses due to free carrier absorption. In the C-band, the losses coefficient $\alpha_{InP(N)}$ is given by the formula [22]:

$$\alpha_{InP(N)} = 0.9 N_D \text{ cm}^{-1} \quad (2.I.2)$$

With N_D also being the doping concentration in 10^{18} cm^{-3} . The last contribution to modal optical losses corresponds to silicon waveguide losses. We will consider that un-doped bulk

Silicon losses are negligible and silicon waveguide losses are due to scattering. For a 300/500nm thick and 2 μ m wide Silicon rib waveguide, we can consider that Silicon losses are under 1dB/cm meaning that the propagation loss α_{Si} would be around:

$$\alpha_{Si} = 0.2 \text{ cm}^{-1} \quad (2.1.3)$$

We will assume that scattering losses are identical for waveguide width between 400nm and 2 μ m. While this assumption is arguable, thin silicon waveguides losses are still much smaller than those of III-V, so the overall III-V/Si waveguide losses would be governed by the III-V ones due to a high confinement inside III-V materials using thin silicon waveguide. Hence, there is no need of taking into account higher value of α_{Si} for thinner silicon waveguide. Then, it is considered that the III-V on Silicon waveguide can be designed in neglecting non-linear Silicon losses related to two photon absorption (TPA) occurring in the telecom bands. However, we keep in mind that TPA losses could set an intrinsic limit of III-V on Silicon DFB quality factor. Finally, total modal losses can be approximated by (2.1.4), where $\{\Gamma_i\}_{i=InP(P),InP(N),Si}$ are the confinement factors in their respective layers.

$$\alpha_i = \Gamma_{InP(P)}\alpha_{InP(P)} + \Gamma_{InP(N)}\alpha_{InP(N)} + \Gamma_{Si}\alpha_{Si} \quad (2.1.4)$$

As confinement factors depend on the silicon waveguide width, modal losses can be minimized using a precise width of silicon. Fig.1.2.b) plotting the optical losses as a function of silicon waveguide width shows that wider silicon waveguides yield reduced propagation losses. Indeed, a wider waveguide tend to pull the transverse mode repartition from the III-V to the silicon, which is much less lossy. The simulated modal losses reach a low value around 0.3 cm^{-1} for a silicon waveguide wide of 2 μ m, which will be suitable for the HQ DFB designs.

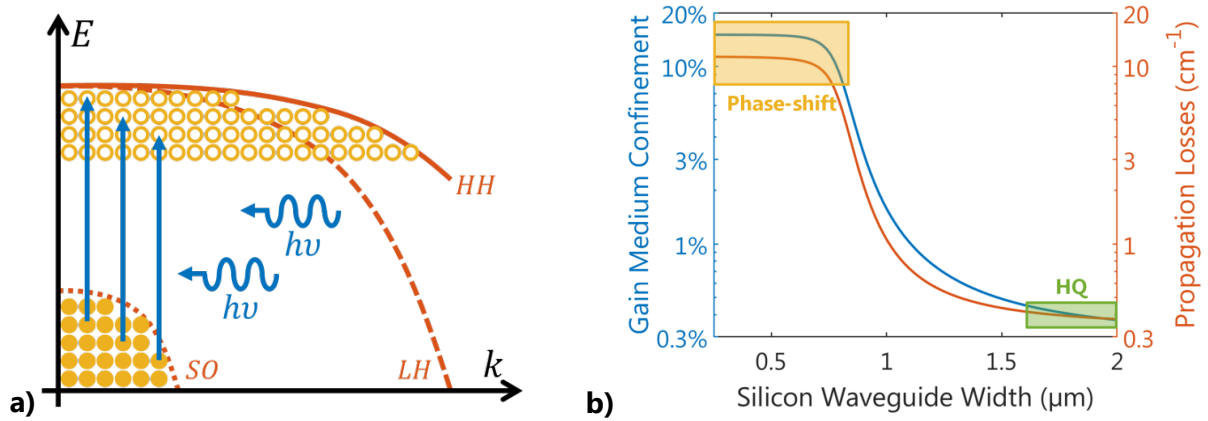


Fig.1.2 a) Illustration of IVBA, yellow plain circles are electrons, yellow empty circles are holes. b) Modal losses and confinement inside MQW as a function of Silicon waveguide width. The yellow region corresponds to traditional DFB design the green region to the HQ DFB presented here.

However, it is also shown in Fig.1.2.b) that wide Silicon waveguides also reduces the modal confinement inside the multiple quantum wells. As traditional DFB lasers uniform grating may induce high extraction losses -which inevitably cause high threshold gain- a relatively high value of gain medium confinement is required to fabricate a DFB with low threshold current. Silicon waveguide widths suitable for phase-shifted DFB are highlighted in yellow in Fig.1.2.b). Hence, the HQ structure relies on a much lower gain medium confinement factor than traditional DFBs and it will be shown in section II, that even with a low value of quantum well confinement, HQ DFBs can achieve great Light-Intensity performances.

I.3. DFB Grating Design with Low Extraction Loss

I.3.a. Introduction to photonic band diagrams

We will now describe how DFB external losses are drastically reduced using a chirped grating design. The photonic crystal community is already striving to achieve very HQ optical resonators [23], [24]. To realize such devices, a part of their work focuses on reducing the resonators external coupling losses. Hence, we will adapt a particular 1D photonic crystal HQ cavity to a DFB grating which induces low DFB equivalent "mirror" losses. As in photonic crystal theory we will define a photonic band structure, giving an intuitive viewpoint on the role of the grating to reduce the referred mirror losses. We will then use some fundamentals of the coupled mode theory (CMT) to obtain the effective index longitudinal profile from a corresponding photonic band structure. The reader can refer to annex B which reminds the basis of CMT applied to wave propagation in periodic media.

Optical wave propagating in infinite periodic media of period Λ can be analyzed using the Bloch-Floquet theorem. It proposes that a monochromatic optical wave ψ propagating along z can be written :

$$\psi(z) = e^{jkz} u_k(z) \quad (2.1.5)$$

with k being the Bloch wavenumber depending on the optical frequency, and $u_k(z)$ a Λ -periodic function. Whether the imaginary part of k is null or not, implies that either ψ freely propagates along z or is evanescent. By analogy with semiconductor theory we call the photonic bandgap, the interval of optical frequencies resulting in an evanescent Bloch waves. This concept is illustrated in Fig.1.3.a) showing transfer matrix simulation results of a uniform grating. The considered structure has its reflectivity centered at 1550 nm, a grating strength of 70 cm^{-1} and a length of $600 \text{ }\mu\text{m}$ which can be regarded as infinitely longer than a grating period ($\sim 0.24 \text{ }\mu\text{m}$).

Fig.1.3.b) shows the imaginary and real parts of k evaluated with the eigenvalues of the grating transfer matrix. As we can see, the Bloch wavenumber imaginary part is null outside the grating reflection band (Fig.1.3.a)), allowing for propagating Bloch wave. However in the grating reflection frequency band k has a strictly positive imaginary part (the negative solution is diverging so not physical) meaning that the Bloch waves vanish. The corresponding photonic bandgap is highlighted in red, it is centered at the Bragg resonant frequency and its value depends on the grating strength. By analogy with semiconductor crystal theory and as in [1], the photonic “valence” and “conduction” bands are defined as the lower and higher frequency limit of the photonic bandgap. They correspond to the black lines of Fig.1.3.

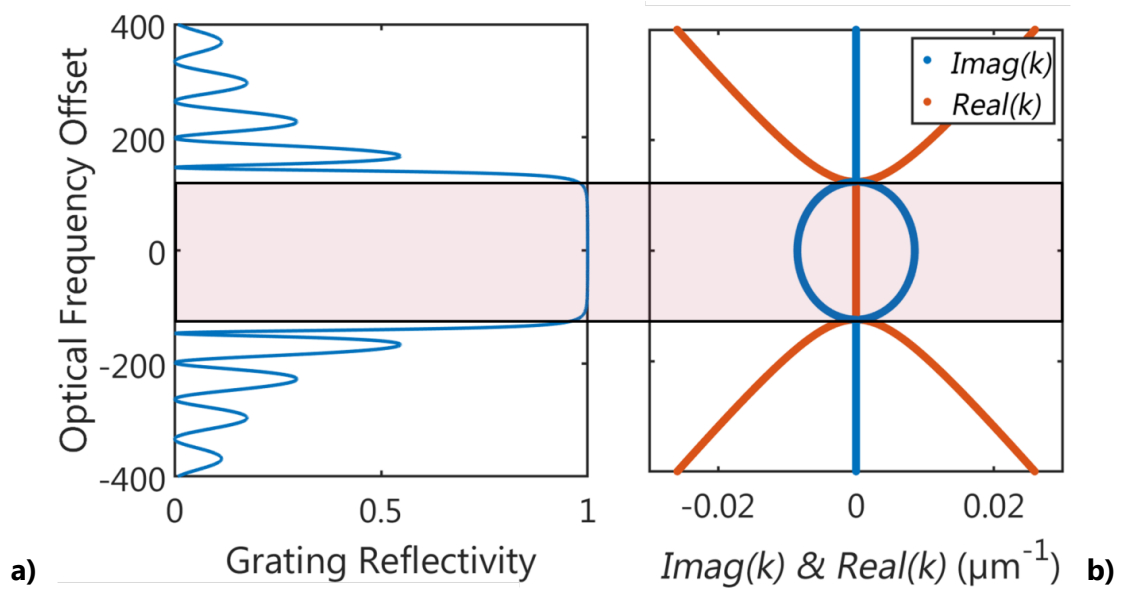


Fig. 1.3 a) Grating reflectivity b) Eigenvalues imaginary and real parts. The optical frequency offset is taken at the grating maximum reflectivity, the highlighted red zone correspond to the bandgap.

I.3.b. HQ DFBs photonic band structure

Fig.1.4.a) shows the photonic band structure of the DFB, with the valence and conduction bands in black and the photonic bandgap highlighted in blue. Contrary to the previous paragraph in which the photonic bands are defined using an infinite uniform grating, here the photonics band frequencies are axially varying using a non-uniform grating. We do think that the photonic band model is still valid, as the corrugated waveguide average effective index is slowly varying during a grating period.

The idea to reduce mirror loss of the HQ DFBs, lies in axially confining the electromagnetic field at the center of the cavity using a photonic potential well. A simple viewpoint is to consider that -as in quantum electronic- a mode may be allowed in the well. This mode which

corresponds to the DFB lasing mode is marked by the red dotted line in Fig.1.4.a) and can be described by a Bloch wave. Inside the well the lasing mode frequency is below the photonic bandgap and can freely propagate. However, outside the well its frequency is in the grating stopband, so the Bloch wave is evanescent and reflected back into the well. Hence, the sections outside the well act as high reflectivity mirrors and will be referred to as the barriers with analogy to quantum electronics.

We have three parameters to choose while designing this laser. The first one is the depth of the well called W_D and given in GHz, the second is the length of the well L_w and the third is the length of the mirror sections L_b . Later, we will present numerical simulations results to show the design parameters leading to optimal laser performances.

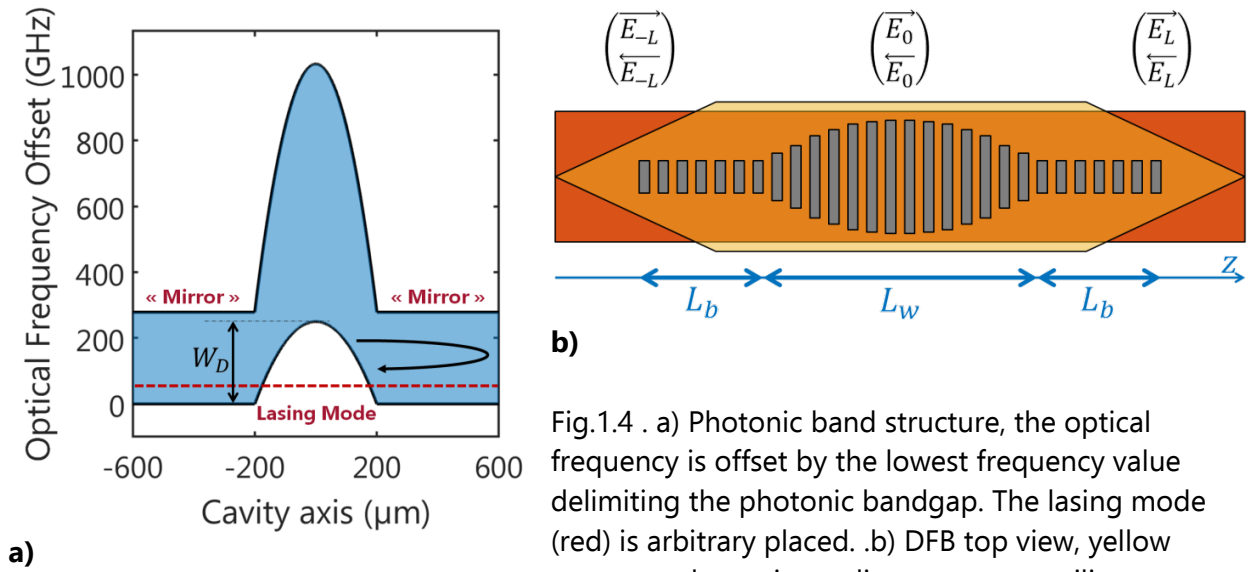


Fig.1.4 . a) Photonic band structure, the optical frequency is offset by the lowest frequency value delimiting the photonic bandgap. The lasing mode (red) is arbitrary placed. .b) DFB top view, yellow correspond to gain medium, orange to silicon waveguide and grey to etched tooth.

I.3.c. Bloch-wave engineering of the III-V on SoI DFB grating

In the following, the technological implementation of the HQ DFB photonic well is discussed. In order to form a well, the corrugated waveguide averaged effective index is reduced which increases the Bragg resonant frequency and curves the photonic valence band upward. Using the III-V on Silicon process described in the introduction, this is made by widening the etched teeth as sketched on the top view illustration of the HQ DFB in Fig.1.4.b). Indeed, the blue curve of Fig.1.5.a) shows that wider etched teeth reduce the corrugated waveguide average effective index, and by considering an etched tooth wide of 120 nm in the barrier region, -being the smallest possible etching feature of the DUV lithography process- we plot the valence band offset in the well in Fig.1.5.a). As we can see, photonic well deep of 350 GHz can be obtained in the III-V on Silicon platform. Moreover, the Silicon DUV lithography allows grating teeth widening within a 1 nm grid, meaning that a very smooth

grating apodization can be achieved. Finally Fig.1.5.b) displays the longitudinal effective index profile in the cavity, confirming the index reduction at the center of the cavity to form the photonic well.

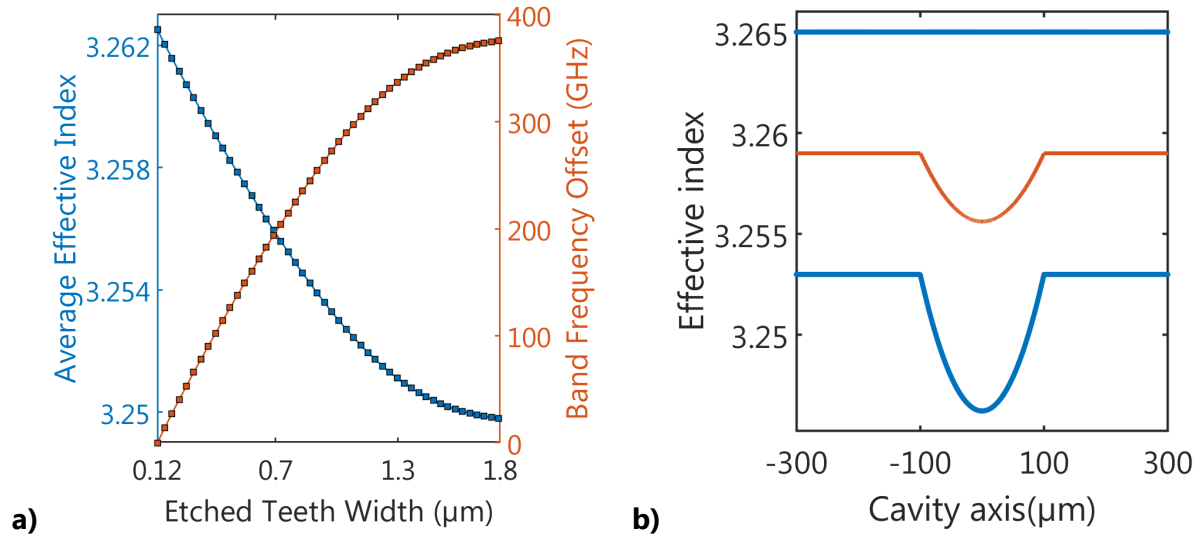


Fig.1.5 a) Grating parameters as a function of grating teeth width. b) longitudinal profile of the effective index. Unetched and etched waveguide effective index (top blue and bottom blue), while orange correspond to the average effective index.

The design methodology of the DFB grating is described in the following. After choosing the DFB length, we fix the width of the grating teeth in the mirror region to a small value achievable in the DUV lithography process. We then retrieve the corresponding effective index of the etched waveguide, and we compute the band structure in the mirror region thanks to annex B equation (B.11). After that, we fix the length of the well L_w to a given value and its depth W_D to a smaller value than the mirrors grating bandgap, this ensures that the lasing mode frequency must be in the grating stop band of the mirror region. The pairs (L_w, W_D) resulting in optimal laser performances will be discussed in part II. In the well, the valence band offset is given by the parabola interpolation of $\{[-L_w/2, 0], [0, W_D], [L_w/2, 0]\}$ as parabolic well profiles minimize the radiative losses [1]. Then, using the notations and equations of annex B, we can retrieve the mode effective index for a etched tooth n_1 as a function of the valence band profile f_v . This is done by solving the polynomial equation :

$$n_1^2 + n_1 \left(2n_0 - 3 \frac{c}{2f_v \Lambda} \right) + n_0 \left(n_0 - \frac{c}{2f_v \Lambda} \right) = 0 \quad (2.I.6)$$

Where n_0 is the un-etched waveguide effective index and Λ the grating period. (2.I.6) is obtained by injecting (B.9) and (B.10) in (B.11). Finally the length of the mirror section will set the external loss and quality factor of the cavity.

I.4. Conclusion

In this section we have seen that both propagation and equivalent mirror losses of a III-V on Silicon DFB laser can be minimized using respectively a particular III-V/Si waveguide structure decreasing the mode confinement in P-doped InP and an photonic bandgap engineered grating forming a “potential well”. We have then related the corrugated waveguide index profile with the photonic bandgap parameters using a polynomial equation. However, we have not precisely quantified the possible phase noise improvements and power characteristics of the HQ DFBs, we have also not found out which photonic well parameters (L_w , W_D) would lead to best performances. Hence, in the next section, we will properly investigate DFB HQ performances using the transfer matrix method based on the retrieved index profile of eq. (2.1.6).

II. Transfer Matrix Simulation of HQ DFB Lasers

In this part, numerical simulation results will yield grating parameters leading to DFB with both narrow linewidth and high output power. We first describe the methodology of the transfer matrix simulations, and then for a given DFB length we will estimate which photonic well parameters (depth and length) lead to high power and narrow linewidth single mode operation. This is, for the first time to our knowledge, that grating optimization of the HQ DFB has been studied using numerical methods.

II.1. Simulation Methodology

After fixing the photonic bandgap parameters and retrieving effective index profiles, HQ DFBs are simulated using the transfer matrix method. In our method we neglect longitudinal effects such as spatial hole burning, spontaneous emission enhancement [7] and nonlinearities such as two photons absorption. These effects could be incorporated to study the intrinsic limit of these HQ DFBs but it would require much longer computational time. Due to transfer matrix simulations being performed using only a 1D model, radiation losses are not taken into account. They occur because of the chirped grating design, indeed the corrugated waveguide can be seen as a series of oscillating dipoles and apodizing the grating makes each dipole oscillating not purely in phase, this leads to out of plan losses. Radiative losses could be either added by performing 3D-FDTD simulations or using analytical methods (see e.g. [25]) .

Most works using the TMM to study DFB properties set a reference plane at one edge of the cavity [26], [27], and it is for instance useful to study feedback effect [26]. However in our case the grating structure is symmetric and setting a reference plane at the center of the cavity reduces the computational cost by ~ 2 . We use the obvious notations \vec{E}_z and \overleftarrow{E}_z to describe the forward and backward propagating wave at position z . In this case we have the field at one extremity of the DFB E_L related to the field at the center of the cavity E_0 by :

$$\begin{pmatrix} \vec{E}_L \\ \overleftarrow{E}_L \end{pmatrix} = \bar{\bar{M}} \begin{pmatrix} \vec{E}_0 \\ \overleftarrow{E}_0 \end{pmatrix}, \quad \bar{\bar{M}} = \begin{pmatrix} m_{11} & m_{12} \\ m_{21} & m_{22} \end{pmatrix} \quad (2.II.1)$$

with $\bar{\bar{M}}$ the transfer matrix obtained by a product of unit corrugation matrix. If we have no light re-injection, we have $\overleftarrow{E}_L = 0$ so we deduce $\overleftarrow{E}_0 = -(m_{21}/m_{22})\vec{E}_0$. Due to symmetry we find the resonant condition :

$$1 - \left(\frac{m_{21}}{m_{22}}\right)^2 = 0 \quad (2.II.2)$$

For a given DFB structure m_{ij} depends on the optical pulsation ω , the propagation losses α_i and the modal gain $g = \Gamma_{MQW} g_{mat}$. To study the HQ DFB properties we first need to find its modes, which correspond to a set $\{(\omega_i, g_{th_i})\}$ being the solution of (2.II.2). The lowest value of g_{th_i} will be referred as g_{th} and correspond to the threshold gain of the lasing mode. After finding the possible DFB operating points and using the formalism detailed in annex C which consists in expanding the resonant condition close to DFB mode, we derive equivalent DFB rate equations :

$$\frac{dP}{dt} + 2P \frac{Re(\partial H / \partial \omega)}{Im(\partial H / \partial \omega)} \frac{d\varphi}{dt} = -2 \frac{Re(\partial H / \partial g)}{Im(\partial H / \partial \omega)} (g - g_{th}) P + R_{sp_{eq}} + F_{p_{eq}} \quad (2.II.3)$$

$$\frac{d\varphi}{dt} - \frac{1}{2P} \frac{Re(\partial H / \partial \omega)}{Im(\partial H / \partial \omega)} \frac{dP}{dt} = - \frac{Im(\partial H / \partial g)}{Im(\partial H / \partial \omega)} (g - g_{th}) + F_{\varphi_{eq}} \quad (2.II.4)$$

With $H(\omega, g) = (m_{21}/m_{22})^2$ being the transfer function of the cavity, while the other physical quantities are detailed in Annex C. In the case of a simple Fabry-Pérot cavity, H would be given by :

$$H = r^2 e^{(g - \alpha_i)L_{act}} e^{j \frac{\omega}{c} n(\omega) 2L_{act}}$$

With r the mirror field reflectivity, L_{act} the length of the active region, n the effective index of the waveguide and α_i the propagation losses. Hence we can identify the terms of (2.II.3) and (2.II.4) as :

$$v_g \stackrel{\text{def}}{=} -2 \frac{Re(\partial H / \partial g)}{Im(\partial H / \partial \omega)} \quad (2.II.5)$$

$$\frac{1}{\tau_p} \stackrel{\text{def}}{=} v_g g_{th} \quad (2.II.6)$$

$$\alpha_{Heq} \stackrel{\text{def}}{=} \frac{Im(\partial H / \partial g)}{Im(\partial H / \partial \omega)} \quad (2.II.7)$$

With v_g an equivalent group velocity, τ_p an equivalent photon lifetime and α_{Heq} an equivalent phase/amplitude coupling factor. And finally we can study the complex DFB structure using the simple and powerful formalism of rate equations.

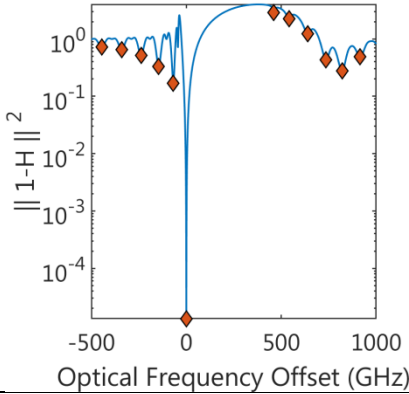
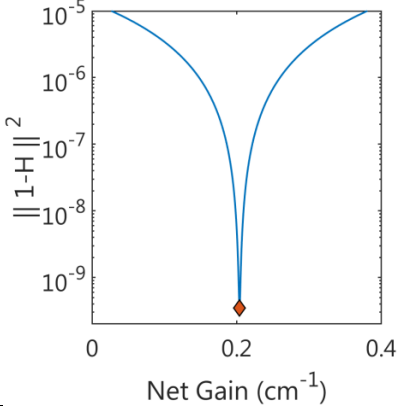
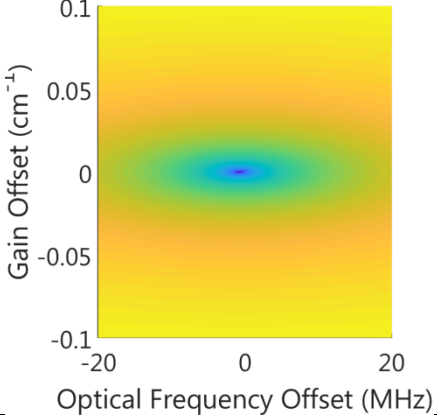
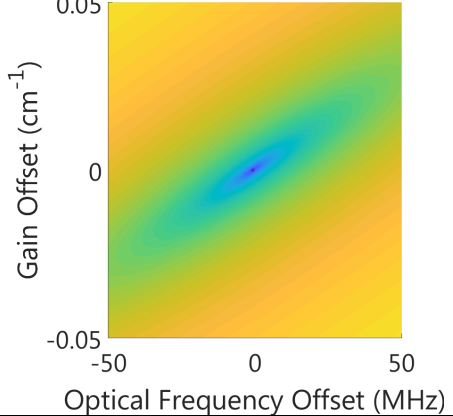
| Steps | Miniature | Description |
|-------|---|---|
| 1 |  | <p>Coarse research of the DFB modes pulsation $\{\omega_i\}$, with $g_{mat} = \alpha_i = 0$ and $\alpha_H = 0$</p> <p>The miniature shows $\ 1 - H\ ^2$ as a function of the optical frequency. DFB modes correspond to local minima of the $\ 1 - H\ ^2$ function and are marked by diamonds.</p> |
| 2 |  | <p>Coarse research of the DFB modes threshold gain $\{g_i\}$, at pulsations $\{\omega_i\}$ assuming $\alpha_H = 0$</p> <p>The miniature shows $\ 1 - H\ ^2$ as a function of the net gain for $\omega = \omega_0$, being the HQ mode pulsation.</p> |
| 3 |  | <p>Fine research of the DFB modes pulsation and threshold gain $\{(\omega_i, g_{th_i})\}$ assuming material $\alpha_H = 0$</p> <p>The figure shows a mapping of $\ 1 - H\ ^2$ as a function of the optical frequency and gain in the vicinity the DFB lasing mode. Blue correspond to values close to 0.</p> |
| 4 |  | <p>Numerical computation of the cavity transfer matrix $H(\omega, g)$ close to the lasing mode (ω_0, g_{th}) assuming $\alpha_H = 2$.</p> <p>As in step 3 the figure shows $\ 1 - H\ ^2$</p> |

Table 1. Details of the simulation method leading to extract rate equation parameters

The numerical simulation methodology is summarized in Table 1. Coarse and fine research means that either golden section search or Nelder-Mead simplex algorithm are used to find local minima. Finally, the equivalent rate equation parameters are computed by expanding $H(\omega, g)$ in step 4.

II.2. Simulation Results

In this section, we will present numerical simulation results showing the impact of the DFB grating on laser performances. We consider a 800 μm long HQ DFB, which photonic well parameters $\{L_w, W_D\}$ vary in the following intervals $\{[30, 280] \mu\text{m}, [35, 325] \text{GHz}\}$ achievable in our III-V on Silicon process. The simulation results are presented using 2D mapping and will be compared to a traditional DFB structure. Some important simulation parameters are summarized in Table 2.

| | HQ | | Phase-shifted |
|-----------------------------|-----------|-------|----------------------|
| $L (\mu\text{m})$ | 800 | | 800 |
| Design parameters | W_D | L_w | $\kappa L = 2$ |
| $\alpha_i (\text{cm}^{-1})$ | 0.4 | | 11 |
| $\Gamma_{MQW} (\%)$ | 0.4 | | 14 |

Table 2. DFB parameters used in the following simulations

In a first section the relation between grating parameters and laser output power is presented, this is done by simulating laser threshold and slope efficiency of different HQ designs. Then the grating parameters leading to maximum side mode rejection are investigated. Finally, we show the DFB designs leading to the narrowest linewidth.

II.2.a. Grating Parameters vs optical power

As we have seen in the introductive chapter, high QAM formats require relatively high value of SNR, which can be obtained with high laser power. We already know that traditional DFB lasers structure made with the III-V on Silicon technology is in the 10 mW class [28]. Hence, using numerical simulation, we will compare both the threshold current and slope efficiency of a HQ DFB with a traditional structure, and discuss the HQ grating parameters allowing high DFB output power.

II.2.a.i. Grating Parameters vs threshold current

At a first look, one might think that the threshold current of a HQ design should be much higher than the one of traditional DFB structures due to a very low confinement in the gain medium (~ 30 times lower for a HQ DFB as shown in Fig.1.2.b)). Indeed the threshold carrier density N_{th} (being proportional to threshold current) is related to the confinement factor, losses and optical gain with the equation :

$$\Gamma_{MQW} g(N_{th}) = \alpha_i + \alpha_m \quad (2.II.8)$$

This shows that $g(N_{th})$ is inversely proportional to Γ_{MQW} , and because g is increasing as a function of N , it means that N_{th} is increasing a function of Γ_{MQW} . However, in the case of a HQ DFB the expected increase of N_{th} due to a low confinement factor should be compensated by much lower propagation and mirror loss of the HQ structure.

Because very similar epitaxial stacks are used in our III-V on Silicon process, the relation between material gain g and carrier density N is assumed to be identical for HQ and traditional DFB designs. This relation could be either approximated with analytic formulas, [29], [30] or precisely obtained with measurements [31]. In our study we assume no particular relation between gain and carriers, so the results can be expanded for a larger variety of technologies.

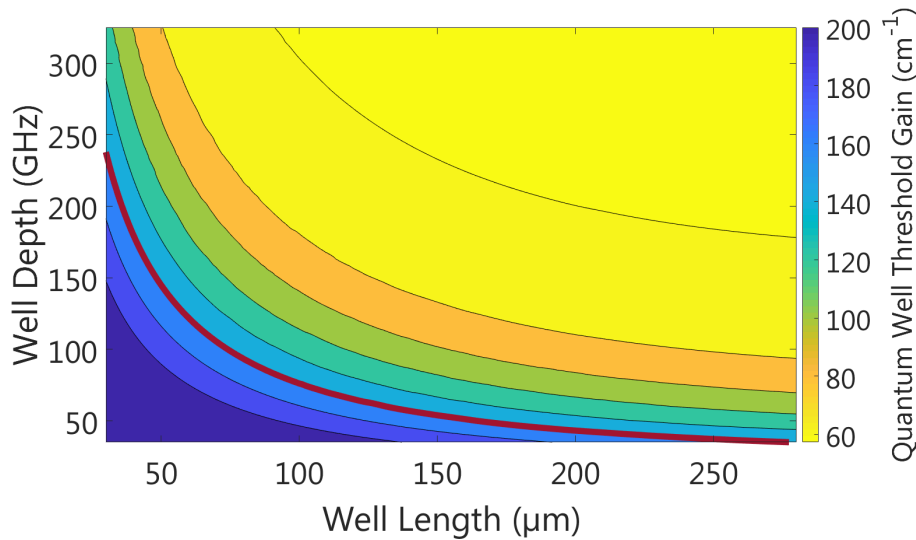


Fig.2.1 Mapping of the material threshold gain for an 800 μm long HQ structure and varying well depth and length. Two adjacent color zones have a threshold gain difference of 20 cm^{-1} , and the red line correspond to a constant gain level of 160 cm^{-1} which is the value obtained for a phase shifted structure.

Fig.2.1 shows the mapping of material threshold gain $g(N_{th})$ for varying parameters of an 800 μm long HQ cavity. As we can see $g(N_{th})$ is as high as 200 cm^{-1} for short and shallow

well. This value is slightly larger than what is expected for an III-V on Silicon 800 μm phase-shifted DFB with a κL of 2 (160 cm^{-1}). However increasing the well depth and length tends to confine the field at the center of the cavity and reduces mirror loss. It reduces the HQ DFB threshold gain to a low value converging to 50 cm^{-1} for very long and deep well. This value is obtained when the modal gain $\Gamma_{MQW} g$ strictly compensates internal losses α_i , because for deep and long well external losses may be negligible. Hence, due to very low losses of the HQ structure counterbalancing its low confinement in the gain medium, the HQ DFB threshold current can be kept as low as the one of a traditional structure

II.2.a.ii. Grating Parameters vs slope efficiency

The laser slope efficiency η_s , link the laser output power and bias current. For bias current higher than threshold and before the thermal roll-off, the laser output power per facet P linearly increase as a function of bias current I with a slope coefficient given by :

$$\eta_s \equiv \frac{dP}{dI} = \eta_I \frac{h\nu}{q} A_s \frac{1}{1 + \frac{\tau_{ext}}{\tau_{int}}} \quad (2.II.9)$$

With A_s a coefficient taking into account power asymmetry per facet, η_I the electrical injection efficiency, τ_{ext} and τ_{int} external and internal photon lifetime. In the presented model, τ_{ext} is obtained by assuming no propagation loss inside the cavity while $\tau_{int} = v_g \alpha_i$.

We will compare the slope efficiency of a HQ DFB with a traditional DFB structure. As we are studying how the DFB grating will affect the laser output power, we will keep η_I constant, because it only depends on the III-V epitaxy. Both the HQ DFB and traditional phase-shifted DFB are symmetric, meaning that the output power for each of their facet is equal, so in both cases $A_s = 1/2$. In future HQ designs, the photonic well could be shifted at one side of the cavity to induce an asymmetry in the cavity power repartition and gain few dB in one of the two facets. We will then compare both types of DFBs extraction efficiency η_e , giving the ratio of photons coupled to the output waveguide with number of photons inside the cavity.

$$\eta_e = \frac{1}{1 + \frac{\tau_{ext}}{\tau_{int}}} \quad (2.II.9)$$

The simulation results are mapped in Fig.2.2. In the case of the traditional phase-shifted DFB structure ($\kappa L = 2$) in the III-V on Silicon technology, the external and internal losses are more or less the same and η_e is roughly 50 %. For the HQ structure the efficiency is as high as 70% in the case of narrow and shallow well. Indeed in this region, the cavity external losses are higher than internal ones, meaning that the extraction efficiency is over 50%. However as previously seen, this region corresponds to a high threshold current and is not practically

usable. Also for long and deep well, the extraction efficiency can drop below 10%. In this region the external losses are very low compared to internal loss, and no power is extracted from the cavity.

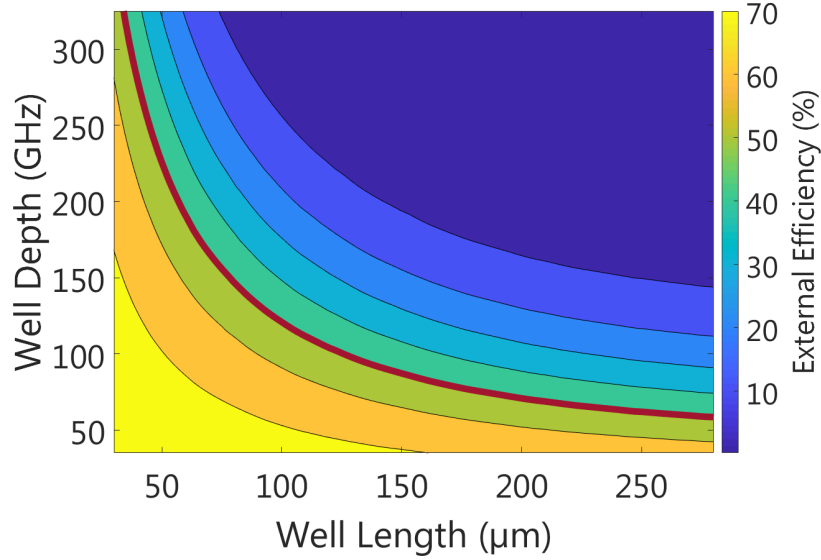


Fig.2.2. Mapping of the extraction efficiency for the HQ structure. Two adjacent colored zones are separated by an external efficiency variation of 10 %. The red line corresponds to a constant extraction efficiency of 50%, corresponding to the phase shifted structure.

II.2.a.iii. Grating Parameters vs output power

After investigating the threshold gain and slope efficiency of the HQ lasers for different grating parameters, we synthesize the achievable output power at a bias current I_{Bias} of 100 mA in Fig.2.3. The gain medium parameters used to compute laser output power are given below. The threshold current I_{Th} can be written as $I_{Th} = I_{Tr} + I_L$ with I_{Tr} the injection current at transparency and I_L the current required to compensate optical losses. We then assume that the threshold carrier density is close enough to the carrier density at transparency N_{Tr} and in this case we have :

$$I_L = \frac{qV}{\eta_I \tau_N} \times \frac{1}{\tau_P} \times \frac{1}{\Gamma_{MQW} G_N} \quad (2.II.10)$$

The output power per facet P is finally given by :

$$P = \frac{hc}{2\lambda q} \eta_I \eta_e \times (I_{Bias} - I_{Th}) \quad \text{with } I_{Bias} > I_{Th} \quad (2.II.11)$$

For the traditional phase shifted DFB used for comparison, the output power per facet is around 11 mW. The HQ DFB output power is simulated in the 6 mW range for short (50 μm) and shallow (50 GHz) well. In this region, the low value of output power is related to the high

HQ DFB threshold gain. Then, for longer and deeper well the HQ DFB output power peaks around 14 mW, which would be larger than the traditional phase-shifted DFB. This value is obtained for an optimal combination of slope efficiency and threshold gain. Then for longer ($> 200 \mu\text{m}$) and deeper ($> 250 \text{ GHz}$) wells the laser output power drastically diminishes as the external losses becomes much smaller than internal losses.

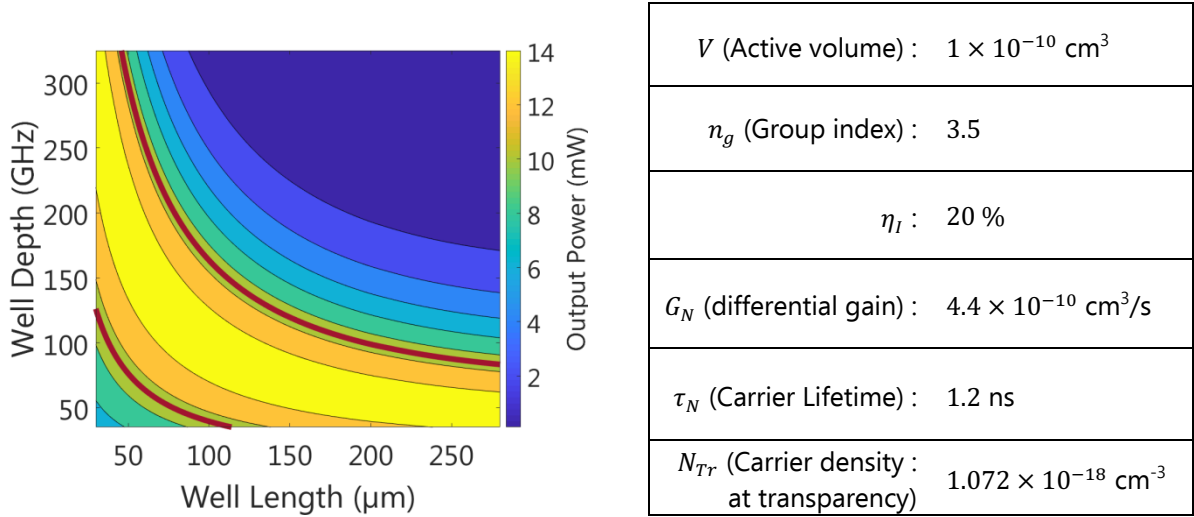


Fig.2.3 Mapping of achievable DFB power at 100 mA.

Two adjacent colored zones are separated by an output power variation of 2mW. The red line corresponds to a constant output power of 11.1 mW corresponding to the phase shifted structure.

II.2.b. Grating Parameters vs side mode suppression ratio

After seeing the grating parameters that would lead to optimum output power, we also need to find the grating parameters determining ideal single-mode lasing. Indeed, in a WDM communication link, a secondary DFB mode with a low rejection ratio would bring noise on the corresponding channel wavelength. The secondary DFB mode will also increase the low frequency relative intensity noise due to mode partitioning noise [32]. Traditional phase shifted structure with κL around 2 usually exhibits a side mode suppression ratio (SMSR) over 50 dB, which is the targeted value for our HQ design.

Precise simulations of DFB laser spectrum above threshold are challenging. Several papers focus on this challenge [33]–[36]. However the simulation time required to obtain DFBs spectra following [34] can be tremendously long. It was then preferred not to simulate the HQ DFB spectrum, but rather focus on the gain margin of different modes. We define the gain margin Δg_{th} as the ratio of threshold gain of the primary and secondary DFB modes.

$$\Delta g_{th_{dB}} = 10 * \log_{10}\left(\frac{g_{th_2}}{g_{th_1}}\right) \quad (2.II.11)$$

In literature, the gain margin has been widely defined as $\Delta g_{th_{bis}}$ which is the difference between threshold gains, normalized by using the DFB length L :

$$\Delta g_{th_{bis}} = g_{th_2}L - g_{th_1}L \quad (2.II.12)$$

In the case of a HQ structure defining the length of the cavity is not straightforward, and taking geometrical length would be an important error due to a very low group velocity of the HQ mode. Also in the HQ structure, the modal threshold gains ($\Gamma_{MQW} g$) can be two orders of magnitude lower than the one of a traditional structure. In this case defining gain margin using a subtraction would results in extremely low value of gain margin, and the simulation results would wrongly claim that the DFBs secondary mode may exist. Using our definition of gain margin, we set an empirical criterion saying that $\Delta g_{th_{dB}} > 3 \text{ dB}$ is sufficient to achieve single mode lasing. This empirical criterion is similar to the one used to study external cavity lasers, and in the case of an ECL this criterion is sufficient for achieving a laser SMSR over 50 dB [37].

Fig.2.4. a) shows the threshold gain margin for different HQ designs, as we can see for very short and shallow well $\Delta g_{th_{dB}}$ is under 3dB, then a maximum of $\Delta g_{th_{dB}}$ is obtained for a well length around 70 μm and well depth close to 300 GHz, and finally $\Delta g_{th_{dB}}$ drops for longer and deeper well. To illustrate why such a dependence of $\Delta g_{th_{dB}}$ is happening, Fig.2.4. b) shows the threshold gain margin of several DFB modes for three laser designs. Design A corresponds to a short and shallow well, design B corresponds to the grating parameters leading to maximum $\Delta g_{th_{dB}}$ and design C corresponds to DFB designs with long and deep well.

- A. For short and shallow wells the DFB grating can be considered as a slightly perturbed uniform grating. As we can see in Fig.2.4.b), in the case of the orange square, corresponding HQ design A, the secondary mode is situated at the other side of the photonic bandgap, and some symmetry can be observed on both sides of the stopband. The threshold gain margin as a function of the optical frequency shows some similarities with uniform DFB grating.
- B. Then for longer and deeper well, the HQ mode threshold gain is reduced which increases the gain margin between the lasing mode and the mode at the other side of the stop band. The purple diamond of Fig.2.4.b) are obtained for the HQ design B, and this shows that the secondary mode is on the same side of the stopband of the lasing mode. This is due to the fact that the mode at the other side of the stop band is perturbed by the top of the photonic well, splitting the uniform grating into two

parts. The simulated gain margin between the first and secondary mode is 9 dB for the HQ design B.

- C. Finally when the well length and depth exceed a certain value, the threshold gain margin falls down to <1 dB. As shown with the yellow circle of Fig.2.4.b), corresponding to the design C, a second mode HQ mode can exist in the well. This second mode is spaced by around 80 GHz in the case of design C, and the gain margin is around 0.7 dB.

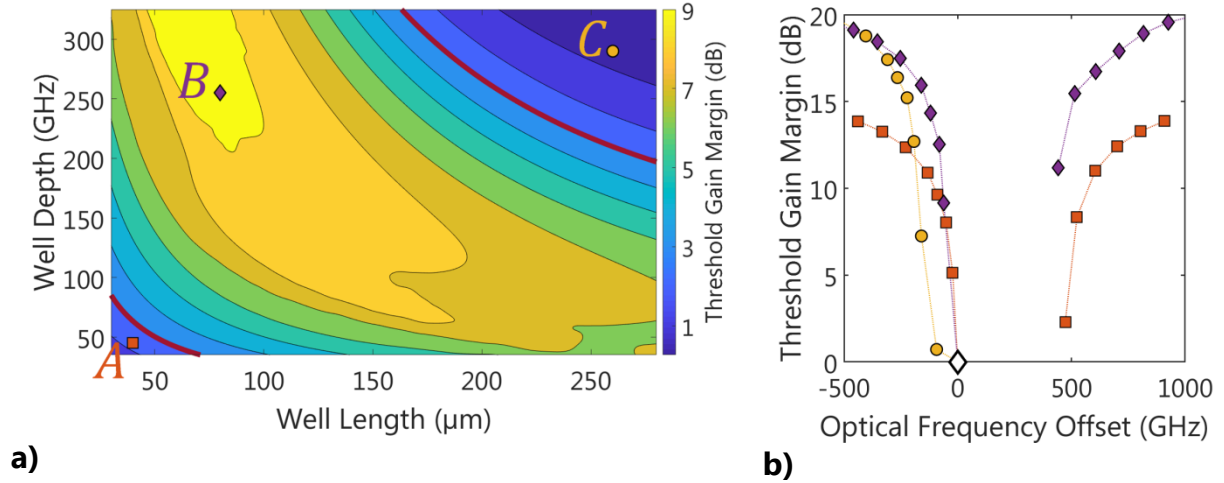


Fig.2.4. Threshold gain margin mapping for different HQ designs. Each level is separated by 1 dB. The red lines correspond to a threshold gain margin of 3 dB. b) Threshold gain of several DFB modes as a function of the optical frequency offset to the lasing mode. Orange squares correspond to the point A in the mapping of a), purple diamonds are for B and yellow circles for C. The main lasing mode is represented by a white diamond.

To summarize, single mode lasing of the HQ cavity should be expected on a wide range of design parameters if two conditions are fulfilled :

- The photonic well is neither too long nor too deep to not allow the existence of a second HQ mode.
- The photonic well is deep and long enough to confine a HQ mode with a much greater photon lifetime than other DFB modes.

II.2.c. Grating Parameters vs photon lifetime

After seeing that HQ DFB grating needs to be carefully chosen to achieve efficient single mode operation, we study grating parameters resulting in best phase noise performances. As stated in the introductory chapter eq. (1.II.12) laser linewidth is quadratically narrowed for increased photon lifetime. Hence, in this part we present simulated photon lifetime given by equation (2.II.6). For a reference, the simulated photon lifetime of the 800 μm long phase shifted laser was found to be 9 ps.

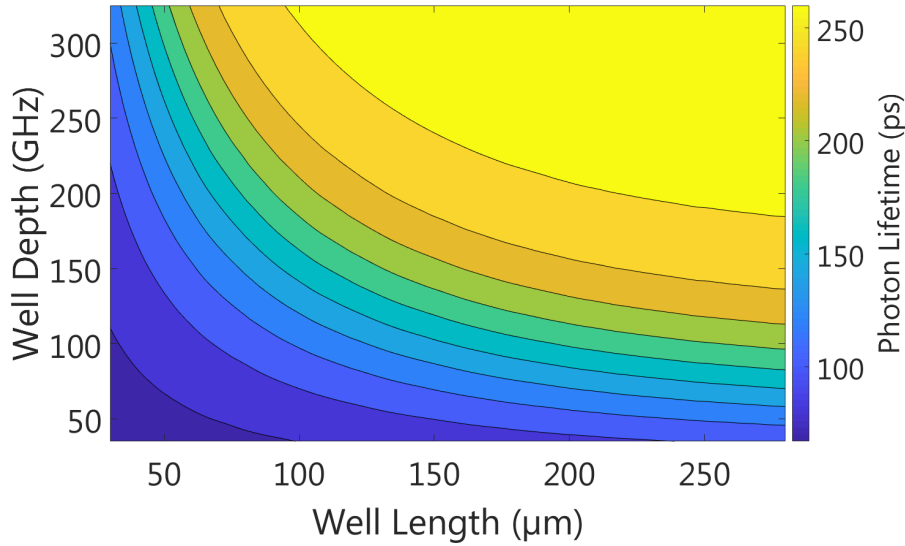


Fig.2.5. Photon lifetime mapping for different HQ designs.

The photon lifetime map as a function of grating parameters is presented in Fig.2.5. Short and shallow wells result in photon lifetime around 90 ps, showing a tenfold increase as compared to a traditional DFB structure. As we have already shown in 2.1 and 2.2, longer and deeper wells better confine the field at the center of the cavity and reduce mirror losses, so increase photon lifetime. Photon lifetime reaches a maximum around 250 ps for well length of 280 μm and well depth over 300 GHz. In this case, photon lifetime value is limited by propagation losses, because for this grating design mirror losses are tremendously smaller than propagation losses. For design parameters giving efficient and single mode HQ DFBs, the photon lifetime is in between 140 ps and 210 ps, implying that DFB linewidth could be reduced by a factor in between 240 and 540. Hence if we assume a phase shifted DFB linewidth of 3 MHz, the HQ designs should lead to laser linewidth in the 10 kHz range.

II.2.d. Conclusion and perspective

In this section, using numerical simulations we have studied how laser grating parameters, such as photonic well depth and length improve laser performances. As a reminder, our simulation model has neglected radiation losses, longitudinal and non linear effects. Including radiative losses would slightly decrease (resp. increase) the simulated photon lifetime (resp. threshold gain). Then, adding spatial hole burning and non linear gain compression to the numerical model would lead to a lower laser efficiency. Finally, taking into account longitudinal spontaneous emission enhancement factor K [7] would give modified Langevin force in rate equations hence modifying the laser phase noise properties. This phenomenon would tend to broaden the HQ DFB optical linewidth by a factor of K , although,

it is unknown whether the K factor of the HQ structures would be greater or smaller than the K factor of traditional structures.

Nonetheless, our simple model has yielded design parameters leading to optimum output power, threshold gain margin and photon lifetime. The red zone in Fig.2.6. shows the HQ DFB grating parameters allowing an output power over 10 mW, a threshold gain margin over 3dB and a photon lifetime over 100ps. By considering $\alpha_H = 3$, $n_{sp} = 2$, $\eta_I = 20\%$, $I_{bias} = 100 \text{ mA}$, and $I_{Th} = 50 \text{ mA}$, a photon lifetime of 100 ps should result in a laser linewidth in the 10 kHz range making the HQ DFB ideal for high order QAM coherent transmission.

As we can see, two design choices lead to high performance HQ DFBs, it is either possible to use short and deep photonic wells (zone A) or long and shallow ones (zone B). Fabricated devices were rather based on a long and shallow well (between 200 and 300 μm) because their radiative losses would be lower leading to overall better performances.

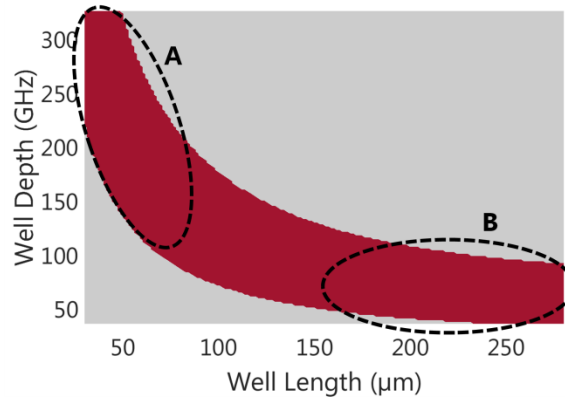


Fig.2.6. Summary of grating parameter leading to HQ DFB high performances

After numerically studying the HQ DFB, we present in the next part, characterizations of fabricated devices. In this following part, the measurement results will be discussed and compared with the simulations.

III. HQ DFBs characterizations

In this section we present characterization results of previously fabricated HQ DFBs within the III-V on Silicon platform from CEA Leti. The characterizations focus on fifteen different designs, conceived by A. de Rossi. All designs share the same well depth, but have varying well and total length. The grating parameters are shown in Table 3, and each design is named for notation simplification in the following part. In addition to previous works [38], [39], we here thoroughly investigate the relation between grating parameters and measurement results which allow us to conclude on grating designs leading to best DFB performances. The measurement results are also used to extract fabricated grating parameters and confirm the accuracy of the numerical model developed in section II. All measurements have been made with DFBs placed above a Peltier cell to control their temperature at 25°C, while the light is extracted from the chip using a Silicon based vertical grating coupler (VGC).

| $L_{tot}(\mu m)$ $L_w(\mu m)$ | 500 | 600 | 700 | 800 | 900 |
|----------------------------------|-----|-----|-----|-----|-----|
| 200 | A1 | B1 | C1 | D1 | E1 |
| 250 | A2 | B2 | C2 | D2 | E2 |
| 300 | A3 | B3 | C3 | D3 | E3 |

Table 3. Fabricated design parameters and name

We first report on measurement results of the different DFBs spectra and it is notably shown how fabricated devices parameters can be estimated with the analysis of sub-threshold DFBs spectra. Then the measured threshold current and efficiency of the HQ DFBs are presented. Finally we report on photon lifetime and linewidth measurements of the HQ lasers.

III.1. Measured spectra

In this part we first investigate sub-threshold DFB emission spectra measurements allowing us to extract grating parameters. Then DFB spectra above threshold are presented showing ideal single mode operation. In this section we use the following notations to refer at different DFB modes optical frequencies : $\vartheta(0)$ is the optical frequency of the lasing mode, $\{\vartheta(i)\}$ are the optical frequencies of the i th mode with higher frequency than $\vartheta(0)$ and $\{\vartheta(-i)\}$ are the optical frequencies of the i th mode with lower frequency than $\vartheta(0)$.

III.1.a. DFB spectrum at threshold

Using the III-V on Silicon integration platform, some geometrical dimensions are not precisely controlled in the fabrication process, leading to unknown devices index profiles and unknown grating parameters. Indeed both bonding oxide thickness and III-V waveguide width are not precisely define in the fabrication process. The oxide thickness is obtained after a chemical mechanical polishing which cannot give a precise value of remaining material ($80 \pm 70 \text{ nm}$) while the III-V waveguide is etched using a wet method, and because misorientation of the III-V wafer during bonding, the angles at the base of the III-V waveguide are not known. Hence, using sub-threshold spectral measurements, we first extract the silicon grating parameters such as the photonic well depth and grating strength in the mirror region.

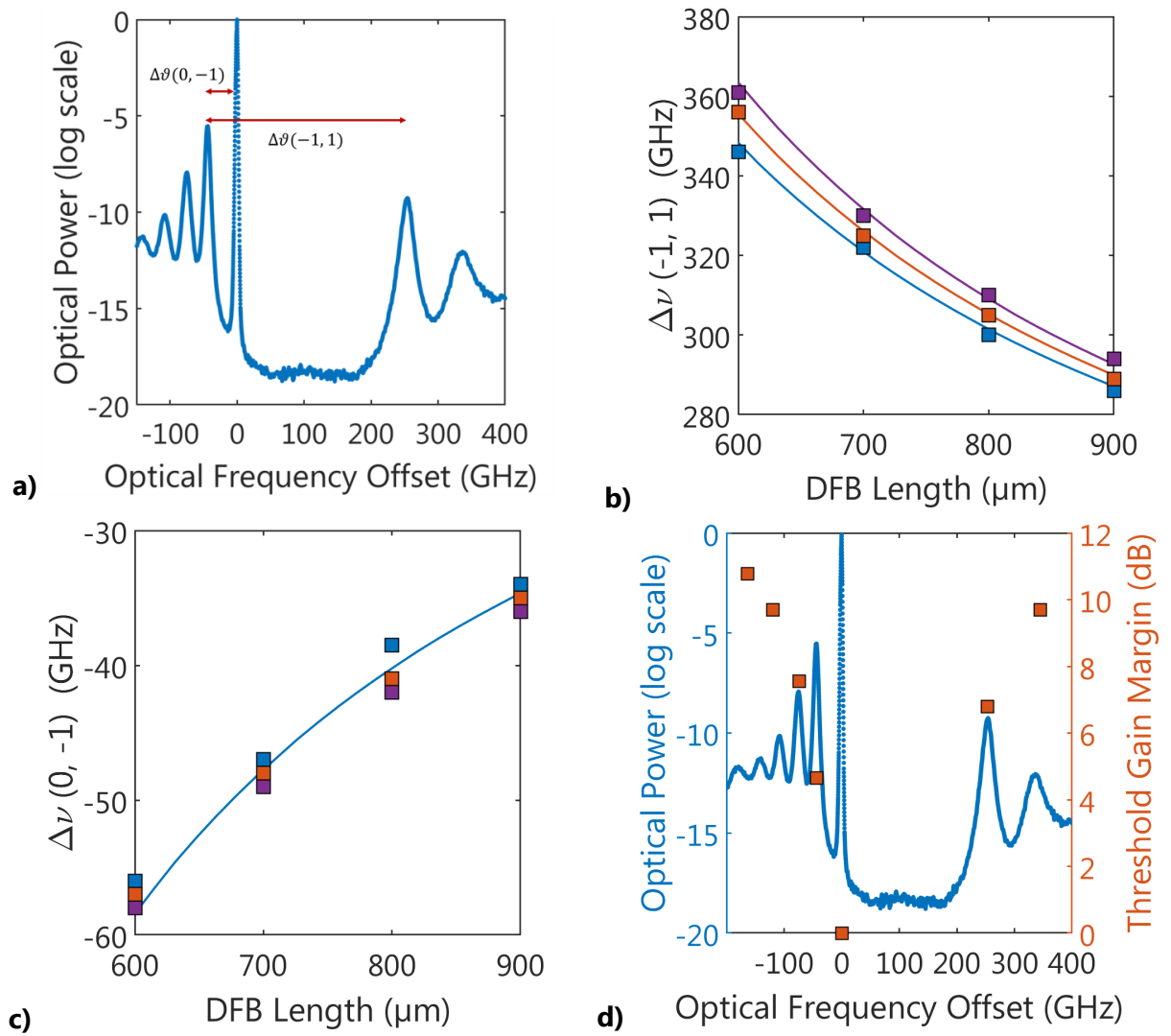


Fig.3.1 a) Measured optical spectrum of DFB D2 at threshold. b) & c) Measured (squares) and simulated (line) of $\Delta\nu(-1,1)$ & $\Delta\nu(0, -1)$ for 200 μm , 250 μm and 300 μm well depth (resp. in blue orange purple). d) Superposition of DFB D2 threshold spectrum and simulated poles.

Fig.3.1.a) shows the sub-threshold spectrum of design E2, with the optical frequency offset defined with respect to the lasing mode. As we can see, the lasing mode is on the red side of a stop-band as expected using the photonic band structure viewpoint. Using the frequency difference between possible DFB modes $\Delta\vartheta(-1, 1)$ and $\Delta\vartheta(0, -1)$ as defined in Fig.3.1.a) we can obtain grating parameters by fitting measurements with simulated results. The measured values of $\Delta\vartheta(-1, 1)$ and $\Delta\vartheta(0, -1)$ has been reported for DFB designs B1 to E3 in both Fig. 3.1.b) and 3.1.c), because DFBs A1, A2 and A3 were not lasing on the targeted HQ mode they are not included in the study. Then $\Delta\vartheta(i, j)$ was simulated for different grating parameters. These simulations have shown that $\Delta\vartheta(0, -1)$ barely depend on the photonic well length, which goes against the quick intuition saying that longer photonic well should give a lasing mode deeper inside the well, increasing the absolute value of $\Delta\vartheta(0, -1)$. Actually simulation also shown that the DFB mode $\vartheta(-1)$ is blue shifted for longer well, explaining that $\Delta\vartheta(0, -1)$ hardly changes for longer well. We finally found the grating parameters minimizing the mean square errors between measured and simulated $\Delta\vartheta(i, j)$ as a function of the total DFB length and found a photonic well deep of 41 GHz, and a grating strength in the mirror region of 59 cm^{-1} . These values should be rather taken as order of magnitude than absolute values. Fig.3.1.d) conclusively show the measured sub-threshold spectrum and simulated gain threshold margin for design E2, showing good agreement between computed DFB modes frequency and their measured values. Only a slight discrepancy can be observed further from the lasing mode, related to the waveguide dispersion which is not accurately known. Fig.3.1.d) also shows correct agreement between simulated threshold gain margin and measured amplitudes of the DFB modes validating our numerical model.

III.1.b. DFB spectra above threshold

We now report on laser spectra above threshold to show the single mode operations of the fabricated DFBs. Fig.3.2.a) shows the optical spectra of DFB D2 at a bias current of three times its threshold current and measured with a 0.03 nm resolution optical spectrum analyzer. As we can see, the side mode suppression ration (SMSR) is greater than 55 dB, which exceed the targeted value of 50 dB. As we can see in Fig.3.2.a), the DFB modes close to 1550 nm are not the ones setting the SMSR value but it is rather a group of modes around 1540 nm. This group of modes corresponds to another transverse mode being the odd (or anti-symmetric) mode of the coupled III-V on Silicon waveguide structure. We can also see a harmonic close to 1546 nm, which cannot be explained so far. This harmonic is not present in other spectral characterizations, and was considered of limited importance. Fig.3.2.b) shows a zoom on the lasing mode. As predicted with our numerical model in Fig.3.1.d) the second DFB mode limiting the SMSR on this frequency range correspond to $\vartheta(-1)$. Finally, DFBs SMSR measured at three times their threshold current are plotted in Fig.3.2.c). For designs B1

to E3, the SMSR exceed 50 dB in all case showing the stable single mode operations of each DFB.

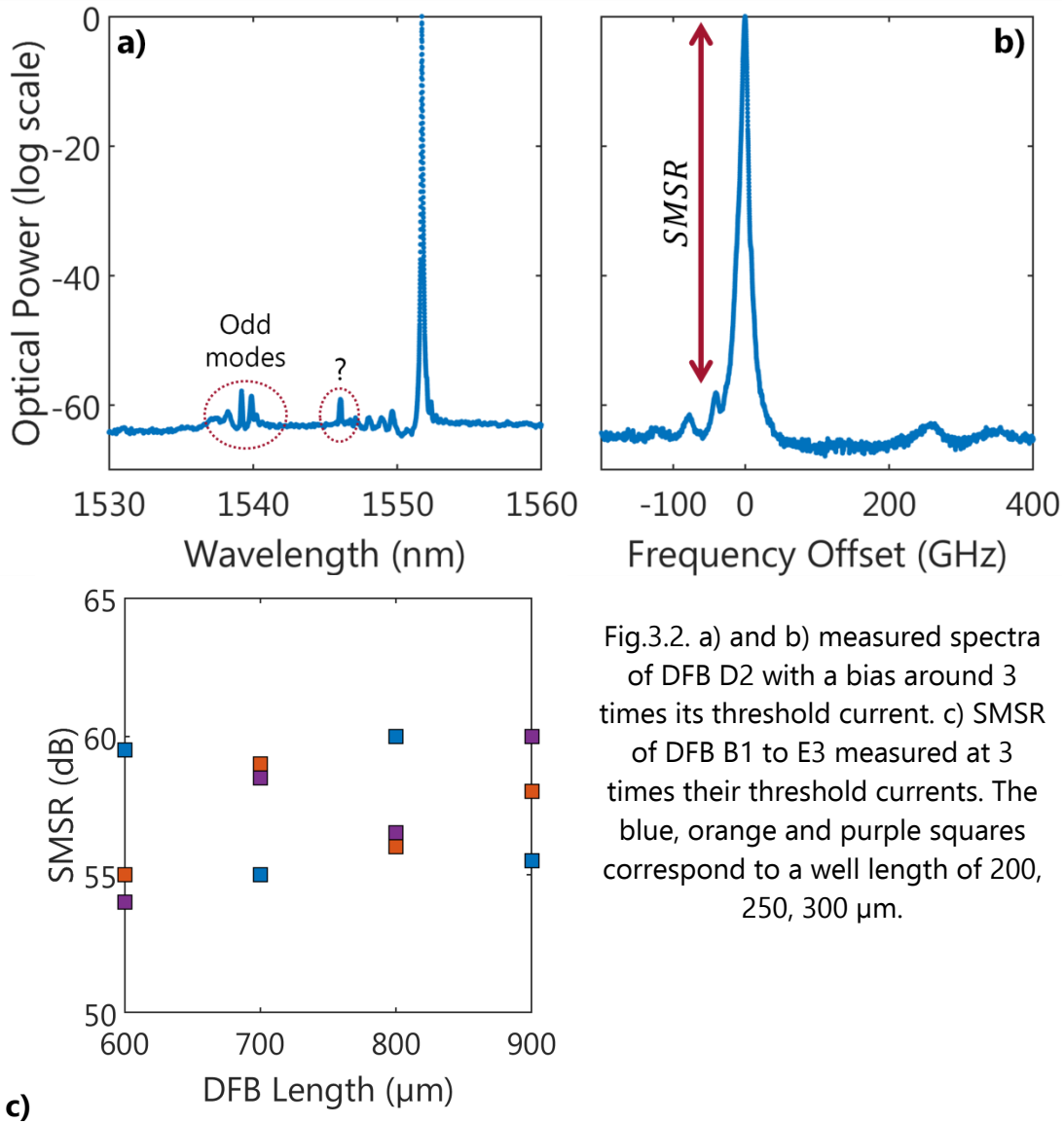


Fig.3.2. a) and b) measured spectra of DFB D2 with a bias around 3 times its threshold current. c) SMSR of DFB B1 to E3 measured at 3 times their threshold currents. The blue, orange and purple squares correspond to a well length of 200, 250, 300 μm.

III.2. HQ DFB Light-Intensity characteristics

In this section, the relation between DFB grating parameters and the light intensity (LI) characteristics is investigated. We first show that a relatively low threshold current can be obtained using specific grating parameters. Then we report on the slope efficiency of the different fabricated HQ DFBs, here simulation results are compared to measured values to study design parameters leading to optimal DFB efficiency. Finally we summarize the maximum achievable output power for each laser design to find which DFB would lead to optimal performances if integrated in a coherent transceiver.

III.2.a. HQ DFB threshold

Because digital coherent modules need to operate with low power consumption in datacenter interconnect, their lasers need to be biased at relatively low current. Hence, laser with low threshold current are required to optimize their power at a given bias. In this context, effect of grating parameters on DFB threshold current is examined. Fig.3.3.a) shows the LI curve of 700 long μm HQ DFBs in the vicinity of their thresholds. The threshold currents of these 700 μm HQ DFBs are measured and their value lies between 48 and 55 mA, which are relatively higher than the threshold current of traditional phase shifted DFB using the same technology (~ 40 mA) [39]. However, as expected using numerical simulations in II.2.a.i, it is now experimentally shown that longer photonic wells lead to lower threshold currents. Fig.3.3.b) shows the simulated modal threshold gain for 700 and 900 μm long HQ DFB with grating parameters extracted in III.1.a and measured threshold currents of three fabricated chips per DFB design.

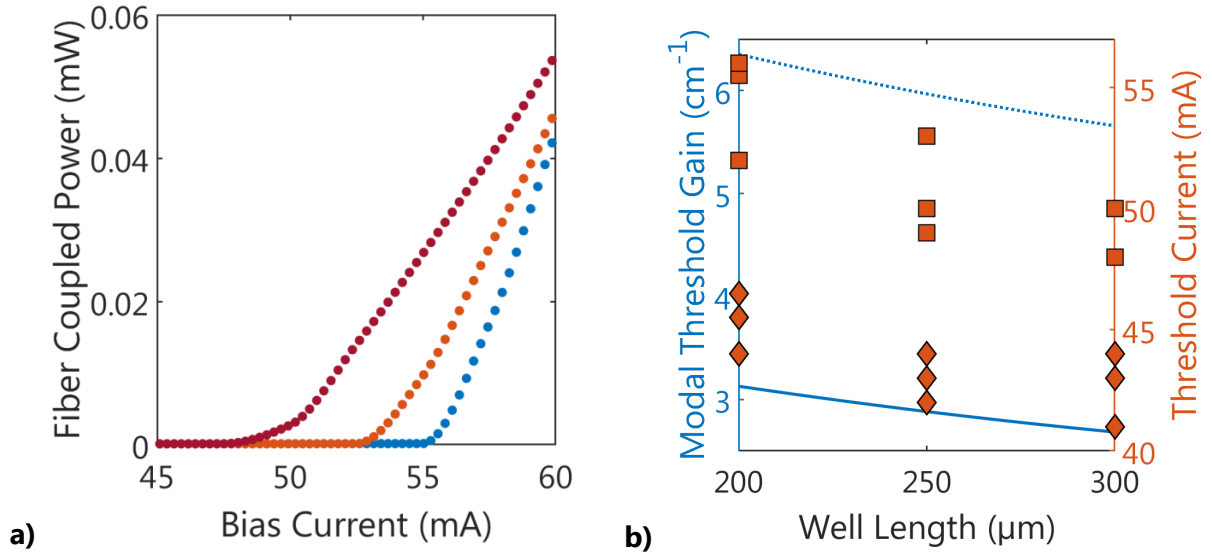


Fig.3.3 a) LI measurements of designs C1 (blue), C2 (orange), C3 (red). b) Blue lines correspond to simulated modal threshold gain ($\Gamma_{MQW} g_{th}$). The dotted (resp. plain) line is obtained for 700 (resp. 900) μm long DFBs. Orange points correspond to measured threshold currents from different devices. The squares (resp. diamonds) correspond to 700 (resp. 900) μm long DFBs.

It can be first noticed that simulation and experiment results follow the same trend, i.e. longer photonic wells would give lower threshold currents. It can be also noticed that 900 μm long HQ DFBs have a lower threshold current comparing to 700 μm long DFB. Actually, 900 μm long HQ DFB designs have threshold in the same range of 900 μm long phase-shifted DFB laser in the same technology (>40 mA) [39]. The threshold current reduction obtained with longer DFBs, is related to external loss reduction (due to longer mirrors) which compensates

for reduced carrier density at a given bias (due a larger active volume). Because the relation between injected carriers density and gain value is neither linear nor precisely known, no other conclusion can be drawn from these measurements. We can simply assume that even longer well ($> 300 \mu\text{m}$) would lead to even lower threshold currents.

III.2.b. HQ DFB Efficiency

In this part we report on the measured laser slope efficiency of several HQ DFB designs. The measured values are compared with simulation results made using the extracted grating parameters in III.1.a. Fig.3.4.a) shows the LI characteristics of $900 \mu\text{m}$ long HQ DFB with photonic well length of 200, 250 and $300 \mu\text{m}$. First, it can be noticed that the LI characteristics of these DFBs does not follow a linear evolution above threshold, but rather have a hyperbolic comportment. This comportment is only observed in the case of longer HQ DFBs (800 and $900 \mu\text{m}$ long) and the author has no clues to explain this phenomenon. He can only say that it is not related to :

- Thermal effects : detuning between gain peak and lasing frequency evolves as a function of bias current, which could lead to improved efficiency at higher bias. In our case, the lasing mode is already at the gain peak frequency at threshold current bias.
- Feedback from the vertical grating coupler : could improve laser efficiency at a particular wavelength and a locking phenomenon could explain the hyperbolic tendency. However, the higher the Q factor of a DFB, the less sensitive it is to feedback [40]. So this phenomenon should be also observed in shorter DFB
- Non linear silicon loss absorption : could only reduce efficiency at higher output power.
- High spontaneous emission rate : high spontaneous emission rate could lead to similar comportment. However, plotting the LI characteristic in log scale shows that the spontaneous emission rate is reduced by a factor >100 as compared to a traditional phase-shifted DFB, which does not have this hyperbolic LI curve.

Therefore, the slope efficiency was evaluated only taking into account the linear part of the LI curve. Measured slope efficiency are reported in 3.4.b) for $800 \mu\text{m}$ and $900 \mu\text{m}$ long DFB. It can be seen that longer photonic wells tend to reduce the laser slope efficiency, as it is predicted using simulations. However, the measured slope efficiency varies of 40% for $900 \mu\text{m}$ long HQ DFBs with photonic well length varying between $200 \mu\text{m}$ and $300 \mu\text{m}$. And the simulated external efficiency only varies of 14 % for the same design variations. This disagreement between simulations and measurements may be due to neglected spatial hole burning and non linear silicon absorption in the numerical model.

Hence, in one hand DFB designs with longer photonic wells tend to have reduced threshold gain, but in the other hand they also have lower slope efficiency. In the following part we conclude on photonic well parameter leading to maximum achievable output power.

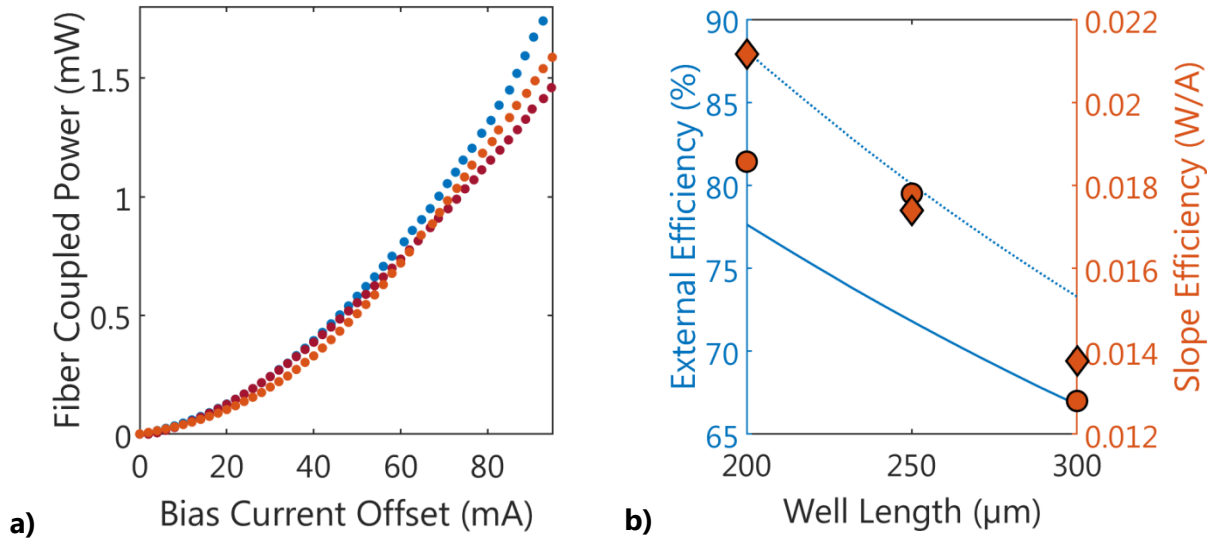


Fig.3.4. a) LI measurements of designs E1 (blue), E2 (orange), E3 (red), the bias current is offset from threshold current to simplify visualization. b) Blue lines correspond to simulated external efficiency η_e for 800 (dotted line) and 900 μm (plain line) long DFBs. Orange points correspond to measured slope efficiency, circles (resp. diamonds) are for 800 (resp. 900) μm long DFBs.

III.2.c. Single mode maximum output power

To conclude on which DFB design should be integrated in IQ transceivers, we measured the maximum fiber coupled power obtained before mode-hopping for different DFB designs. Fig.3.5.a) shows the LI curve of a 900 μm long DFB with a well length of 200 μm. For current bias over 170 mA, mode hopping occurs. This mode hopping is due to the fact that the gain peak wavelength thermal drift is 0.6nm /°C, whereas the DFB wavelength drift is 0.1nm /°C. Hence, for a given bias current a large detuning occurs between the HQ mode and the gain peak wavelength, and a parasitic cavity formed by the VGCs starts lasing. Fig.3.5.b) reports the maximum fiber coupled power P_{max} for designs B1 to E3. For each design six DFBs were tested, the value marked by a square correspond to the average value of P_{max} while the line correspond to its standard deviation. First, we can notice that the standard deviation is relatively high for all designs, this is due both to the fact that only six chips could be tested per design and some fabrication process steps are not precisely controlled from one wafer to another one. However, the tendency shows a 3dB evolution of maximum emitted power before mode hopping between that 600μm and 900μm long DFBs. However, no relation between grating parameters and DFB power can be noticed.

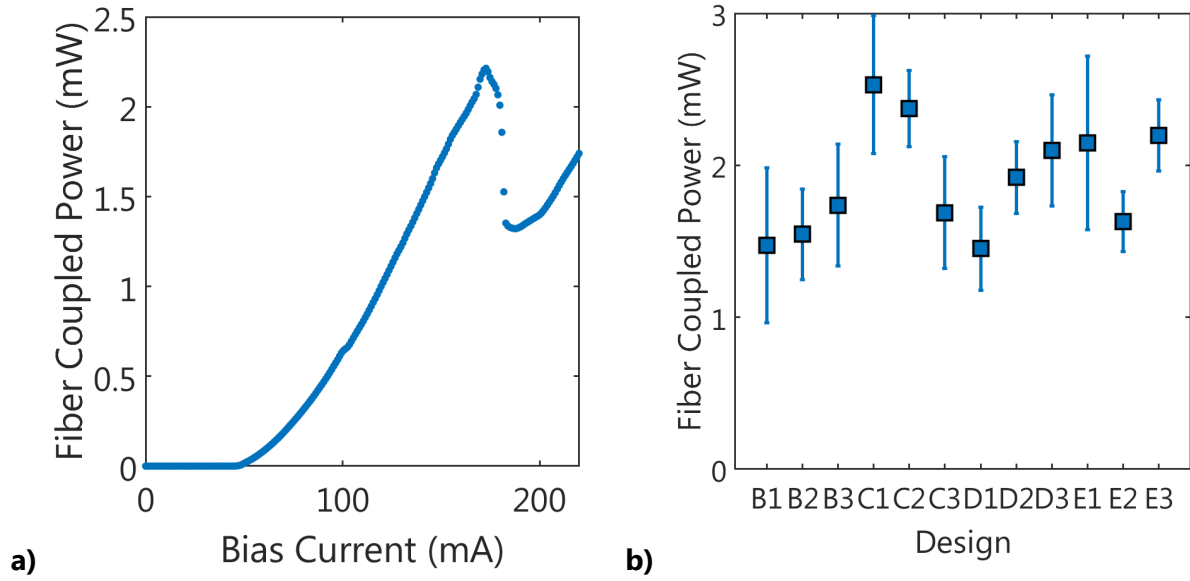


Fig.3.5. a) LI measurement of design E1. b) Measured fiber coupled power before mode hopping for 8 devices. The square is the average value and the line is the standard deviation.

III.3. HQ DFB noise characteristics

At last, the noise characteristics of the HQ DFBs are presented. First, the relation between grating designs and photon lifetime is investigated. Then, measurements of DFBs Schawlow-Towns and Henry (STH) linewidth are presented.

III.3.a. HQ DFB Photon Lifetime

Lasers photon lifetime can be precisely extracted using their small-signal electro-optic response. It is well known that lasers S21 parameter, defined in 2.III.1 with δI being the small signal modulation current applied on the laser diode and δP its output power modulation response, follows a second order transfer function that can be written:

$$H(\omega) \equiv \frac{\delta P}{\delta I}(\omega) = \frac{\omega_R^2}{\omega_R^2 - \omega^2 + j\omega\gamma} \quad (2.III.1)$$

With ω_R the relaxation oscillation pulsation and γ the damping factor. Following [41], it can be shown that γ is related to the laser photon lifetime τ_p as :

$$\gamma = \tau_p \omega_R^2 + \gamma_0$$

With γ_0 mostly depending on the differential carrier lifetime. Because γ_0 is assumed to be constant and ω_R^2 linearly increases as a function of the laser bias current, τ_p can be obtained by measuring $H(\omega)$ at different laser bias. Fig.3.6.a) shows the small signal modulation response of design B3 at different bias current. The plotted S21 are obtained after de-embedding electrical parasitic response and transport effects [42] following [43]. It can first be noticed that the relaxation oscillation frequency is <2GHz for bias current up to three times the threshold current. This relatively low value of relaxation oscillation frequency results from both the low differential gain of the structure (owing to a low quantum well confinement) and the long photon lifetime.

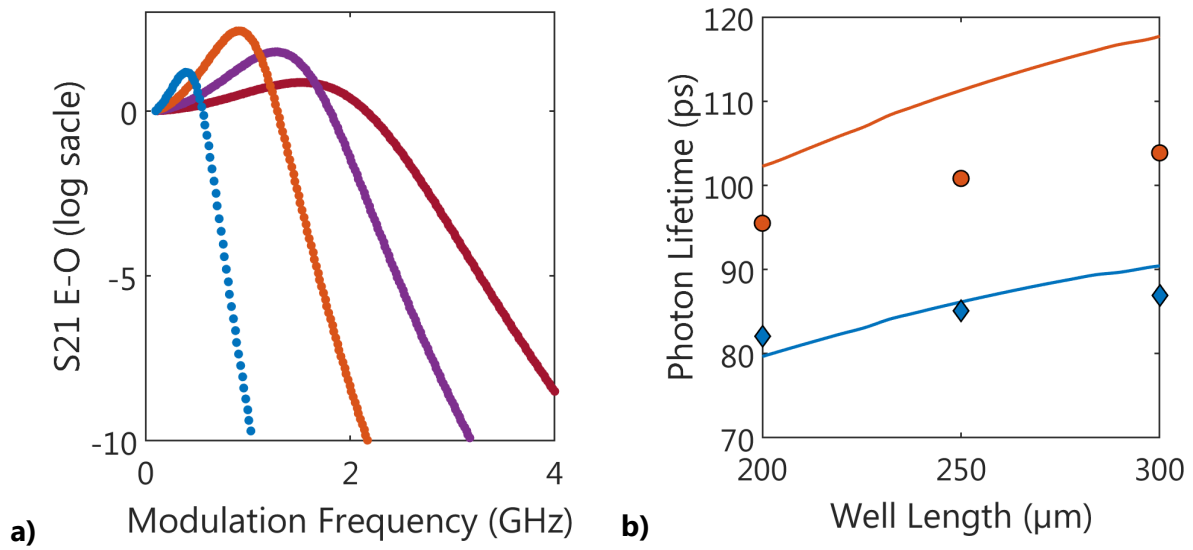


Fig.3.6. a) S21 electro-optic response of design B3 at different bias. Blue orange purple and red respectively correspond to bias current of 58, 70, 95, 150 mA. b) Measured (dots) and simulated (lines) photon lifetime of HQ DFBs. Orange (resp. blue) corresponds to a DFB length of 600 μm (resp. 800 μm).

Fig.3.6.a) also shows that both the damping factor and oscillation relaxation frequency are increasing functions of the bias current. Then plotting the function $\omega_R \rightarrow \gamma(\omega_R)$ allows us to extract the DFB photon lifetime (86 ps in this case). Fig.3.6.b) shows the deduced photon lifetime as a function of the photonic well length for 800 μm and 600 μm long DFBs. As expected from simulations, measurements show that longer photonic wells tend to increase the photon lifetime. Using the design parameters extracted in III.1.a), numerical model seems to overestimate the beneficial effect of having a longer well to increase the photon lifetime. It can also be noticed that the simulated photon lifetime is slightly higher than the measured one in the case of 800 μm long cavity. It is not known if the discrepancy between measurements and simulation come from neglected longitudinal effect in simulation or because of the reliability of the extracted photon lifetime using the small signal analysis. However, the simulated photon lifetime is in a 15% error margin from measurements, which undoubtedly confirm the validity of the numerical modeling. The good agreement between

measurements and simulation also shows that the value of the photon lifetime in this HQ DFB designs is limited by external laser losses rather than non-linear silicon and radiative losses.

III.3.b. HQ DFBs Linewidth characteristics

We conclude the HQ DFBs characterizations by presenting their linewidth characteristics. The measurements were made using a self-heterodyne testbed which optical signal is analyzed through a real-time scope to retrieve frequency noise power spectral density. We define the linewidth as the white noise floor measured around 50 MHz – 80 MHz, hence it correspond to a Schawlow-Townes and Henry (STH) Linewidth as the relaxation oscillation is in the 1 GHz range (Fig.3.6.a)). Only HQ DFBs with a photonic well long of 250 μm could have been characterized and the results are shown in Fig.3.7 plotting the measured linewidth as a function of bias current offset from threshold. As we can see, the three designs (corresponding to DFBs long of 600, 800 and 900 μm) have their linewidth below 50 kHz at high bias current. This confirms the low phase noise operation of these lasers.

Moreover, the $1/\Delta I_{Th}$ dependence of the linewidth show that longer DFBs have a longer photon lifetime. Simulated STH linewidth with photon lifetime of 80, 100, 120 ps are also plotted (these values correspond to the one obtain with the modulation characteristics form Fig 3.6.). This shows that with a phase/amplitude coupling factor of 2.8, and injection efficiency of 20% and an inversion population factor of 2.8, the theoretical STH formula gives good approximation of the measurements.

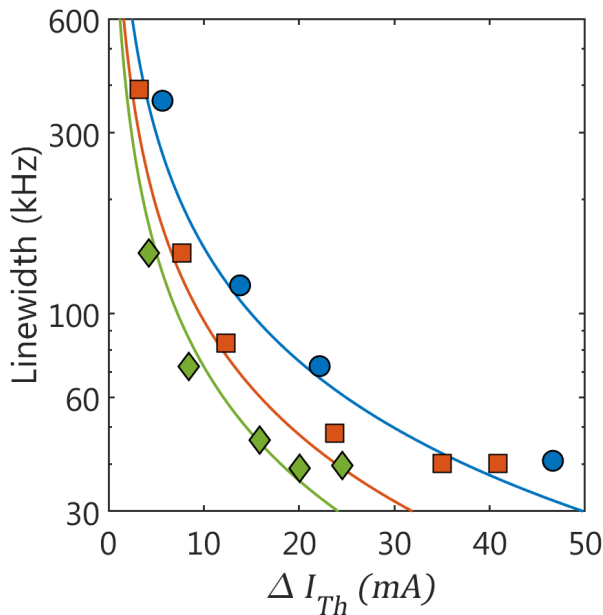


Fig.3.7. Linewidth characteristics of HQ DFBs.

Blue dot, orange square and green diamond correspond to DFB of length 600, 800, 900 μm .

Blue, orange and green line correspond to simulated linewidth with a photon lifetime of 80, 100, 120 ps.

IV. Conclusion

In this chapter we have seen how much benefits can be taken from the III-V on Silicon platform to fabricate very narrow linewidth DFBs. The grating design was based on previous works from Caltech, but for the first time of our knowledge we study the impact of grating parameters on the laser performances. To achieve this goal, a numerical model based on the transfer matrix method was developed, and the challenging issue of precisely obtaining the poles of the resonant condition was overcome. The simulation model does not take into account neither longitudinal and travelling effects nor radiative losses. Hence, the model does not require heavy computational resource but it –for instance- cannot precisely give laser characteristics on a frequency band higher than the cavity roundtrip frequency. This model cannot also be used to study the intrinsic limit of these lasers. Future works could integrate the more complex longitudinal effects. However, this simple yet efficient model, shown that –as the intuition suggest- deeper photonic well may reduce laser extraction losses, hence narrowing its linewidth at the cost of a lower extraction efficiency. It also shows that for long and deep well, a second HQ mode may exist in the well yielding to multimode operation.

Then, measurements on previously designed and fabricated lasers showed that this DFB architecture leads to single mode operation of III-V on Silicon lasers with an output power in the 3 dBm range and with a linewidth < 50 kHz. It is obvious that future work should focus on increasing the DFB output power, for instance an asymmetrical grating design, optimized epitaxy, and a better alignment between III-V and Silicon waveguides, should lead to higher DFB output power. Measured laser characteristics for different photonic well length were also in agreement with numerical results, confirming that longer well tend to be beneficial for HQ DFBs noise properties. The author thinks that using both a deeper photonic well and a stronger grating strength in the mirror region would be even better for the overall laser performances, as the fabricated DFB performances seemed to be limited by a too high value of extraction losses.

V. References

- [1] C. T. Santis, S. T. Steger, Y. Vilenchik, A. Vasilyev, and A. Yariv, "High-coherence semiconductor lasers based on integral high-Q resonators in hybrid Si/III-V platforms," *Proc. Natl. Acad. Sci. U. S. A.*, vol. 111, no. 8, pp. 2879–2884, 2014.
- [2] S. Ogita, Y. Kotaki, K. Kihara, M. Matsuda, H. Ishikawa, and H. Imai, "Dependence of Spectral Linewidth on Cavity Length and Coupling Coefficient in DFB Laser," *Electron. Lett.*, vol. 24, no. 10, pp. 613–614, 1988.
- [3] S. Takano, T. Sasaki, H. Yamada, M. Kitamura, and I. Mito, "Sub-MHz Spectral Linewidth in 1.5 μm Separate-Confinement-Heterostructure (SCH) Quantum-Well DFB LDs," *Electron. Lett.*, vol. 25, no. 5, pp. 356–357, 1989.
- [4] H. Bissessur *et al.*, "VERY NARROW-LINEWIDTH (70kHz) 1p55 μm STRAINED MQW DFB LASERS," no. August 1973, pp. 998–999, 1991.
- [5] G. W. Yoffe, S. Y. Zou, S. A. Rishton, R. W. Olson, M. A. Emanuel, and B. Pezeshki, "Widely-tunable 30mW laser source with sub-500kHz linewidth using DFB array," *Conf. Proc. - Lasers Electro-Optics Soc. Annu. Meet.*, pp. 892–893, 2008.
- [6] M. Faugeron *et al.*, "High-power tunable dilute mode DFB laser with low RIN and narrow linewidth," *IEEE Photonics Technol. Lett.*, vol. 25, no. 1, pp. 7–10, 2013.
- [7] G. H. Duan, P. Gallion, and G. Debarge, "Analysis of the Phase-Amplitude Coupling Factor and Spectral Linewidth of Distributed Feedback and Composite-Cavity Semiconductor Lasers," *IEEE J. Quantum Electron.*, vol. 26, no. 1, pp. 32–44, 1990.
- [8] H. Yasaka, M. FUKUDA, and T. Ikegami, "CURRENT TAILORING FOR LOWERING LINEWIDTH FLOOR," vol. 147, no. 100, p. 52, 1984.
- [9] X. Pan, H. Olesen, and B. Tromborg, "INFLUENCE OF NONLINEAR GAIN ON DFB LASER LINEWIDTH," *Electron. Lett.*, vol. 26, no. 14, pp. 5–7, 1990.
- [10] U. Krüger and K. Petermann, "The Semiconductor Laser Linewidth Due to the Presence of Side Modes," *IEEE J. Quantum Electron.*, vol. 24, no. 12, pp. 2355–2358, 1988.
- [11] H. Yamazaki, M. Yamaguchi, and M. Kitamura, "Spectral Linewidth Rebroadening in MQW-DFB LDs Caused by Spontaneous Emission Noise in SCH/Barrier Layers," *IEEE Photonics Technol. Lett.*, vol. 6, no. 3, pp. 341–343, 1994.
- [12] Y. KONDO, K. SATO, M. NAKAO, M. FUKUDA, and K. OE, "EXTREMELY NARROW LINEWIDTH (~ 1 MHz) AND HIGH-POWER DFB LASERS GROWN BY MOVPE," *Electron. Lett.*, no. 3, pp. 175–177, 1989.
- [13] F. Kano, M. Fukuda, and J. Yoshida, "Correlation of Noise Characteristics and Line Shape with Linewidth Rebroadening of MQW DFB Lasers," *IEEE Photonics Technol. Lett.*, vol. 4, no. 1, pp. 13–15, 1992.

- [14] Y. Inaba, M. Kito, T. Takizawa, H. Nakayama, M. Ishino, and K. Itoh, "Reduced spectral linewidth in high output power DFB lasers," *Conf. Dig. - IEEE Int. Semicond. Laser Conf.*, pp. 85–86, 2000.
- [15] K. Takaki, T. Kise, K. Maruyama, N. Yamanaka, M. Funabashi, and A. Kasukawa, "Reduced linewidth re-broadening by suppressing longitudinal spatial hole burning in high-power 1.55- μm continuous-wave distributed-feedback (CW-DFB) laser diodes," *IEEE J. Quantum Electron.*, vol. 39, no. 9, pp. 1060–1065, 2003.
- [16] H. Ishii, K. Kasaya, and H. Oohashi, "Wavelength-tunable lasers for next-generation optical networks," *NTT Tech. Rev.*, vol. 9, no. 3, 2011.
- [17] T. Septon *et al.*, "Large linewidth reduction in semiconductor lasers based on atom-like gain material," *Optica*, vol. 6, no. 8, p. 1071, 2019.
- [18] M. Okai, T. Tsuchiya, K. Uomi, N. Chinone, and T. Harada, "Corrugation-Pitch Modulated MQW-DFB Lasers with Narrow Spectral Linewidth," *IEEE J. Quantum Electron.*, vol. 27, no. 6, pp. 1767–1772, 1991.
- [19] M. Okai, M. Suzuki, and T. Taniwatari, "Strained multiquantum-well corrugation-pitch-modulated distributed feedback laser with ultranarrow (3.6 kHz) spectral linewidth," *Electron. Lett.*, vol. 29, no. 19, pp. 1696–1697, 1993.
- [20] C. T. Santis, Y. Vilenchik, A. Yariv, N. Satyan, and G. Rakuljic, "Sub-kHz quantum linewidth semiconductor laser on silicon chip," *Conf. Lasers Electro-Optics Eur. - Tech. Dig.*, vol. 2015-Augus, pp. 1–2, 2015.
- [21] H. C. Casey and P. L. Carter, "Variation of intervalence band absorption with hole concentration in p-type InP," *Appl. Phys. Lett.*, vol. 44, no. 1, pp. 82–83, 1984.
- [22] O. K. Kim and W. A. Bonner, "Infrared reflectance and absorption of N-type InP," *J. Electron. Mater.*, vol. 12, no. 5, pp. 827–836, 1983.
- [23] K. J. Vahala, "Optical microcavities," *2005 Eur. Quantum Electron. Conf. EQEC '05*, vol. 2005, no. August, p. 352, 2005.
- [24] Q. Qiao, J. Xia, C. Lee, and G. Zhou, "Applications of photonic crystal nanobeam cavities for sensing," *Micromachines*, vol. 9, no. 11, pp. 1–31, 2018.
- [25] N. H. Sun, C. C. Chou, H. W. Chang, J. K. Butler, and G. A. Evans, "Radiation loss of grating-assisted directional couplers using the floquet-bloch theory," *J. Light. Technol.*, vol. 24, no. 6, pp. 2409–2414, 2006.
- [26] B. Tromborg, H. Olesen, X. Pan, and S. Saito, "Transmission line description of optical feedback and injection locking for fabry-perot and dfb lasers," *IEEE J. Quantum Electron.*, vol. 23, no. 11, pp. 1875–1889, 1987.
- [27] G. Björk and O. Nilsson, "A New Exact and Efficient Numerical Matrix Theory of Complicated Laser Structures: Properties of Asymmetric Phase-Shifted DFB Lasers," *J. Light. Technol.*, vol. 5, no. 1, pp. 140–146, 1987.

- [28] S. Keyvaninia *et al.*, "Heterogeneously integrated III-V/silicon distributed feedback lasers," *Opt. Lett.*, vol. 38, no. 24, p. 5434, 2013.
- [29] Y. Arakawa and A. Yariv, "Quantum Well Lasers—Gain, Spectra, Dynamics," *IEEE J. Quantum Electron.*, vol. 22, no. 9, pp. 1887–1899, 1986.
- [30] O. Qasaimeh, "Optical gain and saturation characteristics of quantum-dot semiconductor optical amplifiers," *IEEE J. Quantum Electron.*, vol. 39, no. 6, pp. 793–798, 2003.
- [31] C. H. Henry, R. A. Logan, and F. R. Merritt, "Measurement of gain and absorption spectra in AlGaAs buried heterostructure lasers," *J. Appl. Phys.*, vol. 51, no. 6, pp. 3042–3050, 1980.
- [32] G. Agrawal, "Mode-partition noise and intensity correlation in a two-mode semiconductor laser," vol. 37, no. 7, 1988.
- [33] H. Soda and H. Imai, "Analysis of the Spectrum Behavior Below the Threshold in DFB Lasers," *IEEE J. Quantum Electron.*, vol. 22, no. 5, pp. 637–641, 1986.
- [34] G. B. Morrison and D. T. Cassidy, "Probability-amplitude transfer matrix model for distributed-feedback laser structures," *IEEE J. Quantum Electron.*, vol. 36, no. 6, pp. 633–640, 2000.
- [35] J. P. Weber and S. Wang, "A New Method for the Calculation of the Emission Spectrum of DFB and DBR Lasers," *IEEE J. Quantum Electron.*, vol. 27, no. 10, pp. 2256–2266, 1991.
- [36] I. Orfanos, T. Sphicopoulos, A. Tsigopoulos, and C. Caroubalos, "A Tractable Above-Threshold Model for the Design of DFB and Phase-Shifted DFB Lasers," *IEEE J. Quantum Electron.*, vol. 27, no. 4, pp. 946–956, 1991.
- [37] A. Verdier, G. De Valicourt, R. Brenot, H. Debregeas, H. Carr, and Y. Chen, "Ultrawideband Wavelength-Tunable Hybrid External-Cavity Lasers," vol. 36, no. 1, pp. 37–43, 2018.
- [38] A. Gallet *et al.*, "Dynamic and Noise Properties of High-Q Hybrid Laser," *Conf. Dig. - IEEE Int. Semicond. Laser Conf.*, vol. 2018-Septe, pp. 45–46, 2018.
- [39] A. Gallet, "Hybrid III-V on silicon lasers for optical communications," *Manuscrit de these*. 2019.
- [40] S. Gomez *et al.*, "High coherence collapse of a hybrid III–V/Si semiconductor laser with a large quality factor," *J. Phys. Photonics*, vol. 2, no. 2, p. 025005, 2020.
- [41] L. Coldren, S. W. Corzine, and M. L. Masanovic, *Diode Lasers and Photonic Integrated Circuits*, 2nd ed. Wiley, 2012.
- [42] R. Nagarajan, M. Ishikawa, T. Fukushima, R. S. Geels, and J. E. Bowers, "High Speed Quantum-Well Lasers and Carrier Transport Effects," *IEEE J. Quantum Electron.*, vol. 28, no. 10, pp. 1990–2008, 1992.

- [43] P. A. Morton, T. Tanbun-Ek, R. A. Logan, A. M. Sergent, P. F. Sciortino, and D. L. Coblentz, "Frequency Response Subtraction for Simple Measurement of Intrinsic Laser Dynamic Properties," *IEEE Photonics Technol. Lett.*, vol. 4, no. 2, pp. 133–136, 1992.

Chapter 3

Fast Tunability of Narrow-Linewidth III-V/Si Extended Cavity Laser

| | |
|--|-----|
| Chapter 3 Fast Tunability of Narrow-Linewidth III-V/Si Extended Cavity Laser | 71 |
| I. Introduction | 73 |
| I.1. Fast Tunable Laser for CBOSS Network | 73 |
| I.2. Fast Tunable Laser State of the Art..... | 74 |
| I.3. Tunable Laser in the III-V on Silicon Technology..... | 76 |
| II. Laser Fast Wavelength Tuning | 80 |
| II.1. Fast tunable longitudinal mode filter | 80 |
| II.2. Laser Fast Tuning Performances | 85 |
| II.3. Conclusion..... | 91 |
| III. Linewidth Properties..... | 92 |
| III.1. Linewidth Properties of ECL..... | 92 |
| III.2. Linewidth Penalty due to carrier injection | 97 |
| IV. Coherent Optical Slot Switching..... | 100 |
| IV.1. State of the art..... | 100 |
| IV.2. Experimental Setup..... | 101 |
| IV.3. COSS results with fixed CMA | 103 |
| IV.4. COSS results with CMA convergence | 104 |
| V. Conclusion..... | 107 |
| VI. References | 108 |

In the last decade, datacenter switching fabric has coped with exponential growth of IP traffic following CMOS Moore's law. However, recent advances in disaggregated network require even larger optical bandwidth and lower latency. This makes it impossible for CMOS systems to keep up with the requirements. Optical switching and routing have the potential to overcome both issues as they enable a much higher throughput, much lower energy consumption and much lower link latency than electronic switched network. Hence, several research groups are proposing different architectures of optically switched network [1]–[4]. For instance the solution from Nokia [3] requires fast reconfigurable digital coherent modules, and fast wavelength tunable lasers would be key enablers. Not only datacenter networks require such components, but also cloud computing and 5G applications are pushing for burst mode communication within passive optical networks.

In this context we present and study a novel design of a fast C-band tunable laser suitable for burst-mode coherent communications. This fast tunable laser is designed and processed using the III-V on Silicon platform, making it ideal for compact integration with Silicon based I/Q transceivers. This laser was first presented in [5].

In this thesis chapter, the specifications required by the fast tunable laser are first investigated, and we present how the heterogeneous integration can be used to design such lasers. Then, the fast tunability characteristics of the extended cavity laser are precisely examined, and for the first time of our knowledge, laser stabilization after wavelength switching is assessed. After that, the linewidth properties of fast tunable laser are thoroughly studied. Finally, record coherent optical slot switching experiments results are discussed. These systems experiments were carried out with the networking team of Nokia Bell Labs.

I. Introduction

In this section, we first explain the benefit of using fast tunable lasers (FTL) within data center networks. In this part, the specifications required by FTLs will be assessed. Then, various proposed FTL designs will be reviewed with their advantages and drawbacks. Finally, we will describe the design of tunable lasers using the III-V on Silicon technology. Because III-V on Silicon tunable laser are already well known, only the design of the precise laser elements will be studied.

I.1. Fast Tunable Laser for CBOSS Network

As seen in the introductory chapter, traditional data center network consist of multiple switching elements aggregated in a tree pattern. The tree topology with modular electro-optical switch was a cost-effective solution to meet the increase of data traffic requirements, but this approach introduces a high network latency and excessive energy consumption [6]. State of the art datacenter switches rely on electro-optic conversions and electronic switches to route optical signals. Because they are both expected to hit a wall [7], a new network topology named the CBOSS (cloud burst optical-slot switching) consisting of optical switching only, was introduced by Nokia [3].

A schematic of the CBOSS architecture with three different servers is depicted in Fig. 1.1.a). It consists of optical nodes connected in a ring network by a dense wavelength division multiplexing (DWDM) channel. Each node receives optical signals on a fixed wavelength while it transmits data using different time slots also allocated in the DWDM grid. Fig. 1.1.b) sketches the node photonic integrated circuit. It first uses a wavelength dropper [3] to filter out one wavelength from the DWDM grid while letting other channels freely propagates through the node. The extracted DWDM channel is detected using a fixed wavelength receiver. Then, a fast tunable transmitter (FT-Tx) is used to transmit data on a succession of wavelength slots. As shown in [8], [9] data center traffic mostly consist of micro burst of <576 bytes, which would fit into 50 ns long optical slots at 100 Gbit/s. Hence, the FT-Tx needs to be reconfigured every 50 ns, and a very short reconfiguration time (<10 ns) would be a decisive parameter to improve the overall network efficiency and latency [4]. Moreover, due to a higher achievable data rate, lower receiver sensitivity and longer transmission reach coherent format would be preferred rather than IMDD format.

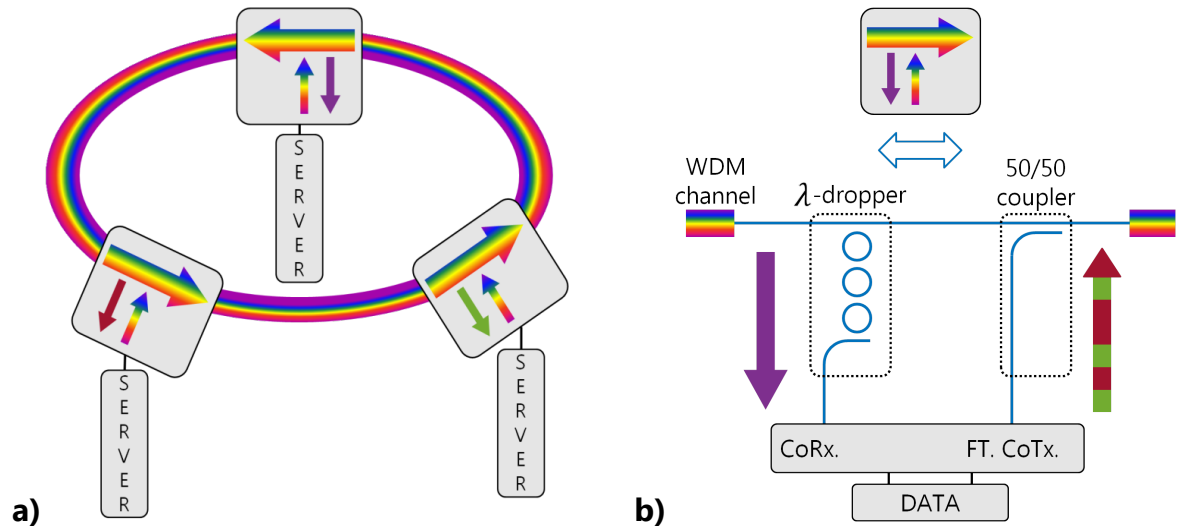


Fig. 1.1. a) CBOSS network architecture. b) Schematic of a network node.

In this context, a fast tunable laser with coherent compliant linewidth and capable of accessing a large number of channels on a DWDM optical grid is a key enabler. The laser should switch its wavelength emitted signal over a DWDM grid in a few nanoseconds, have a linewidth less than 500 kHz to support coherent formats up to 32 QAM and access as many channels as possible to increase the number of available nodes.

I.2. Fast Tunable Laser State of the Art

In order to provide fast tunable optical sources, several solutions were devised. A straightforward approach would be to use an array of single-mode lasers [10] in which each laser can be switched on and off to provide the desired wavelength. However, this solution presents several drawbacks. It first requires one laser per DWDM channel increasing the device footprint, cost and complexity. For instance, 44 lasers are needed to provide a 100 GHz spacing C-band switchable source. This approach is also very sensitive to thermal chirp, indeed after switching on a laser (nanosecond timescale), its temperature will slowly increase (10 μ s timescale) due to power dissipation in the gain region. Therefore the lasing mode will drift to higher wavelength for a few microseconds before thermal stabilization. In order to reduce the complexity of a laser array, several FTL designs were considered, and the performances of each FTL design are summarized in Table 1.1

Oldest reported FTLs were based on digital-sample distributed Bragg reflector (DS-DBR) lasers in the InP monolithic platform [11]. DS-DBR lasing wavelength is tuned using carrier injection inside both (back and front) DBR regions. Because carriers in III-V semiconductor have relatively low effective mass, it makes the electro-optical effect efficient [12] enough to

achieve 35 nm tuning. However, monolithic DS-DBR lasers tend to exhibit a wide optical linewidth, making them less suited for coherent transmission.

Nanosecond wavelength tuning using slotted Fabry-Pérot (SFP) lasers was reported in [13]. While this laser design shows improved linewidth properties compared to DS-DBR lasers, it can only access widely spaced longitudinal modes, thus making it impossible to be used in a DWDM frequency grid.

By taking advantage of III-V on Silicon integration, a switchable AWG laser design has been reported in [14]. However, this laser architecture requires one gain medium per attainable channel, making it impractical to provide numerous channels. Also, because this optical source relies on SOA gate switching to tune its wavelength, it is very sensitive to thermal chirp.

Then Ueda et al. [15] proposed a new laser architecture using both a tunable mirror and switching gain elements. This device showed both wavelength tuning over 35 nm bandwidth with a very energy-efficient mirror frequency response tuning. Nonetheless, as their device relies on multiple gain elements, the fast switching properties were not demonstrated on the entire laser working range, and their claim results need to be carefully used for comparison

Finally, de Valicourt et al. [16] used an optical gate to quickly switch between wavelengths emitted by two independent slowly tunable lasers. This approach showed a much narrower linewidth compared to other FTL designs and can provide a very stable lasing frequency in the long term owing to the absence of thermal chirp. However, this device inherently brings in latency to the network because each laser needs to be slowly adjusted at the desired wavelength before performing fast switching.

| Research Group | Lumentum [11] | Tyndall / DCU [13] | IMEC / Ghent Uni. [14] | NTT [14] | NBL III-V Lab [16] |
|------------------|-------------------|--------------------|------------------------|------------------------------|--------------------------------|
| Laser design | DS-DBR | Slotted FP | Switchable ECL | Switchable Tunable ECL | Switchable Tunable ECL |
| Tuning Mechanism | Carrier Injection | Carrier injection | Optical Gate (SOA) | QCSE | Optical Gate + Thermal |
| Tuning Range | C-band | 4 channels = 40 nm | 4 channels = 12nm | 35 nm ? | C-band |
| Tuning Speed | 5 ns | 1 ns | 1.5 ns | Filter : ~500 ps Gain : ? | 35ns switching 55µs latency |
| Tuning Power | < 12 mW | Not reported | > 25 mW | Filter : 10 mW Gain : ? | 220 mW : VOA 20 mW : filter |
| STH Linewidth | > 1 MHz | 600 kHz | ? | 350 kHz | Not in [16] (< 200 kHz) |

Table 1.1. Reported Widely FTL characteristics. Green means great performances with respect to other reported results, red means laser design drawbacks, and yellow refers to questionable claimed results.

I.3. Tunable Laser in the III-V on Silicon Technology

In this section, the design of C-band tunable laser using the III-V on Silicon technology is briefly recalled while the fast tunability is later investigated. Numerous works e.g. [17]–[19] have already reported on III-V on Silicon tunable lasers (TL), making them very common components. Indeed, they may be compact tunable narrow linewidth sources, which integration with complex Silicon based circuit would be ideal. As shown in Fig. 1.2. the laser is composed of a III-V Gain Medium adiabatically coupled to a silicon passive circuit. Two silicon based mirrors are used to form a Fabry-Pérot cavity, while a dual-ring filter is employed to select one longitudinal mode and allows for single mode lasing. In order to understand how fast tunability is achieved, we first discuss the tunable dual ring filter.

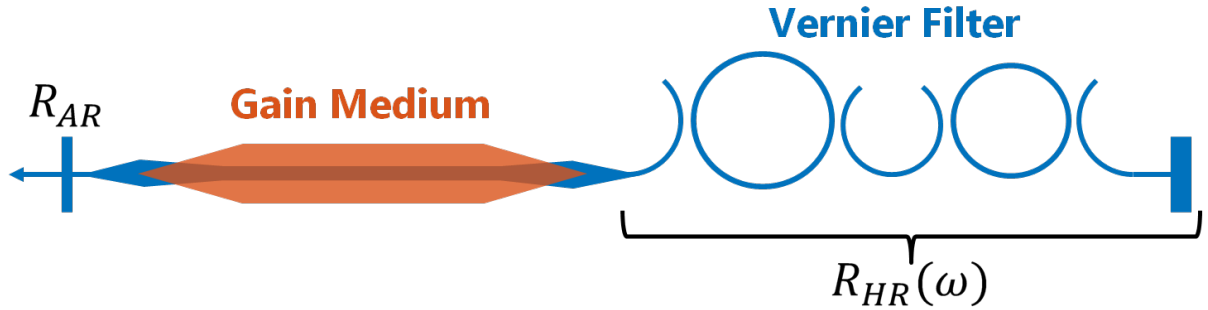


Fig. 1.2. III-V on Silicon widely tunable laser using Vernier filter

I.3.a. Vernier Filter

Filtering performances of dual ring Vernier mirror have been thoroughly studied in [20]–[22]. As sketched in Fig. 1.2, this consists of two serial ring resonators of slightly different sizes followed by a broadband mirror. Therefore, if we consider a 100% reflectivity mirror with a flat frequency response, the selective mirror response corresponding to $R_{HR} \stackrel{\text{def}}{=} |E_R/E_{in}|^2$ with E_{in} and E_R the field leaving and reflected back into the gain medium is given by the product of both ring transfer function. A standalone ring frequency response consists of a comb of Lorentzians with free spectral range (FSR) given by $c/(n_g L)$ where L is the perimeter of the ring. Because the two rings are designed with slightly different FSRs, their transmittance will be coincident only at a precise resonance at a wavelength called λ_0 . Therefore the dual ring mirror will select a Fabry-Pérot longitudinal mode in the vicinity of λ_0 .

Laser ideal single mode operation will occur if the Vernier filter induce a gain margin between the lasing mode and side ones by at least 3 dB (empirical). Due to Vernier effect this occurs under two conditions :

- First the selective mirror 3dB bandwidth is smaller than the ECL roundtrip frequency which takes into account propagation inside the gain medium and group delay of the dual ring mirror.
- The adjacent reflected bands of the selective mirror are also rejected by a factor exceeding 3dB.

Both conditions can be fulfilled using low loss silicon waveguides, low power coupling between the bus waveguide and the rings and relatively small rings. Indeed, low losses and coupling power is required to obtain a ring transmission consisting of a comb of narrow Lorentzian. While smaller rings induce a greater ring FSR difference for a same Vernier periodicity, helping to fulfill the second condition. Ring design characteristics achieving the maximum margin between lasing mode and side modes threshold gain are discussed in [22]–[24].

Then modifying the waveguide effective index of one ring waveguide by Δn will produce a frequency shift Δf of the transmitted comb given in eq. (3.I.1)

$$\Delta f = -\frac{c}{\lambda_0 n_g} \Delta n \quad (3.I.1)$$

Then, due to the Vernier effect, tuning the frequency response of a single ring resonator will allow to switch the mirror selected wavelength on a grid given by the second ring FSR.

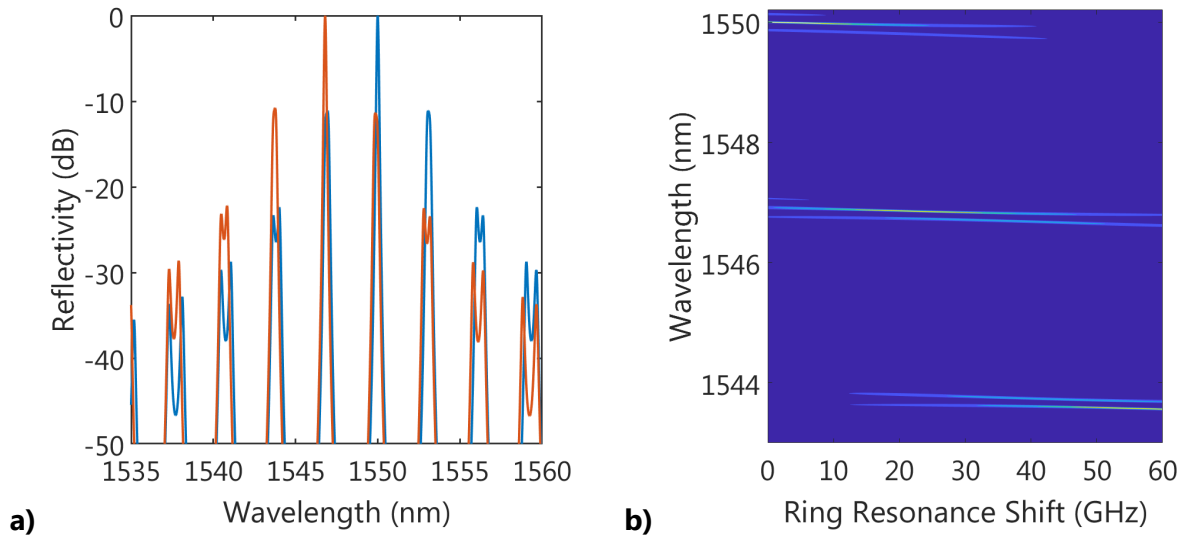


Fig. 1.3. a) Vernier Mirror reflectivity b) Mapping of the lasing mode wavelength for varying resonant frequency detuning.

Fig. 1.3.a) shows in blue the dual-ring mirror reflectivity using 200 μm and 187 μm ring resonators with 20% bus waveguide coupling. The blue curve is obtained when the index of each ring is chosen to center the mirror maximum reflectivity at 1550 nm. We can see that adjacent transmitted bands are rejected by over 13 dB, allowing ideal single mode lasing.

Then a single ring waveguide effective index is tuned to achieve a 25 GHz continuous ring response tuning following (3.1.1). In this case the Vernier mirror reflectivity is plotted in orange, and it selects a longitudinal mode close to 1547 nm. This illustrates possible laser wavelength switching obtained by continuous tuning of a single ring in a Vernier filter.

Lasing mode wavelengths of an ECL using the Vernier ring mirror are mapped in Fig. 1.3.b) for a single ring frequency tuning. In this curve the x-axis correspond to the continuous tuning of a single ring, the y-axis correspond to the laser wavelength, and the colormap corresponds to the value given by $10 \log_{10}|C(\lambda)|$, with $C(\lambda)$ the laser cavity transfer function defined in eq. (3.1.2). In this case the achievable lasing wavelengths correspond to the poles of $C(\lambda)$ and are represented in yellow. Note that because we are studying the laser emitted spectra on a wide frequency band (~ 800 GHz) and lasing mode are obtain for a precise wavelength value, the poles of C might be difficult to see on this mapping.

$$C(\lambda) = \frac{1}{1 - r_1 r_2(\lambda) e^{-j \frac{2\pi}{\lambda} n_{eff}(\lambda) 2L_{act}}} \quad (3.1.2)$$

First, we assume that ring resonances are superimposed at 1550 nm (let's say with no carriers injected within both ring resonators). Then, as shown in Fig. 1.3.b), continuously tuning a single ring resonance on a 60 GHz bandwidth allows lasing wavelength switching on three channels spaced by ~ 400 GHz shown by the yellow color. Because the color map in Fig. 1.3.b) does not depict side mode suppression ratio (SMSR) between ECL modes, the single mode operation of the laser is also not clearly represented. Nevertheless, color difference between the light blue and yellow color of two adjacent side mode corresponds to a gain margin over 15 dB ensuring ideal single mode operation. The phase noise properties and stability of the ECL mode will be studied in part III.

I.3.b. Sagnac Mirror

A simple way to provide wideband reflections inside the gain medium is to use a silicon based Sagnac mirror. A Sagnac loop mirror is sketched in Fig. 1.4.a), it consists of an evanescent coupler with both outputs connected. Contrary to Bragg Reflector the processing of this mirror does not require any additional precise lithography step. Moreover, a Sagnac mirror only brings very low excess losses whereas a multimode interference reflector [25] would be much more lossy. It can easily be shown that the Sagnac mirror reflectivity $R \equiv |E_R/E_0|^2$ is equal to $4t^2(1-t^2)$, with t being the evanescent coupler transmission coefficient. Hence, Sagnac mirror reflectivity can carefully be set by designing an evanescent coupler with the desired coupling coefficient. As we are studying widely tunable laser which should be covering an extended C-band, it is needed to study the Sagnac mirror wideband frequency response. Indeed, as t and k are wavelength dependent, Sagnac mirror reflectivity

may significantly vary on a wide optical band. Let's assume a front mirror of 20% reflectivity and a fully reflecting back mirror designed at 1550 nm. In this case, Fig. 1.4.b) shows the back and front mirror reflectivity spectra using a phase-matched evanescent coupler [26]. As we can see, the back reflectivity varies more than 20% over a 100 nm optical band while front mirror reflectivity varies more than 50%. By considering an 800 μm long gain medium with 5 cm^{-1} propagation losses, we also plot the corresponding modal threshold gain across a 100 nm band in Fig. 1.4.b). The increase of threshold gain at shorter wavelengths indicates that optical channels on the blue side of the spectrum may be harder to access. In order to tackle this problem, a Sagnac Mirror based on non phase-matched evanescent couplers may be used.

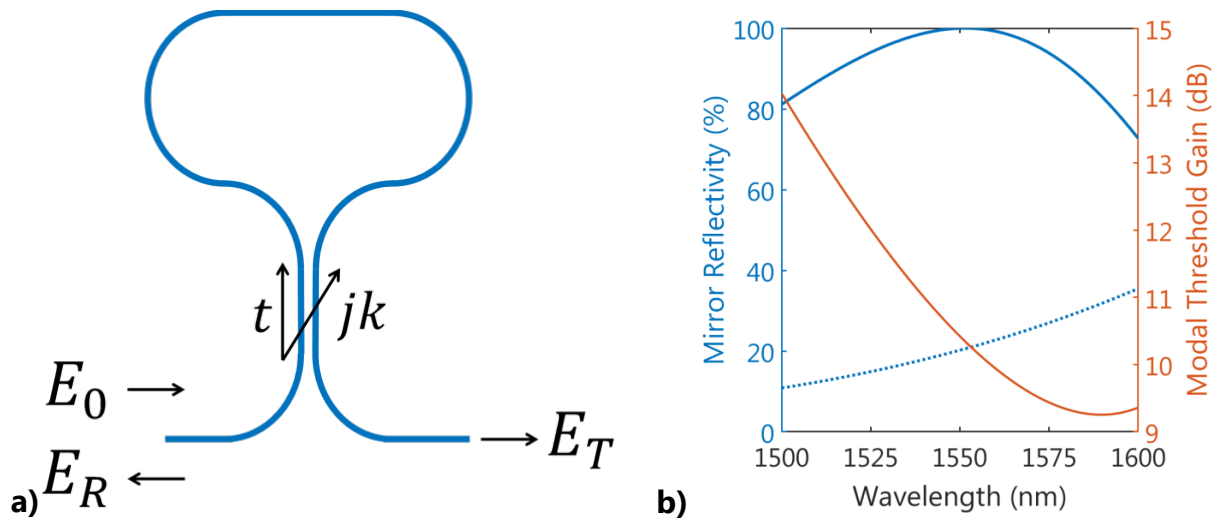


Fig. 1.4. a) Sagnac Loop Mirror. b) Simulated back and front mirrors reflectivity spectra (plain blue and dotted blue, modal threshold gain (orange).

II. Laser Fast Wavelength Tuning

In traditional integrated tunable lasers, the thermo-optic (TO) effect is used to tune the laser emitted wavelength. However, thermal tuning is only effective in the tens of μs timescale [27]. In this work carrier effects inside the silicon selective mirror are used to rapidly switch the laser frequency. First, the selective mirror design is presented and the tuning characteristics of standalone ring resonator using carrier injection are investigated. Then, for the first time to our knowledge laser fast tuning dynamics is thoroughly studied.

II.1. Fast tunable longitudinal mode filter

II.1.a. Tunable Vernier Filter using carrier effect

As shown in I.3.c, the ECL emitted frequency can be tuned by changing silicon ring waveguides effective index. It has been reported that a change of carrier density within bulk silicon is an efficient effect to alter its refractive index [28]. Indeed, injecting carriers increases Silicon losses due to free carrier absorption which contributes to a change of refractive index because of the Kramers-Kronig relations. Silicon free carriers density can be easily modified using several devices such as a PIN [29], PN [30], or capacitive junction [31].

| | PIN (Carrier injection) | PN (Carrier depletion) | Capacitive (Carrier accumulation) |
|---------------------------------|--|---|---|
| Bandwidth | <1 GHz [32] (long carrier lifetime) | >20 GHz [30] (RC response) | >10 GHz [33] (RC response) |
| Power consumption | High (current circulating in forward biased diode) | Low (reverse biased diode) | Low, (no DC current) |
| Index Change $\frac{dn}{dV}$ | $2\text{e}^{-3} \text{ V}^{-1}$ [30] (large mode overlap with intrinsic region) | $4\text{e}^{-5} \text{ V}^{-1}$ [29] (small depletion layer) | $4\text{e}^{-4} \text{ V}^{-1}$ [33] (small accumulation region) |

Table 2.1. Benefit and drawbacks of silicon devices for index modulation

Table 2.1. summarizes benefits and drawbacks of each silicon phase shifter. The second line giving the electro-optic bandwidth shows that all silicon based devices can tune silicon ring waveguide index in the nanosecond timescale, hence allowing for very fast laser wavelength reconfiguration. The following line shows that only carrier injection within PIN junction dissipates parasitic heating, which induces a slow thermal chirp. Hence, wavelength tuning

through carrier depletion and accumulation could be preferred. However the last line of Table 2.1. shows that carrier injection gives a five (resp. fifty) times larger electro-optic effect than carrier accumulation (resp. carrier depletion). To achieve C-band tuning with the Vernier mirror presented in I.3.a), ring resonances need to be tuned over 400 GHz. Using the figures of Table 2 and assuming no saturation effects, either a forward bias $\sim 4V$ on a PIN junction, or a reverse bias $\sim 210V$ on a PN junction, or $\sim 20V$ on a capacitive junction, would be required. Hence, only carrier injection can be realistically used to design a widely tunable laser, and the parasitic thermal chirp could be corrected using counter-heating techniques [34].

Fig. 2.1.a) shows dual ring filter top view. As we can see both ring waveguides (blue) are surrounded by P and N doped silicon. Then, two micro strip RF lines are used to independently forward bias each ring. The micro-strip lines are fabricated using two metallic layer depositions. The bottom layer corresponds to the ground and is connected to the P-doped silicon while the top metallic layer is used to route both electrical signals to the N-doped Silicon. Fig. 2.1.b) represents the cross section of a ring waveguide taken on the dotted line of Fig. 2.1.a). As we can see, a guard distance of intrinsic silicon is used to avoid unnecessary optical losses when the rings are not biased.

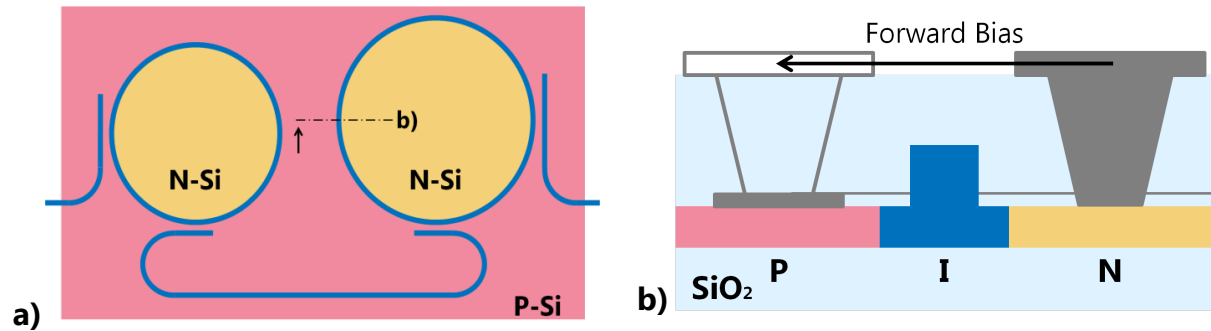


Fig. 2.1.a) top view schematic of the PIN controlled Vernier filter. b) Schematic of the ring waveguide cross section also showing metallic routing elements, gray for metal on the foreground, transparent for metal in the background.

II.1.b. Ring resonator tuning using carrier injection

Before reporting on fast laser wavelength switching, the frequency tuning of a standalone ring resonator using carrier injection is investigated. When the ring PIN junction is forward biased, two effects are modifying the ring waveguide effective index. First, injected carriers with density N_c tend to decrease the silicon refractive index n_{Si} . Then the Joule dissipated power P inside intrinsic silicon tends to heat the ring which inevitably increases n_{Si} . Using eq. 3.I.1. we can show that the shift of frequency resonance Δf is equal to :

$$\Delta f = -\frac{c}{\lambda_0 n_g} \Gamma_{Si} \left(N_c \frac{\partial n_{Si}}{\partial N} + P \frac{\partial T}{\partial P} \frac{\partial n_{Si}}{\partial T} \right) \quad (3.II.1)$$

With λ_0 the resonant wavelength under investigation, n_g the waveguide group index, Γ_{Si} the silicon confinement. Injected carriers density can be assumed as linearly increasing with bias current I while the Joule heating power would be proportional to I^2 . In this case, Δf is written as :

$$\Delta f = -\frac{c}{\lambda_0 n_g} \Gamma_{Si} (I \partial_{EO} n_{Si} + Z_D I^2 \partial_{TO} n_{Si}) \quad (3.II.2)$$

With $\partial_{EO} n_{Si}$ and $\partial_{TO} n_{Si}$ related to variation of silicon refractive index due electro-optic and thermo-optic effect, while Z_D is the diode impedance. Hence, the frequency shift of one ring resonance should first be linearly increasing then quadratically decreasing as a function of bias current.

Fig. 2.2.a) shows the measured transmission of a ring resonator for different current bias before thermo-optic effect occurs. As expected the ring resonance is blue shifted, confirming that carrier injection is operational. Fig 2.2.b) reports on the ring resonance shift as a function of injected current. First, measurement results (orange squares) show that the resonance is blue shifted at bias current under 2 mA and once it exceeds 2 mA, the ring resonance starts to be pulled to the red side due to thermal effect. The PIN serial resistance has been measured between 700 and 800 Ω for eight different PIN ring resonators. This value is around three times higher than reported measurements from [32], [35] using fifteen times smaller ring resonators, and explains that thermo-optic effect takes the lead over carriers effect at very low bias current. We do believe that our unexpectedly high value of serial resistance is due to un-optimized ohmic contact in between doped silicon and metallic element.

Using the polynomial model of eq. 3.II.2 no reliable fit could be obtained on the measured resonance shift. As mentioned in [32], it might be due to a decrease of carrier lifetime as a function of injected carriers. By writing the carrier lifetime τ_c as

$$\tau_c = \frac{\tau_0}{1 + \frac{N_c}{N_0}} \quad (3.II.3)$$

with τ_0 the carrier lifetime without carrier injection and N_0 the carrier density at which carrier lifetime is halved. In this case Δf can be approximated as :

$$\Delta f = -\frac{c}{\lambda_0 n_g} \Gamma_{Si} \left(\frac{\Delta n_0}{2} \left(-1 + \sqrt{1 + 4I/I_0} \right) + Z_D I^2 \partial_{TO} n_{Si} \right) \quad (3.II.4)$$

with Δn_0 the refractive index change for a carrier density of N_0 and $I_0 \equiv qV_R N_0 / \tau_0$, with V_R the ring resonator volume. By fitting the measured resonant frequency shift with formula 3.II.4 for

several ring resonators, we found I_0 between 9 and 16 mA, Δn_0 around -5×10^{-4} and a thermo-optic coefficient closes to $3 \times 10^{-5} \text{ mW}^{-1}$. These results can be carefully compared with [32] and [35] after noticing that our 400 GHz FSR ring resonator is fifteen times larger than their ring modulators.

Finally, Fig. 2.2.b) also shows the fitted Δf as a function of bias current in black and the resonant frequency variation due to both carrier and thermal effects only are plotted in blue and red. The blue curve shows that carrier injection allows 60 GHz ring tuning for bias current under 7 mA. Considering the Vernier filter presented in I.3.c), we deduce that ~ 5 channels spaced by 400 GHz can be accessed with EO effect for bias voltage under 5 V using both ring resonators. However, the red curve shows that these channels will not be stable on the tens of μs timescale due to the TO effect.

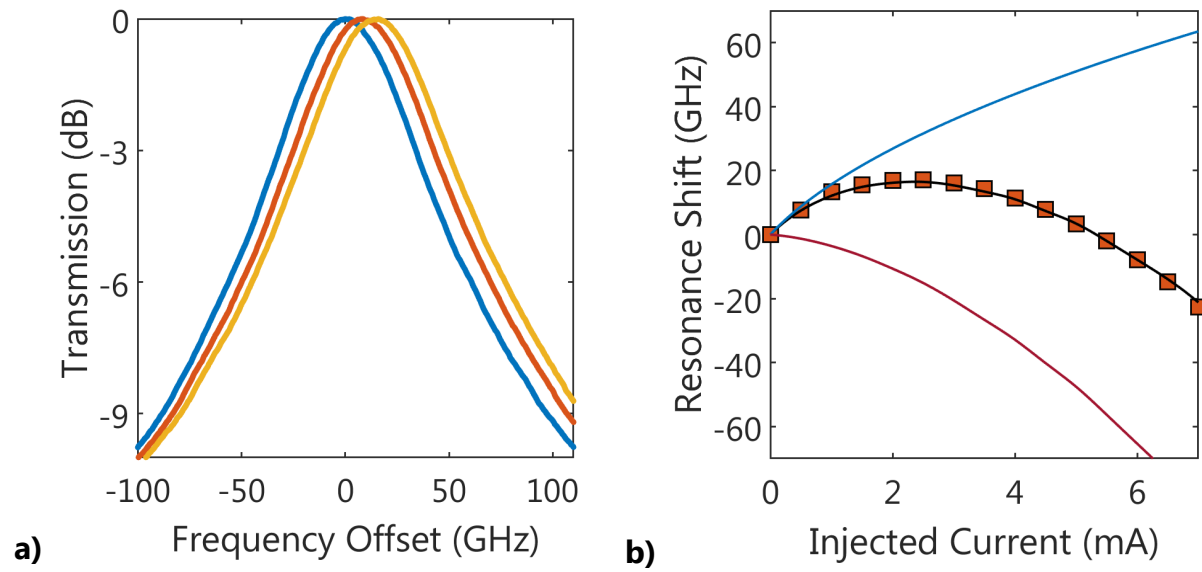


Fig. 2.2. a) Ring transmission in the vicinity of a resonance at 0, 0.5 and 1 mA bias current (resp. in blue, orange, yellow). 0 GHz frequency offset correspond to a wavelength of 1547.9 nm. b) Resonance shift as a function of current injection, orange squares corresponds to the measured values. Model of total frequency shift, EO frequency shift and TO frequency shift are respectively in black, blue and red.

II.1.c. Ring filter tuning dynamics

Here, we study the small signal electro-optic (EO) response of a standalone ring resonator. The EO bandwidth will be later related to the laser switching speed. As silicon free carriers lifetime is in the nanosecond range, only RF signals in 1 GHz bandwidth are considered. Fig. 2.3.a) shows the lumped element circuit of a standalone PIN ring resonator. Lumped model should be valid because the total length of the chip is less than 350 μm which is 850 times smaller than the wavelength of a 1 GHz signal. Using the Silicon platform at CEA Leti and III-V

Lab backend process, Silicon based Mach-Zehnder modulators with over 20 GHz bandwidth have already been demonstrated [23] showing that both Silicon substrate and contact Pad capacitance can be neglected. Moreover, micro-strip lines have also been characterized in [23] showing a 3dB bandwidth higher than 50 GHz.

Silicon ring dynamic response has extensively been studied both theoretically [36]–[38] and experimentally [39]. All of these studies concern modulation properties of single bus ring resonator, whereas we use add/drop ring filters. Nevertheless, formalisms from [36]–[38] can still be applied to study our device and the empirical formula mentioned in [40] and detailed in eq. 3.II.5 giving a ring modulator bandwidth f_{3dB} can still be considered.

$$f_{3dB} = \frac{f_{PIN} f_{ph}}{\sqrt{f_{ph}^2 + f_{PIN}^2}} \quad (3.II.5)$$

In eq. (3.II.5) f_{PIN} is the EO effect bandwidth and $f_{ph} \stackrel{\text{def}}{=} 1/(2\pi\tau_p)$ is the optical bandwidth with τ_p being the photon lifetime. As f_{ph} is estimated over 50 GHz by measuring the ring resonance full width at half maximum, it is much higher than f_{PIN} and complex optical dynamic effects within the ring resonator can be neglected. In this case the fluctuating optical power $P_{outAC} \stackrel{\text{def}}{=} |E_{outAC}|^2$ of E_{out} can be expressed as :

$$P_{outAC} \propto 2 \delta N \left(\frac{1}{\tau_p(N_c)} \frac{\partial \alpha}{\partial N} - \Delta\omega \frac{2\pi}{\lambda_R(N_c)} \frac{\partial n}{\partial N} \right) \quad (3.II.6)$$

with δN the fluctuating carrier density and N_c the carrier density due to bias current. Then, λ_R the ring resonant wavelength, $\Delta\omega$ the detuning between ring resonance pulsation and input field optical pulsation. $\partial\alpha/\partial N$ and $\partial n/\partial N$ are the variation of waveguide loss and effective index due to the injected carriers. Eq. (3.II.6) can be derived with the first order expansion of a Lorentzian ring response. For our device at a 50 GHz frequency detuning between the ring resonance and input field optical frequency :

$$\frac{1}{\tau_p(N_c)} \frac{\partial \alpha}{\partial N} \sim 4 \times 10^{-15} \text{cm}^2/\text{ns} \quad \Delta\omega \frac{2\pi}{\lambda_R(N_c)} \frac{\partial n}{\partial N} \sim 3 \times 10^{-14} \text{cm}^2/\text{ns} \quad (3.II.7)$$

These values mean that, the effective index change will be predominant over the change in quality factor of the ring resonator on the electro-optical response. As the variation of carrier density δN can be related with the modulation current δI using simple rate equation :

$$\frac{d \delta N}{dt} = \frac{\delta I}{qV} - \frac{\delta N}{\tau_c} \quad (3.II.8)$$

we can deduce that the EO modulation response of the ring resonator corresponds to a first order low pass filter whose bandwidth is given by $f_{3dB} = 1/(2\pi\tau_c)$

Fig. 2.3.b) shows the measured S21 EO response of a standalone ring resonator for bias current varying between 0.5 and 3 mA. Measurements are made using a lightwave component analyzer whose electrical output is connected to the μ -strip line and its optical input detects the modulated field at the ring output waveguide. It can be seen that all measured S21 are identical, confirming that carrier lifetime is barely affected by bias current up to 3 mA. The S21 EO response can be fitted using a first order low pass filter with a 3dB frequency cut off around 150 MHz validating the first order model discussed above. This EO bandwidth value should be sufficient for laser switching in the nanosecond timescale. Indeed the ring response to a square excitation should have a rising time close to 2 ns considering 90%-10% thresholds. If required switching time could be drastically shortened using pre-emphasis techniques [39].

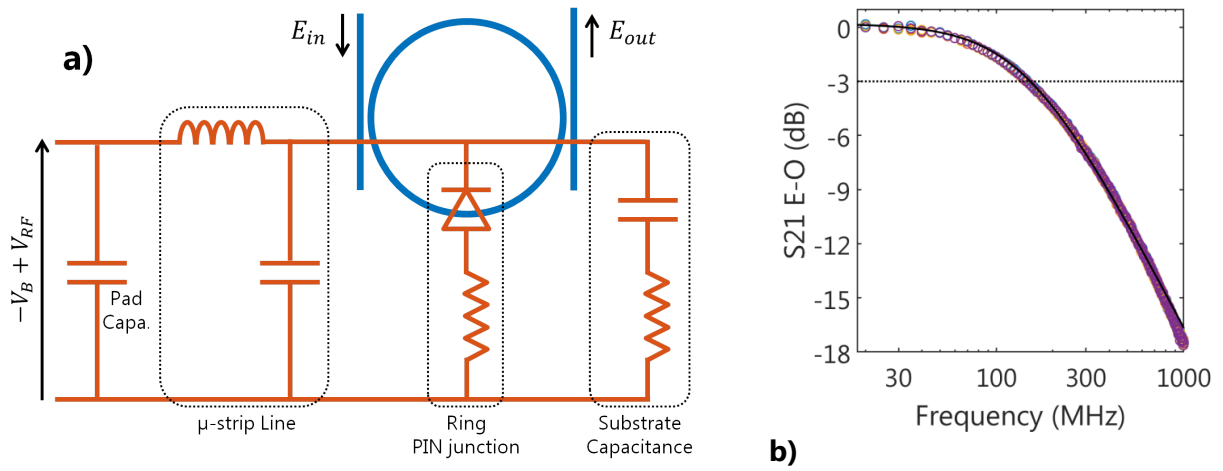


Fig. 2.3. a) Electrical model of a RR modulator using carrier injection effect b) circles correspond to the measured S21 for bias between 0.5 and 3 mA. Black is a fit using first order low pass filter.

II.2. Laser Fast Tuning Performances

Before investigating FTL switching dynamics, laser emitted spectra and static characteristics are presented. Measured laser spectra at a gain section bias of 150 mA and for different voltages applied on one ring resonator are plotted in Fig. 2.4.a showing that the laser can cover up to 42nm optical bandwidth. As mentioned in I.3.a) the continuous tuning of a ring response switches the laser emitted wavelength in a wavelength grid spaced by the second ring FSR. In this measurement, the 42 nm band is mostly covered due to thermal tuning, indeed as explained in II.1.b) thermo optic effect takes the lead over electro-optic effect after a mirror tuning of around 20

GHz corresponding to only a single emitted wavelength jump. The laser emitted power side mode suppression ratio of each wavelength channel is plotted in Fig 2.4.b). We can see that the optical power (in the mW range) drops by about 2.5 dB across the laser operating range. This is attributed to the spectral response of the vertical grating coupler (VGC) used for fiber to chip coupling. Indeed the VGC 3dB bandwidth is around 40 nm, and centered at 1550 nm. The SMSR oscillates between 35 dB and 45 dB. This relatively low value of SMSR is related to the poor quality factor of the silicon ring resonator due to overly coupled bus waveguides. However no relation between the emitted wavelength and measured SMSR could be established, showing that additional losses due to injected carriers do not degrade the laser SMSR. Excess losses due to carrier injection will be more detailed in section III.2)

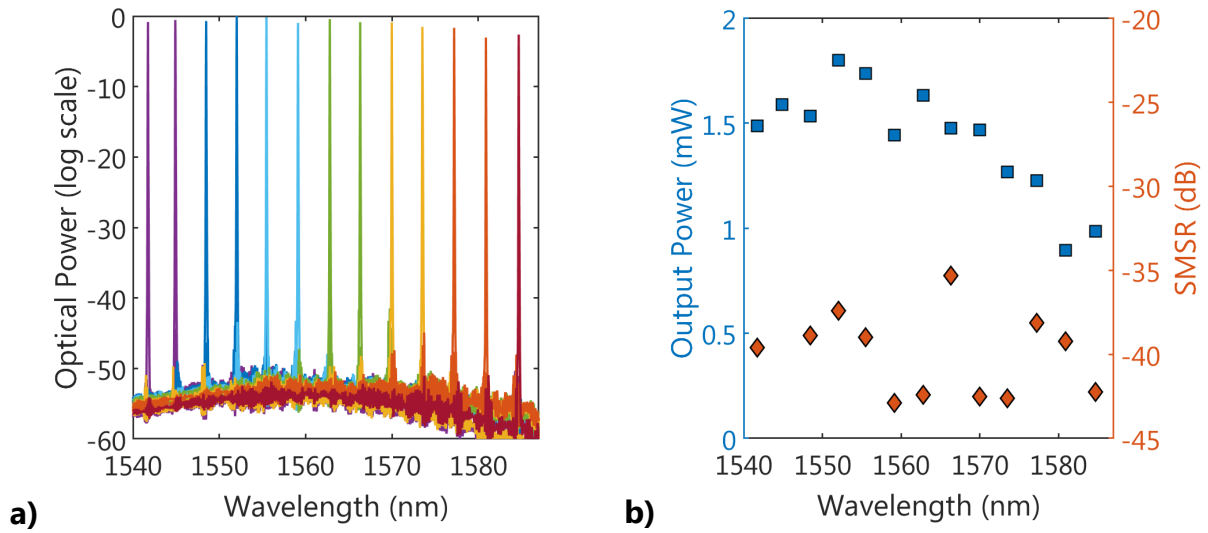


Fig.2.4. a) Superposition of the laser spectra, b) FTL output power (blue), SMSR (orange) of the different emitted wavelength

II.2.a. Multi Wavelength Switching

To assess the laser fast tuning capabilities, switching experiments were made in partnership with "IP and Optical Networking" Nokia's research group. The testbed is sketched in Fig 2.5.a), the FTL laser optical frequency is tuned using a waveform generator providing multi-level square signals within [0V, 6V]. Emitted wavelengths are then demultiplexed using a 12.5 GHz bandwidth demux and analyzed on a real-time oscilloscope. In these experiments the laser frequency is switched every 200 ns in a round Robin manner within sets of four channels spaced by multiples of ~400 GHz. For the set of channels ch1, ch2, ch3, ch4 corresponding to 1558.8, 1552.1, 1548.7, 1542.1 nm, the reported oscillograms and the long term integrated optical spectrum are reported in Fig. 2.5. b) and c). In Fig. 2.5.b) the oscillograms of ch1, ch2,

ch3 and ch4 are plotted in blue, purple, yellow and orange. Moreover, only four channels appear in Fig. 2.5.c1), showing that the laser is single mode during switching operation. We can notice a transitory mode close to 1555.4 nm, which appears when the laser wavelength is tuned from ch1 to ch2 and from ch4 to ch1.

As we can see in b1) the power of each channel seems stable during the 200ns slots. This confirms that the laser output power does not drift more than 10% for a slot duration, and the laser emitted frequency remains within a 12.5 GHz optical bandwidth. Fig. 2.5.c2) shows a zoom of c1) in the vicinity of ch2 obtained with a 180 MHz resolution OSA. We can notice that most of the optical power is contained in a <2GHz bandwidth confirming that the laser emitted frequency drifts by less than 2 GHz during a slot. However, these results are not precise enough to conclude on the laser stability during a slot. Therefore, using a different experimental setup, more precise characterizations of the laser stability in switching operation will be presented in II.2.b)

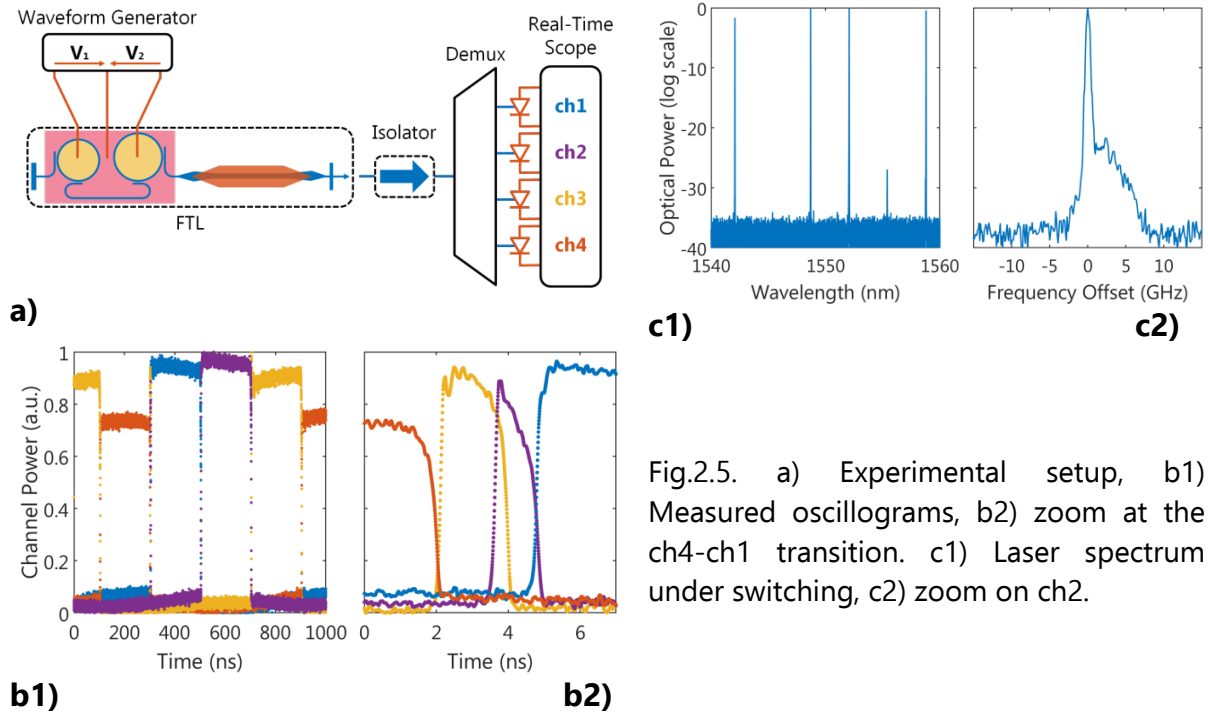


Fig.2.5. a) Experimental setup, b1) Measured oscillograms, b2) zoom at the ch4-ch1 transition. c1) Laser spectrum under switching, c2) zoom on ch2.

The laser switching time can be evaluated as the time interval between power falling in one channel to power rising in the next channel (using 90% level threshold). The switching time was measured for several sets of channels covering a 21 nm optical band, given by the demux operating bandwidth. All switching times were measured under 4 ns and no relation between the laser switching time and wavelength spacing was identified. For instance the transition between ch4 and ch1 is plotted in Fig. 2.5.b2) showing a 3 ns switching time for channel spaced by over 2 THz. Fig. 2.5.b2) also shows that ch2 and ch3 were briefly excited while the laser Vernier mirror was tuned from ch4 to ch1. In addition to that, the frequency drift which occurs during wavelength tuning is captured in Fig. 2.5.c2). It is contained in a 10

GHz optical band. In these experiments the laser switching time was limited by the multilevel source transition time, which was measured around 4 ns. Moreover, as this measurement method does not capture laser frequency stabilization time after tuning, the measured switching time needs to be carefully taken into consideration, and rigorous investigations of the laser switching and stabilization time will be presented in II.2.b).

Hence, in this part we have shown that our III-V on Silicon FTL is a promising component for an optically switched network. First, the laser can reconfigure its emitted frequency at the nanosecond time scale to access optical channels spaced by multiple of 400 GHz within a 21 nm optical band. During a 200 nanosecond timeslot the laser emitted frequency seems to be stable in a 2 GHz optical band, which should make it suitable for coherent optical slot switched transmission.

II.2.b. Precise investigation of switching dynamics

In the previous section laser response under switching was roughly examined using a straightforward experimental setup and laser transitions among a dozen of different channels were tested. However, the measured switching time was first limited by the waveform generator transition time. Because a 12.5 GHz demux was used, both the laser frequency stabilization time and laser frequency stability during a slot could not be precisely assessed. In this part, for the first time to our knowledge, rigorous measurement of the laser switching time comprising the process of frequency stabilization are presented. However, only switching between two channels can be assessed.

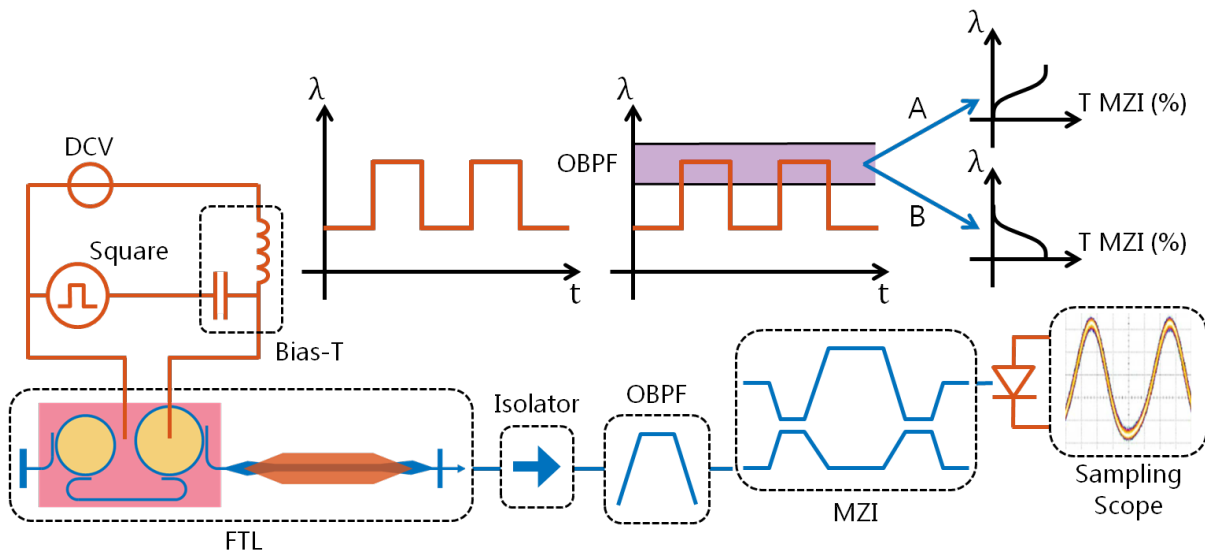


Fig. 2.6. Setup for laser response measurement in switching operation

The experimental setup is depicted in Fig.2.6. and derived from the one presented in [41] used for wideband chirp characterization. One ring of the laser mirror is driven by a square signal using a 12.5 Gbit/s pulse pattern generator (PPG) with 30ps transition time. Hence, the laser emitted frequency switches between two channels spaced by ~ 400 GHz corresponding to the free spectral range (FSR) of the second ring resonator. The laser signal travels through a 50 GHz optical bandpass filter (OBPF) selecting one of the two emitted wavelengths, followed by a 50 GHz spacing Mach-Zehnder interferometer (MZI) and is finally analyzed on a sampling oscilloscope. Using the method introduced in [41] and more precisely described in [42] the laser signal power variation and optical frequency drift during wavelength tuning can be obtained for one channel. The method is based on two consecutive measurements of the power signal at the output of the MZI biased in its linear points. Then, the OBPF is tuned to select the second channel and the process is repeated.

II.2.b.i. FTL channel switching

Fig.2.7.a) and b) shows the laser amplitude and frequency response during wavelength switching. In 2.7.b) the optical frequency is offset by the optical frequency value after stabilization. The blue (resp. orange) curves are obtained when the OBPF is centered at 1541 nm (resp. 1544 nm), in the following section the channels centered at 1541 and 1544 will be referred to as ch.x and ch.y. Both measurements can be superimposed because the optical setup overall dispersion is negligible (below 1 ps/nm).

Fig.2.7.a1) and b1) show the laser power and frequency response for a transition from ch.x to ch.y. As we can see in a1) the power drops from one channel and rises in the next one with a transition time less than 1.8ns. In Fig.2.7.b1) the optical drift from ch.x to ch.y also stabilizes in less than 1.8 ns. Then, Fig. 2.7.a2) and b2) show the laser response for the transition from ch.y to ch.x. In this case the laser switching time comprising stabilization time is below 3 ns.

Hence, we measured a FTL switching and stabilization time below 3 ns for a 400 GHz optical frequency jump. The laser reconfiguration time was further characterized by testing other sets of wavelength and all measured switching times were less than 3.5 ns. This is more than twelve times shorter than results reported with Oclaro SG-DBR in [11], [43], [44]. Moreover, the claimed switching time of 500 ps in [15] might not capture the laser optical frequency stabilization time after switching and must be carefully considered for any comparison purposes.

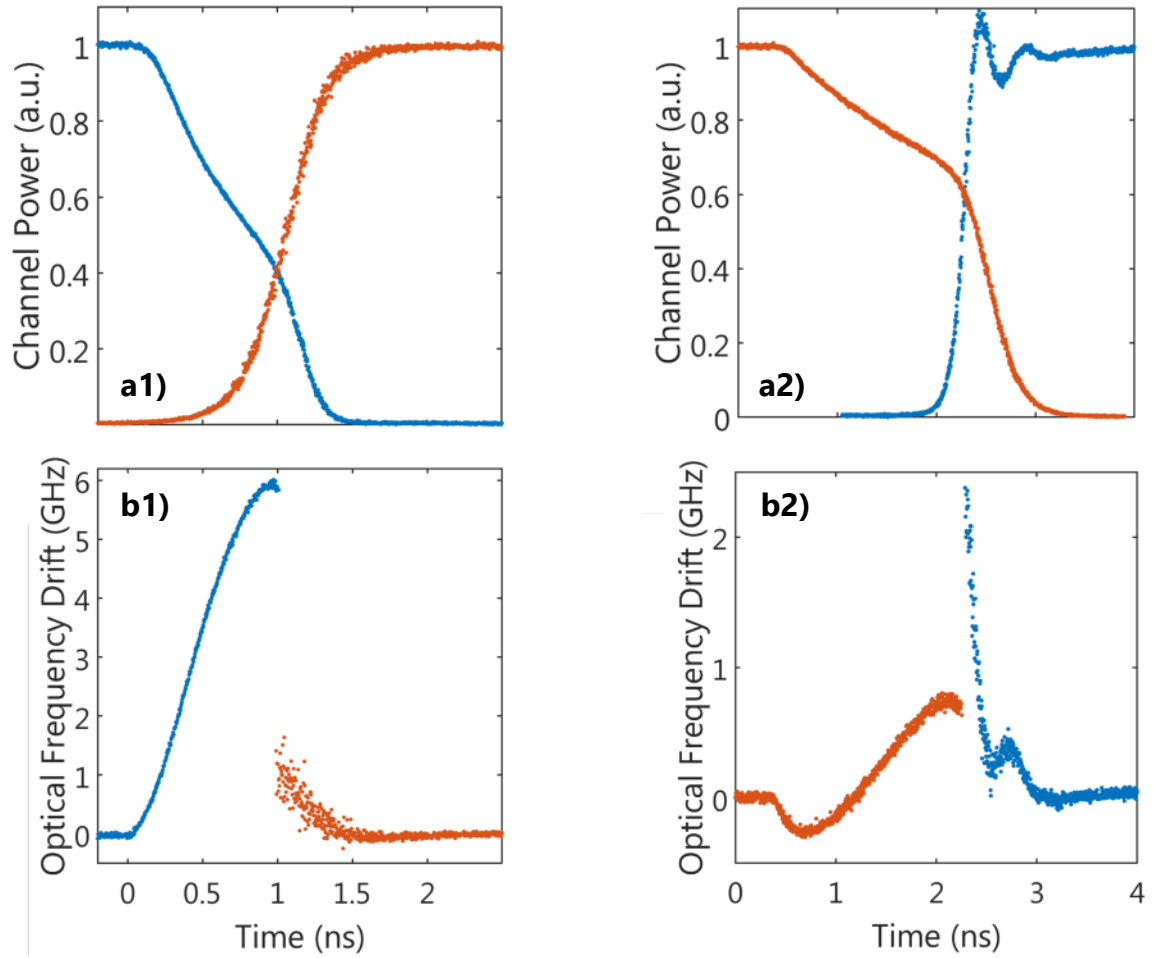


Fig.2.7. a) & b) Measured channel power and frequency offset during wavelength switching.

II.2.b.ii. Long term Stability

Tuning the laser frequency requires to adjust carrier injection inside each ring resonator, implying that the Vernier filter dissipated power will be different for each fast wavelength reconfiguration. Hence, after fast wavelength switching the silicon mirror temperature will slowly drift at the μs timescale to another stationary regime. Due to the thermo-optic effect this temperature drift induces a slow wavelength drift of the Fabry-Pérot mode and might also induce mode hopping due to Vernier effect. However, using our III-V on Silicon FTL, the required power for a 400 GHz frequency tuning is below 5 mW which is an order of magnitude lower than that of a switchable external cavity laser [14]. Hence temperature drifts are expected to be small enough to allow coherent optical slot switching.

Using the same experimental setup presented in II.2.b) we record the optical power variation and frequency drift during a slot. They are respectively plotted in Fig. 2.8. a) and b) for a 1 μs slot time. For a 400 GHz laser frequency tuning, these two variations remain below 0.5 dB and 800 MHz meaning that the FTL would be stable enough for coherent burst mode

in datacenter interconnect. Nonetheless, using this FTL wavelength stability could not be achieved during a 125 μs slot time, which would be required for time division multiplexed passive optical network. Either silicon processing with lower resistivity ohmic contact between metal and PIN ring junction, or the counter heating method could be used to improve the laser long term stability.

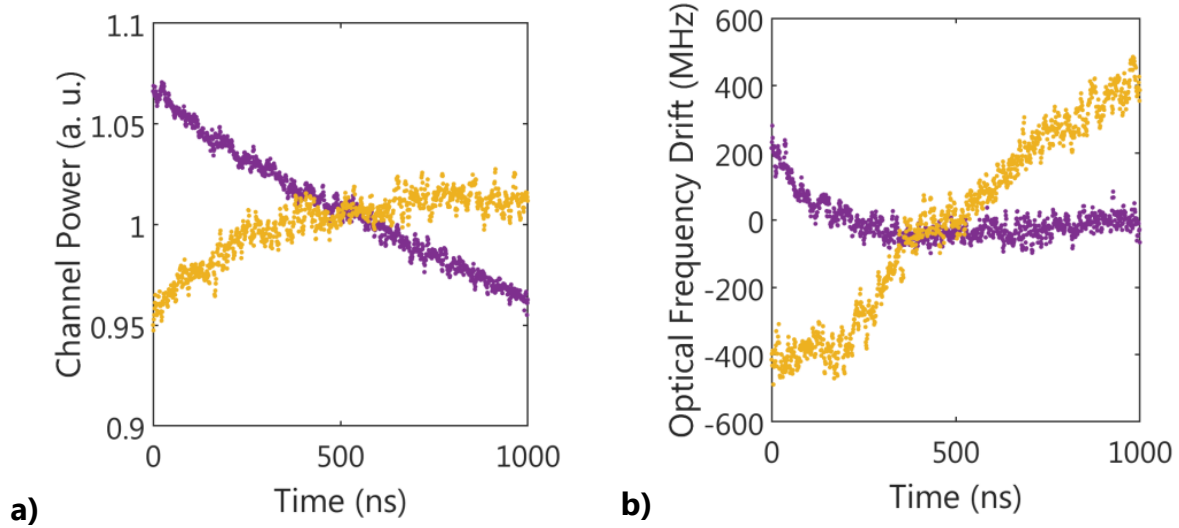


Fig. 2.8. a) & b) Measured power variation and frequency drift during a 1 μs slot when the OBPF is centered in 1545 nm (yellow) and 1548 nm (purple). In b) the optical frequency is offset from the average optical frequency of each channel.

II.3. Conclusion

In this part we have seen that carrier injection inside Silicon waveguide is an efficient method to achieve III-V/Si lasing wavelength tuning. We have first study the tuning range and dynamic of a standalone ring resonator, showing that carrier injection was efficient enough to achieve wavelength switching over five lasing mode spaced by ~ 400 GHz using our Vernier mirror design. We have also shown that the EO response of these PIN rings was in the 200 MHz bandwidth, allowing nanosecond lasing wavelength reconfiguration. Then, after presenting the laser static performances, a novel measurement method was described allowing to precisely estimate laser switching and stabilization time and we have notably demonstrated a laser switching and stabilization time below 2 ns. Finally using the same characterization setup, we evaluated the laser thermal chirp due to the PIN junction power consumption, and this would be sufficient to enable coherent transmission in switching operation.

III. Linewidth Properties

Phase noise properties of extended cavity lasers can be studied using a modified Schawlow–Townes and Henry formalism. In this part, we first theoretically and experimentally investigate linewidth characteristics of III-V on silicon ECLs. Then we review the linewidth properties of the fast tunable laser using carrier injection.

III.1. Linewidth Properties of ECL

III.1.a. Theory

ECLs linewidth characteristics have been extensively studied in the 1980's [45]–[51]. Most of these works considered the longitudinal mode filter of the cavity as a selective lumped mirror. In ring extended cavity III-V on Silicon lasers, the selective mirror is placed at the back of the cavity, and as depicted in Fig. 3.1.a) we write its reflectivity $\tilde{r}_{HR}(\omega)$. The main difference between linewidth characteristics of ECL and the Schawlow–Townes and Henry (STH) model is that the selective mirror has a wavelength dependent reflection which will both introduce phase / amplitude coupling and increase cavity roundtrip time thus modifying the laser resonator phase noise properties [52].

Fig. 3.1.b) shows the superposition of a silicon ring mirror reflectivity, and a hypothetical lasing mode (orange). It can be seen that optical frequency detuning might occur between the reflectivity maximum of the selective filter and the laser emitted optical frequency. First this detuning introduces excess loss which will tend to decrease the photon lifetime and broaden the linewidth. Then the detuning might stabilize the laser depending on the slope of the frequency dependent mirror. As shown in Fig. 3.1.b) the mirror reflectivity increases as a function of the optical frequency when the lasing mode frequency is at a red position relative to the selective mirror resonance. In this case, if a spontaneous emission event increases the laser emitted frequency, it results in an increase of the mirror reflectivity, which will reduce laser threshold gain thus reducing threshold carrier density. In this case the laser waveguide index increases which will finally tend to reduce its emitted frequency. This stabilization loop is depicted in Fig. 3.1.c).

The beneficial effect of the selective mirror on the phase noise properties can be investigated using equivalent laser rate equations. As in [47] the selective mirror reflectivity

can be linearized in the vicinity of the lasing mode optical frequency. In this case formalism from Annex C can be used, and by assuming that the resonant condition $H(\omega, N)$ is written :

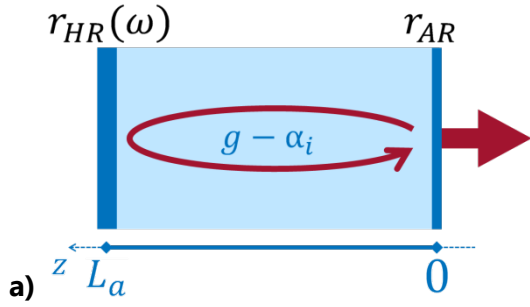
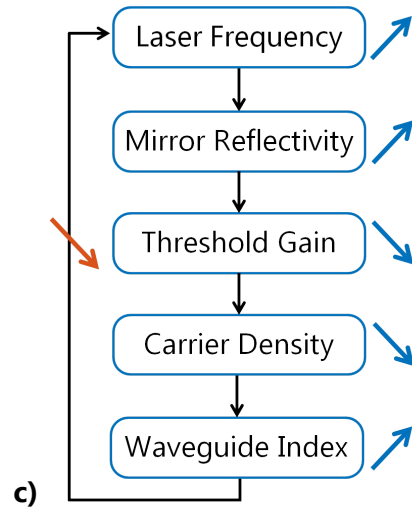
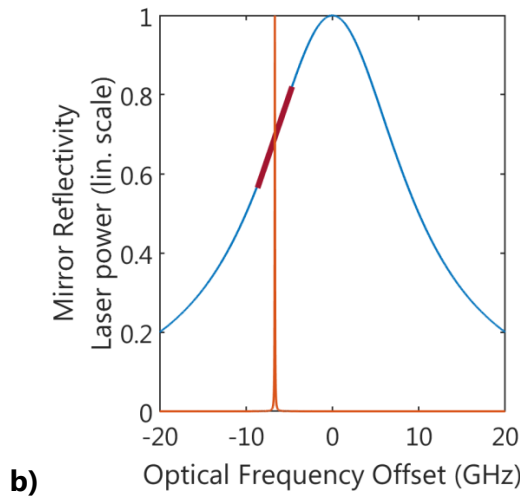


Fig. 3.1.a) Schematic of the extended cavity laser diode. b) Superposition of the mirror reflectivity (blue), linear model (red), lasing mode (orange) c) negative feedback loop due to detune loading



$$H(\omega, N) = \tilde{r}_{HR}(\omega) r_{AR} e^{-j\beta(\omega, N)2L_a} e^{(g(N) - \alpha_i)L_a} \quad (3.III.1)$$

With the notation detailed in Fig. 3.1.a), we obtain (3.III.2 – 3) where τ_{RT} is the roundtrip time inside the gain medium and $\tilde{r}_{HR} = r_{HR} e^{j\phi_r}$. Then, by injecting (3.III.2) and (3.III.3) in (C.9) and (C.10), we can deduce equivalent rate equation similarly to [47].

$$\frac{\partial H}{\partial \omega} = \frac{1}{r_{HR}} \frac{\partial r_{HR}}{\partial \omega} - j \left(\tau_{RT} + \frac{d\phi_r}{d\omega} \right) \quad (3.III.2)$$

$$\frac{\partial H}{\partial g} = \frac{1}{L_a} (1 + j\alpha_H) \quad (3.III.3)$$

$$(1 + A) \frac{dP}{dt} - \frac{2B}{\alpha_H} P \frac{d\phi}{dt} = (G - G_{th})P + R_{sp_{eq}} + F_{p_{eq}} \quad (3.III.4)$$

$$(1 + A) \frac{d\phi}{dt} + \frac{B}{2\alpha_H} \frac{1}{P} \frac{dP}{dt} = \frac{\alpha_H}{2} (G - G_{th}) + F_{\phi_{eq}} \quad (3.III.5)$$

$$(3.III.6) \quad A \stackrel{\text{def}}{=} - \frac{1}{\tau_{RT}} \frac{d\phi_r}{d\omega}$$

$$B \stackrel{\text{def}}{=} \frac{\alpha_H}{\tau_{RT}} \frac{1}{r_{HR}} \frac{\partial r_{HR}}{\partial \omega} \quad (3.III.7)$$

A is related to the increase of roundtrip time due to the selective mirror and B corresponds to the detune loading term detailed above. In this case it can be shown [47] that the laser linewidth is given by :

$$(3.III.8) \quad \Delta\vartheta_{STH} = \frac{\Delta\vartheta_{ST}(1 + \alpha_H^2)}{F^2} \quad F = 1 + A + B \quad (3.III.9)$$

Hence, linewidth properties of III-V on Silicon lasers will be closely related to the F factor of the dual-ring mirror.

III.1.b. Design Optimization

In this part we study the F factor of our III-V on Silicon design. Fig. 3.2.a) superimposed the photon lifetime and F factor of a silicon dual ring filter in the vicinity of the selected lasing mode frequency. The optical frequency is offset by the filter maxima. For the silicon part, we consider waveguides with 2dB/cm losses (being higher than state of the art results from UCSB), ~400 GHz rings resonators having 10% coupling with silicon waveguides and back mirror (resp. front mirror) with 100% (resp. 20%) reflectivity. We also assume III-V waveguides with 20 cm^{-1} loss coefficient. In this case the F factor reaches a value of 12 for 5 GHz detuning with maximum mirror reflectivity. Because the photon lifetime only decreases by 25% of its maximum at 5 GHz detuning, we can assume minimum linewidth value close to 5 GHz detuning. As we may see in Fig. 3.2.a), F factor is only plotted for positive values because the laser is unstable for negative F factor.

Then Fig. 3.2.b) shows the modified Schawlow–Townes and Henry (STH) linewidth value as a function of frequency detuning obtained considering III-V on Silicon laser with 800μm long gain medium biased at 100mA. We can see that the STH linewidth is minimum for around 3.5 GHz detuning and as low as 25 kHz. This detuning value is slightly lower than that discussed above because the reduced photon lifetime for larger detuning tends to both increase the lasing mode threshold current and broaden the Schawlow–Townes linewidth proportionally to τ_p^2 .

Fig. 3.2.c) depicts the optimum STH linewidth that can be obtained for various silicon waveguide losses and ring coupling coefficients for the gain medium considered above. It shows that <100 Hz STH linewidth can be achieved with state of the art silicon waveguides [53] and <1 % ring coupling. This mapping also yields the optimum ring coupling value for a given Silicon platform and targeted laser linewidth. Indeed, the lower the coupling coefficient is, the higher mirror excess losses will be, thus reducing laser output power. Hence, the higher ring coupling coefficient granting the targeted linewidth value will also achieve maximum output power, therefore optimizing the laser dual ring mirror. The white region,

means that selective mirror excess losses induces a threshold current over 100 mA which was the gain bias current considered in the simulation.

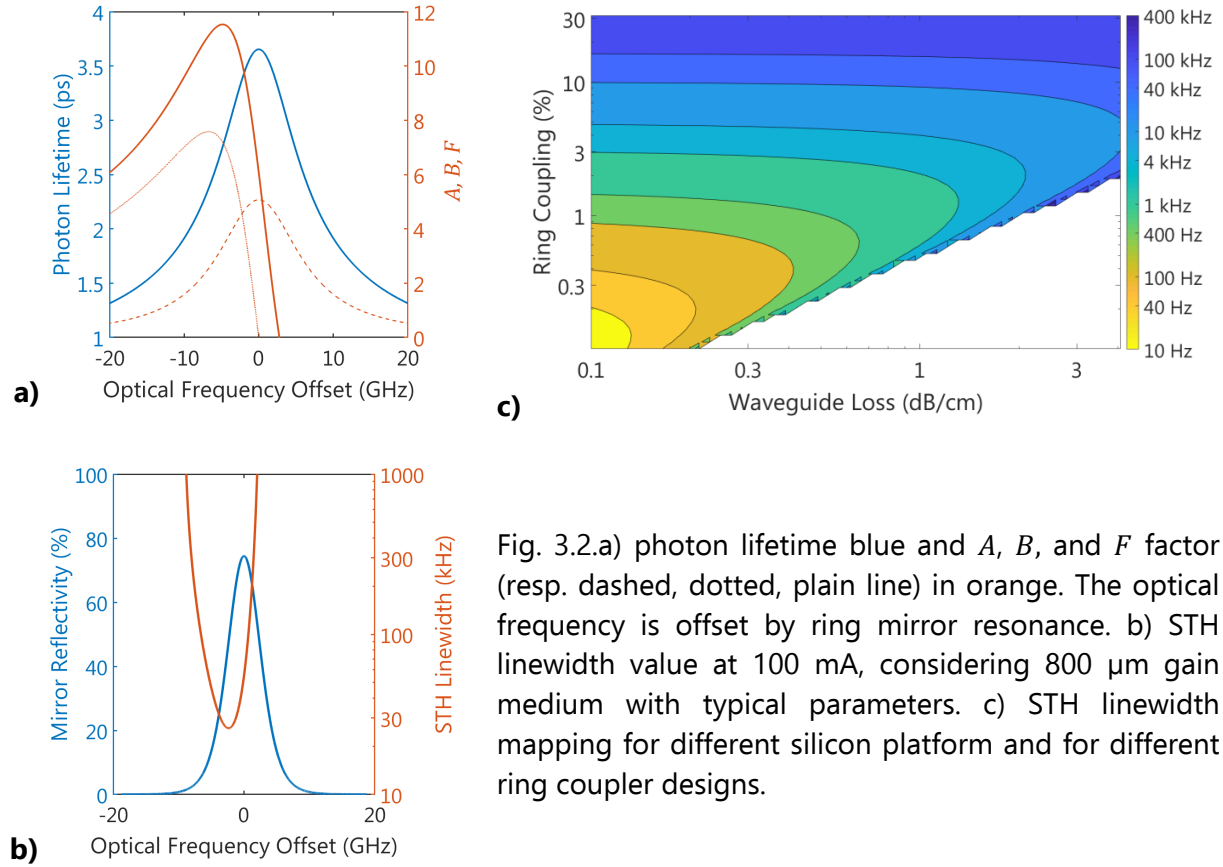


Fig. 3.2.a) photon lifetime blue and A , B , and F factor (resp. dashed, dotted, plain line) in orange. The optical frequency is offset by ring mirror resonance. b) STH linewidth value at 100 mA, considering 800 μm gain medium with typical parameters. c) STH linewidth mapping for different silicon platform and for different ring coupler designs.

III.1.c. Investigation of the lasing mode Stability

In section III.1.a) and III.1.b) we have shown that the negative feedback loop resulting from phase-amplitude coupling inside the selective mirror could improve laser linewidth characteristics and in these sections, the stability of the lasing mode was assumed. Here, and for the first time to our knowledge, we investigate the stability of the steady state solution of the equivalent rate equation. This part complements both [47], [54] which assumed a stable lasing mode. After linearization, the equivalent laser rate equations can be written as :

$$\bar{S} \frac{d}{dt} \begin{pmatrix} \delta N \\ \delta P \\ \varphi \end{pmatrix} = \bar{M} \begin{pmatrix} \delta N \\ \delta P \\ \varphi \end{pmatrix} \quad (3.III.10)$$

With $\{\delta N, \delta P\}$ small perturbations of the steady state solution $\{N_0, P_0\}$, and \bar{S} , \bar{M} given in (3.III.11) and (3.III.12).

$$\bar{\bar{S}} = \begin{pmatrix} 1 & 0 & 0 \\ 0 & 1 + A & -(2BP_0)/\alpha_H \\ 0 & B/(2\alpha_H P_0) & 1 + A \end{pmatrix} \quad (3.III.11)$$

$$\bar{\bar{M}} = \begin{pmatrix} -\Gamma_N & -(G_P P_0 + 1/\tau_p) & 0 \\ G_N P_0 & -\Gamma_P & 0 \\ \alpha_H G_N/2 & \alpha_H G_P/2 & 0 \end{pmatrix} \quad (3.III.12)$$

with G_N and G_P being the differential gain and nonlinear gain compressions, and Γ_N , Γ_P are damping factors which are given in [54], [55]. Note that, the derivation of $\bar{\bar{S}}$ and $\bar{\bar{M}}$ is further detailed in [54]. In this case the lasing mode may be stable only if the eigenvalues $\{V_1, V_2, V_3\}$ of $\bar{\bar{S}}^{-1} \bar{\bar{M}}$ all have negative real parts. Fig.3.3. superimposes the mirror reflectivity spectrum with the mirror F factor and p defined as

$$p = \max(\text{Re}(\{V_1, V_2, V_3\})). \quad (3.III.13)$$

We can see that p is negative when F is positive. This result shows that a lasing mode can only exist for frequency detuning corresponding to $F > 0$.

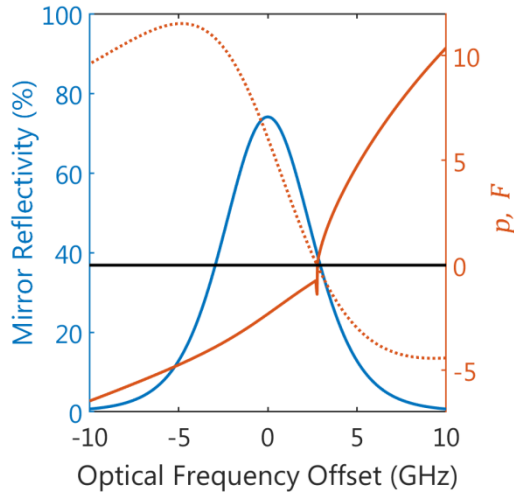


Fig. 3.3. Blue corresponds to the dual ring mirror reflectivity. Plain (resp. dotted) orange corresponds to p (resp. F).

III.1.d. Measurement Results

In this part we compare linewidth measurement results to simulated values obtained with the theory detailed above. Measurements presented here are performed using a thermally tuned III-V on Silicon laser and not the FTL under study, however both lasers use similar ring filter designs and because of no injected carriers, experimental results are more straightforward to analyze using the theory described in III.1.

Fig. 3.4.a) displays the measured STH linewidth as a function of frequency detuning. In this measurement, the lasing mode frequency was tuned within the dual ring filter bandwidth using a thermal phase section. Then, the frequency offset was measured by recording laser

spectra for different phase section bias as shown in Fig. 3.4.b). The offset value corresponds to the optical frequency giving maximum output power. Then we simulate STH linewidth as a function of the detuning from the selective mirror peak frequency. In this simulation, silicon losses, ring coupling coefficient and most III-V gain medium parameter were extracted from measurements. For instance silicon waveguide losses are 2.9 dB/cm, rings coupling coefficient is 15% and $\alpha_H = 2.8$. Some other laser parameters such as, the electrical pumping efficiency and spontaneous emission factor were obtained using a fit. The accurate fit of the theoretical model with experimental data confirms the validity of the theory discussed above. For instance we notice that the minimum linewidth value (100 kHz) is obtained for a ~2GHz negative detuning. We also notice that linewidth drastically broadens for a blue detuning of the lasing mode related to the mirror resonance.

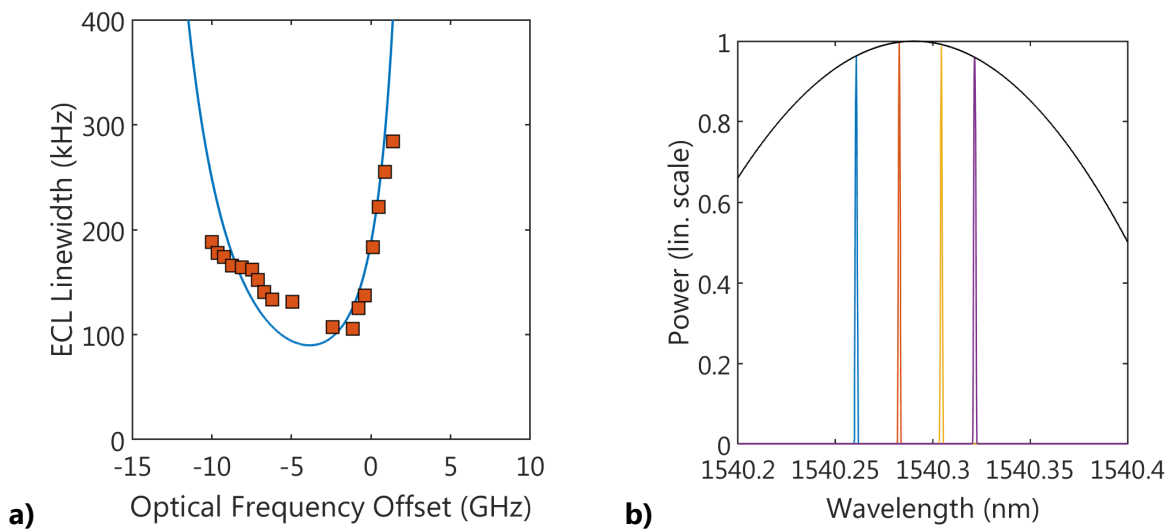


Fig. 3.4.a) Orange squares correspond to measured linewidth. Blue lines corresponds to simulated STH Linewidth. b) Laser emitted spectra for different voltages applied in the thermal phase section. The maximum of the parabola gives the wavelength corresponding to 0 frequency offset.

III.2. Linewidth Penalty due to carrier injection

In III.1) we have carefully investigated the linewidth properties of III-V on Silicon ECL using a dual ring filter. We have notably shown that ECL linewidth greatly depends on a factor F related to the longitudinal mode filter characteristics. For a Vernier ring mirror, the maximum value of F within the mirror reflectivity bandwidth depends on the rings quality factor. Indeed for increased waveguide losses, B may drastically decrease due to a smoother filter slope. However, injected carriers increase waveguide losses due to free carrier absorption (FCA), which can thus drastically impact the lasing mode linewidth.

To study this phenomenon, we first retrieve additional ring waveguide losses due to FCA. For this purpose, we measure the transmission spectra of a standalone ring filter at current injection I between 0 and 7 mA. Measured spectra offset by their resonant frequency are plotted in Fig. 3.5.a). We can notice the broadening of ring resonances due FCA excess losses. Then, ring filter FWHM are reported in Fig. 3.5.b), and we may notice saturation of the FWHM value as a function of bias current. As in II.1. b) this is related to the variation of Silicon carrier lifetime as a function of carrier density. In this case, the excess losses due to FCA α_{FCA} can be written [32]:

$$\alpha_{FCA} = \frac{\alpha_{N_0}}{2} \left(\sqrt{1 + 4I/I_0} - 1 \right) \quad (3.III.14)$$

with α_{N_0} and I_0 the excess losses and bias current at N_0 defined in II.1.b). Then we can fit measured FWHM as a function of bias current, and after assuming 3 dB/cm propagation losses due to scattering we retrieve the following values : ring coupling $K = 35\%$, $\alpha_{N_0} = 5 \text{ cm}^{-1}$, $I_0 = 3 \text{ mA}$. Because, I_0 value deduced in II.1.b) was in between 9-16 mA, we believe the discrepancy with the 3mA value found here is mainly due to the precision of the FWHM measurements. We can finally extract ring waveguide propagation losses as a function of current injection, the results of which are displayed in Fig 3.5.b). Propagation loss increases from 0.7 cm^{-1} up to 8.9 cm^{-1} but this substantial increase of the loss coefficient had a moderate impact on the ring FWHM because the ring resonator external coupling losses $\alpha_{ext} = (2/L) \ln(1/(1 - K)) = 41 \text{ cm}^{-1}$ are much greater than the propagation ones.

In order to quantify the possible broadening of laser linewidth we simulated the maximum achievable F^2 -factor of the Fast-Tunable III-V on Silicon laser by considering carrier injection in only one ring of the Vernier mirror. Simulated results are depicted in Fig. 3.5.c), and we can see that the value of F^2 varies by about 10% for PIN forward current between 0 and 7 mA. This very slight penalty of the F^2 factor is due to the fact that ring resonator external losses are still clamping the value of PIN ring resonator quality factor at high bias current. As ring resonators perimeter is only around 208 μm , excess cavity losses due to injected carriers are negligible, and should not affect laser emitted power and linewidth value.

Finally we measured our FTL optical linewidth of the different channels spaced by around 400 GHz. Linewidth values are reported in Fig. 3.5.d). When no bias current is applied on a ring resonator, the laser emitted wavelength is around 1542 nm while injecting carriers switch the laser emitted wavelength in the red side of the spectrum due to Vernier effect. We can see that the FTL linewidth broadens from 300 kHz to 500 kHz at high carrier injection. As we have seen in Fig. 3.5.c) the dual ring mirror F^2 should decrease by only 10% at high current injection. Hence it is not sure that the linewidth broadening on the red side of the spectrum is related to injected carriers. The linewidth broadening might be attributed to :

- Parasitic reflection from the silicon vertical grating coupler (VGC) used for laser to fiber coupling which increases on the red side of the C-band.

- Detuning between the gain medium peak wavelength and lasing mode [50], [56].

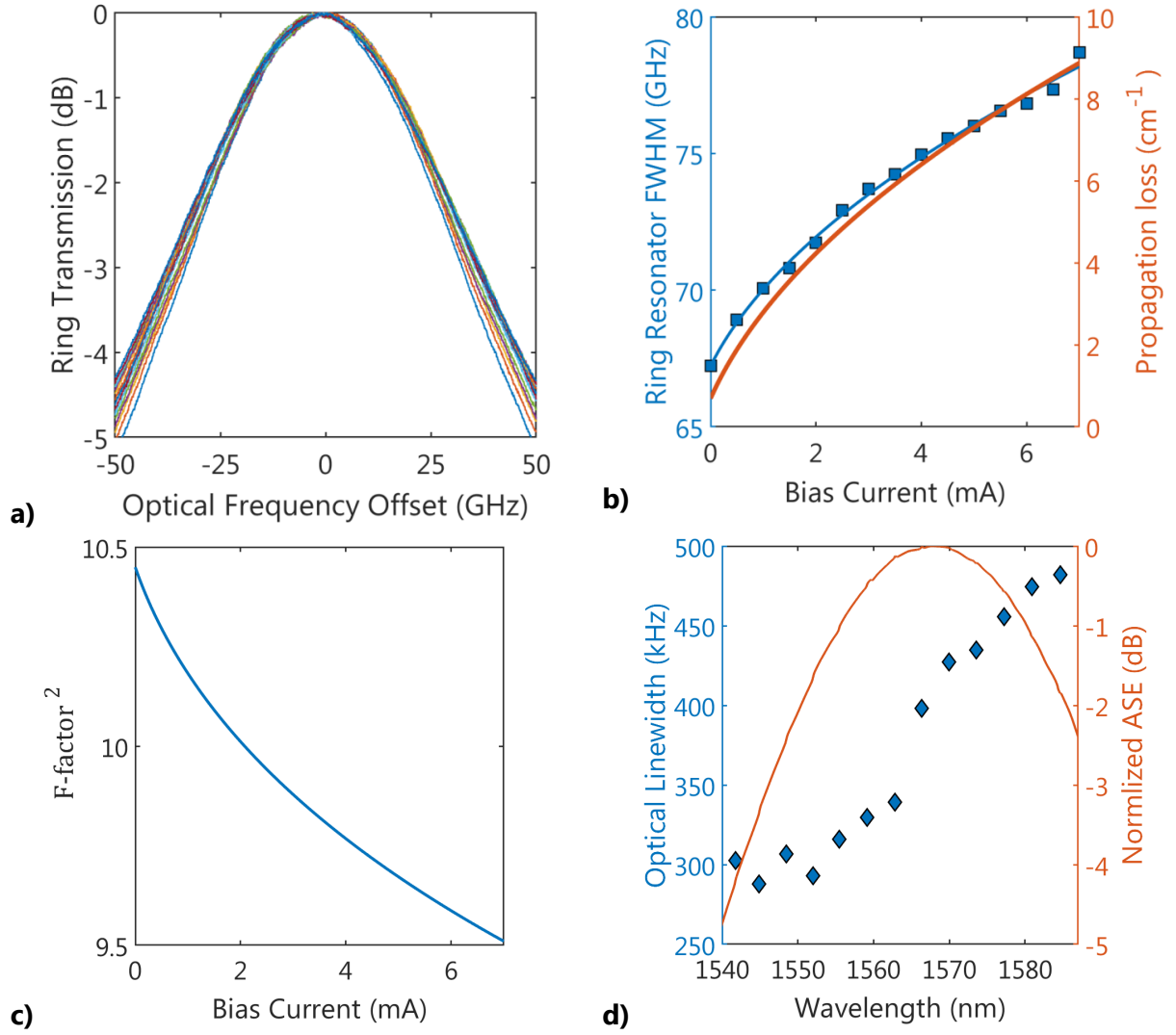


Fig. 3.5.a) Superposition of single ring transmission spectra. b) Blue squares correspond to the measured ring FWHM, blue line is the fitted FWHM as a function of current bias. Orange line corresponds to the extracted propagation losses. c) Simulated F^2 -factor. d) Measured FTL optical linewidths (blue diamond), measured ASE spectrum (orange line).

Linewidth values presented here are higher than the one reported using a thermally tuned III-V on Silicon tunable laser in III.1.d). This is attributed to the ring coupling coefficient of the FTL being higher than the ring coupling coefficient of the laser presented in III.1.d). Hence the ring quality factor and mirror F -factor of the FTL are lower than the thermally tuned III-V on silicon ECL, explaining the broader linewidth of the FTL. Nevertheless, linewidth values under 500 kHz should be sufficient for coherent communication up to 16-QAM.

IV. Coherent Optical Slot Switching

In the following, we focus on coherent optical slot switching (COSS) experimental results obtained with our III-V on Silicon FTL. First, previously reported COSS experimental results are presented, then, the coherent testbed used during the experiments is detailed, and finally, COSS results are discussed.

IV.1.State of the art

COSS experimental results are summarized in the following. We recall the type of laser that was used during the experiments along with the phenomenon limiting transmission performances. Fig.4.1. shows the system waiting time and net data rate of each reported COSS experimental results. The waiting time is defined as the time interval required between two consecutive slots to achieve acceptable BER.

COSS experiments were first demonstrated by Bell-Labs in [57]. In this work, a switchable laser array with 5 ns reconfiguration time similar to [10] was used as a fast tunable local oscillator in a coherent testbed. Using dual-polarization (DP) QPSK signaling at 56 Gbaud, they achieved a waiting time under 70 ns in between optical slots. It was claimed that the waiting time between slots was not limited by laser dynamic properties but rather the constant modulus algorithm (CMA) [58] convergence time used for polarization recovery.

The same year, Dublin City University (DCU) reported COSS results using single-polarization (SP) QPSK signaling at 10.7 Gbaud using a slotted Fabry-Pérot (SFP) laser [59]. Due to the absence of polarization multiplexing, they had not to rely on CMA during digital signal processing (DSP) and achieved only 16 ns of waiting time between slots.

In 2011 University College of London (UCL) reported COSS using the commercially available DS-DBR from Oclaro [43]. They demonstrate 28 Gbaud DP-QPSK with 150 ns of waiting time between slots. This relatively long waiting time is due to both the convergence time of the CMA, accounting for around 70 ns and the relatively long laser stabilization time after wavelength tuning (around 80 ns). In 2014, using a similar experimental setup to the one of [43] Nokia also demonstrates COSS using the same DS-DBR from Oclaro [60]. However, using both phase compensation inside the DBR region along with a wavelength locker, and a faster CMA they achieved a system waiting time under 25 ns with 28 Gbaud DP-QPSK format. One year later DCU also demonstrates COSS experiments at 10 Gbaud with DP-QPSK signaling and using the Oclaro SG-DBR laser [61]. They achieved a system waiting time

around 30 ns, which was slightly slower than the results of [60] but because they were using a lower baud-rate they had to rely on less symbol to let converge the CMA.

COSS experiments using DP-16QAM format was first reported by UCL in 2014 [62]. With 6 Gbaud baud rate, they required one microsecond of waiting time between slots and no explanation was given to justify this much longer waiting time than other reported results. In 2018, DCU showed SP-16QAM COSS with 70 ns waiting time which was limited by the long wavelength stabilization time of their fast-tunable laser [44]. Finally in 2019, NTT showed COSS experiments at 32 Gbaud and using DP-QPSK format they achieved a system waiting time under 50 ns [15].

To conclude, no COSS results with less than 16 ns system waiting time has been shown. This result was obtained by using SP-QPSK format, with a spectral efficiency of only 2 bit/s/Hz. In this part, we will report on COSS results with less than 4 ns waiting time in DP-QPSK and 15 ns in DP-16QAM.

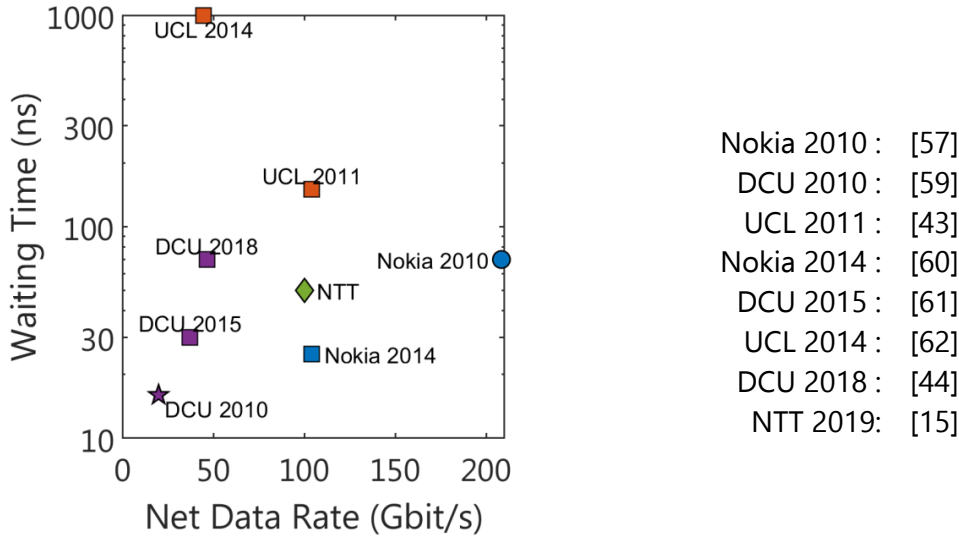


Fig. 4.1 Reported COSS experimental results

IV.2. Experimental Setup

The COSS experimental setup is depicted in Fig.4.2.a) At the transmitter (Tx) side the FTL switches between two channels spaced by ~400 GHz and are centered at 1548 nm (ch.i) and 1552 nm (ch.ii). The laser output signal which travels through an isolator is then modulated at 32 Gbaud with dual polarization (DP) coherent format using a 92 GS/s digital to analog converter and an I/Q modulator. No synchronization was made between the optical modulator and waveform generator used for wavelength switching. After amplification through an EDFA, both optical channels are selected using a Finisar FlexGrid™ filter and a

variable optical attenuator (VOA) followed by another EDFA is used to control the emitted optical signal to noise ratio (OSNR). The transmitted signal is detected using a coherent receiver fed by two local oscillators matching ch.i and ch.ii. The received signal is sampled using a 40 GS/s real-time oscilloscope with <30 GHz optical bandwidth. Because the scope bandwidth is lower than that of the signal one, the frequency detuning between the FTL and both local oscillators will affect the measured bit error rate (BER). This also means that the FTL emitted signal thermal frequency drift will degrade the BER if it exceeds the GHz range. The numerical signal is processed offline using the following digital signal processing (DSP) steps : re-sampling at 2 samples per symbol (SPS), channel estimation using constant-modulus-algorithm (CMA), down-sampling at 1 SPS, carrier frequency estimation (CFE), carrier phase estimation (CPE) and finally error counting. The CPE is made using Viterbi and Viterbi [63] algorithm, which is less tolerant to laser phase noise than a blind phase search algorithm but is more adapted to datacenter communication as it requires lower computational power [64].

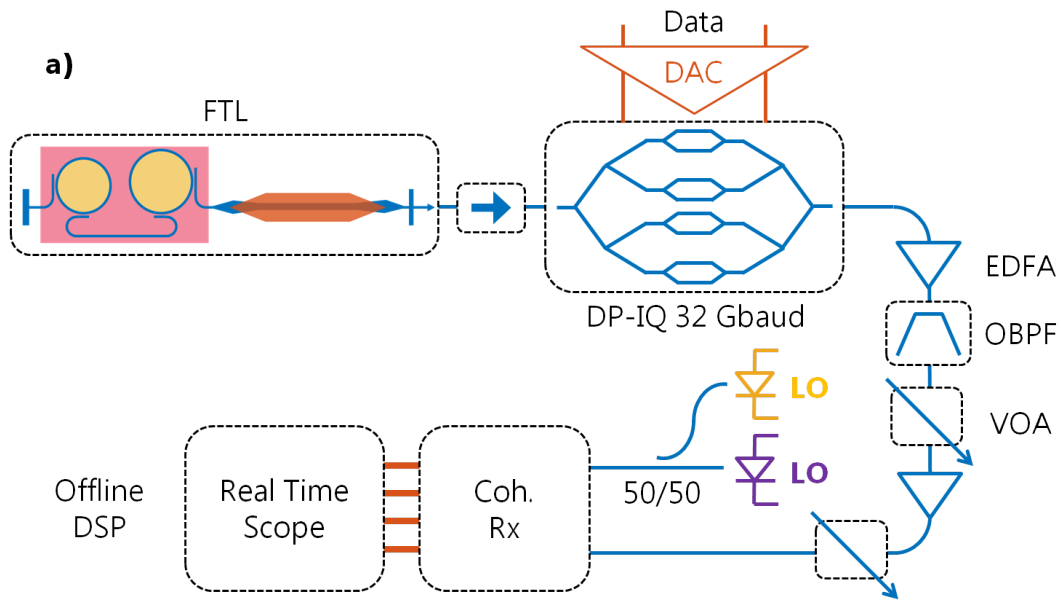
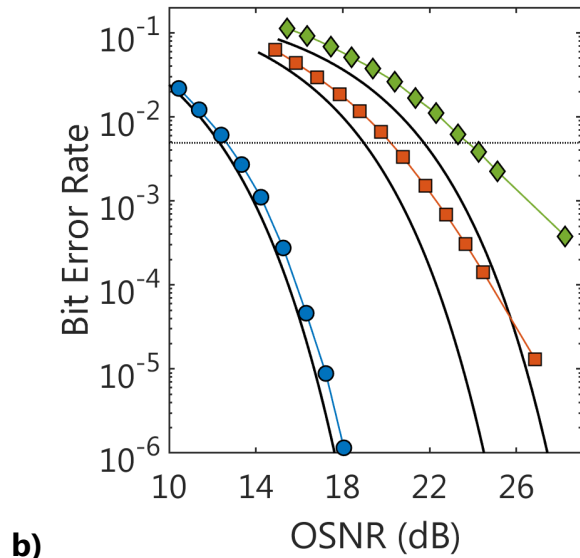


Fig.4.2. a) Experimental setup for coherent slot switching. The FTL is cooled at 25°C, its gain medium is biased at 150 mA, and the Vernier mirror is driven using the waveform generator of II.2.a).

b) BER vs OSNR performance of the FTL without switching. Blue, orange and green respectively correspond to QPSK, 16QAM and 32QAM. The black curves correspond to the optimum BER using the AWGN theory, the dotted black curve correspond to a 7% FEC threshold.



We first test the coherent setup BER vs OSNR performances without laser switching. The measured BERs are plotted in Fig. 4.2.b) for dual polarization QPSK, 16QAM and 32QAM with direct Gray decoding aided by pilot sequence to remove possible cycle slips. In these experiments the laser wavelength is around 1552 nm. If we consider a 7% FEC limit of 4.9×10^{-3} , the penalty in DP-QPSK is of only 0.3 dB showing that the FTL noise properties are suitable for 119 Gbit/s coherent communication. Using DP-16QAM and DP-32QAM format, the penalty at the FEC limit increases up to 1 dB and 2 dB. This penalty increase is related both to the laser phase noise and scope bandwidth. Nonetheless, for the first time to our knowledge DP-16QAM and DP-32QAM transmission results are presented using a III-V on Silicon tunable laser showing the suitability of III-V on Silicon laser for highly efficient QAM format.

IV.3. COSS results with fixed CMA

COSS experiments were performed in DP-QPSK and DP-16QAM format using differential decoding. Because of the absence of synchronization between the waveform generator and I/Q modulator, it was not possible to synchronize the pilot sequences and the beginning of the slots. Hence, using direct decoding cycle slips would have occurred between slots starting time and pilot sequence. In these experiments the CMA equalizer was evaluated only using the first detected slot for each channel. Then, the CMA was freeze and applied on all following slots. This method enables to assess the fast tunable transmitter switching dynamic regardless of the CMA convergence time. Fig.4.3. shows the counted BER as a function of time with each point corresponding to the accumulated error over all recorded slots for each channel. In this section we define the waiting time between slots as in IV.1. being the time interval starting when BER goes above the FEC limit and ending when BER returns below the FEC limit. We choose a 7% FEC limit of 4.9×10^{-3} [65].

Using DP-QPSK format, the measured BER as a function of time is plotted in Fig.4.3.a) with a slot duration T_s fixed at 80 ns. No error was recorded during a slot, meaning that the BER is below the measurement limit of 6×10^{-6} . This result confirms the FTL wavelength stability during a slot. The waiting time is measured to be below 3 ns for both transition (ch.i to ch.ii and ch.ii to ch.i), which is five times faster than the best reported result with single-polarization QPSK only [59]. This waiting time corresponds to the laser switching time measured in II.2.b.i

Fig.4.3.b) shows the counted BER as a function of time in DP-16QAM format and this case, the slot was fixed at 320 ns. The BER is around 3.5×10^{-4} and 8.5×10^{-4} for ch.i and ch.ii. It is also stable during a full slot duration confirming a very small wavelength drift. The slight BER discrepancy among the different slots could be related to different measured OSNR for different slots. Indeed the fiber to I/Q modulator coupling is polarization dependent, and a polarization controller is used in between the FTL and the modulator. Because the

polarization controller is wavelength dependent, it brings a different value of coupling loss for both channels. The waiting time between slots is around 16ns and 12ns for both transitions. This result is four times faster than the results reported in [44] using single polarization double-star 16 QAM. This difference between slot waiting time to achieve acceptable BER and laser switching time is still under investigation, as claimed in [43], [44], [60], it could be linked to the laser linewidth stabilization after switching.

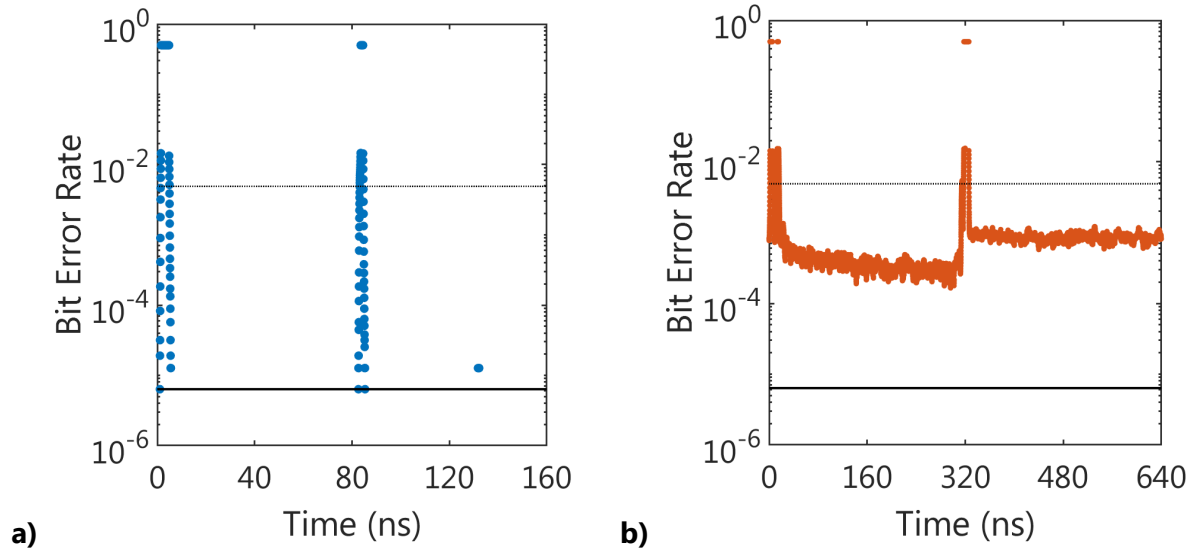


Fig.4.3. Time resolve BER in DP-QPSK (a)), DP-16QAM (b)). The dotted line corresponds to the 7% FEC limit and the plain line to error rate measurement limit.

IV.4. COSS results with CMA convergence

In the previous section, the CMA equalization filter was obtained considering the first optical slots and then applied on the full recorded data. This method worked because the signal polarization of each channel did not vary while recording the oscillograms. However, in a more realistic scenario, the light polarization of a given channel may vary from a slot to another. In these experiments, the channel estimation is performed at the beginning of each slot during a header. Then, the obtained equalizer is used to process each slot independently. Hence, this method is robust to polarization variation in between slots. It is however not robust to polarization rotation during a given slot, but because optical slots are shorter than $1\mu\text{s}$ this scenario is very unlikely to happen. Using this DSP method, we measure the overall BER accumulated in ~ 3000 slots of 80 ns for DP-QPSK and in ~ 750 slots of 320 ns for DP-16QAM. This BER value is reported in Fig.4.5. for different header times. In this measurement, it was also ensured that the BER of all individual decoded slots was below the FEC limit.

The blue circle in Fig.4.4. shows that a BER below the 7% FEC limit can be obtained using a header time T_{H0} as short as 3.5 ns. When a header time smaller than T_{H0} is used, some slots

could not be decoded, and their error rate was equal to $5e^{-1}$. If the header used is longer than T_{H0} , the total BER decrease to the smallest measurable BER. For the first time to our knowledge we perform, laser switching, laser stabilization and channel estimation as fast as 4 ns being a 6-fold improvement compared to reported results [60]. We believe that this result was made possible because of the much faster optical frequency stabilization time than results reported in [60].

Using the same DSP method, COSS results using DP-16QAM format are displayed with the blue squares of Fig.4.4. b). It shows that a BER lower than the 7% FEC limit can be obtained with a header time T_{H1} around 30 ns. As in QPSK, using shorter header time does not allow to retrieve the transmitted data and the error rate become equal to $5e^{-1}$. For longer header time the error rate slightly decrease to $1e^{-3}$. This results shows for the first time to our knowledge COSS using DP-16QAM format with CMA convergence in the nanosecond timescale. We also believe that using a specific header instead of the transmitted random sequence, the channel estimation could converge faster [66].

After retrieving the header time T_H needed for CMA convergence, it is possible to estimate the slot duration required to transmit a given number of byte N_B using both DP-QPSK and DP-16QAM. The slot duration T_s given by the formula 3.IV.1 is plotted in Fig.4.4.b) for both vectorial format.

$$T_s = T_H + \frac{N_B}{B_R}$$

B_R being the net data rate. T_s 3.IV.1

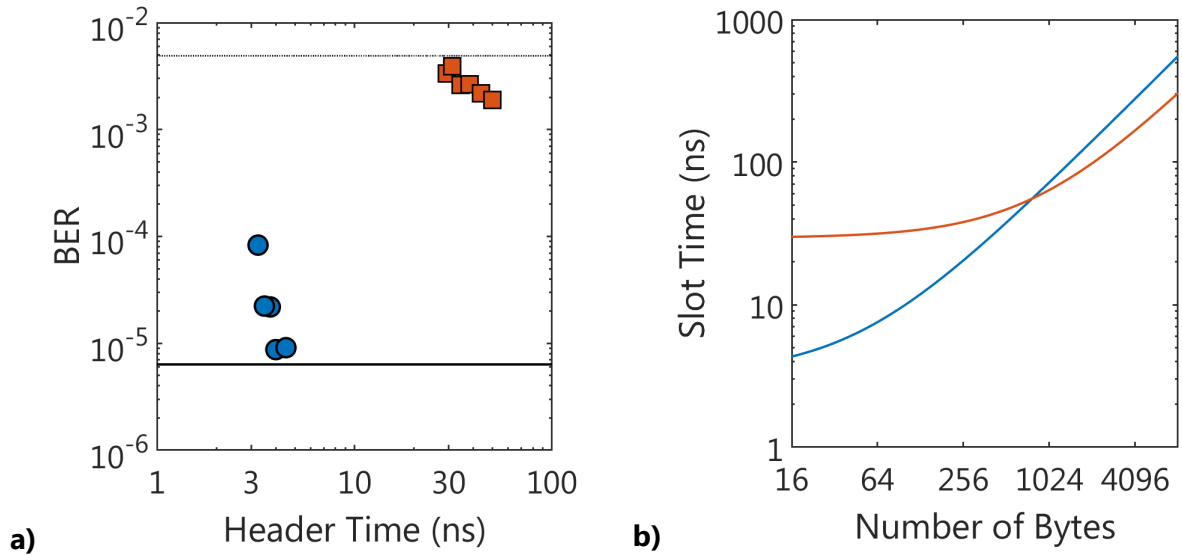


Fig.4.4. a) Measured BER as a function of the header time used for CMA convergence. Blue circles, (resp. orange squares) represent DP-QPSK (resp. DP-16QAM). The dotted line corresponds to the 7% FEC limit while the plain line shows BER measurement limit. b) Required slot duration to transmit a given number of bytes. Blue (resp. orange) corresponds to DP-QPSK (resp. DP-16QAM).

Because the header time required for CMA convergence is much shorter in DP-QPSK, it is the preferred modulation format to transmit small packets. Nonetheless DP-16QAM allows for higher data rate meaning that is more efficient to use to transmit longer packets. Considering a header time of 3.2 ns and 29.4 ns in DP-QPSK and DP-16QAM, we have shown that DP-QPSK allows for shorter slots if the number of byte to transmit is lower than 790 bytes, while DP-16QAM would be more efficient for packet size exceeding 790 bytes.

V. Conclusion

In this chapter we have presented a new type of fast tunable lasers. This laser can cover the entire C-band with a fiber coupled power over 1 mW. Improvement of the laser output power up to 10 mW should be feasible in a near future using more optimized III-V layer stack. We have also shown that the laser linewidth is between 300 kHz and 500 kHz across its operating bandwidth. This relatively high value of linewidth was shown to be compliant with coherent communication up to 32QAM at 32 Gbaud. For the first time to our knowledge we have precisely characterized laser switching dynamics in the nanosecond timescale and have shown that the FTL switching time comprising wavelength stabilization was below 4 ns. However, the laser tuning relies on carrier injection within a silicon PIN junction, and slow thermal chirp was shown to be detrimental to the laser functioning. We believe that the laser long term stabilization can be achieved in the next generation using an additional thermal section and a wavelength locker.

Hence future work should focus on the improvement of the laser output power, linewidth and thermal stabilization. Laser output power could be improved using a III-V epitaxy containing fewer quantum wells (as a high value of 8 quantum wells was used in this work). Then the laser linewidth can be easily narrowed using a dual ring mirror with higher F -factor, meaning that the ring to bus waveguide coupling needs to be decreased down to $\sim 10\%$. Finally more engineering work needs to be performed to stabilize the laser using counter heating.

In this chapter we have investigated phase noise properties of extended cavity laser, but we have not thoroughly studied the effect of carriers on the laser linewidth. Indeed free carriers within ring resonators induce a negative phase/amplitude coupling which might act as another negative feedback loop to reduce the laser random phase fluctuations. A model based on the expansion of the resonant condition can still be used to study this phenomenon and an additional equation corresponding to silicon carriers dynamics should also be added in the laser equivalent rate equations. This model could also incorporate two photons absorption within silicon waveguides.

In addition more theoretical work needs to be done to properly understand fast laser switching. First a two mode rate equation model could be used to link laser switching time with the filter tuning speed. Then a more complex travelling wave model should be used to properly analyze the laser stabilization time after switching. The author believes that laser stabilization time will be greatly affected by the frequency detuning between the lasing mode emitted after switching and the selective mirror resonance. The travelling wave model would also be helpful to study the FTL random phase fluctuations in switching mode.

VI. References

- [1] G. I. Papadimitriou, C. Papazoglou, and A. S. Pomportsis, "Optical switching: Switch fabrics, techniques, and architectures," *J. Light. Technol.*, vol. 21, no. 2, pp. 384–405, 2003.
- [2] P. Bakopoulos *et al.*, "NEPHELE: An End-To-End Scalable and Dynamically Reconfigurable Optical Architecture for Application-Aware SDN Cloud Data Centers," *IEEE Commun. Mag.*, vol. 56, no. 2, pp. 178–188, 2018.
- [3] N. Benzaoui *et al.*, "CBOSS: Bringing traffic engineering inside data center networks," *J. Opt. Commun. Netw.*, vol. 10, no. 7, pp. B117–B125, 2018.
- [4] Y. Pointurier, N. Benzaoui, W. Lautenschlaeger, and L. Dembeck, "End-to-end time-sensitive optical networking: Challenges and solutions," *J. Light. Technol.*, vol. 37, no. 7, pp. 1732–1741, 2019.
- [5] T. Verolet *et al.*, "Hybrid III-V on Silicon Fast and Widely Tunable Laser Based on Rings Resonators with PIN Junctions," *Asia Commun. Photonics Conf. ACP*, vol. 2018-Octob, no. 644453, pp. 2018–2020, 2018.
- [6] H. J. S. Dorren, E. H. M. Wittebol, R. De Kluijver, G. Guelbenzu De Villota, P. Duan, and O. Raz, "Challenges for optically enabled high-radix switches for data center networks," *J. Light. Technol.*, vol. 33, no. 5, pp. 1117–1125, 2015.
- [7] H. Ballani *et al.*, "Bridging the last mile for optical switching in data centers," *2018 Opt. Fiber Commun. Conf. Expo. OFC 2018 - Proc.*, pp. 1–3, 2018.
- [8] Q. Zhang, V. Liu, H. Zeng, and A. Krishnamurthy, "High-resolution measurement of data center microbursts," *Proc. ACM SIGCOMM Internet Meas. Conf. IMC*, vol. Part F1319, pp. 78–85, 2017.
- [9] K. Clark *et al.*, "Sub-Nanosecond Clock and Data Recovery in an Optically-Switched Data Centre Network," *Eur. Conf. Opt. Commun. ECOC*, vol. 2018-Septe, no. 1, pp. 9–11, 2018.
- [10] G. Souhaité *et al.*, "wavelength laser for DWDM applications," pp. 16–17.
- [11] J. E. Simsarian, M. C. Larson, H. E. Garrett, H. Xu, and T. A. Strand, "Less than 5-ns wavelength switching with an SG-DBR laser," *IEEE Photonics Technol. Lett.*, vol. 18, no. 4, pp. 565–567, 2006.
- [12] B. R. Bennett, R. A. Soref, and J. A. Del Alamo, "Carrier-Induced Change in Refractive Index of InP, GaAs, and InGaAsP," *IEEE J. Quantum Electron.*, vol. 26, no. 1, pp. 113–122, 1990.
- [13] F. Smyth, E. Connolly, B. Roycroft, B. Corbett, P. Lambkin, and L. P. Barry, "Fast wavelength switching lasers using two-section slotted Fabry-Pérot structures," *IEEE Photonics Technol. Lett.*, vol. 18, no. 20, pp. 2105–2107, 2006.
- [14] S. Dhoore, A. Rahim, G. Roelkens, and G. Morthier, "125 Gbit/s discretely tunable InP-on-silicon filtered feedback laser with sub-nanosecond wavelength switching times," *Opt. Express*, vol. 26, no. 7, p. 8059, 2018.
- [15] Y. Ueda, T. Shindo, S. Kanazawa, N. Fujiwara, and M. Ishikawa, "ELECTRO-OPTICALLY TUNABLE LASER WITH < 10-mW TUNING POWER DISSIPATION AND HIGH- SPEED Π -SWITCHING FOR COHERENT NETWORK," *EcoC*, pp. 1–4, 2019.
- [16] G. De Valicourt *et al.*, "Dual hybrid silicon-photonic laser with fast wavelength tuning,"

- 2016 *Opt. Fiber Commun. Conf. Exhib. OFC 2016*, pp. 1–3, 2016.
- [17] S. Keyvaninia *et al.*, "Heterogeneously integrated III-V/silicon distributed feedback lasers," *Opt. Lett.*, vol. 38, no. 24, p. 5434, 2013.
 - [18] J. C. Hulme, J. K. Doylend, and J. E. Bowers, "Widely tunable Vernier ring laser on hybrid silicon," *Opt. Express*, vol. 21, no. 17, p. 19718, 2013.
 - [19] G. H. Duan *et al.*, "Hybrid III - V on silicon lasers for photonic integrated circuits on silicon," *IEEE J. Sel. Top. Quantum Electron.*, vol. 20, no. 4, 2014.
 - [20] T. Kita, K. Nemoto, and H. Yamada, "Silicon Photonic Wavelength-Tunable Laser Diode with Asymmetric Mach-Zehnder Interferometer," *IEEE J. Sel. Top. Quantum Electron.*, vol. 20, no. 4, 2014.
 - [21] T. Komljenovic and J. E. Bowers, "Monolithically Integrated High- Q Rings for Narrow Linewidth Widely Tunable Lasers," *IEEE J. Quantum Electron.*, vol. 51, no. 11, pp. 1–10, 2015.
 - [22] H. Elfaiki, K. Hassan, G.-H. Duan, and C. Jany, "Ultra Wide Hybrid III-V On Silicon Tunable Laser," *Proceeding ECOC*, no. 1, pp. 3–5, 2018.
 - [23] H. Elfaiki, "These_Hajar.pdf."
 - [24] A. Gallet, "Hybrid III-V on silicon lasers for optical communications," *Manuscrit de these*. 2019.
 - [25] E. Kleijn, M. K. Smit, and X. J. M. Leijtens, "Multimode interference reflectors: A new class of components for photonic integrated circuits," *J. Light. Technol.*, vol. 31, no. 18, pp. 3055–3063, 2013.
 - [26] A. Yariv, "Coupled-Mode theory for guided-wave optics," *IEEE J. Quantum Electron.*, vol. 9, no. 9, pp. 919–933, 1973.
 - [27] G. H. Duan *et al.*, "Hybrid III-V/silicon photonic integrated circuits for optical communication applications," *IEEE J. Sel. Top. Quantum Electron.*, vol. 2016-Novem, pp. 50–51, 2016.
 - [28] R. Soref and B. R. Bennett, "Electro-optical effects in Silicon," *J. quantum Electron.*, vol. 74, no. 1, pp. 305–307, 1987.
 - [29] W. M. Green, M. J. Rooks, L. Sekaric, and Y. A. Vlasov, "Ultra-compact, low RF power, 10 Gb/s silicon Mach-Zehnder modulator," *Opt. Express*, vol. 15, no. 25, p. 17106, 2007.
 - [30] A. Liu *et al.*, "High-speed optical modulation based on carrier depletion in a silicon waveguide," *Opt. Express*, vol. 15, no. 2, p. 660, 2007.
 - [31] K. Debnath *et al.*, "All-silicon carrier accumulation modulator based on a lateral metal-oxide-semiconductor capacitor," *Photonics Res.*, vol. 6, no. 5, p. 373, 2018.
 - [32] R. Wu, C.-H. Chen, J.-M. Fedeli, M. Fournier, K.-T. Cheng, and R. G. Beausoleil, "Compact models for carrier-injection silicon microring modulators," *Opt. Express*, vol. 23, no. 12, p. 15545, 2015.
 - [33] A. Shastri *et al.*, "Ultra-low-power single-polarization QAM-16 generation without DAC using a CMOS photonics based segmented modulator," *J. Light. Technol.*, vol. 33, no. 6, pp. 1255–1260, 2015.
 - [34] H. Debregeas *et al.*, "TWDM-PON Burst Mode Lasers with Reduced Thermal Frequency Shift," *J. Light. Technol.*, vol. 36, no. 1, pp. 128–134, 2018.
 - [35] S. Manipatruni, K. Preston, L. Chen, and M. Lipson, "Ultra-low voltage, ultra-small mode volume silicon microring modulator," *Opt. Express*, vol. 18, no. 17, p. 18235, 2010.
 - [36] J. Müller *et al.*, "Optical Peaking Enhancement in High-Speed Ring Modulators," *Sci.*

- Rep.*, vol. 4, 2014.
- [37] O. Dubray *et al.*, "Electro-optical ring modulator: An ultracompact model for the comparison and optimization of p-n, p-i-n, and capacitive junction," *IEEE J. Sel. Top. Quantum Electron.*, vol. 22, no. 6, 2016.
 - [38] S. Karimelahi and A. Sheikholeslami, "Ring modulator small-signal response analysis based on pole-zero representation," *Opt. Express*, vol. 24, no. 7, p. 7585, 2016.
 - [39] Q. Xu, S. Manipatruni, B. Schmidt, J. Shakya, and M. Lipson, "12.5 Gbit/s silicon micro-ring silicon modulators," *Opt. Express*, vol. 15, no. 2, pp. 430–436, 2007.
 - [40] G. Li *et al.*, "Ring resonator modulators in silicon for interchip photonic links," *IEEE J. Sel. Top. Quantum Electron.*, vol. 19, no. 6, 2013.
 - [41] R. A. Saunders, J. P. King, and I. Hardcastle, "z -5 10," vol. 30, no. 76, pp. 1336–1338, 1994.
 - [42] J. G. Provost and F. Grillot, "Measuring the chirp and the linewidth enhancement factor of optoelectronic devices with a Mach-Zehnder interferometer," *IEEE Photonics J.*, vol. 3, no. 3, pp. 476–488, 2011.
 - [43] B. C. Thomsen, R. Maher, D. S. Millar, and S. J. Savory, "Burst mode receiver for 112 Gb/s DP-QPSK with Parallel DSP," *Opt. Express*, vol. 19, no. 26, pp. 770–776, 2011.
 - [44] F. Liu, Y. Lin, A. J. Walsh, Y. Yu, and L. P. Barry, "Doubly differential star-16-QAM for fast wavelength switching coherent optical packet transceiver," *Opt. Express*, vol. 26, no. 7, p. 8201, 2018.
 - [45] E. Patzak, A. Sugimura, S. Saito, T. Mukai, and H. Olesen, "Semiconductor laser linewidth in optical feedback configurations," *Electron. Lett.*, vol. 19, no. 24, pp. 1026–1027, 1983.
 - [46] K. J. Vahala and A. Yariv, "Detuned loading in coupled cavity semiconductor lasers - Effect on quantum noise and dynamics," *Appl. Phys. Lett.*, vol. 45, no. 5, 1984.
 - [47] R. F. Kazarinov and C. H. Henry, "The Relation of Line Narrowing and Chirp Reduction Resulting from the Coupling of a Semiconductor Laser to a Passive Resonator," *IEEE J. Quantum Electron.*, vol. 23, no. 9, pp. 1401–1409, 1987.
 - [48] P. Gallion and G. Debarge, "Relationship between linewidth and chirp reductions in gain-detuned composite-cavity semiconductor lasers," *Electron. Lett.*, vol. 23, no. 25, pp. 1375–1376, 1987.
 - [49] B. Tromborg, H. Olesen, X. Pan, and S. Saito, "Transmission line description of optical feedback and injection locking for fabry-perot and dfb lasers," *IEEE J. Quantum Electron.*, vol. 23, no. 11, pp. 1875–1889, 1987.
 - [50] G. H. Duan, P. Gallion, and G. Debarge, "Analysis of the Phase-Amplitude Coupling Factor and Spectral Linewidth of Distributed Feedback and Composite-Cavity Semiconductor Lasers," *IEEE J. Quantum Electron.*, vol. 26, no. 1, pp. 32–44, 1990.
 - [51] D. R. Hjelme, A. R. Mickelson, and R. G. Beausoleil, "Semiconductor Laser Stabilization By External Optical Feedback," *IEEE J. Quantum Electron.*, vol. 27, no. 3, pp. 352–372, 1991.
 - [52] K. Kurokawa, "Some Basic Characteristics of Broadband Negative Resistance Oscillator Circuits," *Bell Syst. Tech. J.*, vol. 48, no. 6, pp. 1937–1955, 1969.
 - [53] M. A. Tran, D. Huang, T. Komljenovic, J. Peters, A. Malik, and J. E. Bowers, "Ultra-low-loss silicon waveguides for heterogeneously integrated silicon/III-V photonics," *Appl. Sci.*, vol. 8, no. 7, 2018.
 - [54] G. P. Agrawal and C. H. Henry, "Modulation Performance of a Semiconductor Laser

- Coupled to an External High-Q Resonator," *IEEE J. Quantum Electron.*, vol. 24, no. 2, pp. 134–142, 1988.
- [55] G. P. Agrawal and N. Dutta, *Semiconductor Lasers*, 2nd Editio. Kluwer Academic Publishers, 1993.
 - [56] S. Ogita, Y. Kotaki, K. Kihara, M. Matsuda, H. Ishikawa, and H. Imai, "Dependence of Spectral Linewidth on Cavity Length and Coupling Coefficient in DFB Laser," *Electron. Lett.*, vol. 24, no. 10, pp. 613–614, 1988.
 - [57] J. E. Simsarian, J. Gripp, A. H. Gnauck, G. Raybon, and P. J. Winzer, "Fast-tuning 224-Gb/s intradyne receiver for optical packet networks," *Opt. InfoBase Conf. Pap.*, pp. 1–3, 2010.
 - [58] K. Kikuchi, "Performance analyses of polarization demultiplexing based on constant-modulus algorithm in digital coherent optical receivers," *Opt. Express*, vol. 19, no. 10, p. 9868, 2011.
 - [59] K. Shi *et al.*, "Fast switching slotted Fabry-Perot laser for phase modulated transmission systems," *J. Light. Technol.*, vol. 28, no. 23, pp. 3409–3416, 2010.
 - [60] J. E. Simsarian, J. Gripp, S. Chandrasekhar, and P. Mitchell, "Fast-tuning coherent burst-mode receiver for metropolitan networks," *IEEE Photonics Technol. Lett.*, vol. 26, no. 8, pp. 813–816, 2014.
 - [61] A. J. Walsh, J. Mountjoy, H. Shams, A. Fagan, A. D. Ellis, and L. P. Barry, "Highly Robust Dual-Polarization Doubly Differential PSK Coherent Optical Packet Receiver for Energy Efficient Reconfigurable Networks," *J. Light. Technol.*, vol. 33, no. 24, pp. 5218–5226, 2015.
 - [62] R. Maher, D. Lavery, M. Paskov, P. Bayvel, S. J. Savory, and B. C. Thomsen, "Fast wavelength switching 6 GBd dual polarization 16QAM digital coherent burst mode receiver," *IEEE Photonics Technol. Lett.*, vol. 26, no. 3, pp. 297–300, 2014.
 - [63] A. M. Viterbi, "Nonlinear Estimation of PSK-Modulated Carrier Phase with Application to Burst Digital Transmission," *IEEE Trans. Inf. Theory*, vol. 29, no. 4, pp. 543–551, 1983.
 - [64] T. Pfau, S. Hoffmann, and R. Noé, "Hardware-efficient coherent digital receiver concept with feedforward carrier recovery for M-QAM constellations," *J. Light. Technol.*, vol. 27, no. 8, pp. 989–999, 2009.
 - [65] J. M. Estarán *et al.*, "140/180/204-Gbaud OOK Transceiver for Inter- and Intra-Data Center Connectivity," *J. Light. Technol.*, vol. 37, no. 1, pp. 178–187, 2019.
 - [66] F. Vacondio *et al.*, "Real-Time implementation of packet-by-packet polarization demultiplexing in a 28 Gb/s burst mode coherent receiver," *Opt. InfoBase Conf. Pap.*, vol. 1, no. d, pp. 45–47, 2012.

Chapter 4

Mode Locked Laser Phase Noise Reduction

| | |
|--|-----|
| Chapter 4 Mode Locked Laser Phase Noise Reduction..... | 112 |
| I. Introduction | 114 |
| I.1. Comb generation methods | 114 |
| I.2. MLL structure and characteristics..... | 116 |
| I.3. Experimental setup for feedback..... | 118 |
| I.4. Feedback strength evaluation | 119 |
| II. SS-QDash-MLL Feedback Regimes | 121 |
| II.1. Reported feedback regimes in 2S-QDot-MLLs..... | 121 |
| II.2. Coherence collapse regime | 124 |
| II.3. Detuned feedback regime | 125 |
| II.4. Coherent feedback regime | 126 |
| II.5. Weak feedback regime..... | 130 |
| II.6. General summary..... | 131 |
| III. Noise properties under Resonant Feedback..... | 132 |
| III.1. Reported RF line narrowing in MLL..... | 132 |
| III.2. RF Linewidth Narrowing in SS-QDash-MLL..... | 133 |
| III.3. Optical Linewidth Narrowing | 134 |
| III.4. Conclusion..... | 139 |
| IV. Transmission Experiments Results | 140 |
| IV.1. Reported transmission results using a MLL | 140 |
| IV.2. Coherent testbed description..... | 142 |
| IV.3. Experimental Results | 143 |
| V. Conclusion | 147 |
| VI. References | 148 |

The tremendously growing demand for cloud computing is pushing datacenter companies to provide access to both massive amounts of data and draconian computing resources. Hence, mega-data centers with over hundreds of thousands of servers are emerging. Not only supplying the electrical power to the datacenter facilities is a technical challenge, but data center operators are also conscious of the ecological footprint of their facilities and push for new technologies allowing data traffic with lower energy consumption.

In this context, optical frequency comb sources are promising alternatives to single mode laser arrays to provide DWDM channels. Indeed, as comb sources inherently emit equidistant optical lines, the complex control system used to manage independent frequency drift of each laser of the array can be suppressed. Single-section (SS) quantum dash (QDash) mode locked lasers (MLL) are appealing components as they may emit a flat and broadband optical comb with low energy consumption, operational simplicity and large-scale low-cost production possibilities.

As we have already discussed in the introductory chapter, optical coherent communications can achieve both higher data rates at higher spectral efficiency and longer transmission reaches with greater link budget than IMDD format at the cost of complexity and price. Hence, combining the efficiency of coherent communication with the simple comb generation of a MLL can be a promising solution to provide energy saving optical links in the Tbit/s class.

Nonetheless, optical carriers derived from a MLL suffer from a high phase noise, making them impractical for highly efficient coherent communication systems. It has long been reported that optical feedback is a simple method to improve the phase noise properties of single mode lasers. In this chapter we use optical feedback to drastically reduce the phase noise of a SS-QDash-MLL, and we notably show that the optical linewidth of each MLL longitudinal mode can be drastically narrowed leading to great performances of a DWDM link based on a MLL under coherent feedback.

In this chapter, which results are also detailed in [1], we first present the experimental setup and method used to investigate optical feedback in single section MLL diodes. Then, similarly to the five well-known feedback regimes of single mode lasers, different feedback regimes of SS-QDash-MLL are highlighted. It is notably shown that one regime of feedback, referred to as the *coherent* feedback regime leads to enhanced mode locking performances. Then the improved noise properties of the SS-QDash-MLL longitudinal modes are carefully studied. And finally, the use of a MLL under coherent feedback in DWDM coherent system is validated with optical transmission experiments showing remarkable link performances.

I. Introduction

In the introduction part, we will first review several approaches widely used to generate optical combs suitable for optical DWDM communication systems. Then, the single section (SS) quantum dash (QDash) mode locked laser (MLL) used in this thesis chapter will be described, and its spectral characteristics will be investigated. After that, the optical testbed used in the feedback study will be detailed. Finally, we will report on the experimental method used to calibrate feedback parameters.

I.1. Comb generation methods

Optical comb generation has been a major topic since the late 1980's, as comb sources could provide optical solitons which were seen as a promising technology for fibered communication systems [2], [3]. Nowadays, optical combs are rather used to generate DWDM channels in which each comb line is used as an optical carrier (e.g. [4], [5]). Some of the widely used optical comb generation techniques are described in the following and summarized in Table 1.1.

The most straightforward approach to generate an optical comb would be to multiplex emitted signals of numerous single mode lasers (SML) with fixed wavelength spacing [6]. However, this approach requires one optical source per channel, each being independently controlled with a wavelength locking system making the comb source complex to operate. The solution presented in [6] also utilizes optical feedback to improve the phase-noise properties of each laser in the array, and might also act as a control loop stabilizing each emitted optical frequency.

Then, strongly pumped non-linear micro ring resonators have also been widely studied to generate optical combs [7], [8]. This approach can lead to a very broad comb and has been used to set the data rate record using a single optical source [9]. However Kerr comb generation is energy demanding [10], may give rise to large phase noise of each optical line [11], and requires additional comb shaping elements to be used for optical communications [9].

A single mode laser followed by Mach-Zehnder modulators (MZM) can also generate optical frequency combs [12], [13]. This approach may result in a comb with low phase noise in each tone, but requires an electrical synthesizer providing a driving signal at the comb spacing frequency. Moreover, MZMs may be bulky and lossy, complicating the overall comb generation system.

Gain-switched (GS) lasers can provide an optical comb with a relatively narrow bandwidth. However, this compact approach also requires an electrical driving signal and individual comb lines might exhibit a high phase noise [14]. Nonetheless [15] proposes a simple technique based on injection locking to stabilize the comb lines emitted by a GS laser.

Mode Locked Lasers (MLLs) are promising devices to generate a relatively broad and flat optical comb [16]–[18]. They are indeed simple to operate as they require only a single DC bias source in the case of single section (SS) MLLs [19], and are also energy saving as a 80% internal quantum efficiency has been reported for quantum dash (QDash) MLLs [16]. The reported comb bandwidth is in the 11 nm (~ 1.5 THz) range in [16]–[19], meaning that these devices can provide a wider comb envelope than more complex approaches based on laser gain switching or on external modulators. However, each individual mode of a MLL suffers from a large phase and intensity noise [20] making them impractical for spectrally efficient DWDM systems. Methods to reduce the phase noise of MLL modes have been devised such as, an optoelectronic feedback loop [21], a feed forward heterodyne technique [22], or the injection locking of the comb with a low noise master laser [23]. However, these methods are complex to implement in an optical transceiver because of the requirement for optoelectronic conversion or a low noise optical source. Hence, in this thesis chapter we will show that optical feedback is an efficient yet simple method to improve phase-noise properties of a MLL, thus leading to high performance coherent transmission.

| | Laser Array | Kerr Comb | Laser + MZM | GS Laser | MLL |
|-----------------------|---|--|-------------------------------------|--------------------------------|---------------------------------------|
| Comb bandwidth | \propto number of SMLs | C+L bands [7] | 1.6 nm [12] | 2 nm [14] | > 10 nm [16] |
| Grid Spacing | Finely Tunable, wide range | MHz – THz $1/\propto$ resonator size | Limitation : synth. bandwidth | Limitation : Laser response | [1 – 100] GHz $1/\propto$ MLL size |
| Noise Characteristics | \propto SMLs noise characteristics | Function of soliton regime | \propto SML noise characteristics | Poor | Poor |
| System complexity | SMLs + Mux + control system | pump laser + resonator + flattening system | Laser + MZM + synth. + EDFA | Laser + synth. + EDFA | Laser + EDFA (for passively MLL) |
| Power consumption | SMLs efficiency, Mux losses, control system | 3% wall plug efficiency [8] | MZM loss compensation | SML efficiency + synth. | Laser + EDFA |

Table 1.1. Summary of the general performances of optical comb generation techniques.
Color code : Green represents an improvement relative to other comb generation techniques while red is a drawback.

I.2. MLL structure and characteristics

For the last two decades or so, low dimensional QDash nanostructures in III-V semiconductor have attracted a lot of interest from a MLL device perspective [16], [17]. Indeed QDash gain medium exhibits both low amplitude/phase coupling and high gain compression both increasing mode-locking performance [24]. Enhanced third order non-linear effect allows efficient mode-locking in a single section Fabry-Pérot (FP) cavity without resorting to a saturable absorber (SA), leading to optimal laser output power [19]. The description of the laser gain medium has already been reported in [16], [17], and the QDash structure used in this work is similar to the dash in a barrier -DBAR- structure of [17]. It has been shown in [25] that the MLL RF beat linewidth decreases with the number of QDash layers in the stack, owing to a smaller optical confinement factor that reduces the coupling of spontaneous emission with the lasing mode.

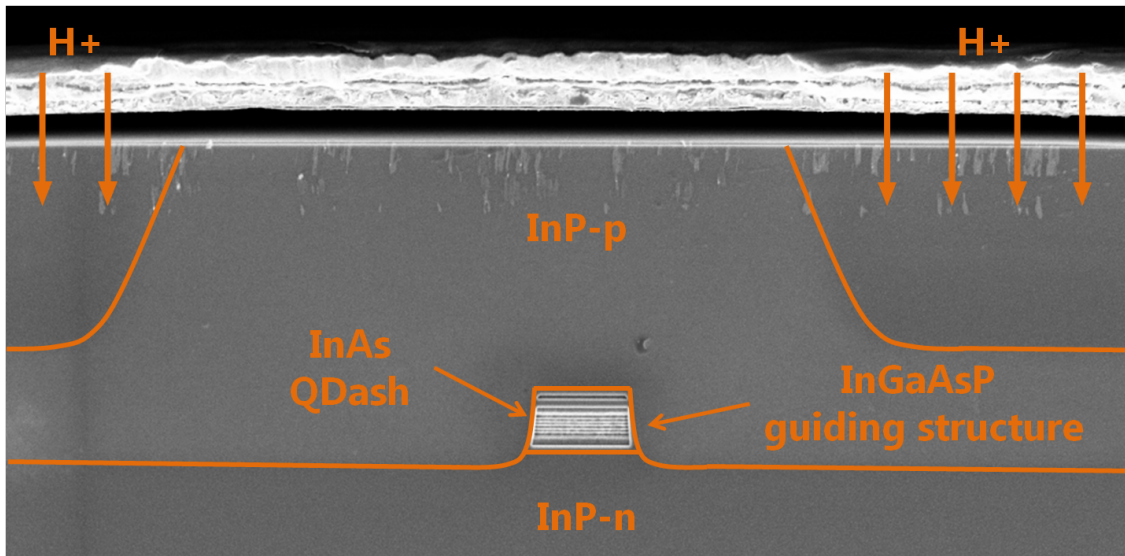


Fig. 1.1. Scanning Electron Microscopy image of a 7 Dash layers MLL.

The retained structure contains only three InAs QDash layers whose emission is within the C-band. A single section buried ridge strip (BRS) guides the single transverse mode within the FP cavity. Fig.1.1 displays the image of a BRS waveguide cross section from scanning electron microscopy (SEM), the layer stack shown in Fig. 1.a) is similar to the one used in our work except that it contains 7 Dash layers. The laser cavity length is chosen to obtain a 32.5 GHz comb line spacing that is suitable to modulate each carrier at around 30 Gbaud. To improve heat dissipation during the experiments, devices are mounted and wire bonded on specific holders.

Typical spectral characteristics of the MLL are presented in Fig.1.2. They are obtained with a bias current of 250 mA, and with the MLL cooled at 25 °C. This operating point will be kept in the entire thesis chapter, and corresponds to a fiber coupled power over 8 mW. The optical spectrum is displayed in Fig 1.2. with the wider line showing the comb envelope. The 3dB

envelope bandwidth is equal to 11.8 nm, corresponding to 46 comb modes spaced by 32.5 GHz. This 3dB bandwidth value is in agreement with previously reported results (e.g. [17], [19]). Then the RF beat note measured using a fast photodiode followed by an electrical spectrum analyzer (ESA) is shown in Fig.1.2.b). The RF peak frequency is around 32.55 GHz, and the signal dynamic (defined as the ratio between the RF peak power and noise floor) is above 60 dB without compression fiber. The beat note linewidth is below 50 kHz, and will be further examined in part III. Finally the relative intensity noise of the entire comb signal is plotted in Fig.12.c), within the frequency range [0, 2 GHz]. The white noise level is around -158 dBc/Hz, while the peak at 200 MHz might be attributed to the MLL relaxation oscillation. Such low value of relaxation oscillation frequency could be attributed to the relatively low value of differential gain provided by the three QDash layer structure, and we note that [26] might also have measured relaxation oscillation frequency in the 100 MHz range using QDash MLLs . Small-signal experimental analysis should be performed to confirm the value of relaxation oscillation frequency.

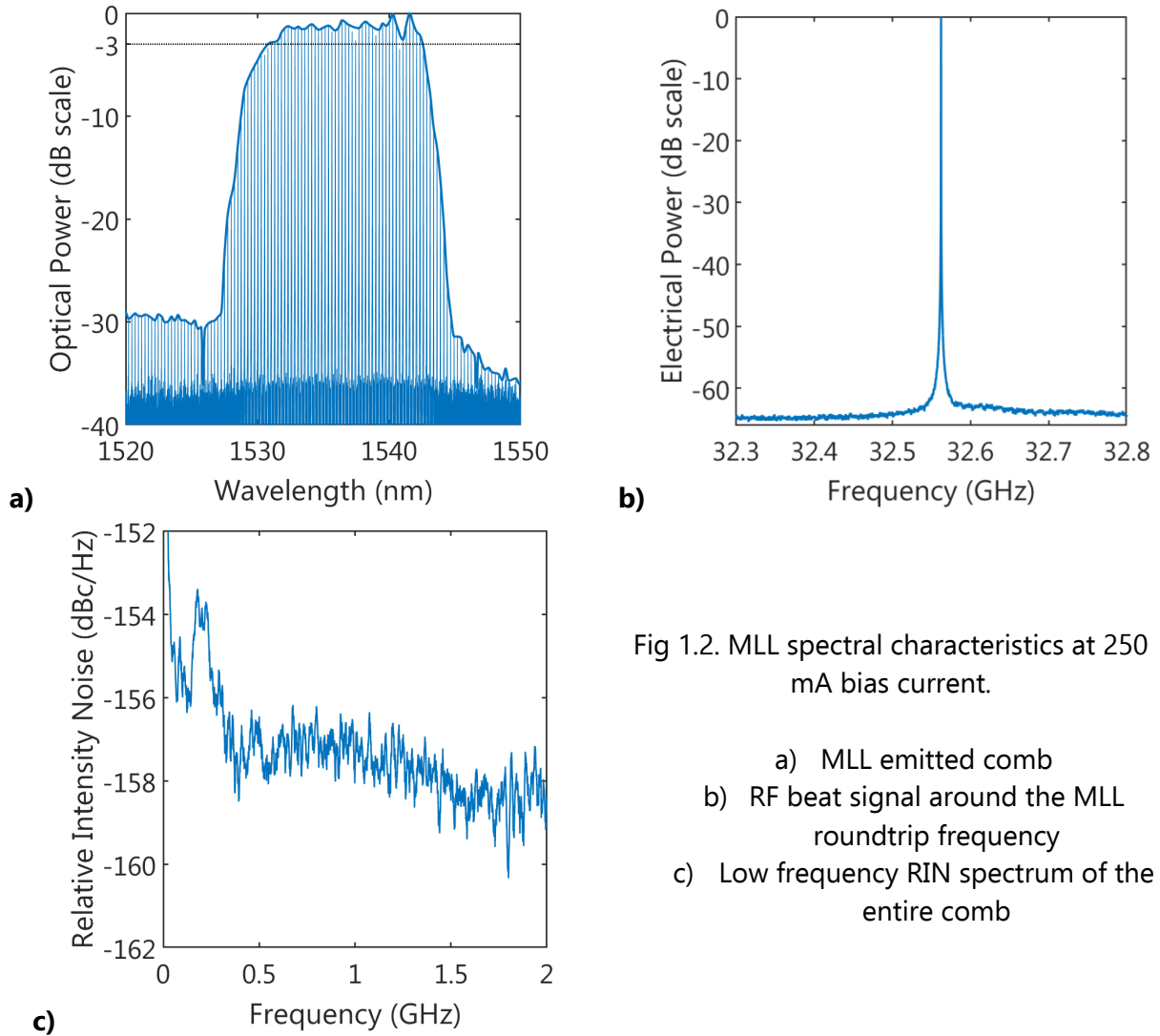


Fig 1.2. MLL spectral characteristics at 250 mA bias current.

- a) MLL emitted comb
- b) RF beat signal around the MLL roundtrip frequency
- c) Low frequency RIN spectrum of the entire comb

I.3. Experimental setup for feedback

The experimental setup used to study feedback effect in SS-QDash-MLL is described in the following, sketched in Fig.1.3 and is based from the work of [27]. First, the SS-Qdash-MLL is mounted and wire bonded on a specific holder, and placed above a Peltier Cell thus allowing to measure feedback effect and MLL noise properties at a stable temperature around 25°C. Then, a low noise current source is used to forward bias the gain medium, in most of the thesis chapter the bias current is kept at 250 mA, ensuring a over 8 mW fiber coupled power. The diverging beam at one end of the cavity is collimated using a spherical lens and directed to a high reflectivity mirror through a free space attenuator. The free space feedback cavity may be of interest comparing to fibered experimental setup used e.g. in [28]–[30], as it eliminates possible polarization rotation and also fiber dispersion in the C-band. However due to the lack of continuous tunable free-space attenuator, phase-shifter and dispersion filter, the study of feedback could only be made as a function of the feedback delay for discrete values of feedback strength. In this thesis chapter, the feedback delay is defined as the signal roundtrip time in the free space cavity, while the feedback strength is defined as the fraction of the power reflected back into the MLL cavity after one round-trip inside the feedback loop to power emitted from the MLL. An anti-reflection coated lensed fiber is used to collect the device emitted signal at the other facet of the MLL cavity, the fiber is directly followed by an isolator ensuring no parasitic reflection from measurement setups.

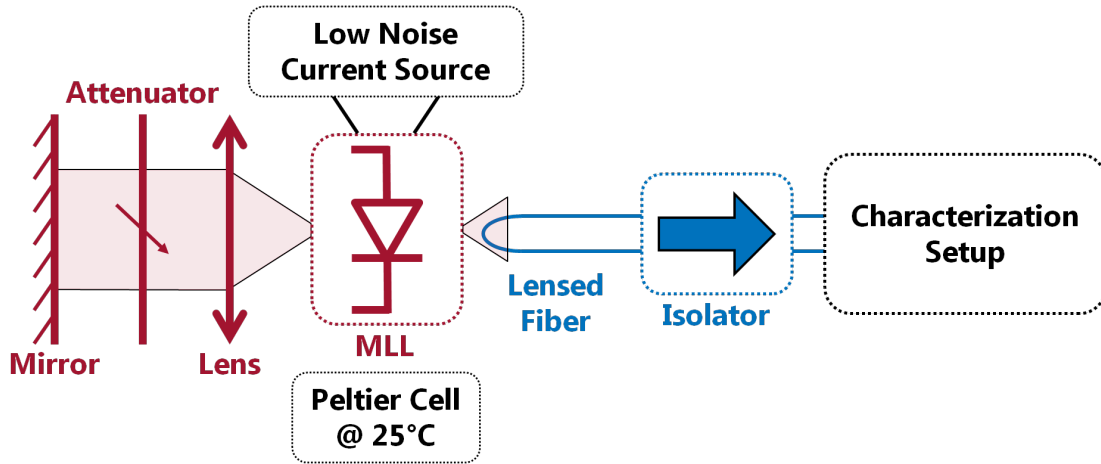


Fig. 1.3. Experimental setup used in this chapter. The characterization setup may consist of an optical (or electrical) spectrum analyzer, or a self-heterodyne testbed used for the noise characterization in part III.

I.4. Feedback strength evaluation

As feedback effects in MLL will be shown to greatly depend on the feedback level, we have developed a simple approach to determine the feedback strength F , which is the fraction of the power reflected back into the MLL after one round-trip inside the feedback loop. First, we assume that F can be written as :

$$F = A^2 R_{HR} C_0^2 \quad (4.I.1)$$

With A the transmission of the free space attenuator, R_{HR} the high reflectivity (HR) mirror reflection coefficient and C_0 the coupling losses between the MLL diverging field and the collimated beam travelling inside the feedback loop. First, the collimating lens, attenuator and HR mirror are modeled as a lumped mirror of field reflectivity $r_{ext} \stackrel{\text{def}}{=} \sqrt{F}$. The feedback cavity is then modeled as in [31] by an equivalent mirror r_{eq} taking into account multiple reflections in the feedback loop written as :

$$r_{eq} = \frac{r + r_{ext} e^{j\omega_m \tau_{ext}}}{1 + r r_{ext} e^{j\omega_m \tau_{ext}}} \quad (4.I.2)$$

with r the MLL facet field reflectivity, τ_{ext} the external cavity round-trip time and ω_m the m^{th} longitudinal mode pulsation. The oscillation conditions of the m^{th} longitudinal modes implies that :

$$r |r_{eq}(\omega_m)| e^{(g-\alpha)L_{act}} = 1 \quad (4.I.3)$$

$$\omega_m \tau_{act} + \arg(r_{eq}(\omega_m)) = m \times 2\pi \quad (4.I.4)$$

with g and α the laser gain and internal loss, L_{act} the MLL length, τ_{act} is the MLL roundtrip time and m an integer. In this chapter thesis g is supposed to be constant inside the MLL comb optical bandwidth.

Then, based on [32], [33], the feedback strength is obtained by studying the variation of MLL threshold current under feedback with respect to its value in the free running operation. Due to feedback the threshold gain is reduced by Δg_{th} deduced from (4.I.3) , then by assuming linear relation between the threshold current and gain variation under feedback, we can write :

$$\Delta I_{th} = \beta_0 \Delta g_{th} = \frac{\beta_0}{L_{act}} \ln \left| \frac{r_{eq}(\omega_m)}{r} \right| \quad (4.I.4)$$

with β_0 the proportionality coefficient relating the threshold current variation ΔI_{th} under feedback and Δg_{th} .

The MLL light-intensity (L-I) characteristics for several attenuation level in the free space cavity are displayed in Fig. 1.4.a). For each feedback level four L-I curves are plotted, each corresponding to a different feedback delay, which was tune over 30 ps (being the MLL roundtrip time). Contrary to a single mode laser [32] it can be noticed that the threshold current is not affected by feedback delay variation. This may be attributed to the fact that the threshold of a Fabry-Pérot laser is obtained once the carrier density reaches a value allowing lasing of at least one longitudinal mode. As the 32 GHz SS-QDash-MLL used in this study emits ~ 40 lasing modes in a 3 dB bandwidth, we may assume that the feedback phase of the first lasing mode $\varphi_0 \stackrel{\text{def}}{=} \omega_m \tau_{ext}$ will be close to $0 \bmod(2\pi)$ for all possible values of τ_{ext} . Indeed the relation $\varphi_0 = 0$ corresponds to constructive interference inside the external cavity and allows for a maximum gain reduction at a given feedback level.

Under this consideration, ΔI_{th} is only function of three unknown parameters : $[C_0, \varphi_0, \beta_0]$. By varying the attenuation within the feedback and measuring threshold currents variations $\Delta I_{th_{meas}}$, $[C_0, \varphi_0, \beta_0]$ can be deduced using the least squares method (4.1.5), and it is found that $C_0 = 1.9 \text{ dB}$, the $\varphi_0 = -0.002 \text{ rad}$, and $\beta_0 = 1.2 \text{ mA.cm}$

$$[C_0, \varphi_0, \beta_0] = \underset{\text{argmin}}{\left([\Delta I_{th_{meas}} - \Delta I_{th}(C, \varphi, \beta)]^2 \right)} \quad (4.1.5)$$

Fig. 2.b) shows the relationship between the feedback strength with respect to the reduction of threshold current. This calibration curve can ultimately be used to evaluate the feedback strength by performing rapid measurement of the threshold current variation due to feedback.

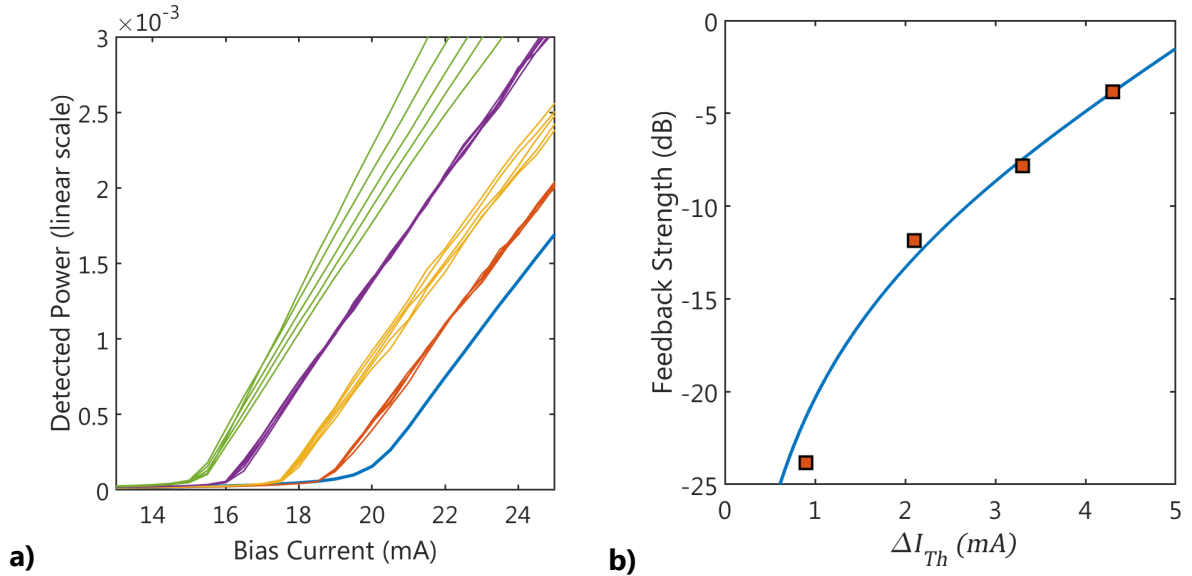


Fig. 1.4. a) L-I characteristics in free running mode (blue), and with 10 dB, 4 dB, 2 dB and 0 dB of single pass attenuation within the free space cavity (resp. in orange, yellow purple and green). b) Relationship between the feedback strength and the threshold current reduction between free running operation and under feedback. Blue line is the fitted curve, orange squares correspond to evaluated feedback strength with 10 dB, 4 dB, 2 dB and 0 dB of single pass attenuation.

II. SS-QDash-MLL Feedback Regimes

In this part, we first review several studies investigating feedback regimes in MLLs. Published works mostly focused on two sections (2S) quantum dot (QDot) MLLs using numerical methods. Then, we will experimentally discern four feedback regimes by observing the MLL optical spectrum envelope, RF beat tone and relative intensity noise for several feedback delays and strengths. Moreover, as the effect of feedback delay has been shown to be periodic in the literature [34], we focus our study in varying the feedback delay in a range corresponding to the MLL roundtrip time. The differences between these regimes and the one highlighted in the literature focusing on 2S-QDot-MLL will be carefully revised. We will notably show that, while most feedback regimes are detrimental to the laser mode locking behavior, one of the regimes, referred to as *coherent* feedback is beneficial for the MLL noise properties. In this part we rigorously point out feedback parameters achieving the *coherent* regime.

II.1. Reported feedback regimes in 2S-QDot-MLLs

Semiconductor lasers feedback regimes were first studied both experimentally [35] and numerically [36], [37] in single mode lasers. While most feedback regimes were shown to be detrimental to laser diode noise properties, it was also reported that one regime referred to as the coherent regime in [38] could narrow the laser optical linewidth. Parameters of the feedback cavity leading to either optical linewidth narrowing or instable operation was extensively studied in the 1980's using rate equations model [38]–[44].

First, [45] have studied feedback regimes in 2S-QDot-MLL using a travelling wave (TW) numerical model. In the case of short feedback, here meaning that the feedback cavity roundtrip time τ_{ext} was in the order of magnitude of the MLL one τ_{act} , [45] identifies three feedback regimes depending on the cavity ratio $r = \tau_{ext}/\tau_{act}$.

- *Resonant* feedback : r is "close" to an integer $n > 1$.
- *Fractional-resonant* feedback : r is "very close" to a rational $q/p > 1$
- *Non-resonant* feedback : r is "far" from a rational $q/p > 1$,

The properties of these feedback regimes are described in Table 2.1, in general, noise properties were enhanced (resp. deteriorate) in the (fractional-)resonant (resp. non-resonant) case. Moreover, in the (fractional-)resonant regime a locking was observed between the emitted pulse train frequency and the feedback cavity roundtrip frequency. The locking range $\delta\tau$ is defined such as $\tau_{ext} \in [\tau_{ext0} \pm \delta\tau/2]$ results in (fractional-)resonant feedback. In [45], $\delta\tau$

was shown to be larger in the resonant case than in the fractional-resonant one. Also considering a 2S-QDot-MLL and using a TW numerical model, the later work of [46] has shown similar feedback properties with however a discrepancy in the case of perfect resonant condition (meaning r is an integer).

Later, [47] numerically studies the effect of short feedback in a generic 2S-MLL using a delay differential equation (DDE) model. This study did not consider phase/amplitude coupling through the Henry's factor. As in [45], they show that the MLL emitted pulse train noise properties could be improved in the case of (fractional-)resonant regime. But, [47] also shows that locking range $\delta\tau$ in which (fractional-)resonant regime occurs drastically narrows as a function of the Farey rank of p/q when τ_{ext} is spanning the MLL roundtrip time. This is in agreement with [45], saying that the locking range was smaller in the fractional-resonant regime than in the resonant one. This study was then completed in [48] focusing on multiple unstable feedback regimes.

Then the effect of feedback in 2S-QDot-MLL was numerically studied in the long feedback case in [49]. The long feedback case is here defined as $\tau_{ext} \gg \tau_{act}$, in [49] they have chosen $\tau_{ext} \sim 250 \times \tau_{act}$. The long feedback regimes were shown to be notably different than the short feedback ones. The feedback regimes are here more related to the feedback strength K rather than the feedback delay. The properties of the long feedback regime from [49] are detailed in Table 2.1. The MLL noise properties were deteriorated for most values of K and enhanced for a certain range of feedback strength. This regime was referred as sufficiently strong feedback and in this case a locking between the MLL emitted pulse train frequency and the external cavity roundtrip frequency would occur on a range $\delta\tau$ in the order of magnitude of τ_{act} . In this regime, the pulse train noise properties were improved for a wide range of feedback delay. The laser was only unstable for r (defined as above) close to a half-integer.

Finally, [34] have experimentally identified feedback regimes in a O-band emitting 2S-QDot-MLL using a $>10\text{m}$ fibered feedback loop. This study focusing on the MLL RF peak power and pulse train timing jitter highlighted five regimes as a function of feedback strength and delay. They discerned feedback regimes similar to the one numerically obtained in [49] and especially demonstrate that only one feedback regime, referred as the resonant regime improves the MLL noise characteristics. We note that this regime was obtained in a locking range greater than 50% of the MLL cavity roundtrip time.

In the next section we thoroughly study feedback regimes of the SS-QDash-MLL using the experimental setup described in I. We will remind differences between the feedback regimes discerned in our work with previously published work.

| | | | |
|----------------------------------|---|---|--|
| Devices and Methods | Two Sections QDot Passive MLL [45] | Two Sections QDot Passive MLL [49] | Two Sections QDot Passive MLL [34] |
| Methods Feedback Type Hypothesis | TW model Short feedback | DDE model Long feedback ? Near Thresholds | Experimental Results Long Feedback Near threshold ? |
| | Non-Resonant General case ($r \in \mathbb{R} \setminus \mathbb{Q}$) <u>Weak feedback</u> : main pulse train followed by a weaker trailing pulse train <u>Moderate feedback</u> : unstable competition between MLL and external cavity | Weak feedback No influences on pulse properties ($\forall r \in \mathbb{R}$) | Weak feedback Deteriorate phase noise properties, Pulses did not seems affected. |
| | | Intermediate feedback Laser is destabilized ($\forall r \in \mathbb{R}$) | Resonant feedback r is close to an integer Feedback level precisely controlled Enhanced noise properties. |
| | | Sufficient feedback Enhanced Noise properties Locking between MLL and external cavity repetition frequency (for all cavity ratio except half integer value). | Moderate Feedback Deteriorated mode locking. ($\forall r \in \mathbb{R}$) |
| | Fractional Resonant $m \times r$ is very close to an integer with $m \in \{2,3,4\}$ <u>Weak feedback</u> : Noisy pulse train <u>Moderate feedback</u> : Stable harmonic mode locking with enhanced noise properties. | | Strong Feedback Chaotic behavior. RF spectrum being unstable. ($\forall r \in \mathbb{R}$) |
| | Resonant r is close to an integer n $r \neq n$ Pulse train with enhanced noise properties. (Stable on a wide range of feedback level) . If $r = n$, noise properties are deteriorated. | | Very Strong feedback Low RF peak power, strong background noise in the temporal trace. High RF phase noise ($\forall r \in \mathbb{R}$) |

Table 2.1. Major works highlighting feedback regimes of 2S-QDot-MLLs

II.2. Coherence collapse regime

The first SS-QDash-MLL feedback regime is obtained when strong feedback is applied on the MLL. For a feedback cavity length around 70 cm, this regime is obtained with feedback strength evaluated over -13 dB. Measured optical envelope and RF beating signal are plotted without and with feedback in Fig.2.1.a) and b). In this regime the comb envelope 3dB bandwidth widens up to 14.2 nm. Moreover, each longitudinal mode linewidth drastically broadens over 12.5 GHz (not shown here). In fact, spectral measurements made using a 0.1 nm OSA of single longitudinal modes reveal optical linewidths wider than the OSA resolution. In this feedback regime, Fig.2.1.b) shows that the MLL beat note close to 32.5 GHz has disappeared in favor of a RF micro comb centered at the MLL repetition rate and which spacing corresponds to the feedback cavity roundtrip frequency (206 MHz). Fig.2.1.c) displays a zoom of the RF trace in the vicinity of the MLL roundtrip frequency showing that the harmonics spaced by the feedback loop roundtrip frequency are relatively broad (tens of MHz 3dB bandwidth). Still in this regime, the RF signal between 0 and 10 GHz also consist of harmonics spaced by the feedback cavity roundtrip frequency. This is further analyze in Fig.2.1.d) showing the MLL RIN between 0 and 5 GHz. In this regime we can see that the RIN floor is over 27 dB higher relatively to the non feedback case.

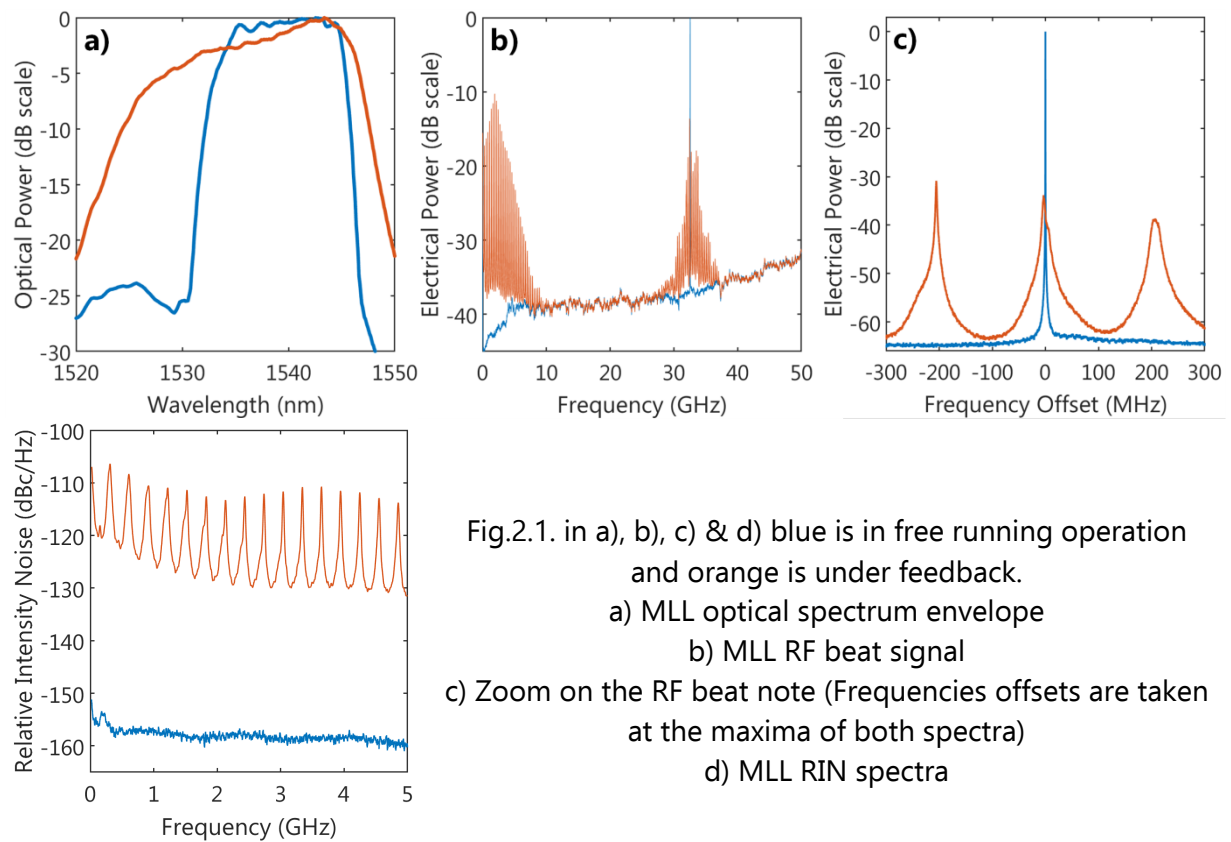


Fig.2.1. in a), b), c) & d) blue is in free running operation and orange is under feedback.
 a) MLL optical spectrum envelope
 b) MLL RF beat signal
 c) Zoom on the RF beat note (Frequencies offsets are taken at the maxima of both spectra)
 d) MLL RIN spectra

This regime shares similarities with the coherence collapse regime in single mode lasers [50], [51], such as very broad optical linewidths and high RIN values in the low frequency range. Hence we will refer it as the coherence collapse (CC) regime, and might be similar to the feedback regime "2" of [34]. In the CC regime varying the feedback strength does not seem to affect the optical comb bandwidth or RF spectrum. However, varying the feedback delay τ_{ext} over $\delta\tau$ spanning the MLL roundtrip time shifts the RF micro-comb harmonics frequency. This is similar to the physical effect observed in the case of resonant feedback and referred as frequency pulling in [34]. This is due to the fact that the RF harmonics appears at frequencies $f_m = m/\tau_{ext}$. Frequency pulling will be more investigated in the case of resonant feedback in II.5.b).

II.3. Detuned feedback regime

Another regime is observed when both the feedback strength is reduced below -13 dB (corresponding to the onset for CC regime) and the external cavity roundtrip time τ_{ext} is not adjusted to a multiple of the MLL one. Moreover, this regime is obtained only if the feedback strength is kept above -29 dB.

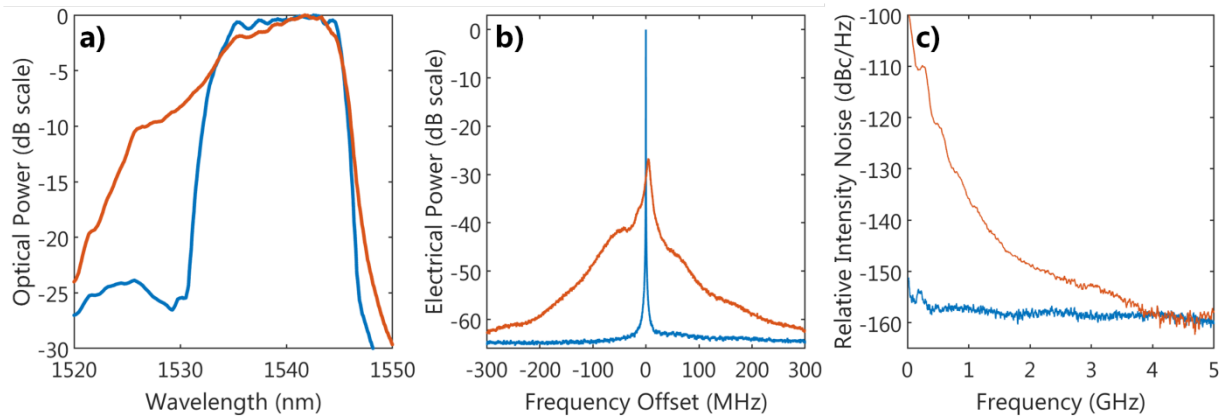


Fig.2.2. in a), b) & c) blue is in free running operation and orange is under feedback.

a) MLL optical spectrum envelope

b) MLL RF beat signal

c) MLL RIN spectra

In this case as shown in Fig.2.2.a) the MLL emitted comb 3dB bandwidth is similar to the case without feedback. However, the optical power of the tones at shorter wavelengths increases relatively to the free running operation. Indeed in a non-resonant regime optical feedback may affect each MLL longitudinal mode with a different phase. Therefore, the threshold gain of all comb modes may be differently altered which could lead to a comb envelope modification. The fact that the envelope modification is only happening in the blue

side of the comb is still under investigation. In this regime, the coherence collapse of a single optical mode is not noticeable by observing them at the OSA as in the procedure of [51]. In the electrical domain, the MLL emitted harmonic widen to tens of MHz (Fig.2.2.b)) showing that this feedback regime is also detrimental to mode locking effect. Fig.2.2.c) compares the measured RIN in free running operation and in this feedback regime. As we can see, the MLL low frequency RIN drastically increases in this feedback regime. The RIN penalty at 100 MHz is over 40 dB. In this regime, varying the feedback strength does not seem to affect neither the optical comb envelope nor the RF beat spectrum. However, when the external cavity length is finely tuned in an interval smaller than the MLL roundtrip time, the peak frequency of the RF beat signal drifts. This frequency pulling will be discussed in II.5.b). To conclude, we refer to this feedback regime as the detuned feedback regime. In [34] this regime and the later discussed "weak feedback" have been considered as a similar feedback regime and have been labeled "5".

II.4. Coherent feedback regime

II.4.a. Spectral characteristics

In this regime the feedback level is kept similar to the detuned feedback case, i.e. between -27 dB and -14 dB while the external cavity roundtrip time is set close to a multiple of the MLL one to achieve resonance between the MLL and feedback cavity. The optical comb envelope measured under these conditions is shown in Fig.2.3.a), where its 3dB bandwidth is identical to the non-feedback case. The envelope is also shifted by ~ 1.2 nm to longer wavelength. This red-shift arises from a slight reduction of laser mirror losses under feedback, which also decreases threshold carrier density, thus reducing the gain peak energy of the QDash gain medium.

Then by studying the electrical spectrum in this feedback regime (Fig.2.3.b)) we notice that the RF beat note exhibits a higher power relatively to the free running operation. Depending on the feedback strength a power increase up to 10 dB can be measured. This phenomenon was also experimentally reported in [34] when the fibered feedback loop optical length was adjusted to a multiple of the MLL one. In this regime a RF linewidth narrowing is also noticeable, revealing the beneficial effect of feedback on the MLL noise properties. The MLL emitted signal phase noise reduction will be carefully examined in part III.

Then, in this regime the low frequency RIN seems 2dB lower than in the non feedback case as shown in Fig.2.3.c). We are not sure whether this phenomenon is a measurement calibration or is related to the output power of the MLL being slightly higher in this feedback

regime or would be linked to another phenomenon. We can however see a narrow spike which appears at the feedback roundtrip frequency. Moreover the RIN increase at $\sim 200\text{MHz}$ in the free running operation is not noticeable anymore in this feedback regime. If we consider that this RIN increase is related to the relaxation oscillation, optical feedback may lead to a reduced relaxation oscillation frequency [52], which could explain its disappearing. This feedback regime which seems beneficial to mode locking will be referred to as coherent feedback. We will further examine the feedback parameters leading to coherent feedback in II.5.b while the phase noise properties of this regime will be studied in part III.

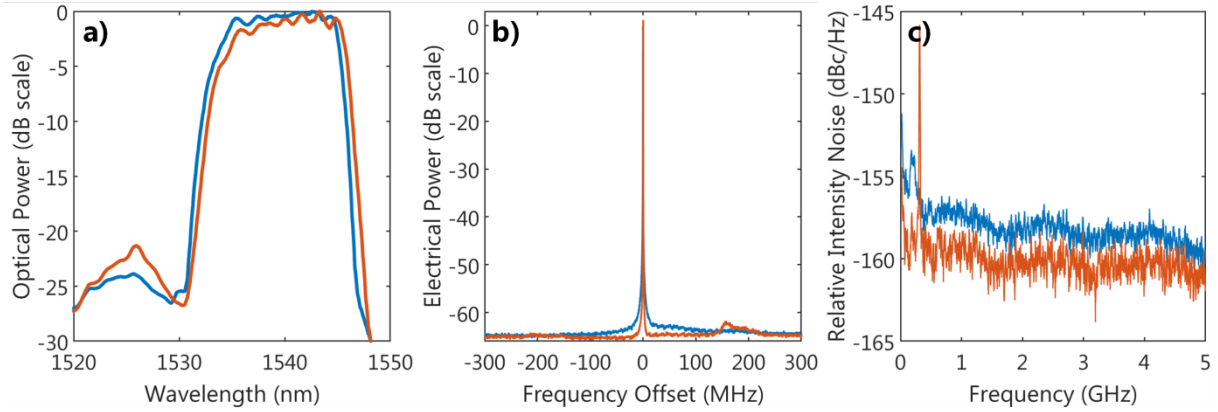


Fig.2.3. in a), b) & c) blue is in free running operation and orange is under feedback.

- a) MLL optical envelope
- b) MLL RF beat signal
- c) MLL RIN spectra

II.4.b. Interval for coherent feedback

In order to study the external cavity parameters leading to coherent feedback we first fix the feedback strength close to -18 dB and we adjust the feedback roundtrip time close to a multiple of the MLL one. Indeed the coherent regime is only obtained in a well-defined range of feedback delay in which the MLL RF beat note is locked onto the external feedback cavity. In these experiments, the feedback cavity length is first set at around 60 cm. Fig.2.4 shows a waterfall plot of the MLL RF beat note for small variations of the free space cavity length achieved through fine tuning of the mirror position. In Fig.2.4. the axis labeled δL represents the feedback cavity length variation in the vicinity of the resonant condition, and $\delta L = 0 \mu\text{m}$ was roughly taken at the center of the interval resulting in the coherent regime. δf corresponds to the electrical frequency offset by the value taken at the peak of the RF spectrum measured for $\delta L = 0 \mu\text{m}$. In the P_{RF} axis, spectra are offset by the maximum electrical power value measured in all traces.

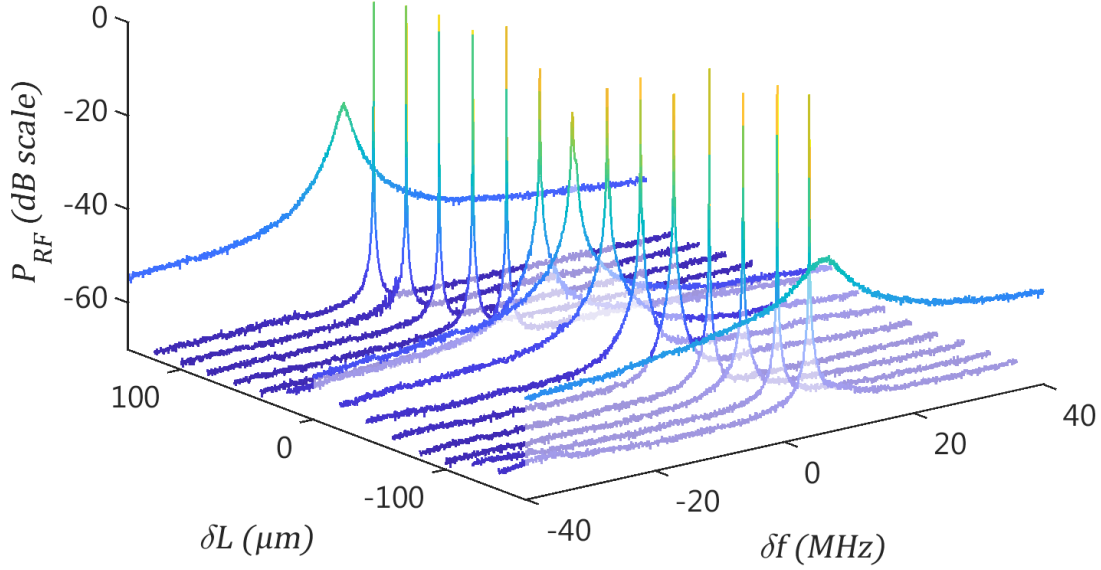


Fig.2.4. waterfall plot of the RF beat spectra for varying mirror positions.

This waterfall plot shows that coherent feedback is obtained for free space cavity length varying across $260 \mu m$ when the external cavity length is around 60 cm , indeed the RF signal drastically broadens for $|\delta L| > 130 \mu m$. This is equivalent to say, that coherent feedback can be achieved in a range of feedback roundtrip time $\Delta\tau$ around 1.7 ps while the overall feedback delay is around 4 ns . As the MLL roundtrip time τ_{act} is close to 30 ps , this means that the regime of coherent feedback is obtained for an interval $\delta\tau$ being 18 times smaller than τ_{act} in this particular condition. We will furthermore study which parameters can increase the range of $\delta\tau$ resulting in coherent feedback.

In the range of δL resulting in coherent feedback we notice that the RF beat note peak power (resp. linewidth) decreases (resp. widens) when δL approaches 0. This trend was measured to be reproducible and appeared for all tested lengths of the free space cavity ($\sim 40 \text{ cm}$, $\sim 60 \text{ cm}$, $\sim 120 \text{ cm}$). The drop of RF peak power can be better evaluated in the orange curve of Fig.2.5.a). This phenomenon is still under investigation, it may be linked to the noise increase simulated at the exact resonant condition in [45]. Another hypothesis would be to assume that a frequency detuning between the MLL RF beat note and the feedback cavity m^{th} mode is required to achieve narrowest RF linewidth similarly to optical linewidth narrowing in single mode laser in presence of feedback [39], [53], [54]. In this case the mechanism inducing minimum RF linewidth in MLLs under feedback should be different to the one observed to reduce the optical linewidth of single mode lasers. Indeed, the RF linewidth of a SS-QDash-MLL subject to coherent feedback narrows down on both sides of the external cavity resonant frequency whereas optical linewidth narrowing in single mode lasers occurs only on the red side of the feedback cavity resonance.

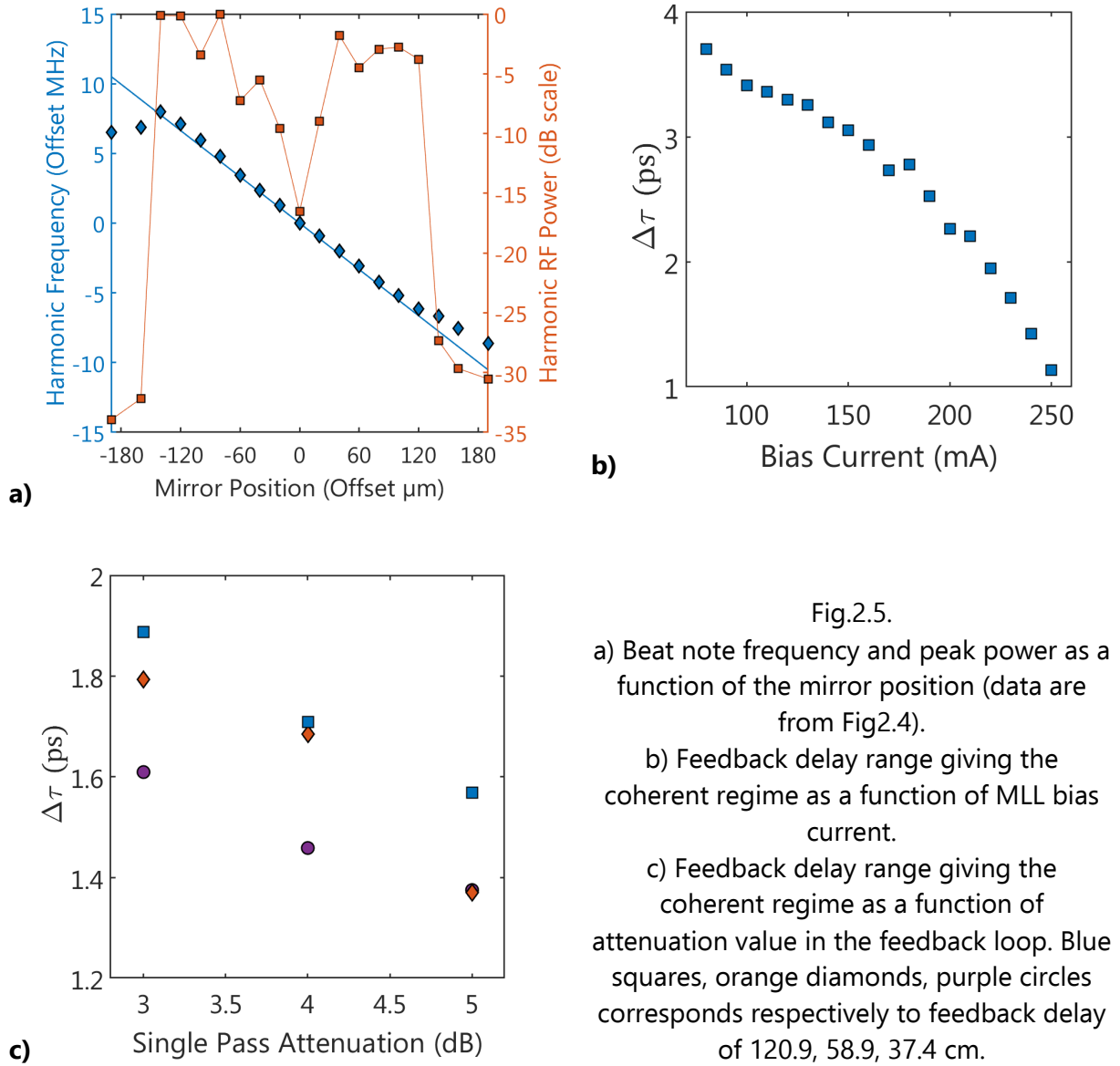


Fig.2.5.

a) Beat note frequency and peak power as a function of the mirror position (data are from Fig.2.4).

b) Feedback delay range giving the coherent regime as a function of MLL bias current.

c) Feedback delay range giving the coherent regime as a function of attenuation value in the feedback loop. Blue squares, orange diamonds, purple circles corresponds respectively to feedback delay of 120.9, 58.9, 37.4 cm.

Using data extracted from Fig.2.4, Fig.2.5.a) reports the RF beat signal peak frequency for varying feedback cavity length. As we can see, varying the mirror position “pulls” the RF beat note. This phenomenon referred to as frequency pulling was also experimentally observed in [29], [34]. The frequency pulling is due to locking between the MLL roundtrip time τ_{act} and feedback delay τ_{ext} such as $\tau_{act} = \tau_{ext}/m$. With straightforward computation we can show that the frequency variation of the emitted signal δf_{MLL} is linked to the variation of feedback delay $\delta\tau_{ext}$ such as :

$$\delta f_{MLL} = -f_{MLL} f_{ext} \delta\tau_{ext} \quad (4.II.1)$$

The blue line of Fig.2.5.a) shows the predicted frequency variation of the emitted beat note using the previous equation with $f_{ext} = 255 \text{ MHz}$ (which is measured by putting the laser in coherence collapse regime), $f_{MLL} = 32.559 \text{ GHz}$, and $\delta\tau_{ext} = 2 \delta L / c$. As we can see, the

predicted δf_{MLL} perfectly fit the measured frequency shift confirming that the observed frequency pulling is related to a locking between the feedback and MLL cavity.

Then, we studied which parameters can increase the range of feedback delay $\Delta\tau$ achieving coherent regime. Fig.2.5.b) shows $\Delta\tau$ as a function of the MLL bias current for a feedback strength around -18 dB, and a cavity length close to 60 cm. As we can see, the range of external cavity length achieving the coherent regime diminishes for increased value of bias current. Then Fig.2.5.c) shows the feedback delay range resulting in coherent feedback for three values of attenuation within the feedback loop and feedback loop roundtrip time. As we can see, the higher the feedback strength is, the larger the range of feedback delay achieving coherent regime.

II.4.a. Coherent feedback regime : summary

To conclude, as evidenced of RF linewidth narrowing, we have seen that coherent feedback regime may improve the phase noise characteristics of a SS-QDash-MLL with no degradation of its comb envelope and RIN spectrum. The beneficial effect of coherent feedback on MLL phase noise will be thoroughly discussed in part III. This regime is obtained when locking occurs between the MLL and external cavity. The feedback delay range resulting in the coherent feedback was shown to increase as a function of feedback strength and decrease as a function of gain medium bias current. For a 250 mA bias current, a feedback strength around -18 dB and an external cavity length around 60 cm, locking between the MLL and external cavity was achieved in a range of feedback delay corresponding to 5.5 % of the MLL roundtrip time. This result shows that the feedback delay needs to be precisely adjusted to achieve coherent feedback.

II.5. Weak feedback regime

When the feedback level is further reduced under a -30 dB value and the feedback cavity length is around 70 cm, the measured optical spectrum does not seem to be affected. However, the RF beat signal linewidth is measured more than ten times wider by comparison with free running operation. Also the RF peak power can decrease by up to 10 dB depending on feedback delay. In this regime no frequency pulling of the MLL 1st RF harmonic is observed. This "weak feedback" regime is also detrimental to the noise properties of the MLL emitted signal and was referred as regime "5" in [34]. This weak feedback regime might have been observed elsewhere in case of weak reflection from the fiber to the MLL facet.

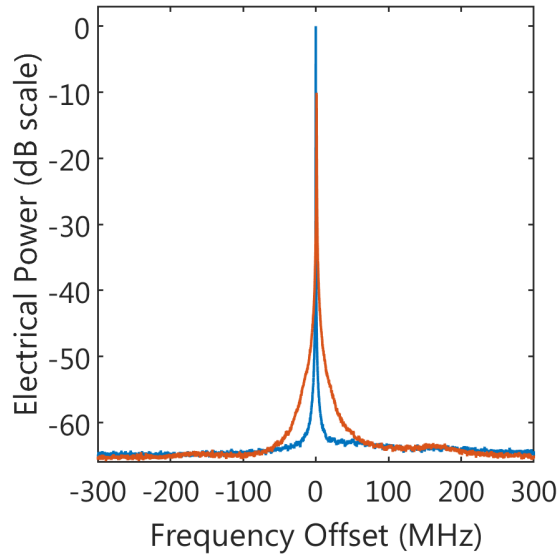


Fig.2.6. MLL RF beat note without feedback (blue), with feedback (orange)
(Frequencies offsets are taken at the maxima of both spectra)

II.6. General summary

We finally summarize the four discerned feedback regimes in a generic graphic shown in Fig.2.7. We represent this graphic for a range of feedback delay τ_{ext} only covering τ_{act} . Indeed if we assume $\tau_{ext} \approx m \times \tau_{act}$ with $m \gg 1$, the areas corresponding to the different feedback regimes should be τ_{act} -periodic. For visibility purpose the regime of coherent feedback has been widened in the x-axis direction as it should only cover around 6% of the represented feedback delay range. The shape of the region corresponding to the coherent feedback delay is also arbitrary as we have only demonstrated that it widens for increasing feedback strength. Further experimental work focusing on the precise delimitation of these regimes is under way.

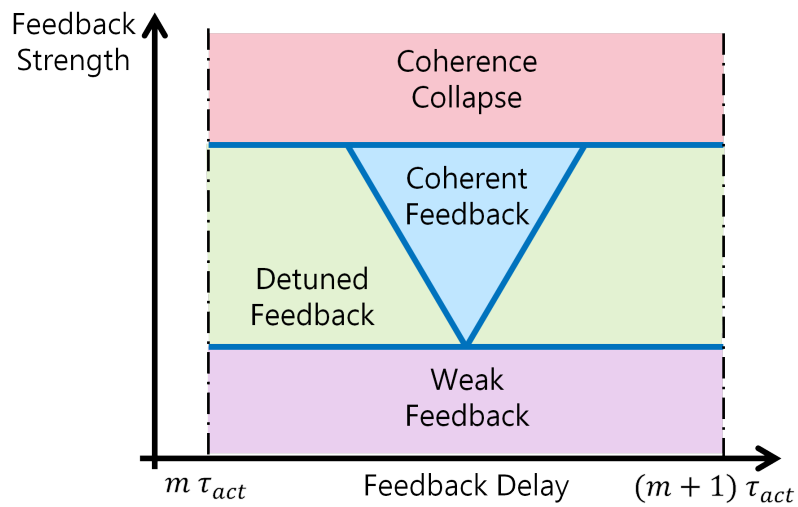


Fig.2.7. Feedback regimes for varying feedback delay and strength

III. Noise properties under Resonant Feedback

In this part we investigate MLL phase noise properties under resonant feedback. First, the main published works focusing on phase noise improvement in comb laser under feedback are reminded. Then, to compare with the literature, we quickly present the RF electrical beat tone narrowing of the SS-QDash-MLL subject to feedback. As this thesis chapter ultimately targets the performance improvement of a MLL-based coherent transmission system using feedback, we will investigate the frequency noise and lineshape of single lines emitted by the MLL. Indeed MLL longitudinal modes could be used as optical carriers in a DWDM coherent link, and their phase noise properties would play a crucial role in the link performances.

III.1. Reported RF line narrowing in MLL

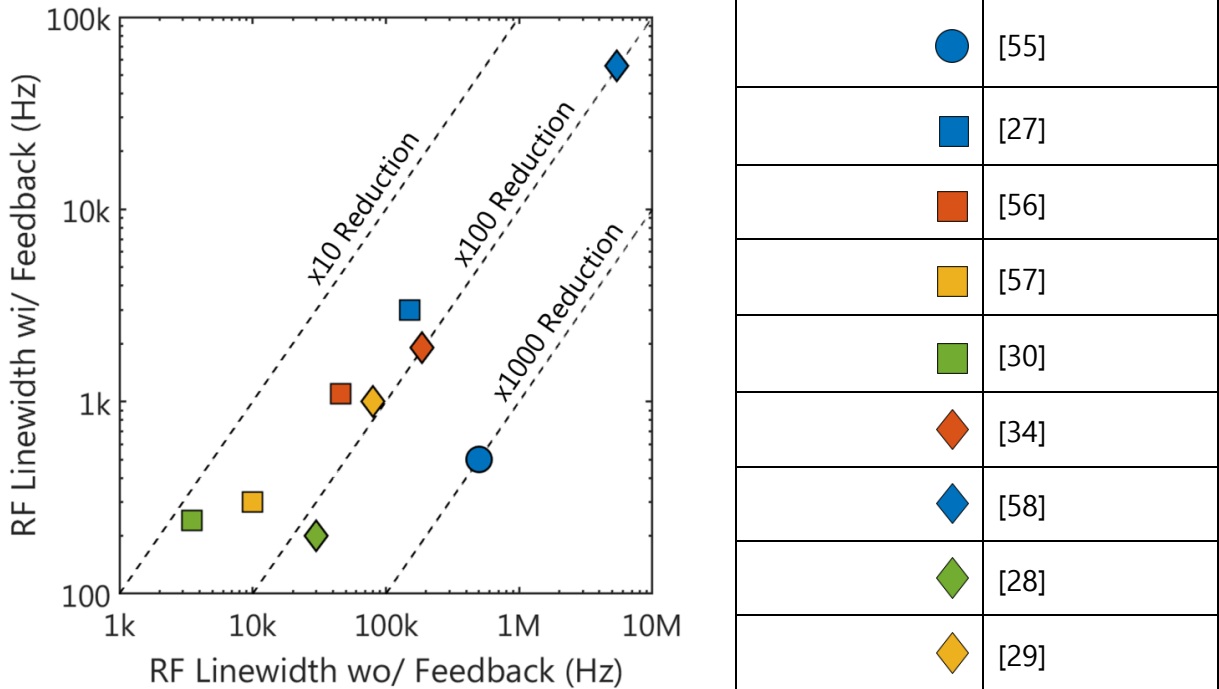


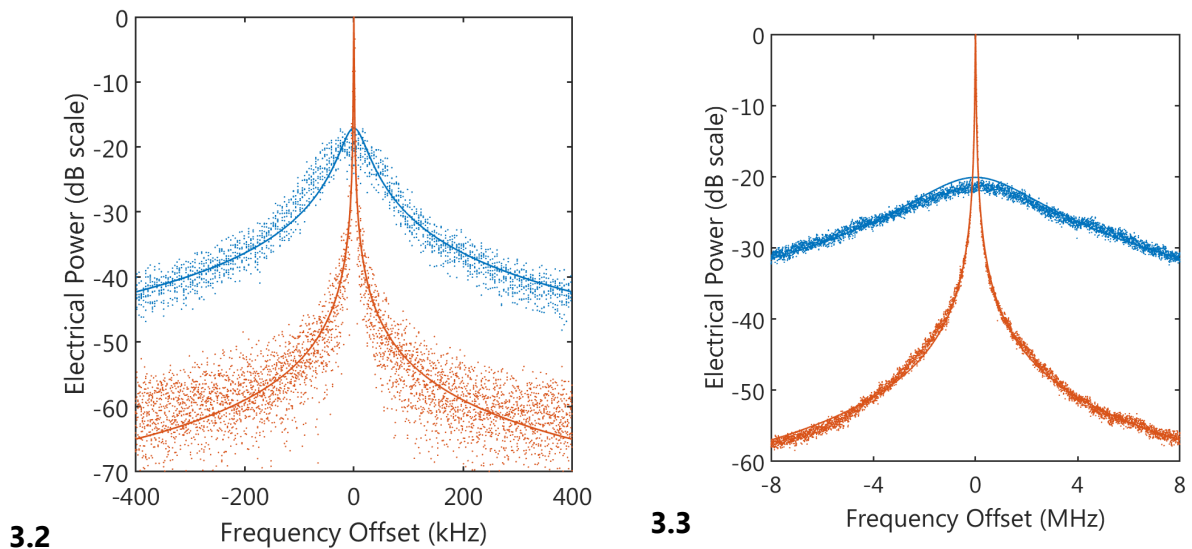
Fig. 3.1. Reported RF beat tone narrowing in the literature

The beneficial effects of feedback on MLLs phase noise properties have been widely outlined in the literature by experimental studies such as [27]–[30], [34], [55]–[58]. These works focused on two sections MLL except [27], [28] who used single section MLLs. The phase

noise reduction was shown by evaluating the RF beat note linewidth narrowing under either fibered or free-space feedback. The reported results are summarized in Fig.3.1. showing the measured RF linewidth both in free running operation and with the MLL subject to feedback. As we can see, a hundred fold linewidth reduction has been largely reported while the work of [55] shows a record RF linewidth narrowing around 1000. However this linewidth reduction value needs to be carefully used for comparison, as the RF beat signal measured is [55] includes strong harmonics at the feedback cavity roundtrip frequency. For instance, this would make the MLL unusable to carry radio signal as in [59].

In addition of demonstrating RF linewidth reduction under feedback, [27], [30] also showed that MLL longitudinal modes linewidth were narrowed under feedback. This particular result indicates the promising use of a MLL under feedback for DWDM coherent transmission system. In the following parts we will experimentally study feedback parameters leading to the optimum linewidth narrowing of MLL single tones.

III.2. RF Linewidth Narrowing in SS-QDash-MLL



In 3.2 & 3.3 blue is without feedback while orange is under coherent feedback.

Fig. 3.2. RF beat tone (without feedback : 44 kHz), (under coherent feedback : 450 Hz)

Fig 3.3. SHE signal measured with the setup based on an acousto-optic modulator.
(without feedback : 2.3 MHz), (under coherent feedback : 11 kHz)

The RF beat linewidth narrowing under coherent feedback is quickly evaluated with a feedback cavity length of ~60 cm being finely tuned to optimize linewidth narrowing and a feedback strength close to -18 dB. The acquired RF linewidth in free running operation and under coherent feedback is plotted in Fig.3.2 showing a Lorentzian linewidth reduced from 44

kHz to 450 Hz. Both values are obtained by fitting a Lorentzian function on data acquired within a 0.8 MHz electrical band. Thus, under these feedback conditions, a 100-fold RF linewidth narrowing is obtained. This linewidth reduction value is in agreement with previously reported results (Fig.3.1).

III.3. Optical Linewidth Narrowing

In this section we study both the optical lineshape and frequency noise spectrum of MLL longitudinal modes under coherent feedback. The experimental setup consists shown in Fig.3.4 of a 20 GHz optical band pass filter (OBPF) selecting a MLL line, then, resolved using two different self-heterodyne (SHE) setups [60]. The first one is based on a Mach-Zehnder interferometer (MZI), with one arm containing a 20 km fiber delay while the other arm is composed of a 160 MHz acousto optic modulator (AOM). This setup is used to analyze the optical lineshape within tens of megahertz bands. The other setup is also based on an unbalanced MZI having a 20 km fiber delay to decorrelate laser emitted signal, while the other arm consists of a 4 GHz single side band (SSB) phase modulator. With this setup the optical lineshape could be analyzed on a wider band (gigahertz range) and frequency noise (FN) spectra were also retrieved. These latter measurements were performed at Dublin City University within the department of Radio and Optical Communication Laboratory directed by Prof. L.P. Barry and the method to retrieve MLL longitudinal mode FN power spectral density (PSD) is detailed in [61].

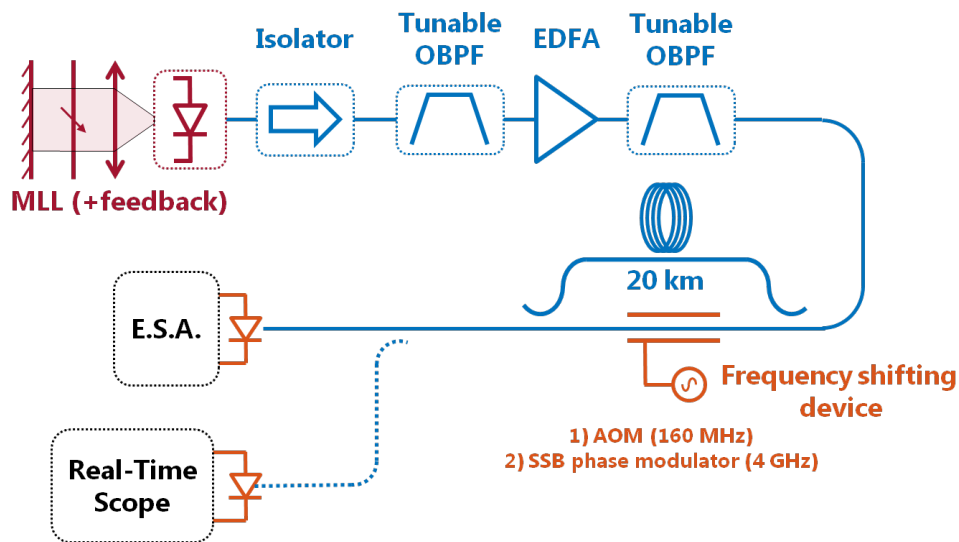


Fig 3.4. Self heterodyne setups to measure MLL longitudinal mode frequency noise and linewidth. The real time scope is only used in the setup based on the phase modulator.

III.3.a.i. Linewidth narrowing of the central MLL mode

In this sub section, we study the linewidth narrowing of a MLL longitudinal mode in the vicinity of the middle of its comb. Typical electrical beat note measured at 160 MHz using the SHE setup based on an acousto-optic modulator is plotted in Fig.3.3. The blue (resp. orange) curve corresponds to the non feedback (resp. feedback) case. In free running operation a Lorentzian linewidth of 4.6 MHz FWHM could be fitted on the acquired data, meaning that the Schawlow-Townes (ST) and Henry (STH) linewidth is around 2.3 MHz. In the presence of coherent feedback, with a cavity length in the 60 cm range and feedback strength evaluated around -18 dB, the optical line narrows down to 11.5 kHz. Hence, under this feedback condition the STH linewidth has been reduced by a factor around 200 which may foretell higher coherent transmission performances using a MLL under feedback.

The optical line reduction shown above is further confirmed by frequency noise (FN) characterization using the second SHE testbed based on a phase modulator. Indeed, the previously presented lineshape measurements made with an electrical spectral analyzer (ESA) integrates the $1/f$ frequency noise related to source noise (being in a [0 MHz – 10 MHz] band), which broaden the measured linewidth. Because the corresponding random fluctuations of the longitudinal mode phase are in the 100 ns timescale, they will be corrected by standard coherent digital signal processing, while only laser random phase drift occurring during few symbol periods (<1 ns) will result in phase errors of the transmitted signal. To study this value of interest MLL longitudinal mode FN-noise spectra are studied in a 1GHz bandwidth and results are plotted in Fig.3.5.a).

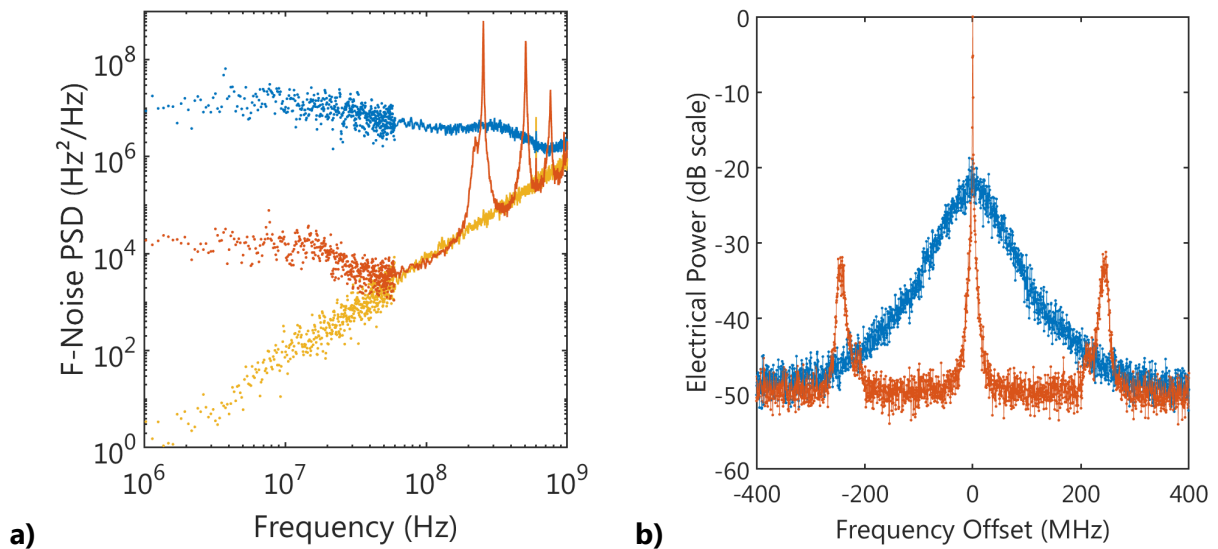


Fig. 3.5. Blue is in free running operation, orange is under coherent feedback.

a) Single tone FN power spectral density. Yellow correspond to a ~ 1 Hz linewidth fiber laser, showing the white phase noise limit of the setup.

b) Corresponding SHE spectrum of b).

The FN-noise spectrum of a single line in free running operation is plotted in blue. We can see a first white noise floor in the [50 MHz – 200 MHz] interval. This white noise floor is below the relaxation oscillation frequency, here maybe at ~300 MHz (this relatively low value of relaxation oscillation frequency might be confirmed by RIN spectra in part II.), meaning that it corresponds to the STH linewidth. Using the procedure of [62], the linewidth value is obtained by multiplying the white floor of the FN-PSD by $\pi/2$, which results in a STH of 6.3 MHz. The difference with the measured linewidth using the acousto-optic setup is not yet clearly understood. Then, the white noise floor at frequency above the relaxation oscillation may indicate a ST linewidth close to 2.0 MHz. Hence, we might be able to estimate the phase/amplitude coupling factor α_H using the following formula:

$$\alpha_H = \sqrt{\frac{\Delta v_{STH}}{\Delta v_{ST}} - 1} \quad (4. III. 1)$$

with Δv_{STH} and Δv_{ST} respectively the STH and ST linewidths. Hence, we deduce $\alpha_H = 1.46$, and this seemingly low value of α_H [16] might be related to the fact that the ST linewidth is over-estimated due to the f^2 -noise of the setup.

Then, the FN spectrum of a single MLL line under coherent feedback is plotted in orange with a feedback cavity length and strength still close to 60 cm and -18 dB. The relaxation oscillation *may* be noticeable at ~15 MHz under coherent feedback and the reduction of relaxation oscillation frequency for a single mode laser subject to feedback has been theoretically explained in [52]. By measuring the white noise floor below 15 MHz we may define a STH linewidth at 25 kHz, while the white noise floor around 40 MHz could express a "linewidth" value close to 5.5 kHz. Note that it is unknown whether the FN-PSD floor stays at $3 \times 10^3 \text{ Hz}^2/\text{Hz}$ for frequency higher than 50 MHz.

Moreover, it is not yet clear whether optical feedback in MLL affects phase/amplitude coupling as in a single mode laser and if the theory in [52] can readily be applied. In the latter case, the B-factor from [52] corresponding to detune loading might be equal to 0 in MLLs under coherent feedback, as the frequency pulling phenomenon described in II.5.b) *could* tend to lock the longitudinal modes on the feedback cavity modes.

Additional experimental studies focusing on small-signal modulation properties of the MLL subject to coherent feedback *need* to be performed to give a better understanding of its dynamic effect in MLL. However, we have shown that Δv_{STH} was decreased by a factor exceeding 250 and while the oscillation relaxation frequency *might* have been reduced by a factor around 20, and these reduction values cannot be explained by [52] when considering a 0 value of B. Indeed according to [52], if we assume no detune loading :

$$\frac{\Delta v_{STH/wi}}{\Delta v_{STH/wo}} = \left(\frac{f_{R/wi}}{f_{R/wo}} \right)^4 \quad (4. III. 3)$$

with $\Delta\nu_{STH/wi}$ and $\Delta\nu_{STH/wo}$ the STH linewidth with and without feedback and $f_{R/wi}$ and $f_{R/wo}$ the oscillation relaxation frequency with and without feedback.

The FN spectrum of single MLL modes also shows spikes at multiples of the feedback cavity roundtrip frequency (here 255 MHz). These spikes will be detrimental to coherent link performances based on a MLL under feedback as these will increase laser phase errors variance. The formalism detailed in [63] could be used to estimate phase error variance for non white FN spectra. Longer delay feedback would result in lower spike frequencies which will then be easier to compensate with standard coherent digital signal processing. The corresponding SHE beat tone is plotted in Fig.3.5.b). As we can see, the noise spikes at the external cavity roundtrip frequencies are rejected by over 30 dB from the optical beat note, this rejection ratio will be shown to be sufficient for coherent transmission performances in part IV, but could also be reduced using a dual-feedback loop as in [64].

III.3.a.ii. Phase noise reduction for several feedback strength

The optical linewidth narrowing of a single MLL mode was studied as a function of the feedback strength for a longer cavity length of 90 cm. The MLL mode selected in this experiment is still close to the emitted comb center frequency. In this section the linewidth was evaluated by averaging white FN spectra between 3 MHz and 30 MHz, as shown in Fig.3.6.a). In this section, frequency noise is supposed white and we assume that evaluated linewidths correspond to Schawlow-Townes linewidth modified by Henry. As we can see from Fig.3.6.a) increasing feedback strength decreases the white noise floor value by orders of magnitude. The narrowest evaluated linewidth is 22 kHz in this experiment.

The measured linewidth narrowing factor corresponding to the ratio of the linewidth value without feedback and under coherent feedback is plotted with the blue squares in Fig.3.6.b). The linewidth narrowing factor reach 310 for feedback strength of -13 dB while trying higher feedback level resulted in coherence collapse. The expected linewidth narrowing using the Lang-Kobayashi (LK) model in the case of a feedback phase adjusted for minimum laser threshold [53] is plotted with the orange line. In this simulation, we assumed a Henry factor of 2.0, and As we can see from Fig.3.6.b) the simple LK model might slightly underestimate SS-QDash-MLL longitudinal modes linewidth narrowing. It could be possible that the feedback strength was under estimated using the method described in I.4, or that the feedback phase [53] affecting each MLL mode has a non-zero value.

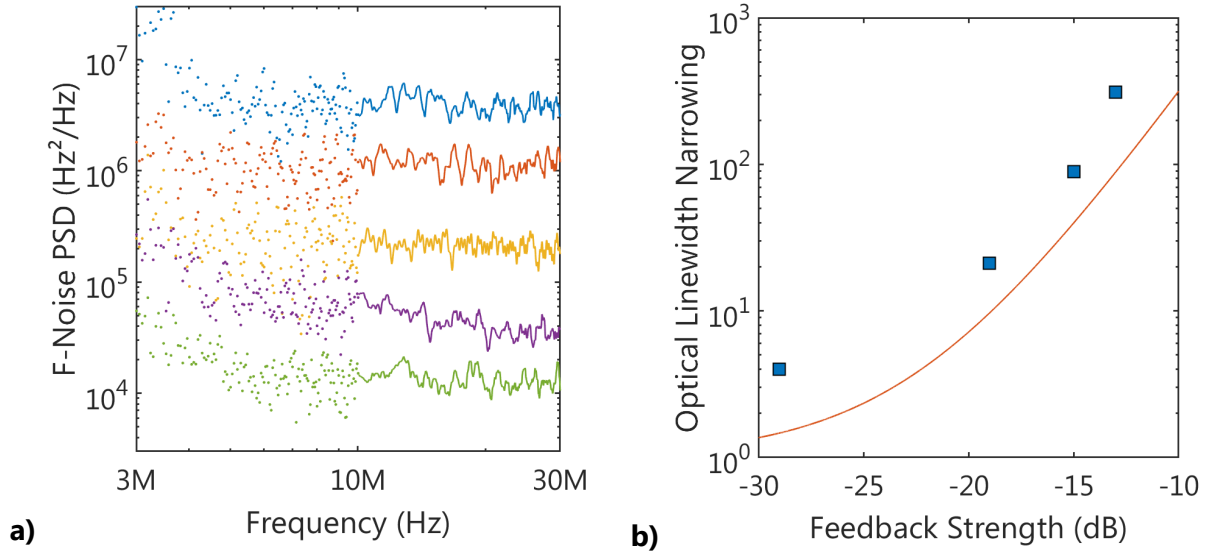


Fig.3.6. a) Measured FN spectra in a 3MHz, 30 MHz frequency band. Blue is without feedback while orange, yellow, purple and green respectively correspond to feedback strength of -29, -19, -15 and -13 dB.
b) Measured linewidth narrowing of the MLL, relative to the non-feedback case, ~ central mode (blue). Lang-Kobayashi model orange).

III.3.a.iii. Linewidth Narrowing across the emitted comb

In this section, optical linewidths are evaluated both under feedback and in free running operation across the whole emitted frequency comb. Measurement results are displayed in Fig.3.7 showing that optical linewidths less than 40 kHz have been obtained over a 1.3 THz bandwidth corresponding to an optical band spanning 40 MLL lines. Inside this frequency range and depending on the mode optical frequency, the linewidth has been narrowed by a factor between 170 and 625. Whereas outside this frequency band, longitudinal modes linewidth broadens exponentially up to the MHz range. This frequency range in which linewidth narrowing occurs could be due to the MLL cavity dispersion which does not match the feedback cavity one. As we clearly see in Fig.3.7 measured optical linewidths follow a quadratic dependence of the optical frequency offset by the comb center frequency both without and with feedback. This parabolic relation is due to phase correlation within the MLL cavity as stated in e.g. [65]. This parabolic relation has been widely reported using MLL in free running operation [65], [66], it is the first time to our knowledge than it is reported using a MLL subject to coherent feedback. Following [65], it can be shown that the optical linewidth $\Delta\vartheta_m$ of the m^{th} mode ($m = 0$ correspond to the MLL mode having the minimum linewidth) is given by :

$$\Delta\vartheta_m = \Delta\vartheta_{m=0} + \Delta\vartheta_{RF} \left(\frac{f_m - f_{m=0}}{f_{MLL}} \right)^2 \quad (4. III. 4)$$

With f_m is the m^{th} comb tone optical frequency, $\Delta\nu_{RF}$ is the RF beat signal FWHM and f_{MLL} is the MLL repetition rate. By fitting the measured optical linewidths with a parabolic function, we evaluate $\Delta\nu_{RF}$ at 28 kHz and around 40 Hz respectively in the non-feedback and feedback case. The RF beat linewidth value under coherent feedback is much lower than the one reported in III.2 (450 Hz) which might be due to the electrical spectral analyzer acquisition that integrates background noise.

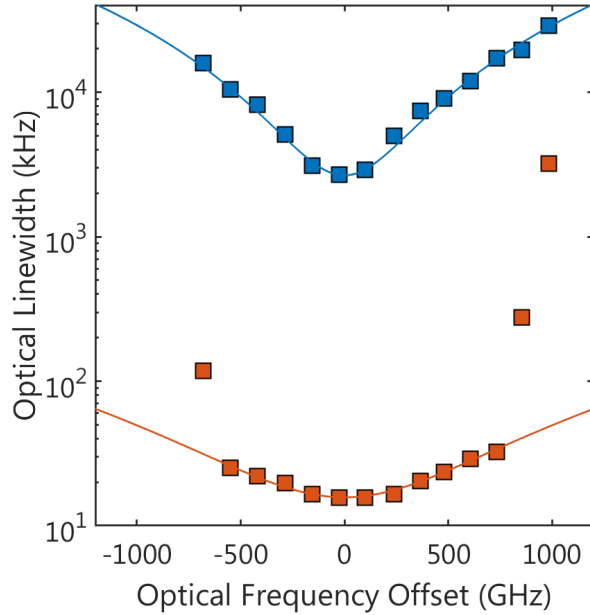


Fig.3.7 Optical linewidth across the MLL comb.

Blue (resp. orange) squares correspond to measurements values without (resp. with) feedback. In both cases the frequency offset is taken at the minimum of the parabolic fit (plain line).

III.4. Conclusion

In this part we have study the Schawlow-Townes and Henry (STH) linewidth narrowing of MLL longitudinal modes under coherent feedback. We have notably shown that at high feedback strength (just below the onset for coherence collapse), the STH linewidth can be narrowed by a factor exceeding 200. However, for these feedback parameters, external cavity modes appear which generate noise spikes at multiple of the feedback cavity roundtrip frequency. In the next part, we will see that a MLL-based coherent transmission system greatly benefits from coherent feedback, meaning that the effect of STH linewidth narrowing is predominant over the detrimental emergence of feedback cavity modes.

IV. Transmission Experiments Results

In this part we present optical coherent transmission results using the MLL to provide single optical carriers at a regular spectral spacing in a DWDM link. As we have seen in part III, phase noise properties of SS-QDash-MLL single lines can be drastically improved using coherent feedback. Hence, we expect significant performance improvements of the coherent transmission system under feedback. We will first report published transmission results based on MLLs. Then, we will present the experimental setup used in our work. And finally we will report on our experimental results, emphasizing the performance improvements (in metrics of signal to noise ratio penalty) between free running operation and under coherent feedback.

IV.1. Reported transmission results using a MLL

In this section, we briefly review some published transmission results based on MLLs. Because MLLs were widely used for fiber communications, we have only mentioned results relevant to datacenter ZR standard communications. We have also omitted published works using a fully integrated transceiver based on a MLL, such as [67], [68] since their performances were limited by the integrated transceiver rather than by the MLL itself. Fig.4.1 summarizes the aggregated net data rates achieved in the literature.

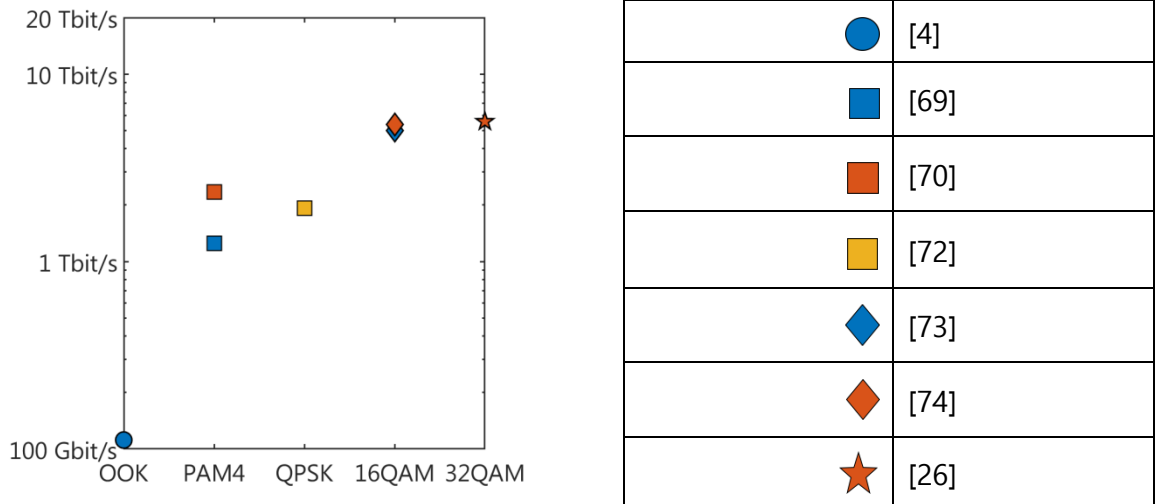


Fig.4.1. Reported fibered transmission results based on a MLL. The y-axis corresponds to the net aggregated data rate using all available channels.

To our knowledge, A. Akrou et al. [4] reported the first experimental demonstration of optical transmission using a MLL as a DWDM comb source. This work is based on a 100 GHz FSR MLL with 12 longitudinal modes within the comb 3dB bandwidth. The channels were demultiplexed and tested one by one in a 10 Gbit/s on-off keying (OOK) testbed. Because MLL lines were modulated at a much lower bit rate than the MLL FSR, a very low aggregated data rate of 112 Gbit/s has been achieved. This result is marked by a blue circle in Fig.4.1. Later the work of V. Vujicic et al. [69] shows PAM4 data transmission using a MLL to provide DWDM channels. As single lines from a MLL suffer from a relatively high RIN value due to mode partitioning noise (MPN), [69] used encoding techniques to overcome the RIN penalty at the cost of a 20 % redundancy. Since the 34 GHz MLL could provide 30 channels which were modulated one by one at 28 Gbaud, an aggregated net bit rate of 1.25 Tbit/s was achieved. This result is marked by a blue square in Fig.4.1. Then C. Browning et al. [70] also shows PAM4 data transmission based on a MLL providing 32 GHz DWDM spaced carriers. Comparing with [69], MLL single line RIN value was reduced in [70]. Hence, no special encoding scheme was used and an aggregated net data rate of 2.3 Tbit/s was demonstrated. This result is obtained using 45 comb channels modulated at 28 Gbaud. This result is marked by an orange square in Fig.4.1.

The previously mentioned works in [4], [69], [70] have shown the feasibility of MLL based DWDM links using intensity-modulation-direct-detection (IMDD) formats. Thus, the transmission results were not limited by the carrier phase noise. However, the following presented results rely on coherent formats to achieve higher data throughput. Hence, their performances are affected by the MLL modes linewidth. Because MLL longitudinal modes may suffer from a relatively high phase noise (evidenced by a Schawlow-Townes linewidth in the MHz range as shown in part III), phase noise mitigation techniques employed to improve coherent transmission performances are discussed. We also want to indicate that the presented results based on coherent formats also rely on polarization division multiplexing (PDM) to achieve a higher bit rate. PDM technology would be feasible using IMDD formats, at the cost of a drastic increment in the system complexity [71].

The work of J. Kemal et al. [72] demonstrated DWDM coherent data transmission using one MLL to provide optical carriers and another MLL to act as a DWDM local oscillator. In their experiments, 23 channels with 50 GHz grid spacing were simultaneously modulated using dual polarization (DP) QPSK format at 45 Gbaud. Since both MLLs longitudinal modes linewidth are in the 2.5 MHz range, they relied on a computational heavy carrier phase estimation (CPE) based on blind phase search (BPS) to retrieve the transmitted data. Finally, the aggregated bit rate is around 3.8 Tbit/s. This result is marked by a yellow square in Fig.4.1.

The recent transmission results presented in [73], show DP-16QAM transmission using a 34 GHz FSR MLL. The MLL longitudinal modes linewidth were around 1.5 MHz which was proven to be sufficient to transmit DP-16QAM at 28 Gbaud over 100 km. No indications are given on the numerical methods used to mitigate phase errors. By modulating 48 MLL tones [73]

achieved an aggregated net bit rate of 10.0 Tbit/s. Their result is marked by a blue diamond in Fig.4.1

DP-16QAM data transmission based on a MLL was also shown in [74]. In this work, a 42 GHz MLL was used which optical linewidths were around 3 MHz and CPE based on the computational heavy BPS algorithm was applied to retrieve transmitted data. By modulating simultaneously 38 carriers at 38 Gbaud, they could achieve a 10.7 Tbit/s net data rate. Their result is marked by the orange diamond of Fig.4.1

Finally, [26] shows DP-32QAM DWDM transmission with optical carriers provide by a 25 GHz MLL. In these experiments, every single line has been modulated at 20 Gbaud and simultaneously transmitted. Since 32QAM data transmission at 20 Gbaud would be highly affected by random phase fluctuations, [26] relies on optical feedback to stabilize the MLL longitudinal modes. Moreover, thanks to optical feedback [26] could employ a lighter CPE based on the Viterbi and Viterbi algorithm. They achieved 11.2 Tbit/s net data rate by modulating 60 DWDM channels. Their results is marked by the orange pentagram of Fig.4.1

IV.2. Coherent testbed description

The coherent transmission setup is sketched in Fig.4.2. These experiments have also been carried out at Dublin City University, in collaboration with Prof L.P. Barry's group. The MLL is placed at the transmitter side in which a single longitudinal mode is selected using a 20 GHz bandwidth optical band-pass filter. The filtered mode is first amplified with an EDFA and then modulated using single-polarization coherent format. In the experiments we tested both QPSK and 16QAM formats at 25 Gbaud. Then the signal at the transmitter output is either detected in back to back (BtB) or after travelling through 50 km of single mode fiber (SMF). In the BtB case we have studied the BER vs OSNR properties of the transmission system with a second EDFA adding spontaneous white noise to the optical signal. This EDFA is connected to the optical channel through a 50/50 directional coupler. The optical signal is down converted in the electrical domain using a standard coherent receiver which local oscillator linewidth is around 50 kHz and output power is close to 16 dBm. The data are finally recovered offline using the following digital signal processing (DSP) :

- Compensating path mismatch of the receiver using a timing deskew
- Re-sampling at two samples per symbols.
- Using the m^{th} -power method to compensate for slow frequency drift between LO and carrier.
- Channel equalization using constant modulus algorithm (CMA) (resp. CMA followed by multi-modulus algorithm (MMA)) for QPSK (resp. 16QAM) case.

- Carrier phase estimation (CPE) using a 2nd order decision directed phase locked loop (DD-PLL) [75]

Then the bit error rate is measured by comparing the transmitted and received sequence of 1e6 symbols. In the experiments, we fix the BER limit at $4.9e^{-3}$ corresponding to a 7% overhead hard decision (HD) forward error correction (FEC) limit [76].

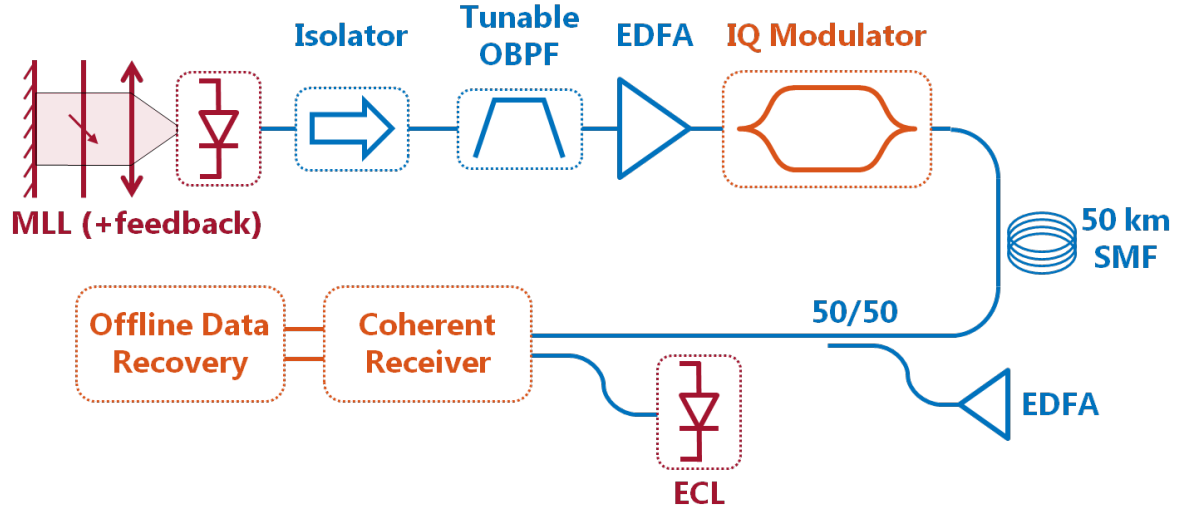


Fig.4.2. 25 Gbaud coherent test bed.

IV.3. Experimental Results

In this section we first details the experimental results obtained in BtB, and then after 50 km transmission. In the BtB case, the experimental analysis highlights the transmission performance improvements with the MLL under coherent feedback. The 50 km transmission results demonstrate that the MLL under coherent feedback would be a promising solution to achieve few Tbit/s links using a single gain chip.

IV.3.a. Back to Back results

In these experiments the selected MLL mode is close to the emitted comb central wavelength. With the MLL under coherent feedback, measured constellations diagrams using QPSK and 16QAM formats are plotted in Fig.4.3.a) and b) at respectively 14 dB and 20 dB OSNR. The color zones represent samples density computed in a 50*50 grid mapping, with the density doubling in between two adjacent color zones. We can see from both constellations symbols are clearly resolved, it is related to the reduced phase of the MLL

longitudinal modes under feedback as, the 16QAM constellation only consisted of two concentric rings when no feedback was applied on the laser (not shown here). However, the oval / turning shape of the QPSK symbols and outer 16QAM ones shows that residual phase noise has not been corrected. We do believe that the remaining phase errors might be due to the noise spikes at multiples of the feedback cavity roundtrip frequency. Monte-Carlo simulations may confirm this hypothesis, and other CPE methods could be tested to see if these narrowband noise spikes can be better tracked.

BER vs OSNR performances are plotted in Fig.4.3.c) for both QPSK and 16QAM signals. Using QPSK format, coherent feedback reduces the transmission system penalty at the FEC limit of 1dB relatively to the non feedback case. This penalty reduction can be seen as a possible transmission reach extension of 5km (assuming SMF losses of 0.2 dB/km in the C-band). This improvement might not seem significant, because QPSK formats remains relatively robust to excessive phase noise. Moreover, under coherent feedback the impairment with the theoretical optimum computed using additive white Gaussian noise (AWGN) theory is below 0.2 dB. Such low value of penalty validates the use of coherent feedback in SS-QDash-MLL for high performances coherent links.

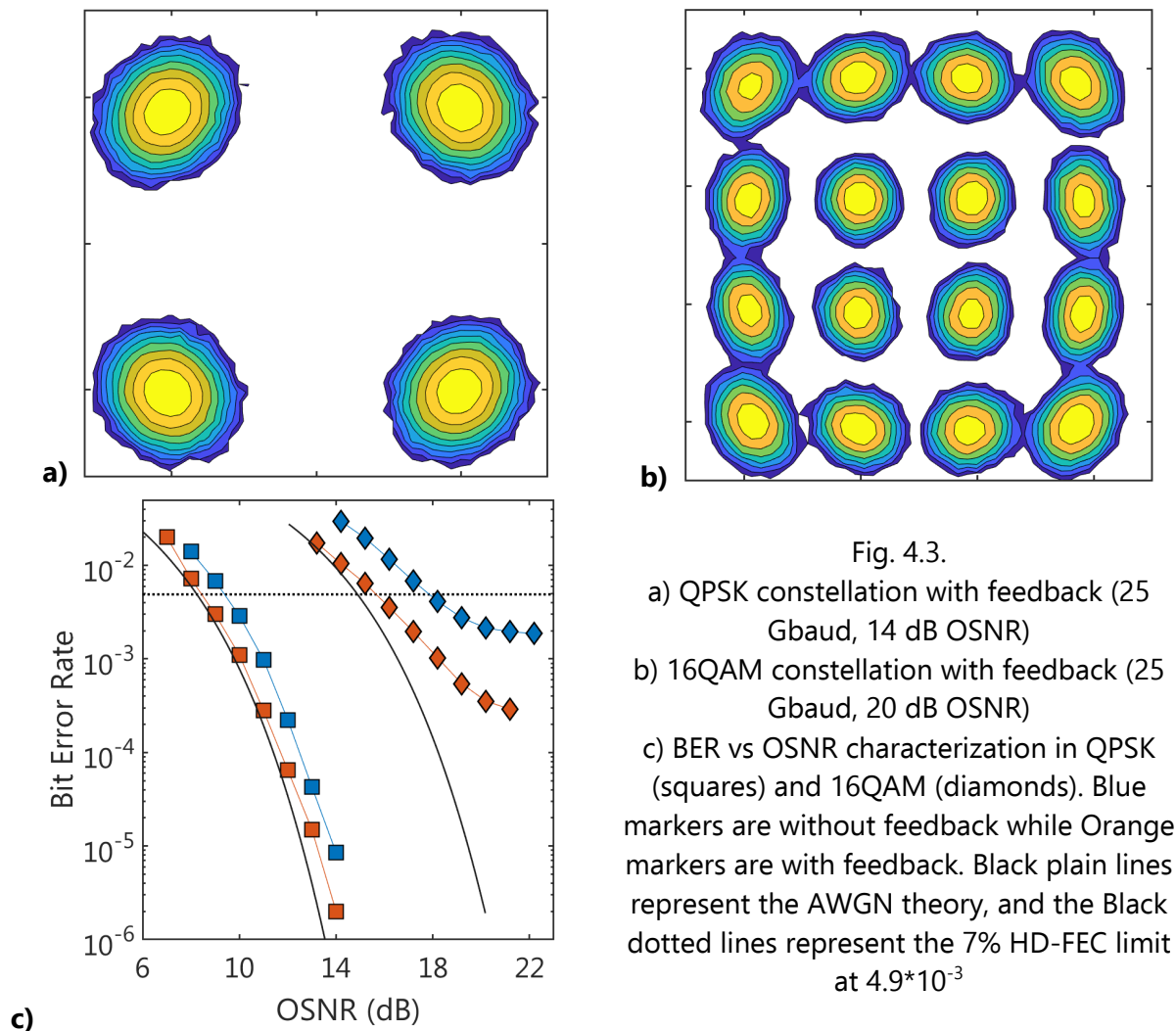


Fig. 4.3.

- a) QPSK constellation with feedback (25 Gbaud, 14 dB OSNR)
- b) 16QAM constellation with feedback (25 Gbaud, 20 dB OSNR)
- c) BER vs OSNR characterization in QPSK (squares) and 16QAM (diamonds). Blue markers are without feedback while Orange markers are with feedback. Black plain lines represent the AWGN theory, and the Black dotted lines represent the 7% HD-FEC limit at 4.9×10^{-3}

As we can see in Fig.4.3.c), coherent feedback greatly benefits the BER vs OSNR performances in 16QAM signaling. The penalty at the 7% HD-FEC limit is reduced by over 2.2 dB between free running operation and when the MLL is subject to optical feedback. In this case, the penalty reduction implies a possible reach extension of 11 km, which is of great importance when targeting data center fibered transmission in the 80 km range. Under coherent feedback the impairment relative to the AWGN optimum is reduced below 0.8 dB, demonstrating the robustness of the coherent system based on a MLL under feedback to higher order QAM formats.

IV.3.b. 50 km transmission results

In this section we assess the suitability of a MLL under coherent feedback for datacenter interconnect DWDM links. In these experiments the MLL is kept under coherent feedback and single longitudinal modes are filtered from the comb and used as carriers in the coherent testbed. The transmission experiments were performed for eight single lines out of the 47 longitudinal modes of the MLL. We remind that the eight filtered modes are not simultaneously modulated, but each comb line is rather tested one after the other.

Error free transmission has been achieved using 25 Gbaud QPSK signals in both BtB and after 50 km of propagation. Here, error-free is defined when no errors was found in a recorded 1e6 symbols sequence. In this case the error vector magnitude (EVM) was evaluated from the constellation, and we plot the results in Fig.4.4.a). In BtB the EVM is between 12% and 15% and is degraded between 13.6% and 16.2% after fibered transmission. As we can see from Fig.4.4.a) the measured EVM is higher at the edge of the MLL comb, which is due to both wider optical lines further from the comb central frequency and lower modal power. The QPSK measurements confirm that a SS-QDash-MLL is suitable for coherent communication with 50 km reach. The net bit rate BR which could be achieved considering simultaneous modulations of all 47 comb lines N_L is given in the following :

$$BR = N_L \times Ba \times \eta \times FEC \quad (4.IV.1)$$

With Ba the baud rate, η the number of bit per symbols and FEC the considered FEC limit. We remind that no pilot was used in our experiments, and adding them would slightly decrease the achievable net data rate. In the single polarization QPSK case the achievable net bit rate using the SS-QDash-MLL under feedback is around 2.2 Tbit/s. This value might be expandable to 4.4 Tbit/s if dual polarization format was successfully used.

In the case of 16QAM, we measured a BER under the FEC limit both in BtB and after 50 km transmission for the eight tested channels. Similarly to the QPSK case the BER increases at wavelengths close to the edge of the comb, due to the linewidth increase and modal power drop near the edge of the comb. By considering the simultaneous modulation of each MLL mode in the 16QAM case, a 4.3 Tbit/s net data rate could be achieved. Then if dual-polarization modulation were successfully demonstrated using the same DWDM optical source, a 8.8Tbit/s of net data bit rate could be hypothetically obtained.

These transmission experiments validate the use of a MLL subject to feedback as a promising solution to achieve multiple Tbit/s line rate with increased transmission reach.

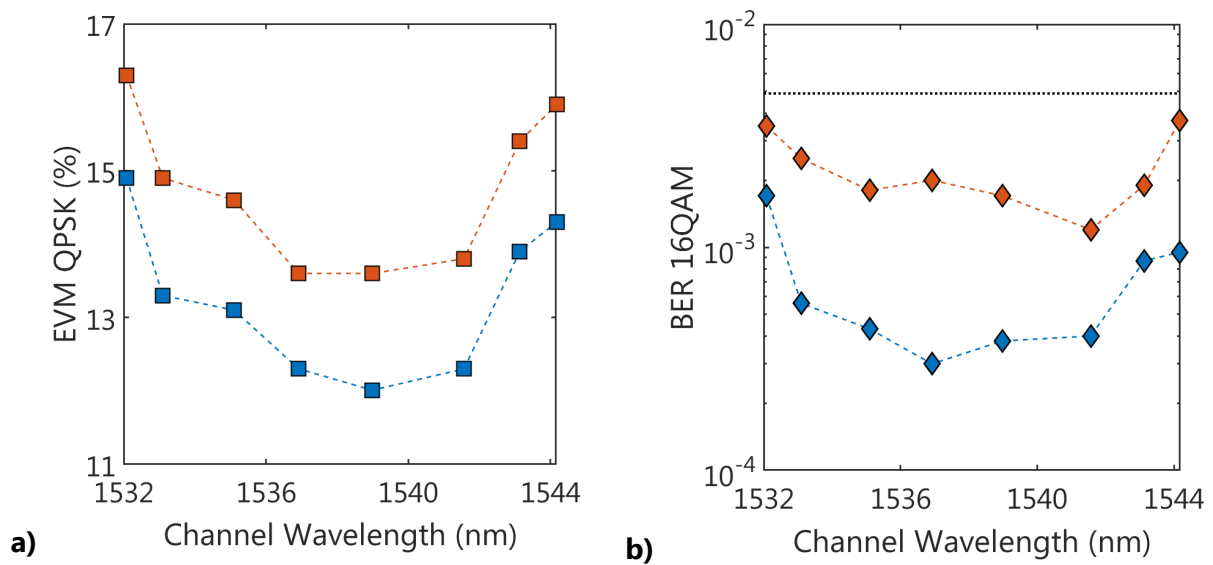


Fig.4.4.a) EVM obtained using 25 Gbaud QPSK signals and with the MLL under coherent feedback. Blue is in BtB, orange is after 50 km transmission.
b) Counted BER obtained using 25 Gbaud 16QAM signals and with the MLL under coherent feedback. Blue is in BtB, orange is after 50 km transmission.

V. Conclusion

In this thesis chapter, we have first presented the spectral characteristics of a 32.5 GHz single section (SS) quantum dash (QDash) mode locked laser (MLL), and as previously reported we have seen that SS-QDash-MLLs were simple devices to efficiently generate a broadband optical comb. However, the optical linewidth of MLL longitudinal modes was shown to be in the 5 MHz range, bringing an important penalty in coherent transmission systems using simple digital signal processing. Optical feedback which was a well-known method to stabilize single mode lasers was used in SS-QDash-MLL to improve its longitudinal mode noise properties.

For the first time to our knowledge we have highlighted four different feedback regimes in SS-QDash-MLL using a 10 cm to a 1m long free space feedback cavity. Among these feedback regimes, only the *coherent* regime was shown, as expected, to be beneficial to laser modelocking. This regime was obtained when locking was possible between the external cavity and the MLL, i.e. the feedback delay needed to be precisely adjusted to a multiple of the MLL one. Moreover this regime required a feedback level below the onset of coherence collapse and over a given threshold resp. around -12 dB and -30 dB in our experiments. The spectral properties of each feedback regime were analyzed, and this work could be a basis in the future to facilitate achieving the coherent feedback regime.

Then, the phase noise of MLL modes subject to feedback was carefully investigated and we show that optical linewidth could be narrowed by a factor exceeding 100. This noise improvement made possible 16QAM coherent transmission over 50 km with an aggregated net data rate over 4.3 Tbit/s. This result demonstrates the promising performances of a DWDM coherent system based on a MLL subject to coherent feedback.

However, in this chapter thesis, the precise delimitation of feedback regimes was not explored. Future experimental work could be performed to precisely set the limit (in the plane of feedback delay and strength) of the coherent feedback regime. Also, in this thesis no feedback model was developed to analytically and numerically study feedback effect in SS-QDash-MLL. A multi-mode rate equation, taking into account four-wave mixing and correlated Lorentz forces could first be implemented. This would allow the study of feedback parameters leading to stable operation and single MLL noise linewidth narrowing. However, a travelling wave model would be required for more precise evaluations such as simulating mode frequency noise on a frequency band wider than the external cavity repetition rate. Finally, additional study devising MLL under feedback using a passive/active integration platform would be necessary to target datacenter interconnects applications.

VI. References

- [1] T. Verolet *et al.*, "Mode Locked Laser Phase Noise Reduction Under Optical Feedback for Coherent DWDM Communication," *J. Light. Technol.*, vol. 38, no. 20, pp. 5708–5715, 2020.
- [2] M. Nakazawa, K. Suzuki, H. Kubota, E. Yamada, and Y. Kimura, "Dynamic Optical Soliton Communication," *IEEE J. Quantum Electron.*, vol. 26, no. 12, pp. 2095–2102, 1990.
- [3] A. Hasegawa, "Soliton-based optical communications: An overview," *IEEE J. Sel. Top. Quantum Electron.*, vol. 6, no. 6, pp. 1161–1172, 2000.
- [4] A. Akroust *et al.*, "Separate error-free transmission of eight channels at 10 Gb/s using comb generation in a quantum-dash-based mode-locked laser," *IEEE Photonics Technol. Lett.*, vol. 21, no. 23, pp. 1746–1748, 2009.
- [5] V. Vujicic *et al.*, "Quantum Dash Mode-Locked Lasers for Data Centre Applications," *IEEE J. Sel. Top. Quantum Electron.*, vol. 21, no. 6, 2015.
- [6] K. E. K. Asai, M. A. N. Akazawa, M. I. I. Shikawa, and H. I. I. Shii, "wavelength tunable DFB LD array with self- optical feedback," vol. 26, no. 5, pp. 5675–5685, 2018.
- [7] P. Marin-Palomo *et al.*, "Microresonator-based solitons for massively parallel coherent optical communications," *Nature*, vol. 546, no. 7657, pp. 274–279, 2017.
- [8] B. Stern, X. Ji, Y. Okawachi, A. L. Gaeta, and M. Lipson, "Battery-operated integrated frequency comb generator," *Nature*, vol. 562, no. 7727, pp. 401–405, 2018.
- [9] B. Corcoran *et al.*, "Ultra-dense optical data transmission over standard fibre with a single chip source," *Nat. Commun.*, vol. 11, no. 1, pp. 1–7, 2020.
- [10] C. Bao *et al.*, "Nonlinear conversion efficiency in Kerr frequency comb generation," *Opt. Lett.*, vol. 39, no. 21, p. 6126, 2014.
- [11] T. Herr *et al.*, "Universal formation dynamics and noise of Kerr-frequency combs in microresonators," *Nat. Photonics*, vol. 6, no. 7, pp. 480–487, 2012.
- [12] L. Zhang, Y. Song, S. Zou, Y. Li, J. Ye, and R. Lin, "Flat frequency comb generation based on Mach-Zehnder modulator and phase modulator," *Int. Conf. Commun. Technol. Proceedings, ICCT*, no. 3, pp. 211–213, 2010.
- [13] Q. Wang, L. Huo, Y. Xing, and B. Zhou, "Ultra-flat optical frequency comb generator using a single-driven dual-parallel Mach–Zehnder modulator," *Opt. Lett.*, vol. 39, no. 10, p. 3050, 2014.
- [14] P. M. Anandarajah, R. Maher, R. Phelan, L. P. Barry, P. Perry, and B. Kelly, "Gain Switching of Discrete Mode Lasers for Generation of Highly Coherent Optical Pulses with Low Timing Jitter and High SMSR," vol. xx, no. xx, pp. 1–12, 2010.

- [15] J. Pfeifle *et al.*, "Flexible terabit/s Nyquist-WDM super-channels using a gain-switched comb source," *Opt. Express*, vol. 23, no. 2, p. 724, 2015.
- [16] F. Lelarge *et al.*, "Recent advances on InAs/InP quantum dash based semiconductor lasers and optical amplifiers operating at 1.55 μm ," *IEEE J. Sel. Top. Quantum Electron.*, vol. 13, no. 1, pp. 111–123, 2007.
- [17] G.-H. Duan *et al.*, "High Performance InP-Based Quantum Dash Semiconductor Mode-Locked Lasers for Optical Communications," *Bell Labs Tech. J.*, vol. 14, 2009.
- [18] R. Rosales *et al.*, "InAs / InP Quantum-Dot Passively Mode-Locked," vol. 17, no. 5, pp. 1292–1301, 2011.
- [19] R. Rosales *et al.*, "High performance mode locking characteristics of single section quantum dash lasers," *Opt. Express*, vol. 20, no. 8, p. 8649, 2012.
- [20] V. Panapakkam *et al.*, "Amplitude and phase noise of frequency combs generated by single-section InAs/InP quantum-dash-based passively and actively mode-locked lasers," *IEEE J. Quantum Electron.*, vol. 52, no. 11, 2016.
- [21] F. van Dijk, A. Enard, X. Buet, F. Lelarge, and G. H. Duan, "Phase noise reduction of a quantum dash mode-locked laser in a millimeter-wave coupled opto-electronic oscillator," *J. Light. Technol.*, vol. 26, no. 15, pp. 2789–2794, 2008.
- [22] Mohamed Omar Sahni *et al.*, "Sahni_blank.pdf," *Opt. InfoBase Conf. Pap.*, vol. 42, no. 19, pp. 4000–40003, 2017.
- [23] A. C. Ramdane, P. Gruning, V. Roncin, and F. Du-Burck, "Frequency stability transfer by optical injection locking into a semiconductor frequency comb," *2017 Jt. Conf. Eur. Freq. Time Forum IEEE Int. Freq. Control Symp. EFTF/IFC 2017 - Proc.*, pp. 769–770, 2017.
- [24] P. Bardella, L. L. Columbo, and M. Gioannini, "Self-generation of optical frequency comb in single section quantum dot Fabry-Perot lasers: a theoretical study," *Opt. Express*, vol. 25, no. 21, p. 26234, 2017.
- [25] A. Shen *et al.*, "Low confinement factor quantum dash (QD) mode-locked fabry-perot (FP) laser diode for tunable pulse generation," *OFC/NFOEC 2008 - 2008 Conf. Opt. Fiber Commun. Fiber Opt. Eng. Conf.*, pp. 25–27, 2008.
- [26] J. Kemal *et al.*, "32QAM WDM transmission at 12 Tbit/s using a quantum-dash mode-locked laser diode (QD-MLLD) with external-cavity feedback," *Opt. Express*, vol. 28, no. 16, p. 23594, 2020.
- [27] K. Merghem, V. Panapakkam, Q. Gaimard, F. Lelarge, and A. Ramdane, "Narrow linewidth frequency comb source based on selfinjected quantum-dash passively mode-locked laser," *2017 Conf. Lasers Electro-Optics, CLEO 2017 - Proc.*, vol. 2017-Janua, pp. 1–2, 2017.
- [28] A. Akrou, A. Shen, A. Enard, G. H. Duan, F. Lelarge, and A. Ramdane, "Low phase noise all-optical oscillator using quantum dash modelocked laser," *Electron. Lett.*, vol. 46, no.

1, pp. 73–74, 2010.

- [29] G. Fiol, M. Kleinert, and D. Arsenijević, "mode-locked laser under external continuous wave light injection or optical," vol. 014006, pp. 1–6.
- [30] Y. Mao, J. Liu, Z. Lu, C. Song, and P. J. Poole, "Ultra-Low Timing Jitter of Quantum Dash Semiconductor Comb Lasers With Self-Injection Feedback Locking," *IEEE J. Sel. Top. Quantum Electron.*, vol. 25, no. 6, 2019.
- [31] E. Patzak, A. Sugimura, S. Saito, T. Mukai, and H. Olesen, "Semiconductor laser linewidth in optical feedback configurations," *Electron. Lett.*, vol. 19, no. 24, pp. 1026–1027, 1983.
- [32] W. Bludau and R. Rossberg, "Characterization of laser-to-fiber coupling techniques by their optical feedback," *Appl. Opt.*, vol. 21, no. 11, p. 1933, 1982.
- [33] J. H. Osmundsen and N. Gade, "Influence of Optical Feedback on Laser Frequency Spectrum and Threshold Conditions," *IEEE J. Quantum Electron.*, vol. 19, no. 3, pp. 465–469, 1983.
- [34] D. Arsenijević, M. Kleinert, and D. Bimberg, "Phase noise and jitter reduction by optical feedback on passively mode-locked quantum-dot lasers," *Appl. Phys. Lett.*, vol. 103, no. 23, 2013.
- [35] R. W. Tkach and A. R. Chraplyvy, "REGIMES OF FEEDBACK EFFECTS IN 1.5- μ m DISTRIBUTED FEEDBACK LASERS," *J. Light. Technol.*, vol. LT-4, no. 11, pp. 1655–1661, 1986.
- [36] N. Schunk and K. Petermann, "Numerical analysis of the feedback regimes for a singlemode semiconductor laser with external feedback," *IEEE J. Quantum Electron.*, vol. 24, no. 7, pp. 1242–1247, 1988.
- [37] K. Petermann, "External Optical Feedback Phenomena in Semiconductor Lasers," *IEEE J. Sel. Top. Quantum Electron.*, vol. 1, no. 2, pp. 480–489, 1995.
- [38] H. Olesen, J. H. Osmundsen, and B. Tromborg, "Nonlinear Dynamics and Spectral Behavior for an External Cavity Laser," *IEEE J. Quantum Electron.*, vol. 22, no. 6, pp. 762–773, 1986.
- [39] R. Lang and K. Kobayashi, "External Optical Feedback Effects on Semiconductor Injection Laser Properties," *IEEE J. Quantum Electron.*, vol. 16, no. 3, pp. 347–355, 1980.
- [40] B. Tromborg, J. H. Osmundsen, and H. Olesen, "Stability Analysis for a Semiconductor Laser in an External Cavity," *IEEE J. Quantum Electron.*, vol. 20, no. 9, pp. 1023–1032, 1984.
- [41] P. Spano, S. Piazzolla, and M. Tamburrini, "Theory of Noise in Semiconductor Lasers in the Presence of Optical Feedback," *IEEE J. Quantum Electron.*, vol. 20, no. 4, pp. 350–357, 1984.
- [42] C. H. Henry and R. F. Kazarinov, "Instability of Semiconductor Lasers Due to Optical

- Feedback from Distant Reflectors," *IEEE J. Quantum Electron.*, vol. 22, no. 2, pp. 294–301, 1986.
- [43] B. Tromborg, H. Olesen, X. Pan, and S. Saito, "Transmission line description of optical feedback and injection locking for fabry-perot and dfb lasers," *IEEE J. Quantum Electron.*, vol. 23, no. 11, pp. 1875–1889, 1987.
 - [44] J. Helms and K. Petermann, "A Simple Analytic Expression for the Stable Operation Range of Laser Diodes with Optical Feedback," *IEEE J. Quantum Electron.*, vol. 26, no. 5, pp. 833–836, 1990.
 - [45] E. A. Avrutin and B. M. Russell, "Dynamics and spectra of monolithic mode-locked laser diodes under external optical feedback," *IEEE J. Quantum Electron.*, vol. 45, no. 11, pp. 1456–1464, 2009.
 - [46] H. Simos, C. Simos, C. Mesaritakis, and D. Syvridis, "Two-section quantum-dot mode-locked lasers under optical feedback: Pulse broadening and harmonic operation," *IEEE J. Quantum Electron.*, vol. 48, no. 7, pp. 872–877, 2012.
 - [47] C. Otto, K. Lüdge, A. G. Vladimirov, M. Wolfrum, and E. Schöll, "Delay-induced dynamics and jitter reduction of passively mode-locked semiconductor lasers subject to optical feedback," *New J. Phys.*, vol. 14, 2012.
 - [48] L. Jaurigue, B. Krauskopf, and K. Lüdge, "Multipulse dynamics of a passively mode-locked semiconductor laser with delayed optical feedback," *Chaos*, vol. 27, no. 11, 2017.
 - [49] C. Simos, H. Simos, C. Mesaritakis, A. Kapsalis, and D. Syvridis, "Pulse and noise properties of a two section passively mode-locked quantum dot laser under long delay feedback," *Opt. Commun.*, vol. 313, pp. 248–255, 2014.
 - [50] K. I. Kallimani and M. J. O'Mahony, "Relative intensity noise for laser diodes with arbitrary amounts of optical feedback," *IEEE J. Quantum Electron.*, vol. 34, no. 8, pp. 1438–1446, 1998.
 - [51] S. Azouigui *et al.*, "Optical feedback tolerance of quantum-dot- and quantum-dash-based semiconductor lasers operating at 1.55 μm ," *IEEE J. Sel. Top. Quantum Electron.*, vol. 15, no. 3, pp. 764–773, 2009.
 - [52] G. P. Agrawal and C. H. Henry, "Modulation Performance of a Semiconductor Laser Coupled to an External High-Q Resonator," *IEEE J. Quantum Electron.*, vol. 24, no. 2, pp. 134–142, 1988.
 - [53] G. P. Agrawal, "Line Narrowing in a Single-Mode Injection Laser Due to External Optical Feedback," *IEEE J. Quantum Electron.*, vol. 20, no. 5, pp. 468–471, 1984.
 - [54] R. F. Kazarinov and C. H. Henry, "The Relation of Line Narrowing and Chirp Reduction Resulting from the Coupling of a Semiconductor Laser to a Passive Resonator," *IEEE J. Quantum Electron.*, vol. 23, no. 9, pp. 1401–1409, 1987.
 - [55] K. Merghem *et al.*, "Low noise performance of passively mode locked quantum-dash-

- based lasers under external optical feedback," *Appl. Phys. Lett.*, vol. 95, no. 13, pp. 34–37, 2009.
- [56] C. Y. Lin, F. Grillot, Y. Li, R. Raghunathan, and L. F. Lester, "Microwave characterization and stabilization of timing jitter in a quantum-dot passively mode-locked laser via external optical feedback," *IEEE J. Sel. Top. Quantum Electron.*, vol. 17, no. 5, pp. 1311–1317, 2011.
 - [57] Z. G. Lu, J. R. Liu, P. J. Poole, C. Y. Song, and S. D. Chang, "Ultra-narrow linewidth quantum dot coherent comb lasers with self-injection feedback locking," *Opt. Express*, vol. 26, no. 9, pp. 1–3, 2018.
 - [58] O. Solgaard and K. Y. Lau, "Optical Feedback Stabilization of the Intensity Oscillations in Ultrahigh-Frequency Passively Modelocked Monolithic Quantum-Well Lasers," vol. 5, no. 11, pp. 1264–1267, 1993.
 - [59] A. Delmade *et al.*, "Quantum Dash Passively Mode Locked Laser for Optical Heterodyne Millimeter-Wave Analog Radio-over-Fiber Fronthaul Systems," *2020 Opt. Fiber Commun. Conf. Exhib. OFC 2020 - Proc.*, pp. 8–10, 2020.
 - [60] T. Okoshi, K. Kikuchi, and A. Nakayama, "Novel method for high resolution measurement of laser output spectrum," *Electron. Lett.*, vol. 16, no. 16, pp. 630–631, 1980.
 - [61] T. N. Huynh, L. Nguyen, and L. P. Barry, "Phase noise characterization of SGDBR lasers using phase modulation detection method with delayed self-heterodyne measurements," *J. Light. Technol.*, vol. 31, no. 8, pp. 1300–1308, 2013.
 - [62] T. N. Huynh, L. Nguyen, and L. P. Barry, "Delayed self-heterodyne phase noise measurements with coherent phase modulation detection," *IEEE Photonics Technol. Lett.*, vol. 24, no. 4, pp. 249–251, 2012.
 - [63] M. Al-Qadi, M. O'Sullivan, C. Xie, and R. Hui, "Phase Noise Measurements and Performance of Lasers with Non-White FM Noise for Use in Digital Coherent Optical Systems," *J. Light. Technol.*, vol. 38, no. 6, pp. 1157–1167, 2020.
 - [64] H. Asghar, E. Sooudi, M. Aslam Baig, and J. G. McInerney, "Recent advances in stabilization of mode-locked quantum dash lasers at 1.55 μm by dual-loop optical feedback," *Opt. Laser Technol.*, vol. 122, no. July 2019, p. 105884, 2020.
 - [65] R. Rosales, K. Merghem, A. Martinez, F. Lelarge, A. Accard, and A. Ramdane, "Timing jitter from the optical spectrum in semiconductor passively mode locked lasers," *Opt. Express*, vol. 20, no. 8, p. 9151, 2012.
 - [66] Y. Mao, Z. Lu, J. Liu, P. J. Poole, and G. Liu, "Pulse Timing Jitter Estimated From Optical Phase Noise In Mode-lock Semiconductor Quantum Dash Lasers," *J. Light. Technol.*, pp. 1–1, 2020.
 - [67] N. Eiselt *et al.*, "Real-time 200 Gb/s (4×56.25 Gb/s) PAM-4 transmission over 80 km SSMF using quantum-dot laser and silicon ring-modulator," *2017 Opt. Fiber Commun.*

Conf. Exhib. OFC 2017 - Proc., pp. 3–5, 2017.

- [68] A. Moscoso-Mártir *et al.*, "8-channel WDM silicon photonics transceiver with SOA and semiconductor mode-locked laser," *Opt. Express*, vol. 26, no. 19, p. 25446, 2018.
- [69] V. V. *et al.*, "Mitigation of relative intensity noise of quantum dash mode-locked lasers for PAM4 based optical interconnects using encoding techniques," *Opt. Express*, vol. 25, no. 1, 2017.
- [70] C. Browning *et al.*, "56 Gb/s/λ over 13 THz frequency range and 400G DWDM PAM-4 transmission with a single quantum dash mode-locked laser source," *Opt. Express*, vol. 28, no. 15, p. 22443, 2020.
- [71] Y. Pan, L. Yan, A. Yi, L. Jiang, W. Pan, and B. Luo, "Simultaneous demultiplexing of 2 × PDM-PAM4 signals using simplified receiver," *Opt. Express*, vol. 27, no. 3, p. 1869, 2019.
- [72] J. U. N. K. Kemal *et al.*, "Coherent WDM transmission using quantum- dash mode-locked laser diodes as multi- wavelength source and local oscillator," vol. 27, no. 22, pp. 31164–31175, 2019.
- [73] G. Liu *et al.*, "A Passively Mode-Locked Quantum Dot Laser with 10.8 Tbit/s Transmission over 100-km SSMF," *2020 Opt. Fiber Commun. Conf. Exhib. OFC 2020 - Proc.*, pp. 21–23, 2020.
- [74] P. Marin-Palomo *et al.*, "Comb-based WDM transmission at 10 Tbit/s using a DC-driven quantum-dash mode-locked laser diode," *Opt. Express*, vol. 27, no. 22, p. 31110, 2019.
- [75] T. N. Huynh, A. T. Nguyen, W. C. Ng, L. Nguyen, L. A. Rusch, and L. P. Barry, "BER performance of coherent optical communications systems employing monolithic tunable lasers with excess phase noise," *J. Light. Technol.*, vol. 32, no. 10, pp. 1973–1980, 2014.
- [76] J. M. Estarán *et al.*, "140/180/204-Gbaud OOK Transceiver for Inter- and Intra-Data Center Connectivity," *J. Light. Technol.*, vol. 37, no. 1, pp. 178–187, 2019.

Conclusion

In this thesis we have studied the theory, design and characterization of novel semiconductor laser sources for future digital coherent systems.

I. Scope of the thesis

In an introductory chapter we have seen that coherent transmission is becoming of great importance to enhance datacenter network performances. While the modulating signal is coded both in phase and amplitude, we have seen that only laser phase noise would be the main limitation of coherent links based on formats up to 64QAM. We remind here that the 400GBase-ZR standard, being currently deployed in the network, requires compact and efficient digital coherent modules operating at 64 Gbaud with dual-polarization 16QAM formats. We have shown, using Monte-Carlo simulations, that this interface would require ~ 200 kHz linewidth lasers if a lightweight DSP is used. Thus, compact and efficient narrow linewidth sources are already of great interest for today's datacenter coherent interconnects. Moreover, coherent transceivers operating for next generation 800G interfaces are becoming a hot topic and only a few research results have already demonstrated 800 Gbit/s single line coherent transmission. As it would be very challenging to reach this data rate by leaning on the bandwidth improvements of transceivers, more advanced QAM formats such as 64QAM or probabilistic shaped constellations format are essential. Hence the transmitter linewidth requirement of future coherent systems might extensively progress to the kHz range.

It is widely acknowledged that low noise lasers can only be fabricated within low loss photonic platforms. Hence, in this thesis we relied on the integration of III-V gain medium on the top of silicon wafers to design and produce simple yet efficient laser sources with coherent compliant linewidth and ideal integration with transceivers. Only in the last chapter of the thesis the phase noise reduction of a comb laser was studied using a free-space testbed, while on-going works focus on the integration of the presented device on the III-V on Silicon platform.

II. III-V on Silicon DFB with very low phase noise

In a first chapter we have numerically and experimentally studied a new class of ultra-low noise III-V on Silicon DFB lasers. While these compact narrow-linewidth sources were first introduced in 2014 by Prof. Yariv's research group, in this thesis we have proposed a numerical model yielding optimal grating design. This model can efficiently compute high quality factor (HQ) laser modes and then extract several useful quantities such as threshold gain, photon lifetime, mirror losses, etc. We could hence deduce grating parameters which

optimize both laser linewidth and output power while maintaining an ideal single-mode regime. Moreover, even though the proposed model does not take into account radiative losses, non-linear effects and non-uniform longitudinal field repartition, measurements results have proven that it was relatively efficient to estimate laser performances.

Future theoretical work could include these more complex effects in order to apprehend the intrinsic limits of the III-V on Silicon DFB lasers. In addition to this numerical study, more technological and engineering work should be performed aiming in particular at increasing these DFB output power. Indeed, the III-V Lab HQ cavity devices are currently emitting <10 mW per facet but coherent technology would greatly benefit from a power increase to the 50 mW range. Finally, the direct integration of this DFB laser in a silicon based coherent transceiver, which should be ideal, has not yet been demonstrated. These compact light sources could also be used in a wider scope of coherent technology rather than datacenter interconnect only. Compared to bulkier extended cavity lasers, they are more robust to operating conditions, but at the cost of not being widely tunable. Hence, they could be of great interest in self-homodyne application such as coherent Lidar, or broadcast applications not requiring DWDM channels. Moreover the concept of the "photonic well grating", which was used to improve phase noise properties, could be extended to other different DFB designs such as :

- Directly modulated lasers using a "mid quality factor" photonic crystal cavity [1].
- III-V monolithic DFB lasers robust to phase errors occurring in the grating process.
- Narrow linewidth RF tone generation using e.g. two injection locked HQ DFBs.

III. Fast Tunable & Narrow Linewidth ECL

In a second chapter we presented a novel design of fast tunable laser (FTL) [2] enabling burst mode coherent transmission. While tunable lasers capable of reconfiguring their wavelength in the nanosecond timescale have already been reported for more than a decade, here we have presented a new compact design with noise properties supporting coherent format up to 32QAM. After describing the principle of the FTL we have introduced a new measurement method to precisely characterize laser switching dynamics. With this method we first demonstrated FTL switching and stabilization time below two nanoseconds, later we have shown that this laser parasitic thermal drift was manageable in a coherent system. We then studied the linewidth properties of the FTL experimentally and theoretically using the formalism introduced by Kazarinov and Henry. At the end we reported on optical coherent slot switching (COSS) experiments performed with the Nokia Bell Labs Networking department, and we demonstrated record results corresponding to a tenfold improvement in latency while also using a two-fold higher data throughput than the state of the art.

However, in this thesis chapter we have not modelled laser switching properties. The author believes that a two modes rate equation model would be suitable to study most switching

dynamics phenomenon while a more complex travelling wave laser model would be required to precisely evaluate switching properties in a timescale below 100ps (corresponding to the laser roundtrip time). Moreover an interesting theoretical work integrating both nonlinear and free carrier effect in the ring resonators could be performed in order to study the stability and linewidth properties of silicon based extended cavity lasers.

It would also be of great interest to perform additional FTL processing run to prevent a fabrication related issue which resulted in a high PIN contact resistance. These lasers could be later packaged to be used as demonstrators which could potentially show the improvement of data traffic in both mega-datacenters and disaggregated networks. In this case, demonstrating a fully packaged nanosecond reconfigurable coherent transceiver would be an outstanding improvement, as state of the art datacenter transceivers are only reconfigurable on a 1 second timescale.

IV. MLL stabilisation using optical feedback

In a final chapter we thoroughly studied the effect of optical feedback on phase noise of single section quantum dash lasers [3]. While several papers had already reported the beneficial effect of feedback in stabilizing two section quantum dot mode locked lasers (MLL) very few results describing the influence of optical self-injection were reported in single section quantum dash MLLs. In a first part we have characterized several feedback regimes as a function of its strength and delay, and we have notably shown that the "coherent" regime can allow drastic RF beat tone and optical longitudinal mode narrowing. After thoroughly studying the MLL phase noise performances improvement under coherent feedback, we demonstrated that this regime can be valuable in coherent communication systems based on phase-locked loop carrier phase recovery. We finally showed that a MLL under coherent feedback could potentially support DWDM coherent links operating at few Tbit/s.

Additional technological studies aiming to integrate a QDash gain section on the top of a Silicon wafer could be performed to fabricate single section hybrid MLLs. This could allow the realisation of ultra compact low noise comb sources as silicon passive waveguides could be used to provide optical stabilisation loops. Later, the integration of these stable comb sources with passive waveguides, modulators and amplifiers, could provide very low cost transceivers suitable for Tbit/s applications.

V. General conclusion

As a general conclusion, in this thesis we have shown that passive/active integration through the III-V on silicon platform was a promising technology to devise low-noise lasers enabling low-cost novel coherent applications. Coherent formats may transmit higher throughput on a longer reach than direct modulation format at the cost of complexity and price. However, integrated technologies are becoming more and more mature so coherent

transceivers are moving from low volume application to mass market ones, as they become less and less expensive.

In this thesis the designed lasers target coherent link in datacenter networks. However, new applications based on disaggregated networks such as edge (& cloud)-computing, or even 5G front hauling may also benefit from the high performances of low-cost coherent systems. The HQ DFB presented here is an ultra simple yet stable laser, it could be useful to decrease the complexity of traditional coherent links to introduce coherent format in the passive optical network. Then, the more complex FTL might be of great interest to virtual point-to-point network as it enables all optical routing, being much less expensive and much more efficient than electrical routing technology. Finally the integrated version of the last device presented in the thesis, might be useful to drastically decrease the cost of Tbit/s fibered links.

VI. References

- [1] T. Verolet *et al.*, "III-V on SOI distributed feedback laser with very low frequency chirp for 10 Gb/s C-band access network," *ECOC*, vol. 2019, no. CP765, pp. 4–6, 2019.
- [2] T. Verolet *et al.*, "Hybrid III-V on Silicon Fast and Widely Tunable Laser Based on Rings Resonators with PIN Junctions," *Asia Commun. Photonics Conf. ACP*, vol. 2018-Octob, no. 644453, pp. 2018–2020, 2018.
- [3] T. Verolet *et al.*, "Mode Locked Laser Phase Noise Reduction Under Optical Feedback for Coherent DWDM Communication," *J. Light. Technol.*, vol. 38, no. 20, pp. 5708–5715, 2020.

Annex A :

A possible justification of laser rate equations

Below lies a possible derivation of the laser rate equation emphasizing their validity only in the vicinity of a cavity mode. The laser diode considered in this section is modeled by a simple Fabry-Pérot cavity (Fig.A), and we assume that it emits on a single longitudinal mode at the optical pulsation ω_0 . Similar to [1], the lasing mode is studied at a laser facet ($z = 0$) and in this reference plane, the field is described as a stationary narrowband signal centered at ω_0 and written $E(t) = E_0(t)e^{j\omega_0 t}$ with $E_0(t)$ its complex amplitude.

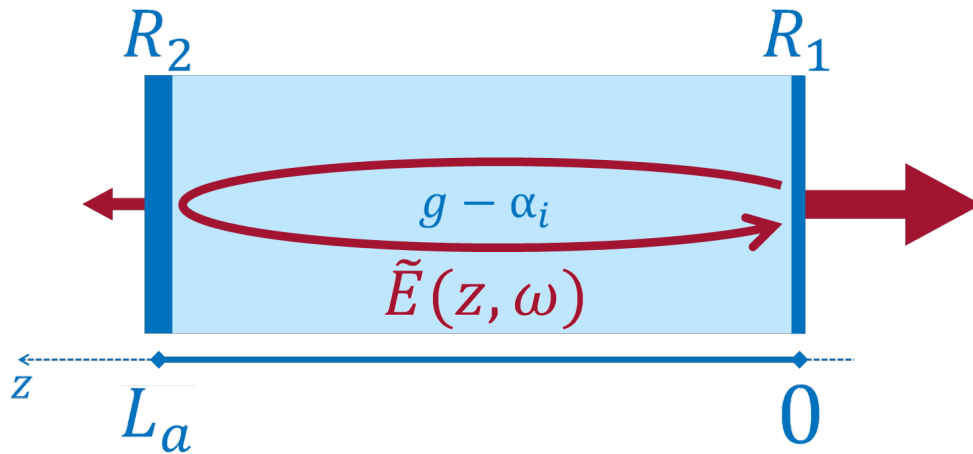


Fig.A Laser diode schematic

When travelling inside the cavity of length L_a , the field is amplified in the gain medium due to stimulated emission. This is modeled by a white modal gain g , mostly depending on the carrier density N . During propagation, the lasing mode also undergoes losses of coefficient α_i , (considered white) and mirrors of reflectivity $R_{i=1,2} \in [0, 1]$ are used to reflect the field back into the cavity.

After one cavity roundtrip, a field Fourier component \tilde{E} at the optical pulsation ω is multiply by the transfer function (ω, N) :

$$H(\omega, N) = \sqrt{R_1 R_2} e^{-j\beta(\omega, N)2L_a} e^{(g(N) - \alpha_i)L_a} \quad (A.1)$$

where $\beta(\omega, N)$ is the field propagation constant. Moreover, spontaneous emission can be coupled into the lasing mode. It is assumed that spontaneous emission events are not correlated, occurs at random time $\{t_i\}$ at an average rate R_{sp} . It is supposed that the field transverse repartition stays constant along the cavity propagation axis, and longitudinal effects such as spatial hole burning are neglected. In this case $R_{sp} = v_g g n_{sp}$, with v_g the lasing mode group velocity and n_{sp} the population inversion factor. Under these assumptions, these events can be modeled as a Langevin force expressed by (A.2).

$$F(t) = \sum_i a_0 e^{j(\omega_0 t + j\psi_i)} \delta(t - t_i) \quad (A.2)$$

with a_0 an unit field amplitude corresponding to the equivalent field of a "single-photon" and ψ_i is a random phase. During one cavity roundtrip, the frequency components of additive noise term can be written as :

$$\tilde{A}(\omega) = \frac{1}{v_g} \oint_{z=0}^0 \tilde{F}(\omega) dz = \tau_{RT} \tilde{F}(\omega) \quad (A.3)$$

$\tau_{RT} = 2L_a/v_g$ being the cavity roundtrip time and $\tilde{F}(\omega)$ the frequency component of the Langevin force. Hence, after one cavity roundtrip, the stationary condition of a field Fourier component \tilde{E} at the optical pulsation ω correspond to :

$$\tilde{E}(\omega) = H(\omega, N) \tilde{E}(\omega) + \tau_{RT} \tilde{F}(\omega) \quad (A.4)$$

The resonant condition is obtain at the zero of $1 - H(\omega, N)$ corresponding to the pair of value (ω_0, N_0) . In this case the longitudinal mode propagation constant $\beta(\omega_0, N_0)$ and threshold gain $g(N_0)$ are given by :

$$\beta(\omega_0, N_0) = m_0 \frac{\pi}{L_a} \quad (A.5)$$

$$g(N_0) = \alpha_{eq} \stackrel{\text{def}}{=} \alpha_i + \frac{1}{2L_a} \ln\left(\frac{1}{R_1 R_2}\right) \quad (A.6)$$

With m_0 being a positive integer, and α_{eq} corresponds to equivalent optical losses including both mirror losses and propagation losses. Close to a given resonance the modal gain and propagation constant can be expanded as :

$$g(N) = \alpha_{eq} + \Delta g \quad (A.7)$$

$$\beta(\omega, N) = m_0 \frac{\pi}{L_a} + \frac{\Omega}{v_g} - \alpha_H \frac{\Delta g}{2} \quad (A.8)$$

With Δg being the gain excess relative to threshold gain, $\Omega \stackrel{\text{def}}{=} \omega - \omega_0$ the pulsation detuning from the resonant one, v_g the group velocity and α_H the phase/amplitude coupling factor, also referred as the linewidth broadening or Henry factor. These quantities are detailed in the following :

$$\Delta g \stackrel{\text{def}}{=} \Delta N \frac{\partial g}{\partial N} \quad (\text{A.9})$$

$$v_g \stackrel{\text{def}}{=} \frac{\partial \beta^{-1}}{\partial \omega} \quad (\text{A.10})$$

$$\alpha_H \stackrel{\text{def}}{=} -2 \frac{\omega_0}{c} \frac{\frac{\partial n}{\partial N}}{\frac{\partial g}{\partial N}} \quad (\text{A.11})$$

By injecting the expression of modal gain and propagation constant into the stationary condition, it is found that :

$$\tilde{E}_0(\Omega) e^{-j\Omega\tau_{RT} + \frac{\Delta G}{2}(1+j\alpha_H)\tau_{RT}} + \tau_{RT}\tilde{F}_0(\Omega) = \tilde{E}_0(\Omega) \quad (\text{A.12})$$

$\Delta G \stackrel{\text{def}}{=} v_g \Delta g$ while $\tilde{E}(\omega)$ and $\tilde{F}(\omega)$ have been replaced by their baseband representation $\tilde{E}_0(\Omega)$ and $\tilde{F}_0(\Omega)$. Under the assumptions $\Omega \ll 1/\tau_{RT}$ and $\Delta G \ll 1/\tau_{RT}$ we can obtain (A.13) using a first order expansion. Note that the condition $\Omega \ll 1/\tau_{RT}$ means that rate equation are only valid at timescale much larger than a cavity roundtrip time.

$$-j\Omega\tilde{E}_0(\Omega) + \frac{\Delta G}{2}(1+j\alpha_H)\tilde{E}_0(\Omega) + \tilde{F}_0(\Omega) = 0 \quad (\text{A.13})$$

In the time domain (A.13) translates to :

$$\frac{dE_0}{dt} = \frac{\Delta G}{2}(1+j\alpha_H)E_0(t) + F_0(t) \quad (\text{A.14})$$

Finally, the field complex amplitude can be expressed as : $E_0(t) = A(t)e^{j\varphi(t)}$. And after injecting the expression of the field complex amplitude in the previous equation and separating the orthogonal terms, we find :

$$\frac{dA}{dt} = \frac{\Delta G}{2}A + F_{E_0//}(t) \quad (\text{A.15})$$

$$\frac{d\varphi}{dt} = \alpha_H \frac{\Delta G}{2} + \frac{1}{A}F_{E_0\perp}(t) \quad (\text{A.16})$$

with $F_{E_0//}(t) = \text{Re}(F_0(t)e^{-j\varphi(t)})$ and $F_{E_0\perp}(t) = \text{Im}(F_0(t)e^{-j\varphi(t)})$ being the collinear and perpendicular term of the Langevin force taken relatively to E_0 . It is more convenient to rewrite the equation governing A using the photon number $= |A|^2/a_0^2$. And in this case we finally obtain :

$$\frac{dP}{dt} = \Delta G P + R_{sp} + F_P(t) \quad (A.15)$$

$$\frac{d\varphi}{dt} = \alpha_H \frac{\Delta G}{2} + F_\varphi(t) \quad (A.16)$$

With F_P and F_φ the Langevin terms detailed in the following. Note that R_{sp} is related to the non zero value of $\langle A(t)F_{E_0//}(t) \rangle$ with $\langle \dots \rangle$ standing for average.

$$F_P(t) = \frac{A(t)F_{E_0//}(t)}{a_0^2} - \frac{\langle A(t)F_{E_0//}(t) \rangle}{a_0^2} \quad (A.17)$$

$$\langle A(t)F_{E_0//}(t) \rangle / a_0^2 = R_{sp} \quad (A.18)$$

$$F_\varphi(t) = \frac{1}{A} F_{E_0\perp}(t) \quad (A.19)$$

The reader may find the justification of (A.18) in [2], while the diffusion coefficient of F_P and F_φ can be obtain with the procedure of [3]. Finally, the rate equation governing carrier density N is written in (A.20), and can be justified by considering the variation of N during a time increment Δt . This resulting ΔN correspond to the carrier density generated with the pump current $(I\Delta t)/(qV)$ minus the carrier density which recombined to generate photons $GP\Delta t$ minus the recombination due to non radiative process $N\Delta t/\tau_N$.

$$\frac{dN}{dt} = \frac{I}{qV} - \frac{N}{\tau_N} - GP + F_N(t) \quad (A.20)$$

Annex B :

Wave propagation in periodic media

In this annex we remind the basis of wave propagation inside a periodic media, and we detail the relation between the photonic band structure and corrugated waveguide mode parameters. The reader may refer to the chapter 12 of A. Yariv *et. al* [4] for more detailed explanations.

First, a transverse mode \tilde{E} with pulsation ω_0 propagating inside a corrugated waveguide of period Λ is given by the solution of the 1D Helmholtz equation :

$$\frac{d\tilde{E}}{dz} + \frac{\omega_0^2}{c^2} n(z)^2 \tilde{E} \quad (B.1)$$

with $n(z)$ being a periodically perturbed effective index. For a propagation constant close to the Bragg resonance, the field can be expanded as a sum of forward and backward propagating waves :

$$\tilde{E} = \vec{E}(z, \omega) e^{j\frac{\pi}{\Lambda}z} + \bar{\vec{E}}(z, \omega) e^{-j\frac{\pi}{\Lambda}z} \quad (B.2)$$

while the periodic effective index can then be written using its Fourier series :

$$n(z)^2 = n_{mean}^2 + \sum_{m: odd} a_m e^{-j\frac{m\pi}{\Lambda}z} \quad (B.3)$$

with n_{mean} , the average effective index. After inserting (B.2) and (B.3) in (B.1), keeping only the slow varying components of \vec{E} , $\bar{\vec{E}}$ and separating phase matched terms we obtain :

$$\frac{d}{dz} \begin{pmatrix} \vec{E} \\ \bar{\vec{E}} \end{pmatrix} = j \begin{pmatrix} \delta & \kappa \\ -\kappa & -\delta \end{pmatrix} \begin{pmatrix} \vec{E} \\ \bar{\vec{E}} \end{pmatrix} = j \bar{C} \begin{pmatrix} \vec{E} \\ \bar{\vec{E}} \end{pmatrix} \quad (B.4)$$

δ being the detuning (in wavenumber) from the Bragg resonance given by (B.5), and κ the grating strength that can be approximate by (B.6) in the case of a sinusoidal corrugation.

$$\delta = \left(\omega_0 - \frac{\pi c}{\Lambda n_{mean}} \right) \frac{n_{mean}}{c} \quad (B.5)$$

$$\kappa = \frac{\pi \Delta n}{4 \Lambda n_{\text{moy}}} \quad (B.6)$$

In (B.5) and (B.6), Δn correspond to the effective index corrugation amplitude. Eigenmodes of the structure may be written :

$$\begin{pmatrix} \vec{E} \\ \vec{E} \end{pmatrix} = \begin{pmatrix} \vec{E}_q \\ \vec{E}_q \end{pmatrix} e^{jqz} \quad (B.7)$$

After injecting the eigenmode in (B.4), we finally found that q is given by :

$$q = \pm \sqrt{\delta^2 - \kappa^2} \quad (B.8)$$

For $|\delta| < \kappa$, q is imaginary, the propagating field is evanescent and reflected back. Optical frequencies giving q imaginary are inside the photonic bandgap (or stopband) which is centered in ν_B and its range is Δf . They are given by (B.10) :

$$\nu_B = \frac{c}{2 \Lambda n_{\text{mean}}} \quad (B.9)$$

$$\Delta f = \frac{\kappa c}{\pi n_{\text{mean}}} \quad (B.10)$$

As electrons in periodic structure, we define a photonic valence band and photonic conduction band, which extrema $f_{v,c}$ are given by :

$$f_{v,c} = \nu_B \mp \frac{\Delta f}{2} \quad (B.11)$$

Annex C :

Generalization of rate equations for complex cavity

In this annex, we generalize standard laser rate equation to more complex cavity. In this case we resume the analysis of Annex A at (A.4) by considering a general cavity transfer function H instead of the one corresponding to the simple Fabry-Pérot cavity.

$$\tilde{E}(\omega) = H(\omega, g)\tilde{E}(\omega) + \tau_{RT}\tilde{F}(\omega) \quad (C.1)$$

Using the same method as in Annex A, rate equations are derived by the first order expansion of the resonant condition $H(\omega_0, g_0) = 1$. Thus, the approximations mentioned in Annex A are still essentials to obtain the rate equations. For instance, we recall that in Annex A the derivation was valid only in a frequency band which upper limit is much below the laser roundtrip frequency. However, in this more general case we require a stronger condition concerning the valid frequency range upper limit, indeed we need to approximate $H(\omega, g)$ by a linear equation (C.2) meaning that the optical response of the passives forming the cavity *must* be linearized. Hence, the more general rate equation derived here will only be valid on frequency band narrower than the optical filter bandwidth used to ensure single mode lasing.

$$H(\omega_0 + \Omega, g_0 + \Delta g) = 1 + \Omega \partial_\omega H + \Delta g \partial_g H \quad (C.2)$$

In (C.2) the notations $\partial_{\omega, g} H$ correspond to the derivative of H with respect to ω, g taken at (ω_0, g_0) . After injecting (C.2) in (C.1) and translating into the time domain we obtain (C.3) with E_0 the complex amplitude (or baseband representation) of the laser emitted field.

$$-j \partial_\omega H \frac{dE_0}{dt} - \Delta g \partial_g H E_0 = F(t) \quad (C.3)$$

Then by writing the field complex amplitude in terms of modulus and phase : $E_0 = A e^{j\varphi}$, we can obtain :

$$j \partial_\omega H \frac{dA}{dt} - \partial_\omega H \frac{d\varphi}{dt} A + \Delta g \partial_g H A = -F(t)e^{-j\varphi} \quad (C.4)$$

We recall that, in Annex A, the equations governing laser photon density and field phase were obtained after separating real and imaginary terms of a complex differential equation governing laser emitted field. As the terms $\partial_{\omega, g} H$ may be complex we need to write them

using their Cartesian form $\partial_{\omega,g}H = \text{Re}(\partial_{\omega,g}H) + j \text{Im}(\partial_{\omega,g}H)$ before separating orthogonal terms. By doing so, we obtain :

$$-\text{Im}(\partial_{\omega}H) \frac{dA}{dt} - \text{Re}(\partial_{\omega}H) \frac{d\varphi}{dt} A - \text{Re}(\partial_g H) \Delta g A = -\text{Re}(F(t)e^{-j\varphi}) \quad (C.5)$$

$$-\text{Im}(\partial_{\omega}H) \frac{d\varphi}{dt} A + \text{Re}(\partial_{\omega}H) \frac{dA}{dt} + \text{Im}(\partial_g H) \Delta g A = -\text{Im}(F(t)e^{-j\varphi}) \quad (C.6)$$

Finally, as in Annex A, it is more convenient to write the laser rate equation using of photon density $P = A^2$. Hence, we multiply (C.5) and (C.6) by $2A$, and after noticing that $2A dA/dt = dP/dt$, we obtain :

$$-\text{Im}(\partial_{\omega}H) \frac{dP}{dt} - 2P \text{Re}(\partial_{\omega}H) \frac{d\varphi}{dt} = 2\text{Re}(\partial_g H) \Delta g P - 2A \text{Re}(F(t)e^{-j\varphi}) \quad (C.7)$$

$$-\text{Im}(\partial_{\omega}H) \frac{d\varphi}{dt} + \text{Re}(\partial_{\omega}H) \frac{1}{2P} \frac{dP}{dt} = \text{Im}(\partial_g H) \Delta g - \frac{1}{A} \text{Im}(F(t)e^{-j\varphi}) \quad (C.8)$$

After defining equivalent Langevin forces $F_{p_{eq}}, F_{\varphi_{eq}}$ and equivalent spontaneous emission rate $R_{sp_{eq}}$, we obtain :

$$\frac{dP}{dt} + 2P \frac{\text{Re}(\partial_{\omega}H)}{\text{Im}(\partial_{\omega}H)} \frac{d\varphi}{dt} = -2 \frac{\text{Re}(\partial_g H)}{\text{Im}(\partial_{\omega}H)} (g - g_{th}) P + R_{sp_{eq}} + F_{p_{eq}} \quad (C.9)$$

$$\frac{d\varphi}{dt} - \frac{1}{2P} \frac{\text{Re}(\partial_{\omega}H)}{\text{Im}(\partial_{\omega}H)} \frac{dP}{dt} = - \frac{\text{Im}(\partial_g H)}{\text{Im}(\partial_{\omega}H)} (g - g_{th}) + F_{\varphi_{eq}} \quad (C.10)$$

References

- [1] B. Tromborg, H. Olesen, X. Pan, and S. Saito, "Transmission line description of optical feedback and injection locking for fabry-perot and dfb lasers," *IEEE J. Quantum Electron.*, vol. 23, no. 11, pp. 1875–1889, 1987, doi: 10.1109/JQE.1987.1073251.
- [2] B. Tromborg, H. Olesen, and X. Pan, "Theory of Linewidth for Multielectrode Laser Diodes with Spatially Distributed Noise Sources," *IEEE J. Quantum Electron.*, vol. 27, no. 2, pp. 178–192, 1991, doi: 10.1109/3.78219.
- [3] C. H. Henry, "Theory of the Linewidth of Semiconductor Lasers," *Quantum*, no. 2, pp. 259–264, 1982.
- [4] A. Yariv and P. Yeh, *Photonics: Optical Electronics in Modern Communications*, 6th ed. Oxford University Press, 2007.

Titre : Diodes Lasers hybrides pour les communications cohérentes avancées dans les datacenters

Mots clés : Diode laser, Transmission cohérente, Circuit Photonique, Bruit de phase, Peigne de fréquence.

Résumé : Alors que le trafic de donnée intra-datacenter augmente exponentiellement, de nouvelles générations de transpondeurs optiques sont étudiées. Ces transpondeurs doivent délivrer un fort débit, tout en restant faible consommation. Les technologies cohérentes –sur lesquelles sont établies les liens intercontinentaux- doivent voir leur taille et bilan énergétique réduits. L'utilisation de formats cohérents avancés améliorera les performances des systèmes cohérents tout en les gardant compacts et efficaces énergétiquement. Cependant ces formats peuvent être déployés seulement si des lasers faibles bruits sont utilisés. C'est dans ce cadre que cette thèse étudie la réduction du bruit de phase de trois types de diodes lasers. Premièrement, nous étudions un nouveau type de laser à rétroaction distribué ayant une faible largeur de raie.

Des simulations montrant les paramètres de conceptions optimaux de ce type de laser III-V/Si sont présentées. Dans le chapitre suivant, nous analysons les propriétés de reconfiguration rapide de lasers accordables faible bruit. Ici, nous proposons d'abord une nouvelle méthode de mesures permettant d'analyser précisément un saut de mode, ensuite nous présentons des résultats record de transmission cohérentes de paquets optiques. Dans un dernier chapitre, nous montrons que la rétroaction optique permet de stabiliser un laser à verrouillage de mode. Après avoir analysé les différents régimes de fonctionnement, nous confirmons les hautes performances de lien de communication cohérente utilisant ces lasers peigne de fréquence.

Title : Hybrid Semiconductor Lasers for Advanced Coherent Formats in Datacenter Interconnects

Keywords : Laser diode, Coherent transmission, Photonic integrated circuit, Phase noise, Frequency comb.

Abstract : As data traffic is exponentially increasing in datacenters, new generation of mass producible optical transceivers delivering high data throughput at very low energy consumption are required. Optical coherent technology has been widely used in the past decade to support intercontinental data traffic, as it benefits from higher performance over direct modulation systems though at the cost of complexity and price. To be efficiently used in datacenters, the size and energy consumption of coherent transceivers need to be scaled down while keeping relatively high data throughput. This could be achieved using higher order coherent formats, improving the transmission link spectral efficiency. However, these advanced communication formats can only be supported by low noise lasers. This thesis hence focuses on the phase noise optimization of three types of compact laser diodes using passive/active integration suitable for datacenter interconnects.

First, a novel design of III-V/Si narrow linewidth high quality factor DFB laser based on a chirped grating is thoroughly studied. Detailed numerical simulations that yield grating parameters leading to optimal performances are presented for the first time to our knowledge. In a second study, we investigate the fast switching properties of a newly designed narrow linewidth extended cavity III-V/Si laser. After detailing the laser operating principles, we propose an experimental method to precisely characterize laser switching dynamics. Record coherent slot switching experiments are then demonstrated using this new laser. In the final part, we first investigate optical feedback regimes in single section quantum dash MLL and show that coherent feedback can induce a drastic phase noise reduction of the MLL longitudinal modes. The potential use of this comb source in a DWDM coherent link is demonstrated through highly spectrally efficient transmission experiments.